FACULTY OF ENGINEERING TECHNOLOGY

# MILD MICROSCOPIC WEAR MODELING IN THE BOUNDARY LUBRICATION REGIME

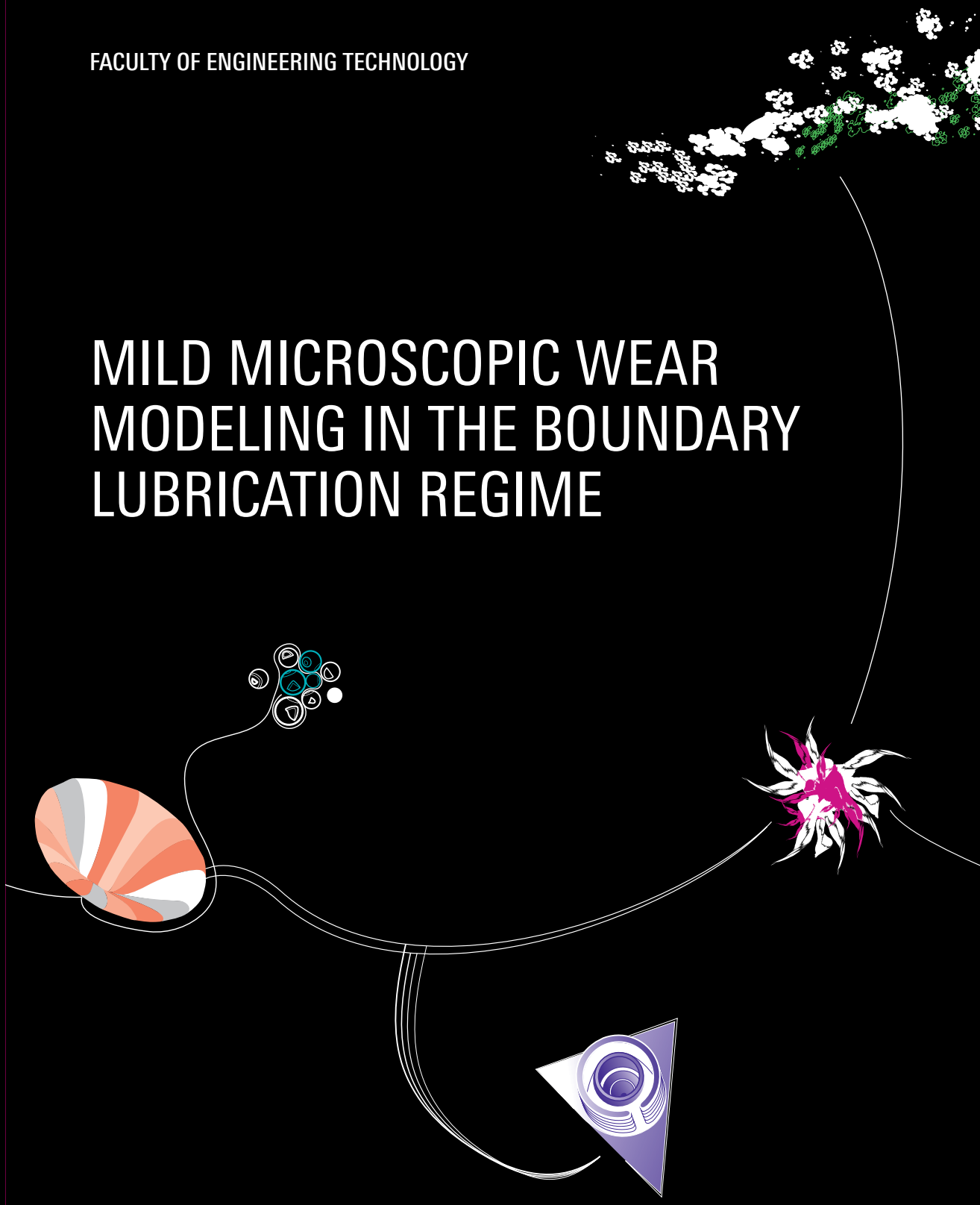

UNIVERSITY OF TWENTE.

R. Bosman

# Mild Microscopic Wear Modeling in the Boundary Lubrication Regime

**Rob Bosman**

De promotiecomissie is als volgt opgesteld:

| | | |
|---|---|---|
| prof.dr.ir. F.Eising | Universiteit Twente | voorzitter en secretaris |
| prof.dr.ir.D.J. Schipper | Universiteit Twente | Promotor |
| prof.dr.ir. T.H. v.d. Meer | Universiteit Twente | |
| prof.dr.ir. J Huétink | Universiteit Twente | |
| prof.dr. D. Nelias | INSA Lyon | |
| prof.dr.ir. P.M. Lugt | Luleå Technical University | |

Bosman, Rob
Mild Microscopic Wear Modeling in the Boundary Lubrication Regime
Ph.D. Thesis, University of Twente, Enschede, the Netherlands,
January 2011
ISBN: 978-90-9025967-3

# MILD WEAR MODELING IN THE BOUNDARY LUBRICATION REGIME

## PROEFSCHRIFT

Ter verkrijging van
de graad van doctor aan de Universiteit van Twente,
op gezag van de rector magnificus,
prof.dr. H. Brinksma,
volgens besluit van het College voor Promoties
in het openbaar te verdedigen
op vrijdag 28 januari 2011 om 15.00 uur

door

Rob Bosman
geboren 22 juni 1983
te Roden, Nederland

Dit proefschrift is goedgekeurd door:
de promotor: prof.dr.ir. D.J. Schipper

## Summary

Currently, the increasing demand for smaller and more efficient systems is increasing the stress put on interacting components. This forces components to operate in the boundary lubrication regime. In this lubrication regime, the normal load put on the components is no longer carried by the lubricant but rather by the interacting asperities, and by doing so solid-solid contact is inevitable. This increases the specific wear seen in these types of systems shortening the lifetime of components and increasing maintenance intervals. This decreases the operational times significantly. Therefore, it is of great importance to get a clear understanding of the concept of corrosive wear under these specific conditions.

In this thesis three different aspects of wear are discussed namely: the transition from mild to severe wear, running-in and the steady state mild wear. The first is modeled using a thermal threshold originating from Blok's hypothesis that the transition to adhesive wear is caused by transcending a predefined critical temperature. The model discussed in the current work is based on a numerical thermal model combined with an elastic-plastic contact solver, which are both using the DC-FFT algorithms combined with CGM iterative schemes. In this way the model is able to incorporate mild wear into the thermal and contact calculations while keeping the computational times within a reasonable range. The model is validated through an experimentally determined transition diagram.

Running-in of surfaces is modeled using the hypothesis that an additive rich oil is able to protect the contacting elements from metal to metal contact therefore, the growth rate should be the same or greater than the layer removal rate. This hypothesis is combined with a wear model based on a maximum equivalent strain assumption. This states that for material to be removed both an equivalent plastic strain threshold should be met and that the volume including this strain should reach the surface. To be able to compute the plastic strain, a Semi-Analytical-Contact solver is developed based on a local friction model.

The mild wear model is based on the dynamic chemical balance at the surface. Through mechanical removal the balance is disturbed and the system will restore the balance through chemical reactions between the base material and additives present in the oil. Since the chemical reaction layers are very thin compared to contact regions, it can be assumed that it has only a limited effect on contact conditions. Using this hypothesis, a model is presented to determine the removal rate of the chemical reaction layer and thus the intensity of corrosive wear. The validation of this model is done using model systems.

This thesis is divided into two parts: the first part is a summary of theory presented in the appended papers presented in the second part. This way the reader is able to keep a clear view on the overall goal of the research by reading the first part while the details are discussed in the second part.

# Samenvatting

Door de huidige toename in de vraag naar kleinere en meer efficiënte systemen neemt de belasting op de in contact zijnde componenten toe in deze systemen. Hierdoor moeten de componenten meer en meer onder condities van grenssmering opereren. In dit regime wordt de belasting niet langer door het smeermiddel gedragen, maar door de contact makende ruwheids toppen. Hierdoor wordt interactie tussen de contact makende oppervlakken onvermijdelijk. De specifieke slijtage aanwezig in deze system neemt toe waardoor de levensduur van de componenten afneemt en de onderhoudsintervallen korter worden. Dit verlaagt de levensduur aanzienlijk. Het is daarom van groot belang om een goed begrip te hebben op wat het concept van corrosieve slijtage onder deze omstandigheden precies inhoud.

In dit proefschrift worden drie verschillende aspecten van slijtage besproken namelijk: de transitie van milde naar ernstige slijtage, inlopen en de stationaire milde slijtage. Het eerste wordt gemodelleerd door gebruik te maken van een thermisch criterium welke voorkomt uit de hypothese van Blok dat de transitie naar ernstige adhesieve slijtage veroorzaakt wordt door het overschrijden van een van te voren gedefinieerde kritische temperatuur. Het model dat in het huidige werk wordt beschreven maakt gebruik van numerieke modellen die gecombineerd worden met elastisch-perfect plastische contact modellen, welke allebei gebruik maken van DC-FFT algoritmes gecombineerd met CGM-iteratie schema's. Op deze manier kan milde slijtage in het model meegenomen worden, zonder dat de rekentijden te hoog worden. Dit model is gevalideerd met een experimenteel bepaald transitiediagram.

Het inlopen van ruwe oppervlakken wordt gemodelleerd door gebruik te maken van de hypothese dat een olie die rijk is aan additieven in staat is om twee in contact zijnde oppervlaken te beschermen tegen metaal-metaal contact. Om dit te doen dient de groei van de grenslaag groter te zijn dan de afname van deze laag. Deze hypothese wordt samengevoegd met een slijtage criterium dat gebaseerd is op plastische rek. Deze hypothese veronderstelt dat aan een tweevoud van voorwaarden voldaan moet worden om materiaal te verwijderen. Ten eerste, moet een kritische equivalente plastische rek overschreden worden. En daarnaast moet dit volume tot aan het oppervlak reiken. Om de plastische rek te bereken wordt gebruik gemaakt van een Semi-Analytisch-Contact (SAM) model gebaseerd op lokale wrijvingsmodellen.

Het milde slijtage model maakt gebruik van de dynamische, chemische balans die aanwezig is aan het oppervlak. Door afname veroorzaakt door mechanische belasting van de chemische laag wordt deze balans verstoord. Het systeem zal deze balans terug proberen te vinden door metaal te souperen. Naar aanleiding van de erg geringe dikte van de chemische lagen aan het oppervlak wordt aangenomen dat dit nauwelijks effect heeft op het contact. Met deze aannames kan de afnamesnelheid van de chemische laag bepaald worden en daarmee de intensiteit van de chemische corrosieve slijtage. Om het model te valideren is er gebruik gemaakt van modelsystemen.

Dit proefschrift is opgedeeld in twee delen: het eerste deel is een samenvatting van de theorie die beschreven staat in het tweede deel. Door het proefschrift zo op te bouwen kan de lezer door het eerste deel te lezen een duidelijk beeld krijgen van het onderzoek, zonder verloren te raken in de details. Deze details worden dan behandeld in het tweede deel.

# Contents

# Part I

# Part II

**Paper A:** Transient Thermal Effects and Heat Partition in Sliding Contacts, R. Bosman and M.B. de Rooij, Journal of Tribology, 2010, Volume 132, Issue 2, (9 pages)

**Paper B:** Mild microscopic wear in the boundary lubrication regime, Materialwissenschaft und Werkstofftechnik, R. Bosman, 2010, Volume 41, Issue. 1, (4 pages).

**Paper C:** On the transition from mild to severe wear of lubricated, concentrated contacts: The IRG (OECD) transition diagram, R. Bosman and D.J. Schipper, Wear, 2010, Volume 269, Issue 7-8, (8 pages)

**Paper D:** Transition from mild to severe wear including running in effects, R. Bosman and D.J. Schipper, accepted for publication in Wear

**Paper E:** Running in of metallic surfaces in the boundary lubricated regime, R. Bosman, J. Hol and D.J. Schipper, resubmitted to Wear in revised form, 31-12-2010.

**Paper F:** Running in of systems protected by additive rich oils, R. Bosman and D.J. Schipper, accepted for publication in Tribology Letters.

**Paper G:** Mild Wear Prediction of Boundary Lubricated Contacts, R. Bosman and D.J. Schipper, submitted to Tribology Letters, 28-10-2010

**Paper H:** Mild Wear Maps for Boundary Lubricated Contacts, R. Bosman and D.J. Schipper, submitted to Wear, 20-12-2010

# Nomenclature

## Abbreviations

| | |
|---|---|
| BL | Boundary Lubrication |
| CGM | Conjugate Gradient Method |
| (E)HL | (Elasto-)Hydrodynamic Lubrication |
| FFT | Fast Fourier Transform |
| ML | Mixed Lubrication |
| NC | Nano-Crystalline |
| ZDDP | Zinc Dithiophosphate |

## Greek Symbols

| | | |
|---|---|---|
| $\alpha$ | [–] | Influence coefficient yield function |
| $\varepsilon_{eq}$ | [–] | Equivalent (plastic) strain |
| $\varepsilon_{ij}$ | [–] | Strain tensor |
| $\Gamma$ | $[m^2]$ | Surface |
| $\phi$ | $[Pa]$ | Yield surface |
| $\lambda$ | [–] | Plastic corrector |
| $\Lambda$ | [–] | Lubrication number |
| $\mu$ | [–] | (local) Coefficient of friction |
| $\rho$ | $[kg/m^3]$ | Density |
| $\sigma$ | [–] | Chapter 1: Standard deviation |
| | $[Pa]$ | Chapter 2-4: Stress |
| $\Theta$ | $[^oC]$ | Temperature |
| $\Omega$ | $[m^3]$ | Volume |

## Sub/Superscripts

| | | |
|---|---|---|
| $\tilde{}$ | [–] | Tilde, FFT |
| $\dot{}$ | [–] | Flux |
| $_i$ | [–] | Dimension, element number |
| $_0$ | [-] | Reference value |

| | | |
|---|---|---|
| $^{pl}_{,pl}$ | [-] | Plastic part |
| $^{e}_{,}{}^{elas}$ | [-] | Elastic part |
| $_{res}$ | [-] | Residual part |
| $_{c}$ | [-] | Contact |

## Roman Symbols

| | | |
|---|---|---|
| C, $C_{ijkl}$ | $[-],[Pa]$ | Concentration, Compliance Matrix |
| $E_f$ | $[Pa]$ | Young's modulus layer |
| $D_{3i}^{n}$ | $[m/Pa]$ | Surface deflection coefficient |
| $E_a$ | $[J]$ | Activation Energy |
| $E$ | $[\,Pa\,]$ | Young's Modulus |
| $F$ | $[N]$ | (Normal) Force |
| $h$ | $[m]$ | (film/layer) thickness |
| $h_1, h_2$ | $[m]$ | Surface profile of body 1,2 |
| $h_f$ | [m] | Fluid film Thickness |
| $H$ | $[Pa]$ | Hardness |
| $k$ | $\left[m^3/(Nm)\right]$ | Specific wear rate |
| $K$ | $[m/\sqrt{s}]$ | (effective) diffusion coefficient |
| $L$ | $[m]$ | Grain size |
| $p(x,y), p_i, p$ | $[Pa]$ | Pressure |
| $R_{eq}$ | $[-]$ | Equivalent Radius |
| $R$ | $[-]$ | Gas Constant |
| $s$ | $[\,m\,]$ | Sliding distance |
| $S_{ijk}^{elas}, S_{ij}^{pl}$ | [-] | Influence Matrix |
| $t$ | $[s]$ | Time |
| $u_j$ | $[m]$ | Displacement in dimension j |
| $V$ | $[m/s]$ | Sliding Velocity |
| $W$ | $[m]$ | Removal of chemical layer |
| $W$ | $[m^3]$ | Volume |
| $W_c$ | [-] | Volumetric percentage |
| X | $[m]$ | Growth of chemical layer |
| $x, y, z$ | $[m]$ | Coordinates of observation point |
| $x', y', z'$ | $[m]$ | Coordinates of excitation point |

# 1. Introduction

Wear in engineering systems containing sliding surfaces is inevitable; however, there are several ways of limiting the amount of wear occurring during the lifetime of a component. Most often, to prevent wear, a lubricant is added to the system. By doing so, different lubrication regimes may be obtained depending on the operating conditions. One of the first to distinguish the different lubrication regimes was Stribeck [1]. For the different regimes, different coefficients of friction are reported and measured. A Stribeck curve is schematically shown in Figure 1-1 in which the coefficient of friction is plotted as a function of the lubrication number defined as [2]:

$$\Lambda = \frac{h_f}{\sigma} \tag{1-1}$$

This number relates the standard deviation *(σ)* of the roughness and film thickness to the lubrication regimes the system is running in. If the film thickness *(h)* formed under the given conditions is greater than the roughness height, the lubrication number will become larger than 3 and the system runs under full film lubrication ((E)HL). If, however, the film thickness formed is in the range of the standard deviation ($0.5 \leq \Lambda \leq 1$) a part of the surface will interact and the system runs under mixed lubrication and the load will be carried by the lubricant as well as the asperities. The final regime is the boundary lubrication, in this case the film thickness formed is significantly smaller than the standard deviation of the roughness and the load will be carried by the asperities rather than by the lubricant.

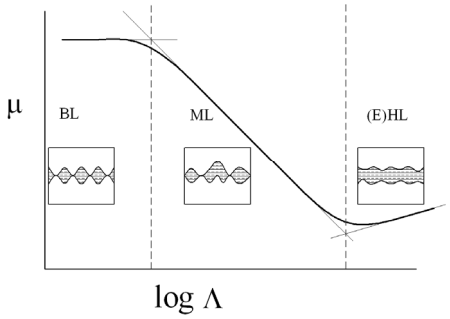


**Figure 1-1:** Stribeck curve, coefficient of friction plotted against sliding velocity for the different lubrication regimes**.**

Concerning wear, the most interesting regime is the boundary lubrication regime. There is an increasing demand for smaller machine components and as a result more and more systems are forced to run in the boundary lubrication regime. Solid to solid contact between the surfaces occurs, which will intensify the wear present in the system.

The current thesis is regarded as a first step in understanding the concept of boundary lubricated wear and the author recognizes that a lot of research still needs to be done to understand the complete concept of wear. In this work the main focus will be on mild oxidative wear and wear during running-in. One of the first steps made at the University of Twente in the research of wear is the PhD work done by van Drogen [3], which will be introduced shortly to give some background on the current work and a general understanding behind the model used, as well as, to show the results of improvements made to the model.

The general hypothesis that the protective nature of a lubricant is limited by a thermal threshold is extended with a mechanical one. The validity of the thermal threshold is a general conclusion following from the work done by van Drogen [3]. In this work the hypothesis made by Blok [4] in the late thirties, that the transition from mild to severe adhesive wear is a thermal phenomenon, is applied with success. On the basis of his models Blok was not able to formulate a uniform failure temperature for a defined system. This was mainly due to the lack of detailed thermal models and sufficient contact models in his time. For this reason he could only predict macroscopic temperatures. However, van Drogen had more sophisticated models at his disposal, which were capable of determining the microscopic temperature as well as the macroscopic one. This enabled him to formulate the total contact temperature as a sum of the macroscopic and microscopic temperature field. It was then concluded that the failure of a boundary lubricated contact was rather a microscopic phenomenon than a macroscopic one.

The models used at microscopic level were deterministic asperity based mechanical and thermal models, which neglect the thermal and mechanical interaction between the neighboring interacting asperities, since each asperity is regarded as a single unique contact spot. Nevertheless, the model greatly improved the prediction of the actual temperature profile occurring at the contact during the transition from mild to severe wear.

The critical temperature used in calculating the transition diagram is determined experimentally by a low speed, low load pin on disk test. Using a low speed and low load it can be ensured that the thermal heating through the dissipation of energy in the contact itself is limited and the oil bath is the main parameter influencing the contact temperature. The test procedure is as follows: on a high temperature CSM pin on disk setup a stainless steel ball and disk are pressed together while sliding under increasing oil bath temperature and the test is stopped if a sudden jump in the coefficient of friction is measured. The temperature at which this occurred is identified as the critical temperature of the oil, see for an example Figure 1-2-a.

The thermal part in the original model of van Drogen was adapted by Bosman, see appended Paper B, to take into account the thermal effect different asperities have on each other by using a multi-scale thermal model, which was based on the thermal model presented in Paper A.

The results show that at the point of transition from mild to severe wear 10 percent of the complete surface transcended the critical temperature rather than only one asperity contact. Another major issue in the modeling of the transition diagram is how to include mild wear. Especially since the mild wear already occurred after a short sliding distance, which will effect the contact situation greatly. In the experiments conducted to determine the transition points, the normal load is not applied instantaneously and this offers the system an opportunity to run in under mild conditions before the full load is reached, see Figure 1-2-b. For more details on the load procedure the reader is referred to the appended Paper B and reference [3].

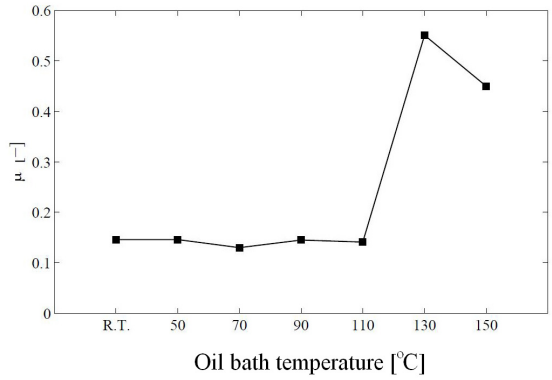


**a)**

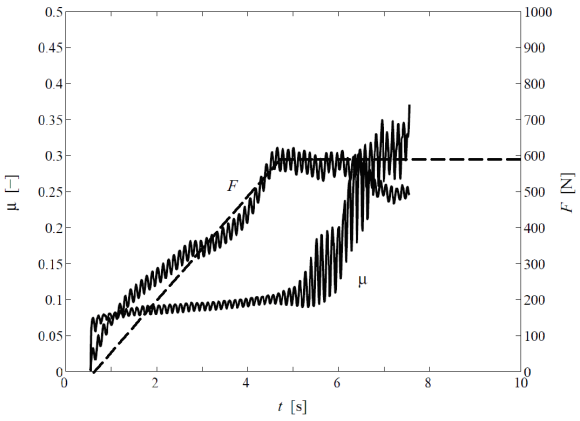


**b)**

**Figure 1-2: a)** Coefficient of friction as a function of the oil bath temperature (reproduced from [3]). For the oil used in this example the critical temperature is set at 130 °C. **b)** Normal load and coefficient of friction as a function of the sliding time for a test resulting in failure. (Dotted line is the load signal used in the simulations.)

To compensate for this effect in the first versions (both van Drogen and Bosman) used an artificially increased macroscopic geometry to compensate for the wear. One of the drawbacks is then the negligence of the influence wear has on roughness level, which will change in reality, however in the model it is assumed constant. To deal with this issue a numerical model was developed and applied in the version of the model discussed in detail in the appended Paper C. The main advantage of this model is that mild wear can be included in a rather easy way; namely applying Archard's linear wear model on a local scale as done in for example [5-7]. In this way, the increasing conformity and wear at roughness level are both included during the running–in period of the system. The results from the theoretical transition diagram are again in good agreement with the experimental results as shown in Figure 1-3.

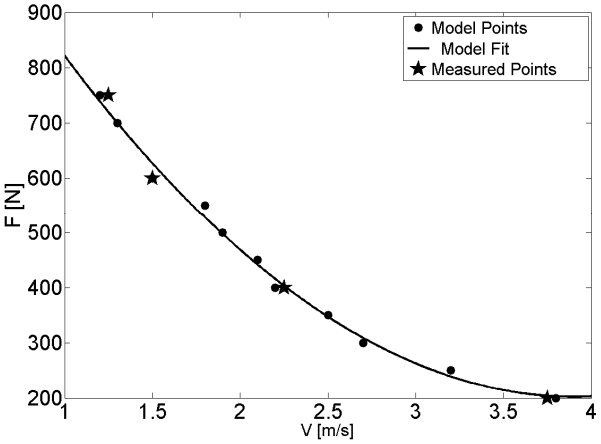


**Figure 1-3:** Transition diagram calculated and measured**.**

The results discussed so far only apply to tests done with additive free lubricants. For heavy duty/fully formulated oils the critical temperature was found to be higher than the flash temperature of the base oil, rendering it impossible to use the low speed and load test to obtain the critical temperature. For this reason the critical temperature for this type of oil was estimated by calculating the temperature for different experimentally obtained transition points, as discussed in Paper C, and resulted in a critical temperature of around 200 $^{o}C$ see Table 1-1. This is in very good agreement with a newer study on the temperature dependency of the mechanical properties of chemical reacted layers originating from heavy duty ZDDP oils. For these types of layers it is seen that at 200 $^{o}C$ the Young's modulus of the surface layers decreases [8 ].

At this point the transition from mild to severe wear is understood to a satisfactory level; a new challenge emerges, namely, to model mild wear itself with the final goal to predict the specific wear rate for a given system under steady state sliding conditions. This would then result in a "wear map" as illustrated in Figure 1-4. When using the normal load and sliding velocity for a given system, the specific wear rate

can be determined at glance, without the need of doing countless experiments to determine it experimentally.

| | Oil Bath Temperature | | | | |
|---|---|---|---|---|---|
| | Room Temperature ($25\ ^oC$) | | Elevated Temperature ($100\ ^oC$) | | |
| $F[N]$ | 700 | 550 | 700 | 400 | measured |
| $V[m/s]$ | 3.25 | 5.75 | 1.25 | 1.88 | |
| $\mu[-]$ | 0.1 | 0.091 | 0.14 | 0.14 | |
| $\Theta_{10\%}[^oC]$ | 210 | 230 | 208 | 200 | Calc |

**Table 1-1:** Calculated critical temperature based on measured transition points for a formulated oil containing ZDDP.

However, such an "engineering diagram" is currently out of reach and in this thesis an attempt is made to identify the main parameters presumed to play a dominant role in mild (oxidative) wear; starting with the determination of how the system is built up and understanding the role the different layers play, as seen in these systems.

A second point of interest is the process roughness which is formed in systems after running-in and then is maintained during the lifetime of the component. The roughness has a great influence on the wear and friction of the contact and thus is a key parameter that needs to be considered. However, first the general theory of the wear mechanism is presented.

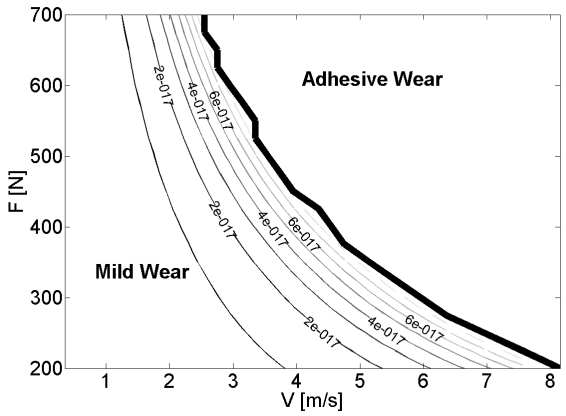


**Figure 1-4:** Example "wear map" with the different iso-lines for the specific wear rate *(k)* indicating the different gradations of mild wear with a combination of normal load vs. sliding velocity for a given system.

# 2. System buildup

To understand the concept of wear in the boundary lubrication regime first sufficient understanding needs to be obtained of the system in which wear is present. Currently a lot of research is done on this topic, mainly motivated by the search for environmentally friendly additives, since the most effective additives used are based on polluting chemicals. The main focus is on the automotive industry, since in this field pollution regulations are becoming stricter in a very rapid manner. A typical combustion engine includes a variety of contact conditions; however the most wear is seen in the contacts which are boundary lubricated. For this reason the research focuses on this lubrication regime in the development of new anti-wear additives. The interested reader is referred to the different case studies for detailed information about analysis methods and exact experimental procedures [10-16]. In this thesis only the most relevant results and general conclusions are presented to give a good base for assumptions made during modeling. The system represented in Figure 2-1 is a schematic view of the tribological layers present on a surface of a mild wearing system lubricated by an additive-rich lubricant, as shown in the TEM image in Figure 2-2, which consists of:

1. Physically/Chemically adsorbed layers: these layers are normally the main protection system an additive free oil offers. This protection is backed up by the native iron oxide on which the layer is adsorbed. These types of layers have a low desorption temperature around 80-120 $^{o}C$. Under very mild operational conditions these layers will provide sufficient protection to prevent high friction levels and severe wear.
2. Chemical reacted layer: this layer is built up out of products of the oil that have reacted with the surface or oxide present at the metallic surface.
3. N(ano)C(rystalline) layer: this layer consists of severely deformed bulk material. This material suffered severe plastic strain at high strain rates under high hydrostatic pressure; under these circumstances a very fine lattice is formed.

The next sections will deal with the different layers and their properties in more detail.

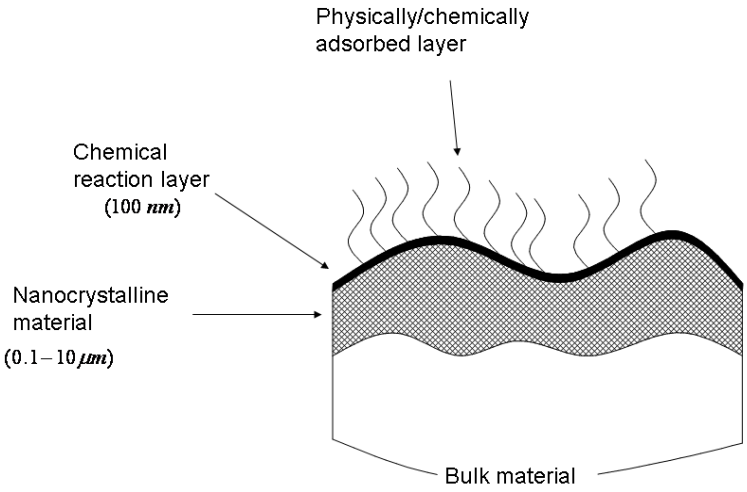


**Figure 2-1:** Layers present in a run-in system. The top layer is a physically/chemically adsorbed layer which only withstands very mild conditions. The second layer is a chemical layer which is a mixture of oxides and chemical products of the lubricant. The third layer is a Nano-Crystalline layer formed at the top of the bulk material by severe plastic deformation under large hydrostatic pressure**.**

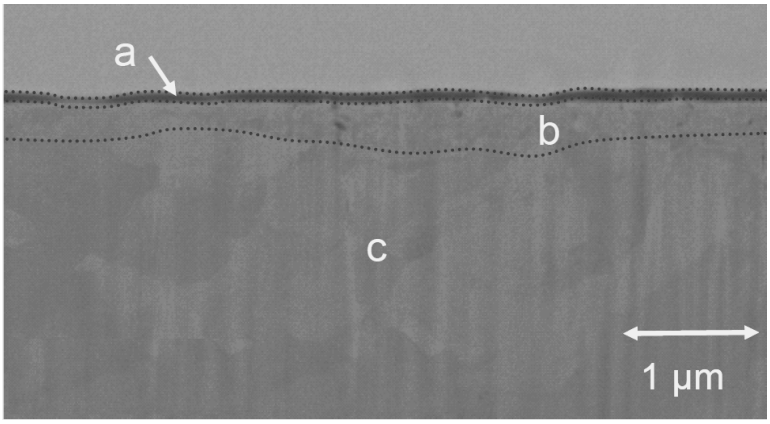


**Figure 2-2:** TEM picture of a tribological system with a) chemical layer b) Nano-crystalline layer c) (heavily) deformed bulk material [9]**.**

## 2.1. Physically adsorbed layer

This layer is the outermost layer present in the system and is only a few molecules thick [10]. The protective nature of this layer originates from the flexibility of the adhered molecules, which by deformation can accumulate the difference in velocity between the two bodies. The molecules are "attracted" to the surface by either van der Waals forces in the case of physical adsorbed molecules or by creating a soapy layer by chemically reacting to the native oxide layer on top of the surface in the case of chemical adsorbed molecules. In both cases there is a very limited amount to no interaction with the base material and if these layers are sheared off or thermally desorbed no base material is lost. For this reason this layer is left out of the wear process and is only taken into account in the friction calculations based on the critical temperature of the given lubricant as discussed in the introduction and Papers B and C.

## 2.2. Chemically reaction layer

Additives are added to base oils to enhance the properties of the base oil such as: shear stabilization, foam prevention, anti-oxidant, anti-wear additives and extreme pressure additives. The latter two are the most interesting when dealing with wear. These additives are designed to form a protective chemical layer on top of the surface to prevent metal-metal contact if the contact situations are such that running under highly loaded boundary lubricated conditions is unavoidable. The current understanding of the role these chemical layers play is that they are used as a sacrificial layer providing protection by ensuring shearing is mainly located inside the layer of chemical products: see for example [11]. In other words, a good wear additive is a corrosive agent of which the chemical products are mechanically tough layers. This assumption is supported by TEM studies done on wear particles originating from mild wearing systems, which mainly consist of chemical products originating from the additives in the oil and having a limited thickness, which is less than the thickness of the chemical layer present at the surface of the system, indicating that the material loss is confined within the layer [12].

The removal of the chemical layer will disturb the chemical balance in the system and the layer will try to restore this through growth of the chemical layer. If this replenishment is sufficiently high, the wear is limited to the loss of chemical products originating from the lubricant combined with the surface material it reacted with. However, this suggests that the layer is capable of growing and that the growth rate should be higher than the removal rate for the layer to provide protection through a dynamic balance situation:

$$\dot{X} \geq \dot{W} \tag{2-1}$$

Here $\dot{X}$ is the growth rate of the chemical layer and $\dot{W}$ the removal rate. To estimate if there is a balance under given conditions both the removal rate and the growth rate should be known.

### 2.2.1. Growth rate

First the growth rate is discussed starting with the assumption that it can be modeled by a diffusion-like process. The hypothesis is that the main parameters playing a role in the increasing layer growth reported in the literature are temperature and concentration, which are also incorporated in the layer thickness based on the diffusion equation [13]:

$$X = \left( \frac{2K(\Theta)C(0)t}{W_c \rho} \right)^{1/2} \tag{2-2}$$

Here $W_c$ is the mass fraction of the diffusion substances in the compounds which are formed with the metal, $\rho$ the density of these compounds, $K(\Theta)$ a temperature dependent diffusion coefficient and $C(0)$ the concentration of the diffusion substances at the surface at time is $t$. The expression for $K(\Theta)$:

$$K = K_0 \exp(-E_a / R\Theta) \tag{2-3}$$

Where $E_a$ is the activation energy (energy needed to produce a space inside the lattice for the molecules to diffuse into), $R$ is the gas constant and $\Theta$ is the temperature. This is a relatively simplistic but sufficient equation for the purpose suggested. Another appealing effect of this equation is that it is physically grounded and also leaves open space for the use of different additives since the activation energy and reference diffusion coefficient can be determined for the different oils as well as the mass fraction of the different active compounds from the oil in the surface layer ($W_c$). However, since it is currently not feasible to determine reliable values of the different parameters the following model is often used where the growth of the layer is expressed by:

$$X = K t_{gr}^{1/2} \tag{2-4}$$

Here $K$ is the effective diffusion coefficient determined for the different circumstances and additives under sliding conditions.

### 2.2.2. Removal rate

To estimate if a balance is present also, a removal rate needs to be determined for the protective chemical layer, which is done on grounds of the solid behavior of the layer [14]. In this study it is shown that the layers are present at the surface of a run-in system and consist of two layers: a viscous layer under which a solid layer is located. This is consistent with the schematic representation in Figure 2-1. The solid behavior enables the use of elasto-plastic modeling of the chemical reacted layer as will be discussed in more detail in the modeling chapter 3. Currently, it is sufficient to mention that the plastic indentation ($\varepsilon^{layer}{}_{plzz}$) is taken as the amount of removal for the chemical layer as schematically shown in Figure 2-3.

In this figure it is also illustrated how wear will occur in the protected situation, namely through the usage of bulk material to restore the chemical balance. As discussed, it is assumed that the removal of the chemical layer is equal to the plastic indentation of the layer. In turn, the plastic properties of the chemical layer determine the amount of plasticity present under the given conditions. However these properties are not as straight forward as it seems at first sight. During indentation of the chemical layer an increase in the elasticity modulus and hardness is seen. This effect is currently only well described for ZDDP-like additives since these are the most commonly used anti-wear agents.

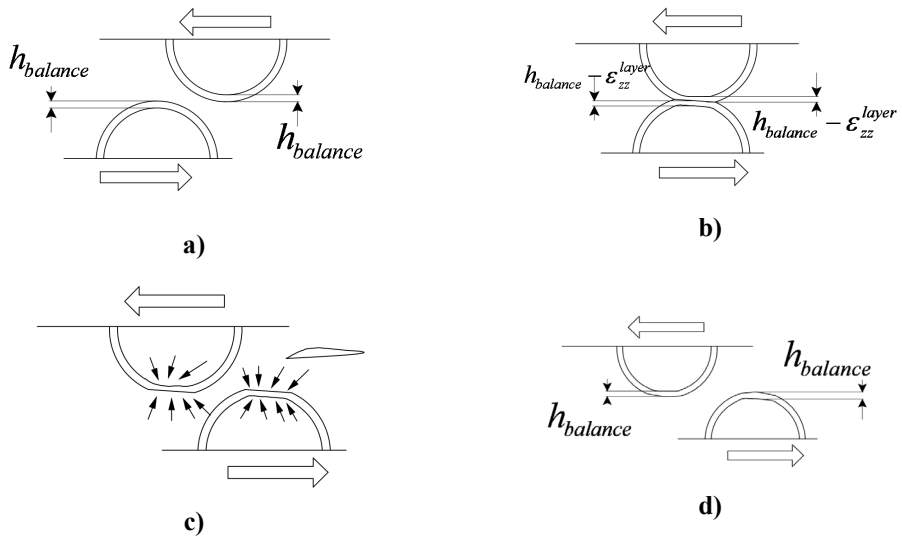


**Figure 2-3) a)** Asperities come into contact **b)** Part of the chemical layer is sheared off **c)** Removed layer is built up again from bulk and additives **d)** The geometry is changed and wear has occurred.

This effect is attributed to the cross-linking in the phosphor-rich chemical layer [15-16]. In these studies molecular dynamics simulations were used to investigate which effect pressure and elevated temperatures would have on the chain length in layers originating from ZDDP additives. It was found that at a relatively low pressure (7 $GPa$) cross-linking occurred. However, Tse and coworkers [17] showed that even at temperatures of 225 $^{o}C$ and pressures up to 18.2 $GPa$ no cross-linking was observed. These results are, however, observed in a static test using a transparent vial pressured under hydrostatic conditions without shear. Nevertheless, the effect of hydrostatic pressure during indentation is seen in [18] in layers formed under dynamic (sliding) experiments. However, in this study the results clearly show a reversible effect, suggesting that no cross-linking is presented but rather the "anvil" effect often seen in soft layers on harder substrates.

## 2.3. Nano-crystalline layer

Underneath the chemical reacted layer a metallurgical altered layer is found. This layer is identified by its very fine crystalline structure. The crystals found in this layer are typically in the nanometer range, as can be concluded from Figure 2-4. Here electron diffraction is used on the system presented in Figure 2-2, the excitation volume is less than a few hundred microns. For the heavily deformed bulk material it is clearly seen that the pattern shows a multi-crystal system suggesting a sub-micron crystal size for the NC-layer and a single crystal orientation for the bulk material indicating a super-micron crystal size.

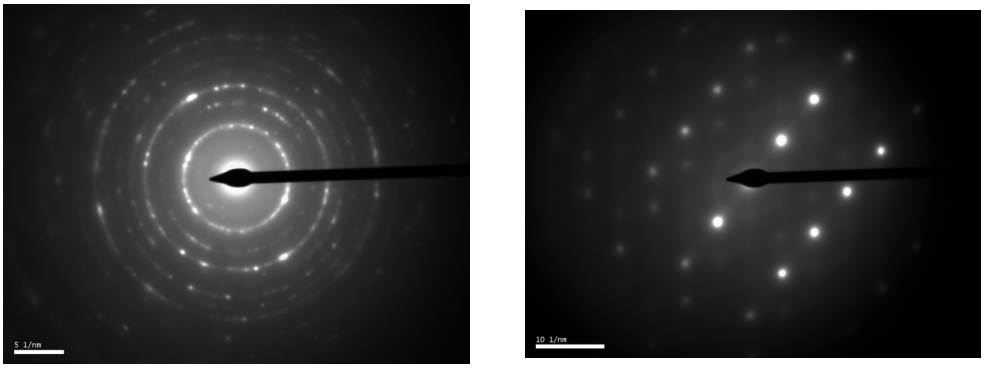


**a)** **b)**

**Figure 2-4:** Electron diffraction patterns for **a)** the NC-layer. Here circles are seen indicating the presence of multiple crystal orientations **b)** the heavily deformed bulk layer. Only spots are seen here indicating a single crystal orientation [9].

The formation process of the NC-layers is presumed to be the formation of high dislocation densities under hydrostatic pressure and high strain rates [19-20]. Using molecular dynamics simulations it has been shown that using a qualitative model to

simulate the nano-crystallinization under shot-peening conditions the main parameters influencing the formation of an NC-lattice are the plastic strain rate and hydrostatic pressure [21]. This theory is also supported by the measurements done in [22]. The hydrostatic pressure is mainly necessary to prevent cracks forming in the material during high strain plasticity and thus providing the material the opportunity to reach high dislocation densities to form new crystal boundaries needed to transform into NC material.

The properties of the NC layer can be split up into two parts; 1) Elastic and 2) Plastic. The discussion will start with the Elastic part. The NC layer present in a tribo-system is formed through severe plastic deformation combined with high hydrostatic pressure; this implies that the porosity of the material remains negligible. Using the theory presented in [23], depicted in Figure 2-5, suggests that if the crystal size is 20 nm or higher the elastic properties will not be significantly influenced in comparison with the coarse grain material. In the different studies on the properties of the NC layer in tribo-systems it has been shown that the grain size is above this critical value, see for example [24-26]. Thus it is valid to assume that in the elastic regime the complete material is homogeneous.

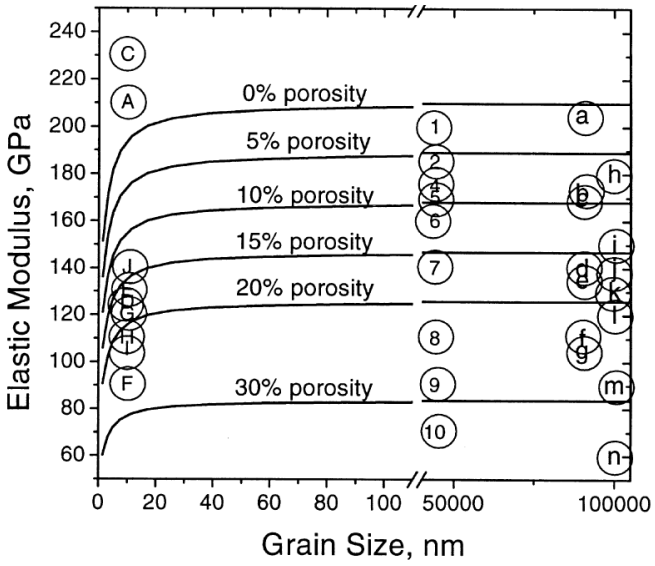


**Figure 2-5:** Elastic modulus of steel as a function of porosity and grain size [23].

The next part is the plastic behavior of the NC layer. This is a topic that is currently receiving a lot of attention in the literature [20, 23, 26-41] since it is shown that NC materials have different plastic properties compared to their coarse grained counterparts. Here the opinions in the literature are not univocal and concerning the layers present in tribo-systems two main trains of thought can be distinguished namely:

an inverse hardening relation between the grain size and the hardness going down to the nano meter scale and secondly an inverse relation between grain size and hardness down to a maximum after which a linear relation is seen. The first is theory is based on the Hall-Petch theory. This hypothesis states that with increasing plasticity grain refinement is seen; due to the grain refinement the energy needed for dislocation diffusion is increased and as a result it increases the yield strength of the material. The second theory is based on the idea that at a critical grain size a change in plasticity mechanism is seen. Instead of dislocation diffusion a grain slip mechanism is supposed to accommodate for the plastic deformation, see Figure 2-6.

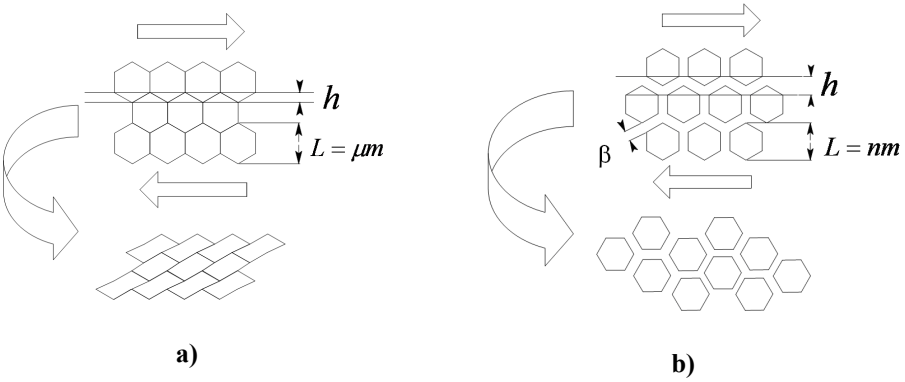


**Figure 2-6: a)** Deformation mechanism in coarse grain materials through deformation of the crystals themselves (dislocation diffusion) here h is the relative roughness of the crystals against grain boundary width δ **b)** deformation through grain slippage.

The energy necessary for plastic deformation in grain boundary slip will decrease as the ratio between the relative roughness ($h$), which is linear dependent on the grain size ($L$), and the grain boundary width is going down ($\delta$). This would then be the reason for a material behavior as shown in Figure 2-7, where a shift from hardening to softening as a function of the reduction in grain size can be seen. This softening and hardening is also seen at surfaces during mild wear conditions as shown in Figure 2-8.

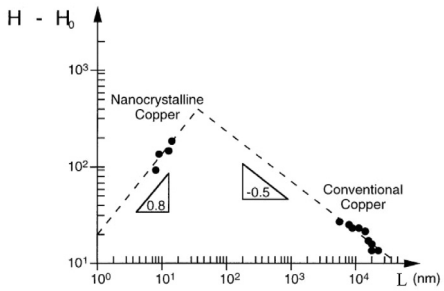


**Figure 2-7:** Hardness of pure copper as a function of the grain size L reproduced from [28]. Here $H-H_0$ is the deviation of the hardness in Vickers against the reference hardness $H_0$= 65 Vickers.

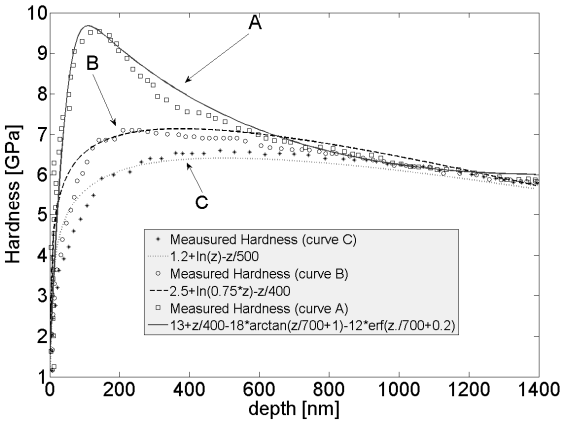


**Figure 2-8:** Hardness profile according to measurements presented in the literature: Curve A polished surface, curve B mild wearing surface and curve C for a severe wearing surface [24].

However, in tribological systems also, a hardening onto the surface is reported suggesting a monotone increase of hardness towards the surface, even at nm scale crystals as discussed in [40, 42].

# 3. Modeling

The wear model which will be used in the current study is based upon the idea that the formation of a wear particle in the case of micro-pitting can be associated with the phase transformation from austenite to ferrite in high strength carbon steels, as discussed in [43], in combination with a local friction model. However, a simplified perspective can be used, since it followed from the measurements that the phase from martensite to a high carbon ferritic phase was mainly contained with the plastic volume of the material. The first person who used this hypothesis in a model to predict the material loss in wearing systems was Nelias [44]. Here it is stated that at a maximum equivalent strain the material will start to tear and the volume that both transcends this threshold and reaches the surface will be removed, as is schematically shown in Figure 3-1.

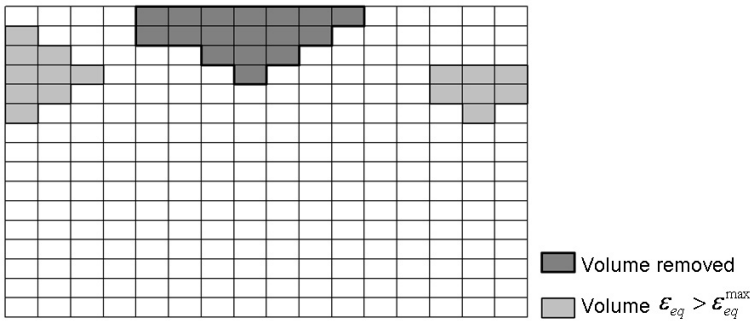


**Figure 3-1:** Graphical representation of the suggested wear criterion (dark gray is the volume removed, light gray is the volume transcending the maximum equivalent plastic strain).

To be able to use this hypothesis, a contact model capable of determining the plastic strain underneath the surface is needed. However, in the first version of the code any plasticity was assumed to result in material removal, this combined with the thermal threshold is discussed in appending Paper D. To model material removal in a more detailed manner a full elasto-plastic contact code is needed. The development of this will first be discussed after some general assumptions with respect to the problem as well as some numerical issues that needed to be resolved.

## 3.1. Elasto-plastic contact code

To be able to determine the plasticity underneath the surface, an elasto-plastic contact code is needed capable of handling the complex non-linear plastic behavior. Usually Finite Element Methods are then applied. However, for the current situation this type of code is not very suitable since contact conditions are hard to satisfy within the code. One of the most popular methods within FEM contact simulations is the penalty method: for this the non-penetration conditions are fulfilled by "pushing back" the elements penetrating the mesh of the opposing body with a predefined nodal force. The quantity of the penalty is then determined in a trial and error based guess in which the penalty is set not too high to guarantee convergence and not too low to keep the solution realistic. A second more "realistic" way of handling contact is using LaGrange multipliers, introducing an extra degree of freedom at the surface nodes to optimize the contact problem. This, however, introduces an enormous increase in the computational times of the contact problem. Therefore an alternative method is used.

Recently a method has been implemented called the SAM (Semi-Analytical Method). This method is very suitable when analyzing semi-infinite bodies with limited plasticity. The semi-infinite body limitation is no hindrance since the point of interest in the study is the microscopic roughness change, e.g. the changes of the surface typography of a body with global dimensions in the millimeter range while the scale looked at inside the contact will be in the microns or even less. The limitation on the amount of plasticity will be discussed further on, as will the exact limit of the code. A more elaborate discussion on the contact code can be found in references [44-48]. Here only the main parts will be discussed.

The reciprocal theory is applied to a semi-infinite volume with boundary $\Gamma$ and volume $\Omega$. For this body different states are defined: an initial state with internal strains ($u$ ,$\varepsilon$ ,$\sigma$ , $f_i$) and a state for the time undefined: ($u^*$,$\varepsilon^*$,$\sigma$, $f^{**}_i$). Using the reciprocal theory and the assumption that the second state is the one in which the surface is loaded by a unit pressure $p_i^*$ at the location $A$ gives:

$$u_3(A) = \underbrace{\int_{\Gamma_c} p_i\, u^*_{3i}(M,A)\, d\Gamma}_{u^e(A)} + \underbrace{\int_{\Omega} \varepsilon^0_{ij}(M)\, C_{ijkl}\, \varepsilon^*_{ij}(p_i(M),A)\, d\Omega}_{u^{pl}(A)} \tag{3-1}$$

Here $u^e(A)$ is the elastic surface displacement and by stating $\varepsilon_{ij}{}^0=\varepsilon_{ij}{}^{pl}$, $U^{pl}(A)$ becomes the surface displacement due to the plastic strains inside volume $\Omega$. The surface displacement of the body can now be expressed as a function of the contact pressure and the plastic strain. To calculate the plastic strains the subsurface stresses are needed. Using the reciprocal theory again and defining a state ($u^{**}$,$\varepsilon^{**}$,$\sigma^{**}$, $f_i^{**}$), which can be seen as the state when a unit force is applied inside volume $\Omega$ at point $B$. This then results in:

$$u_k(B) = \underbrace{\int_{\Gamma_c} u_{ki}^{**}(M,B)\, p_i(M) d\Gamma}_{u_k^e(B)} + \underbrace{\int_{\Omega_p} \varepsilon_{ij}^0(M) C_{ijkl} \varepsilon_{ij}^{**}(M,A) d\Omega}_{u_k^{pl}(B)} \tag{3-2}$$

Here stating $\varepsilon_{ij}^{\ 0} = \varepsilon_{ij}^{\ pl}$ and only integrating over the volume where the plastic strains are not zero $\Omega = \Omega_{pl}$ the displacement field is written as a function of the elastic and the plastic strains. Using Hooke's law:

$$\sigma_{ij}^{tot}(B) = C_{ijkl}\left[\left(\frac{1}{2}\left(u_{k,l}^e(B) + u_{l,k}^e(B)\right)\right) + \left(\frac{1}{2}\left(u_{k,l}^{pl} + u_{k,l}^{pl}\right) - \varepsilon_{kl}^{pl}\right)\right] \tag{3-3}$$

Rewriting eq. (3-3):

$$\sigma_{ij}^{tot}(B) = \sigma_{ij}^{e}(B) + \sigma_{ij}^{res}(B) \tag{3-4}$$

If now the unit pressure and unit force are replaced by the complete pressure and force fields, a solution can be found for a complete rough contact situation. This is done by discretization of the surface $\Gamma$ into surface elements $N_s$ of size $\Delta x \times \Delta y$ and the volume into elements $N_v$ of size $\Delta x \times \Delta y \times \Delta z$ on which uniform pressures at the surface are acting and in the volume the strains inside each volume element are uniform. Starting with the elastic surface displacement which then becomes the sum of the individual pressure patches:

$$u_3^e(x,y) = \sum_{n=1}^{N=N_s} D_{3i}^n(x - x'_n, y - y'_n)\, p_i^n(x'_n, y'_n) \tag{3-5}$$

Here $x, y$ are the coordinates of observation and $x'_n, y'_n$ are the coordinates of the center of the excitation patch $n$, the expressions of $D^n_{3i}$ are given in Appendix B, where $i$ can have the value of 3 for the displacement due to normal force and 1 for the displacement due to traction. Next is the displacement due to the plastic strains $\varepsilon_{ij}^p$. Using the assumption of uniform strains within the volume elements:

$$u_3^{pl}(x,y) = \sum_{n=1}^{N=N_v} K_{ij}^{pl}(x - x'_n, y - y'_n, z'_n)\, \varepsilon_{ij}^p(x'_n, y'_n, z'_n) \tag{3-6}$$

Here $(x, y)$ is the location of the point of observation on the surface and $(x'_n, y'_n z'_n)$ are the coordinates of the excitation volume $n$. The expression for $K^{pl}_{3i}$ is given in Appendix C. The stresses for the total system, given in eq. (3-4), can also be expressed in a summation:

$$\sigma_{ij}^{tot}(x,y,z) = \sum_{n=1}^{N=N_s} S_{ijk}^{elas}(x-x_n^{'}, y-y_n^{'}, z-z_n^{'})p_k + \sum_{n=1}^{N=Nv} S_{ij}^{pl}((x-x'_n, y-y'_n, z-z_n^{'}, z+z_n^{'}) \varepsilon_{ij}^{pl}(x_n^{'}, y'_n, z'_n)) \quad (3\text{-}7)$$

Here the expressions for $S_{ijk}^{elas}$ are the influence matrices presented in Appendix B for the elastic stress field as is the elastic part of the code and $S_{ij}^{pl}$ are given in Appendix C, where the expressions originally used in the code discussed in [47] and [48] are replaced by more efficient equations originating from [49]. Now the surface displacement and the stress inside the bulk material of an elastic half space with plastic strains inside the volume are described by equations, it can be used to model the contact of the elasto-plastic contact between two half spaces by using the model depicted in Figure 3-2 of which the flow chart is shown in Figure 3-3.

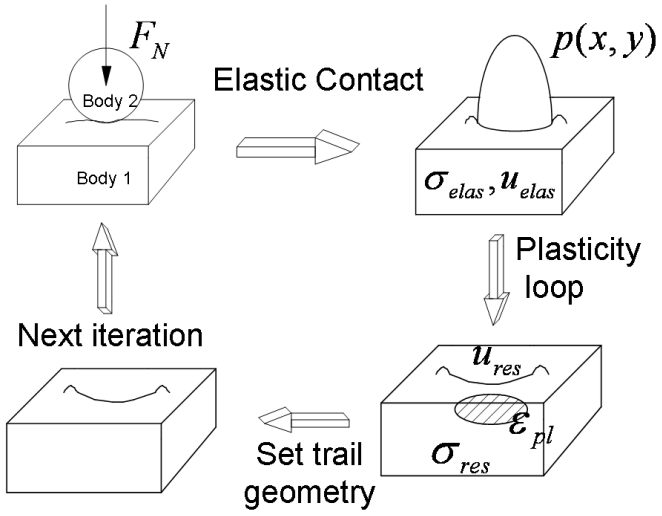


**Figure 3-2:** The iterative process of solving the elasto-plastic contact.

One part will be discussed here in detail with respect to the plastic loop and the validation of the code. In the original code the Prandtl Reuss method is used to compute the plastic strains. This is later on adapted by Nelias [48] to a return mapping algorithm to increase the efficiency of the code.

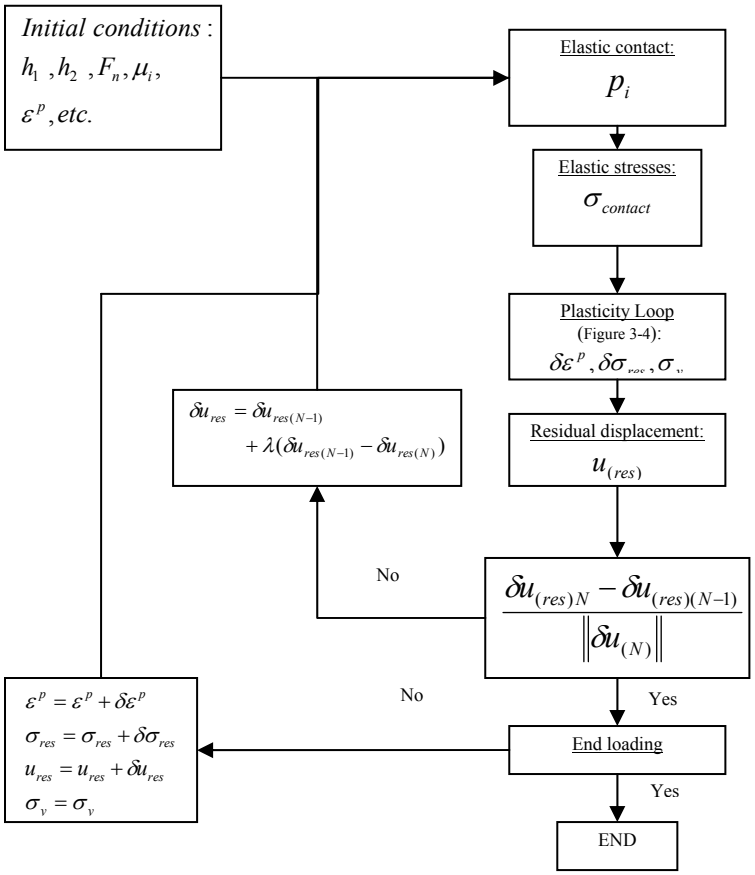


**Figure 3-3:** Flow chart of SAM (elastic-plastic) contact model.

The current model also uses a return mapping algorithm; however, in the current version the plastic loop is changed to a stress-related one rather than strain. As can be seen in reference [47] the plasticity loop is stopped if convergence of the plastic strain is reached. However, the basis of the plasticity theory states that for a system to stay in the elastic regime the elastic stresses should be on the yield surface:

$$\phi(\sigma_{ij}) \leq 0 \tag{3-8}$$

This is not satisfied per definition if the convergence criterion used is based on the plastic strain inside the body. In the current model the plasticity loop used is depicted in Figure 3-4. Here the yield surface is defined by the von Mises yield criterion and the loop is stopped if the stress state in the complete meshed volume is either within the yield surface or within the predefined error outside the yield surface. Also, the iteration on the stress rather than on the strain ensures that the plasticity loop stays stable, since the return mapping algorithm is unconditionally stable.

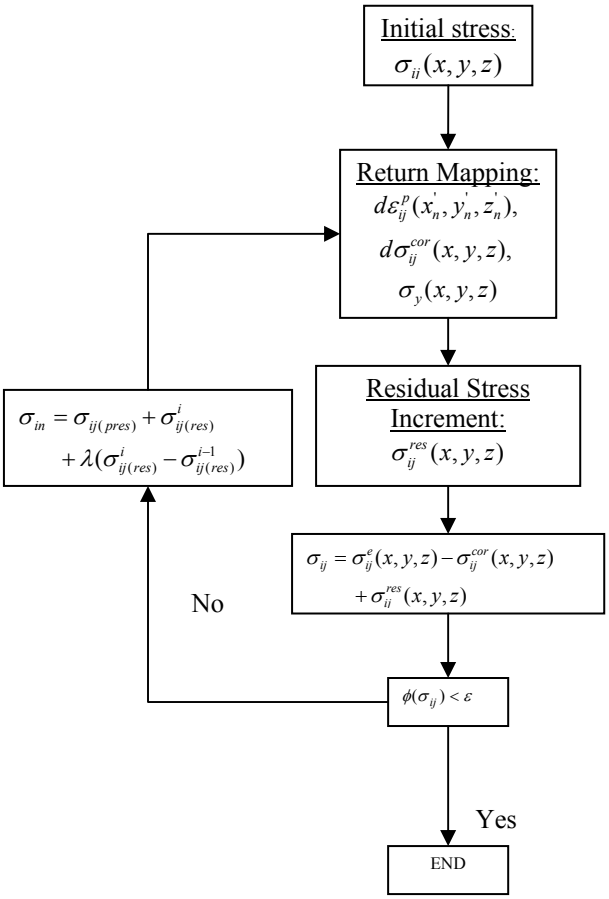


**Figure 3-4:** New "plasticity loop" based on the stress relaxation.

To validate the new plasticity loop the examples given in [48] Figure. 5 are reproduced and the results are presented in Figure 3-5. It can be concluded that the current code gives approximately the same results for the low friction situation and slightly better results for the high friction situation.

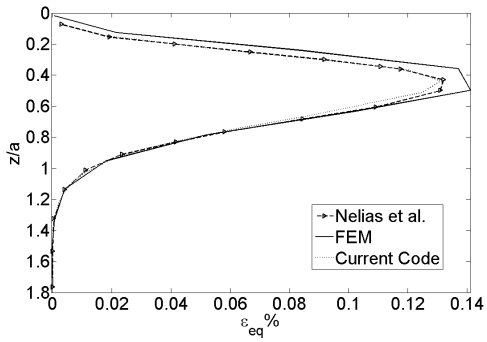


**a)**

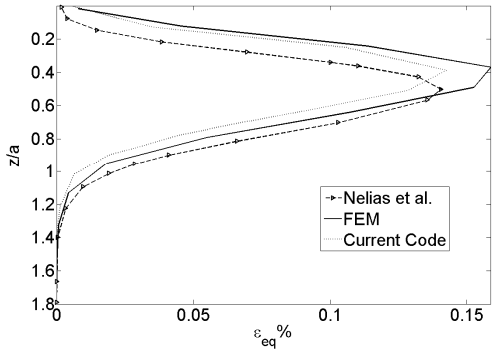


**b)**

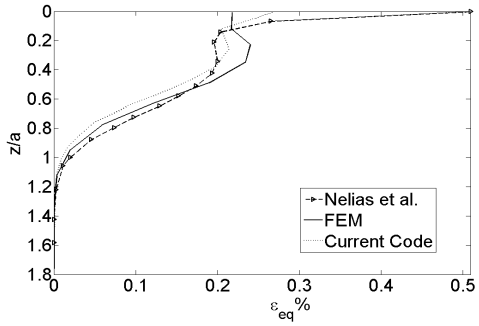


**c)**

**Figure 3-5:** Equivalent plastic strain for the elasto-plastic solutions given in [48] compared with the current code and FEM results **a)** for the frictionless case **b)** $\mu$=0.2 **c)** $\mu$=0.4

The next step is to validate at what state the assumption that the SAM is only capable of handling small equivalent strains is valid. To do so the indentation of a steel sphere made of AISI 52100 with a radius of 0.5mm is simulated both using the SAM code

discussed here and a non-commercial FEM code (DIEKA) [50]. The hardening model used for the material is an isotropic Swift model:

$$\sigma_y = B\left(C + \varepsilon_{eq}\right)^{(n)} \tag{3-9}$$

Where in the current simulations $B$=1750 $MPa$, $C$=16 , $n$=0.067 and $\varepsilon_{eq}$ is the equivalent plastic strain expressed in micro strain. The elastic properties are set to $E$=210 $GPa$ and $\nu$=0.3 using these material properties and the assumption the contact is frictionless the critical load at which yielding will start according to the Tresca yield criterion is given by [51]:

$$F_{critical} = \left(\pi\sigma_{yield}\right)^3 \left(\frac{3R_{eq}}{E_{eq}}\right)^2 \tag{3-10}$$

If now the contact is loaded onto 100 times the onset of plasticity the results for both methods are shown in Figure 3-6. Here it can be clearly seen that the results concur very well and the SAM model developed can be used for the elasto-plastic computation. However, if the load is increased more it can be seen in Figure 3-7 that at 500 times the critical load the SAM model starts to deviate by approximately 10 percent from the FEM solution and shows instable behavior. It is therefore concluded that the SAM model can be used onto an equivalent plastic strain of 10 percent without making a substantial error.

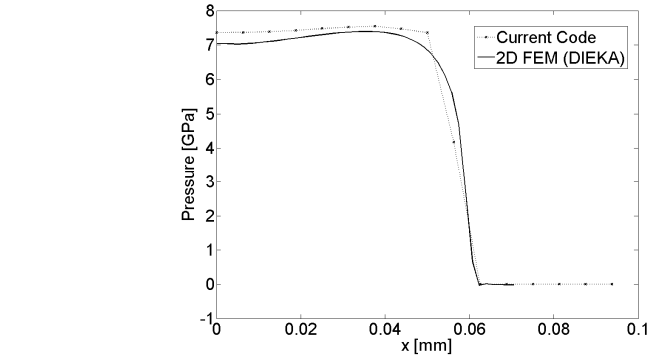


**a)**

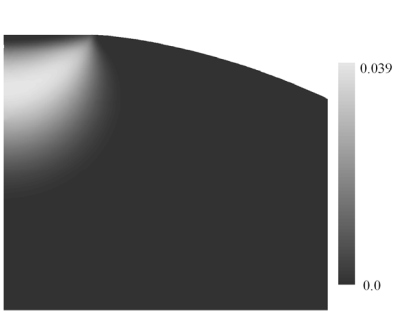


**b)**

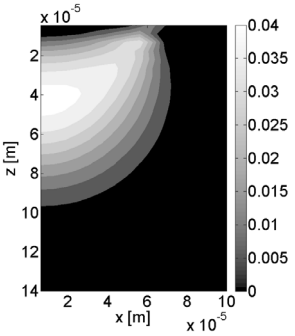


**c)**

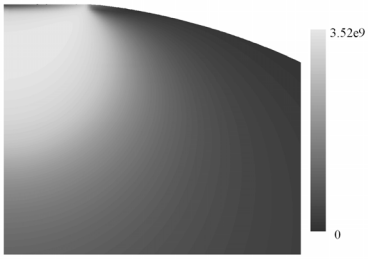


**d)**

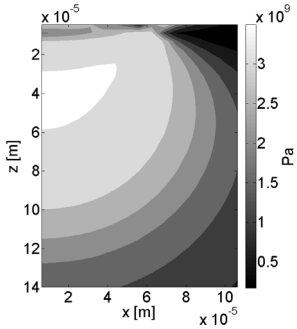


**e)**

**Figure 3-6: a)** Normal pressure resulting from the calculation with the FEM package and SAM package**. b)** Equivalent strain calculated using FEM. c) equivalent strain calculated using SAM. **d)** Von Mises stress underneath the surface using FEM and **e)** SAM.

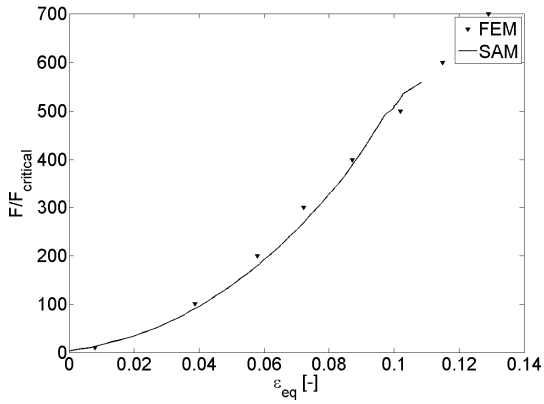


**Figure 3-7:** Equivalent plastic strain vs. normal load normalized with the critical load.

## *3.2. General considerations*

As discussed in chapter 2 the system being studied is a layered system, see Figure 2-1. The aforementioned elasto-plastic contact model is, however, not capable of handling a layered system. Therefore some well-educated assumptions need to be made.

### 3.2.1. Chemical reaction layer

The first step in estimating the effect the chemical reaction layer will have on the contact conditions and subsurface stress is retrieving the properties of this layer. To do so an example system is currently investigated. This system is composed of steel components which are lubricated using ZDDP-rich oil. This type of system is currently thoroughly investigated in the literature, since environmental rules are restricting the use of this very effective anti-wear agent. However, the mechanism offering the protection provided by the ZDDP additives can be seen as a general mechanism for most anti-wear agents, with only the mechanical properties varying in comparison with the values currently used. The model will still have a very general nature and if the general assumptions made for the current model are treated in a correct manner a wide range of boundary lubricated systems can be modeled with it. Table 3-1 shows the various values reported in the different studies done on the behavior of boundary lubricated contacts using ZDDP/ZDDP derived lubricants. As can be concluded from this table the average layer thickness of the layer is 100 nm, under the conditions studied in the different investigations having a Young's modulus of around 80-100 *GPa*. For details on the measurements the reader is referred to the different dedicated articles cited in the table.

| Ref. # | $P_n$ $[MPa]$ | $V$ $[m/s]$ | $\Theta_{bath}$ $[C^o]$ | $h_{balance}$ $[nm]$ | $E_{ridge}$ $[GPa]$ | $E_{valley}$ $[GPa]$ |
|---|---|---|---|---|---|---|
| [52] | 504 | 0.3 | 100 | 115 | 85-75 | 25-30 |
| [53] | 504 | 0.3 | 100 | 60-120 | - | - |
| [54] | 700 | 0.03 | 83 | 40-100 | - | - |
| [55] | 700 | - | 83 | 100 | - | - |
| [56] | 500 | ~0.3 | 100 | 30-60 | - | - |
| [11] | - | - | - | 100 | 81 | 25 |
| [57] | 400 | ~0.3 | 100 | 70 | 96 | - |
| [58] | 500 | ~0.3 | 100 | 300 | 120-90 | - |
| [59] | ~300-500 | 0.03 | 83 | <100 | 130 | - |
| [60] | 10-50 | 0.25-55 | 100 | <100 | | - |
| [61] | 360 | - | 100 | 140 | 90 | - |
| [62] | ~425 | 0.34 | 100 | 160> | 122.7 | - |
| [63] | 590 | ~0.3 | 100 | ~160 | 81 | 36 |
| [64] | 600 | 0.01 | 80 | <60 | - | - |
| [8] | 135 | ~0.35 | 100 | 60-180 | 90-120 | |
| [65] | 300 | ~0.3 | 100 | 30-60 | - | - |
| [66] | 950 | 0.1 | 100 | 120 | - | - |

**Table 3-1**: Results for thickness and Young's modulus for the chemical reaction layer retrieved from the literature resulting from rubbing experiments in ZDDP-rich oils.

To estimate the effect this layer will have on the mechanical behavior of the contact a typical input geometry used for the wear simulations, which has a lateral resolution of 1 micron as shown in Figure 3-8, is used combined with the theory presented in [67]. The input parameters used for the simulation are given in Table 3-2 and the influence coefficients for the coated half space in the contact model are given in Appendix B.

| Input Parameter | Value |
|---|---|
| $E_{coating}$ | 80 $[GPa]$ |
| $E_{substrate}$ | 210 $[GPa]$ |
| $\nu_{coating}$ | 0.3 $[-]$ |
| $\nu_{substate}$ | 0.3 $[-]$ |
| $F_N$ | 0.6 $[N]$ |
| $\mu$ | 0.1 $[-]$ |

**Table 3-2:** Input parameters layered calculation.

The results show (Figure 3-9) that the influence of the chemical reaction layer on the contact pressure and subsurface stress field is very limited. It is therefore valid to conclude that the effect of the chemical reacted layer on the normal pressure and

subsurface stress field is negligible and the main effect the chemical reaction layer will have is on the level of friction.

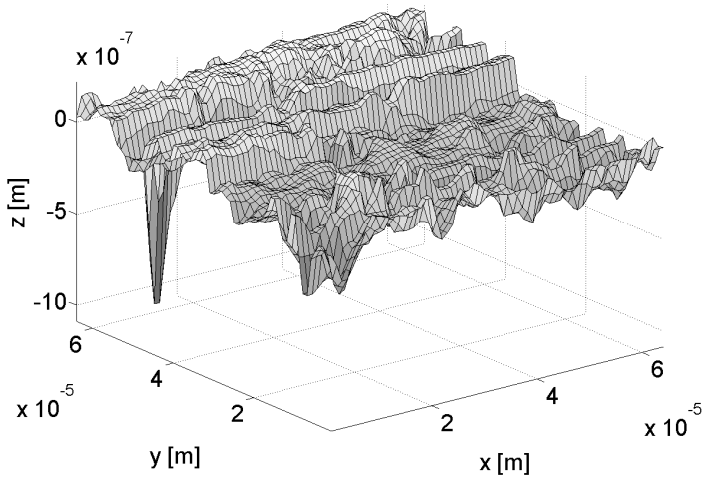


**Figure 3-8:** Interference microscopy surface measurement used in the layered calculations.

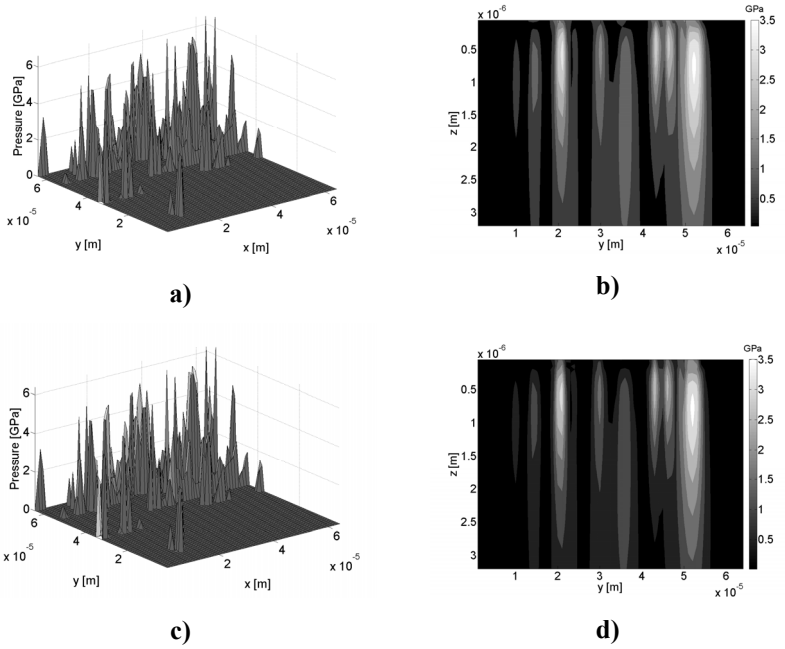


**Figure 3-9:** Pressure profile for **a)** coated surface ($p_{max}$=6.4 *GPa*) and **c)** uncoated surface ($p_{max}$=6.5 *GPa*).Von Mises stress underneath the surface, maximum von Mises stress **b)** coated material $\sigma_{vm}^{max}$=3.5 *GPa* d) and uncoated material $\sigma_{vm}^{max}$=3.55.

### 3.2.2. Friction model

In the first version of the wear model published by Nelias [44] an overall coefficient of friction of 0.4 is used to ensure that the plastic core reaches the surface of the contact. This is, however, not the case in practical engineering situations. During normal operational conditions boundary lubricated contacts will have a coefficient of friction in the range of 0.1-0.15. However, if the oil is not capable of providing enough protection, metal to metal contact will occur, and the coefficient of friction will increase. A typical value seen in this situation is 0.4. This transition from a well-protected situation into a more severe wear behavior is described in more detail in Paper C and Paper D. In both these papers a thermal threshold is used to describe the transition from mild to severe wear in either a local (Paper D) or global level (Paper C). In Paper E this local variant is used combined with the elasto-plastic model discussed to create a wear model based on local conditions.

As discussed in section 2.2 it is stated that a sufficient layer thickness is needed, supplied by the additive packages, to provide protection against metal to metal contact and thus lower the coefficient of friction. This theory is supported by the fact that in mild wearing systems the main wear particles found are composed of products originating from the chemical reaction of base material with additives originating from the oil [68]. This suggests that the removal rate of the layer needs to be lower than or equal to the growth rate.

The way the growth is dealt with is already discussed in section 2.2.1. For the modeling a time of growth needs to be defined. The system studied is the pin-on-disk configuration, which represents tribo-systems as present in a lot of applications. The contact situation is a stationary part is pressed against a moving disk. As the contact area on the sliding component is the one that is in almost constant contact with the oil and its additives, it is assumed the lubricant layer is built on the sliding component. If the time between contacts is assumed to be in the range of the typical wavelength of the surface, thus in the order of $50\mu m$, this gives contactless times of only micro seconds, while the area outside the contact is in contactless times in the range of seconds. This is particularly the case because the stationary part is in constant contact and unreachable for the lubricant and additives. The time for the layer to build up is then defined as the time the wear track is outside the apparent contact area, see the schematic representation of Figure 3-10. The time of growth can now be used in eq. (2-4) giving:

$$t_{gr} = \frac{s_{track} - a}{|V_1 - V_2|} \tag{3-11}$$

The next step is defining the removal rate of the chemical layer. As discussed in 2.2.2, mechanical testing resulted in the chemical reaction layer reacting as a solid layer to

dynamic indentation and it will thus be regarded as an elasto-plastic amorphous solid in the modeling.

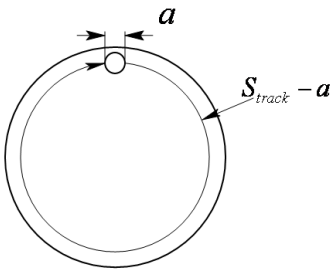


**Figure 3-10:** Wear track vs. apparent contact area with diameter $a$ .

The assumption that the elastic stress state underneath the surface is influenced very little due to the presence of the chemical layer, gives rise to the idea that the different contact patches can be regarded as separate ones. The next assumption which can be made is that the layer is in a plain stress state due to its limited thickness:

$$\frac{\partial \sigma_{ij}^{layer}}{\partial z} = 0 \tag{3-12}$$

The amount of the chemical layer removal is indicated by the plastic strain in the direction normal to the surface ($\varepsilon^{layer}{}_{\mathrm{pl}zz}$). To calculate the plastic strain, the following assumption of the conditions the layer has to withstand are made. From the bulk side the layer is stretched by the strain of the bulk material, because it sticks to the bulk material (no slip condition between layer and bulk material). From the bulk side only elastic strains are taken into account, since plastic deformation is permanent and thus the layer grows on the already deformed bulk, not needing to adapt to the already existing plastic deformation. At the top the pressure and shear is put on the surface of the layer. Here the statement that the strain $\varepsilon_{zz_{bulk}}$ is set to zero should be made since over each element this strain is uniform and thus puts no stress on the chemical layer. This results for the pre-strain in:

$$\sigma_{ii_{layer}} = \frac{E_{layer}}{(1+\nu_{layer})}\varepsilon_{ii_{bulk}} + \frac{\nu_{layer} E_{layer}}{(1+\nu_{layer})(1-2\nu_{layer})}(\varepsilon_{ii_{bulk}} + \varepsilon_{jj_{bulk}} + \varepsilon_{kk_{bulk}}) \tag{3-13}$$

Where *i, j* and *k* can be *x, y* or *z* and the external pressures from the top side are given by the normal load and the traction:

$$\sigma_{zz_{layer}} = \sigma_{zz_{layer}} + p \tag{3-14}$$

$$\sigma_{xz_{layer}} = \mu\, p \tag{3-15}$$

Using these stress conditions the plastic strain can be calculated combining eq. (2-1), (2-4) and eq. (3-11). The maximum amount of plastic strain in the thickness direction normal to the surface can be calculated by the assumption that the removal of the chemical layer is equal to the plastic strain:

$$\varepsilon_{zz\max}^{pl} = \sqrt{t_{gr}} K / h_{balance} \tag{3-16}$$

Here $h_{balance}$ is the layer thickness. Using this definition a high and a low friction regime can be computed;

$$\begin{aligned} &\varepsilon_{pl_{zz}}^{layer} < \varepsilon_{zz_{\max}}^{pl} \rightarrow \mu = \mu_{low} \quad (0.1 - \text{Boundary Lubrication}) \\ &\varepsilon_{pl_{zz}}^{layer} \geq \varepsilon_{zz\max}^{pl} \rightarrow \mu = \mu_{high} \quad (0.4 - \text{Dry Sliding}) \end{aligned} \tag{3-17}$$

# 4. Results

In the previous chapters the basic assumptions and hypothesis which are used as the building bricks of the wear models are discussed. In this section some results obtained using the discussed wear models are presented and discussed to show the potential of the models. Also, different material models are used for both the chemical layer and for the NC-layer to show the influence that different material models have on the wear behavior of the system studied.

## 4.1. Basic Model for direct base material removal

At first the most basic system is studied: a homogeneous bulk material with on top a chemical layer which has neither pressure nor temperature sensitive properties; for more details the reader is referred to the appending Paper E. For the bulk material two different steels, one ductile and one brittle are used with the mechanical parameters given in Table 4-1. For both steels the hardening behavior is described by a Swift hardening law:

$$\sigma_{yield}(\varepsilon_{eq}) = B\left(C + \varepsilon_{eq}\alpha\right)^{(n)} \tag{4-1}$$

Here the parameter $\alpha$ is used either to represent a brittle high strain hardening material or a more ductile less strain hardening material as represented in Figure 2-8.

| Parameter | Value |
|---|---|
| $E\,[GPa]$ | 210 |
| $\nu\,[-]$ | 0.3 |
| $B\,[MPa]$ | 1280 |
| $n\,[-]$ | 0.095 |
| $\alpha_{brittle}\,[-]$ | $10^6$ |
| $\alpha_{ductile}\,[-]$ | $10^5$ |
| $\varepsilon_{eq\,\max}^{brittle}\,[-]$ | 0.002 |
| $\varepsilon_{eq\,\max}^{ductile}\,[-]$ | 0.02 |

**Table 4-1:** Material properties used for both brittle and ductile steel.

Now the material parameters are set, an input geometry needs to be defined starting with the macroscopic geometry. For the example simulation, a line contact with an apparent contact width of 300 $\mu m$, total wear track of 314.15 *mm* (wear track diameter of 100 *mm*), an oil bath temperature of 100 $^oC$ and a sliding speed of 1 *m/s* gives a

growth of the chemical layer of approximately 2 *nm* each contact cycle. This value is calculated using eq. (2-4) and (3-11) combined with the values for $K_0$ given in Table 4-2.

| Oil bath temperature $\Theta\,[^oC]$ | Eff. Diffusion Coefficient $K_0$ $[nm\ s^{-1/2}]$ |
|---|---|
| 50 | 2.451 |
| 100 | 3.644 |
| 150 | 4.620 |
| 200 | 4.916 |

**Table 4-2:** Effective diffusion coefficients measured [13] at different oil bath temperatures at nominal contact pressures of 22 *MPa*.

If now the thickness of the chemical layer from Table 3-1 is used, e.g. 100 *nm*, a maximum equivalent strain of 2 % is allowed for the lubricant to provide protection against metal to metal contact.

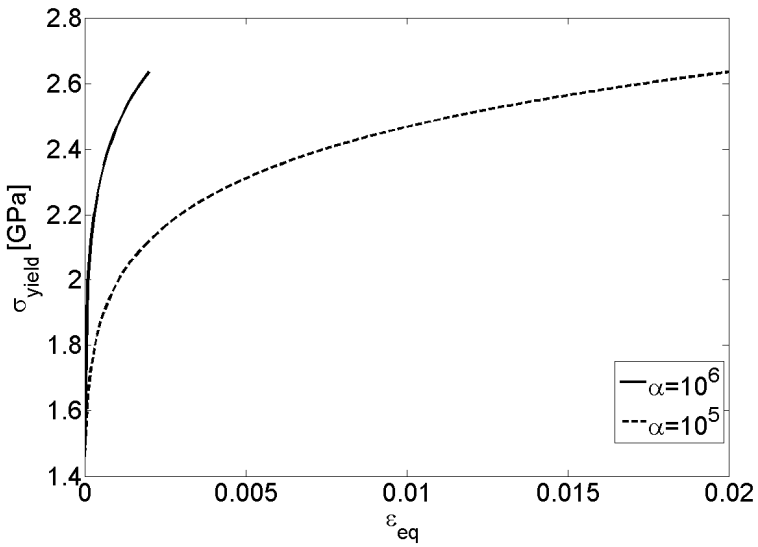


**Figure 4-1:** Yield stress as a function of the equivalent plastic strain for the two different material models used**.**

The next step is to select a microscopic geometry. For this two different systems will be used; a smooth one and a rough one which are both presented in Figure 4-2. The smooth surface originates from a cylinder of a standard SKF roller bearing (CLA roughness 70 nm) and the second is one of a hard turned surface (CLA roughness 270 nm).

If the properties of the chemical reacted layer are set to ν=0.3, $E_{layer}$=80 *GPa* and $\sigma_{yield}^{layer}$=700 *MPa* the results for both the ductile and brittle behavior for the smooth surface load at 500 *MPa* are given in appending Paper E, here it is quite clear that under these circumstances only limited corrosive wear will be present. This is, however, not yet modeled and will be discussed in section 4.4.

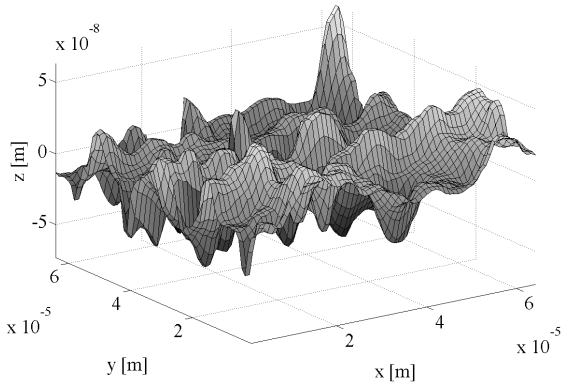


**a)**

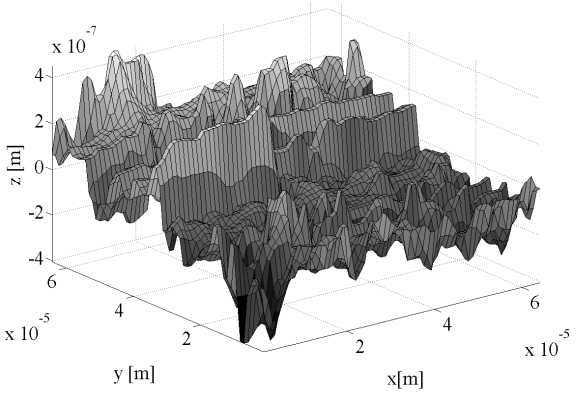


**b)**

**Figure 4-2:** Surface profile of the surfaces used in the simulations: **a)** relatively smooth polished bearing surface **b)** relatively rough, hard turned surface**.**

If now the rough surface is used with a normal pressure of 150 MPa the results for the brittle material and ductile material are given in Figure 4-3. As can be seen the surface stops running in after only a few cycles in the case of the brittle material. This would suggest that in the system only mild oxidative wear will be present through the removal of chemical products.

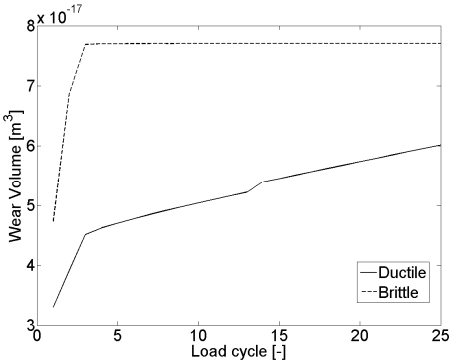


**a)**

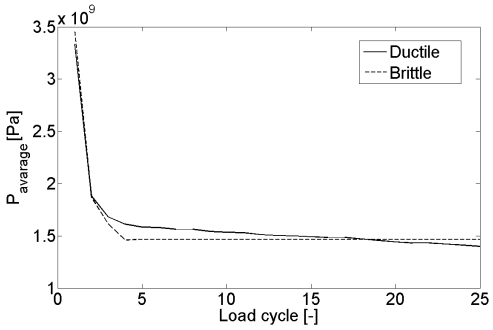


**b)**

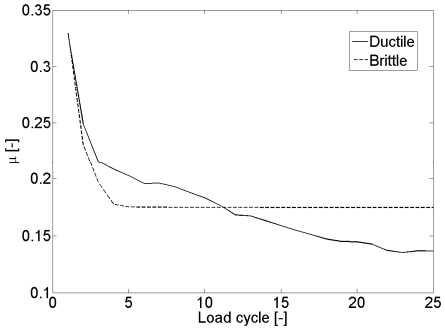


**c)**

**Figure 4-3: a)** Wear volume as a function of the load cycle **b)** Average pressure of over the contact elements as a function of the load cycle **c)** Coefficient of friction as a function of the load cycle.

As can be concluded from the results, a more ductile layer on top of the bulk material will increase the conformity with only a limited amount of wear. As can be seen in Figure 4-3 with a smaller wear volume the ductile material is already capable of creating a lower coefficient of friction, suggesting less harsh running conditions. This would be beneficial for the system during the complete lifetime of the component.

This behavior can be explained with the current simulations, because during the running in at high energetic levels it is more likely the system forms softer more ductile NC layers. This ensures that the wear is limited in the first sub-micron region of the material and the roughness is decreasing creating a more compliant situation at asperity level, giving the lubricant more opportunity to protect the surface. Meanwhile the harder bulk material reduces the apparent contact area decreasing wear at a macroscopic level. This is in contrast to the situation where the brittle bulk material behavior will prevail onto the surface, because in this situation the coefficient of friction stays at a higher level rendering the system more sensitive to micro pitting and fatigue types of failure.

## 4.2. Effect of the NC-layer on the direct base material removal model regarding friction and wear

The next step is introducing the NC layer in more detail into the model. The complete theory is presented in appended Paper F. The NC-layer is included using an adapted yield model using the measurements and curve fitting as presented in Figure 4-4 where either a monotone increasing hardness is modeled (Figure 4-4-a) or a fluctuation (Figure 4-4-b). As discussed in section 2.3 it is assumed that the elastic properties of the NC layer are the same as the bulk material. The only difference is in the plastic and failure behavior. In the literature there are two main theories dealing with the superior wear behavior seen in systems which have NC layers present on top of the bulk material. The first is that the NC layer is a harder layer, able to withstand higher mechanical loading without yielding and thus less prone to fatigue, shearing off and fracture. The second one is however the opposite; this hypothesis states that the NC layer is a softer more ductile and relatively thick layer, enabling the system to accommodate to the harsh situations at asperity level by plastic deformation. It is then supposed that through this mechanism the pressure at asperity level is lowered and the brittle bulk material is stressed less and thus protected against failure. From the literature studied on NC-material the plastic behavior and mainly failure of these materials is very sensitive to the state the crystals are in [69]: equilibrium (e.g. low grain angles) or non-equilibrium (high grain angles). Since currently this is not very well understood the maximum equivalent strain is set to 2 percent [70], which is a realistic value. For the softer material (curve B/C) also a simulation for a more ductile behavior (5 percent) is simulated, since in general softer materials are more ductile. The results of these simulations are labeled with B5 in the following figures. From the simulation results it is concluded that the difference between the use of material model curve C and B, see appending Paper F and Figure 4-4, is very limited, therefore only the results of curve B are presented.

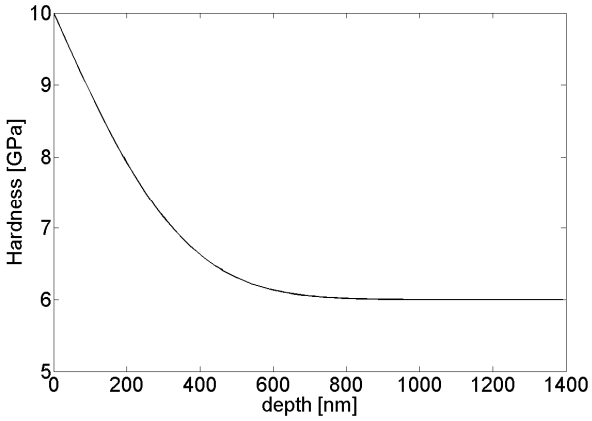


**a)**

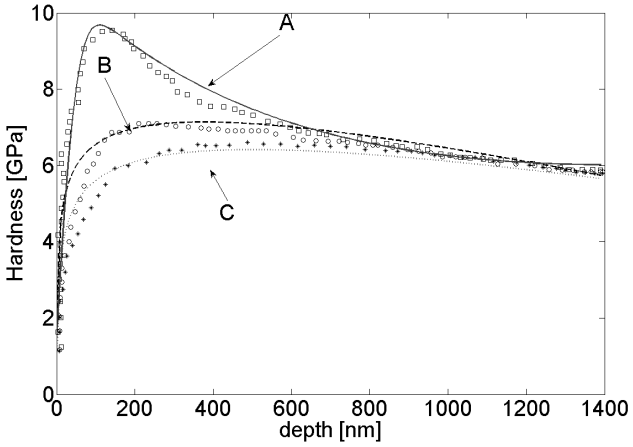


**b)**

**Figure 4-4:** Hardness profile according to measurements presented in the literature. **a)** Increasing hardness towards the surface $H=6+(1\mathrm{erf}(z/400))^4$. **b)** Different hardness profiles for curve A polished surface H=13+z/400-16arctan(z/700-1)-12erf(z/700+0.2), curve B mild wearing surface H=2.5+ln(0.75z)-z/400 and curve C for a severe wearing surface H=1.2+ln(z)-z/500 [24].

If the wear volumes and frictional behavior of the different materials are compared in Figure 4-5 it is seen that the wear volume after 25 load cycles, see for more details on load cycle appending Paper F, is the lowest for material A. This is logical since this material is formed under the most harsh contact conditions, namely the polishing. The material needs to adapt to plowing of the hard abrasive particles. Concerning long term wear behavior the difference between a monotone hardening material and material A will be close since the slope after 25 cycles is approximately the same. If friction is also taken into account, material A is the most efficient material to be present at an engineering surface.

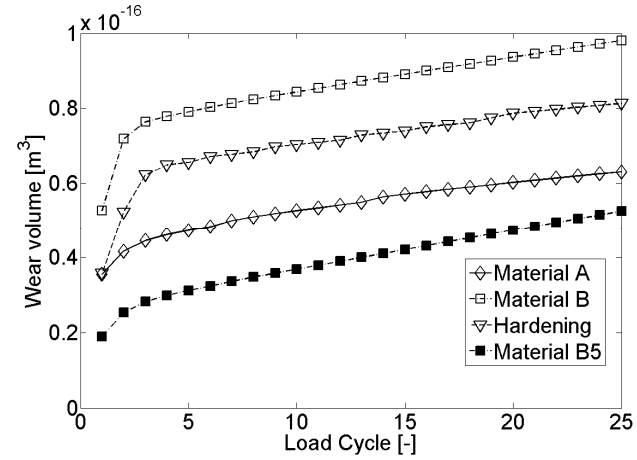


**a)**

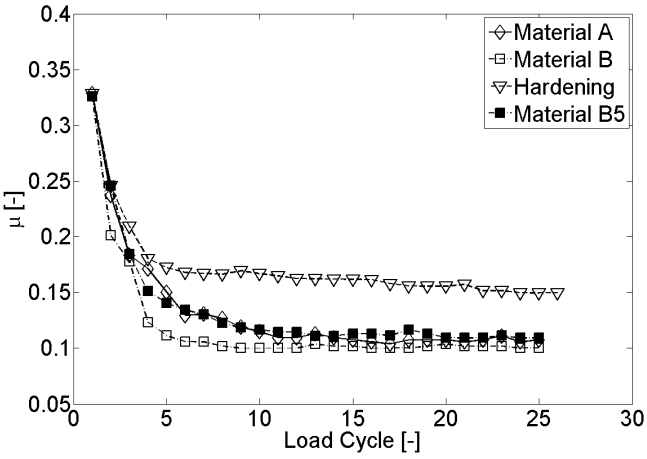


**b)**

**Figure 4-5: a)** Wear volume as a function of load cycles for the three different materials**. b)** Coefficient of friction vs. load cycle.

The influence of the increase in ductility from 2 percent to 5 percent has a very limited effect on the wear of the surface as can be concluded from Figure 4-5. The first few cycles are influenced by the increase; however the slope of the wear curve is nearly the same as for the less ductile case suggesting a comparable long-term wear behavior.

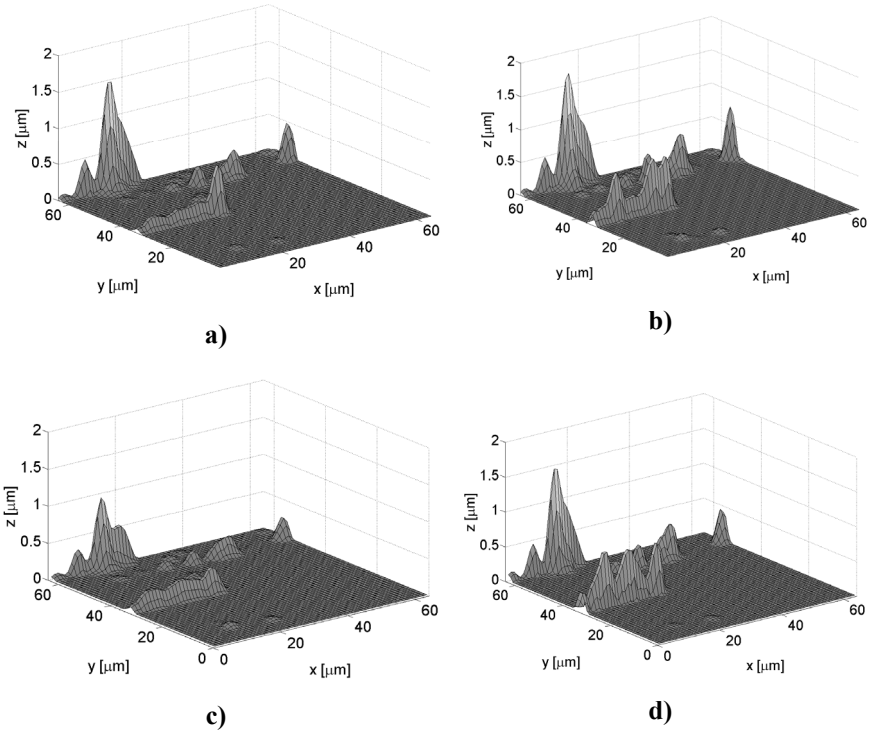


**Figure 4-6:** Wear expressed in height plots at the final load cycle for the different materials **a)** Material A **b)** Material B **c)** Material B 5 percent and **d)** Hardening only.

The wear behavior for all materials expressed in a height plot is quite similar, as can be seen in Figure 4-6 where the resulting wear volume is presented after 25 load cycles.

## *4.3. The effect of the "Anvil effect" on the direct base material removal model regarding friction and wear*

As discussed in the introduction, the chemical properties of the chemical reaction layer are influenced by the pressure put on it during contact. Typically, this is seen in the increase of the Young's modulus. The cause of this increase is still a point of intense research and is outside of the scope of the current study. However, the presence of the effect is clearly shown in [18] and a linear dependency on the pressure is reported, see Figure 4-7. Here the slope of the curve from the threshold pressure onwards is measured to be 35 and this value will thus be used in the current simulation. The material of the chemical layer is characterized as a polymer glass, yielding that the effect of the hydrostatic pressure on the yield stress can be assumed to be in the same

range as for polymers, which can also be expressed as a linear function [71] of the hydrostatic pressure and is also a good representation of the curve given in [72]:

$$\sigma_{yield} = \sigma_{yield0} + \alpha \sigma_{hydro} \tag{4-2}$$

Here $\sigma_{yield0}$ is the yield stress at zero hydrostatic pressure, which in the current case is estimated at 500 *MPa*. This is, however, only a rough estimation and in the future more research is needed since all the measured values for the yield stress of the chemical layer are indentation measurements and thus are measured under hydrostatic pressure. For the parameter $\alpha$, in equation (4-2)**,** three different values (0.1, 0.2, 0.3) are used to see how this affects the wear behavior and frictional behavior of the system.

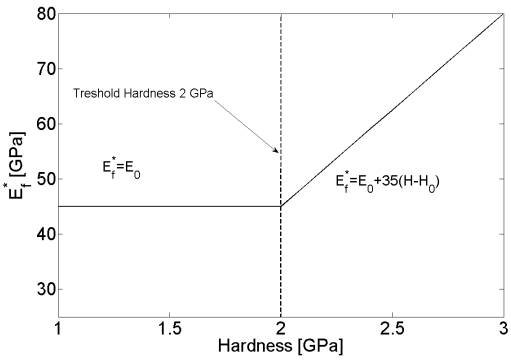


**Figure 4-7:** Young's Modulus of the chemical layer as a function of the hardness $E=E_0+35(H-H_0)$ for $H>H_0$ e.g. the maximum pressure applied to it). Figure is reproduced using the data presented in [18]**.**

The hardness of the NC layer is included in the calculation with curve B (see Figure 4-4) and a thickness of 1 $\mu m$ with an equivalent maximum stress of 5 percent, since in the author's opinion this is the most realistic situation. The rough surface is used as the input geometry combined with a nominal pressure of 150 *MPa* and a sliding velocity of 1 *m/s*.

As can be concluded from Figure 4-8, the effect of the "anvil" effect is the most pronounced when $\alpha$ is increased from 0 to 0.2 after which the effect is limited to the first few cycles. However, since the effect is currently only studied on the assumption that the yield stress is indeed influenced by the hydrostatic pressure it is strongly advised to investigate if and to what extend this effect really occurs.

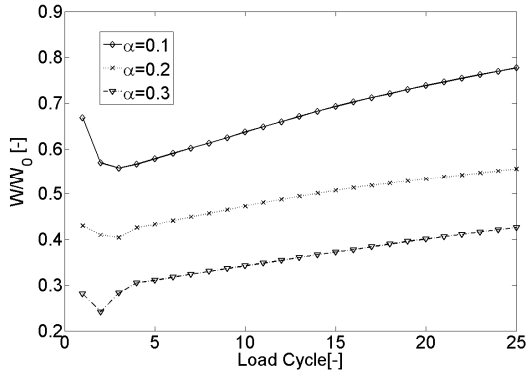


**a)**

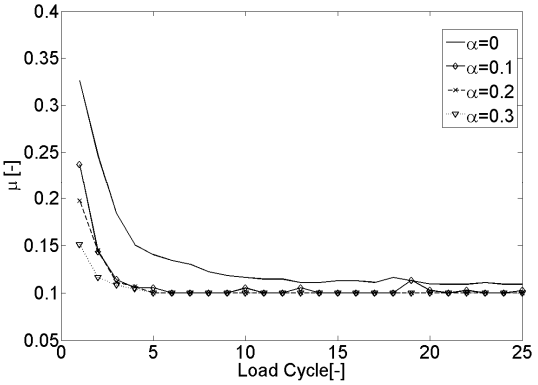


**b)**

**Figure 4-8: a)** Wear volume ($W$) normalized with the wear volume of $\alpha$=0 and no hydrostatic effect on the Young's modulus ($W_0$) for the different values of $\alpha$ **b)** coefficient of friction for the different values of $\alpha$.

## *4.4. Chemical removal of base material*

So far it is assumed that base material is directly removed through a mechanism triggered by plastic deformation. However, using only this hypothesis as a wear mechanism it would be feasible for a boundary lubricated system to run under zero wear conditions as long as the maximum equivalent strain criteria is not met. In reality a system will never operate without wear. In the situation that the additives in the oil are capable of preventing metal to metal contact, e.g. preventing high friction drawing plasticity towards the surface, wear will take place through the use of base material to restore the chemical balance, see for example Figure 2-3. This principle can be regarded as light chemical polishing. In the current model the assumptions are the same as for the direct base material removal model, with the major difference in the

contact model. As for the chemical removal model, the contact solver is an elastic-plastic one, which is discussed in more detail in appended Paper D.

The elements on top of the system previously used to determine the local friction coefficient (see appending Paper D, E and F) will now be used for a different purpose: to determine the volume removed during contact as discussed in more detail in Paper G and H. The indentation in the thickness direction of the layer is now multiplied by the element size creating a wear volume. It is then determined how much base material this volume contains, as the system will use the same amount to restore the balance. This can be regarded as the loss of material and thus the wear of the system.

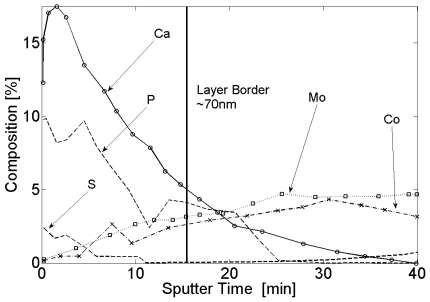


**a)**

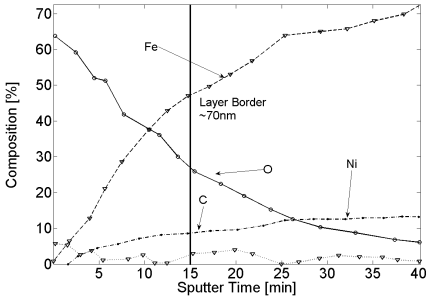


**b)**

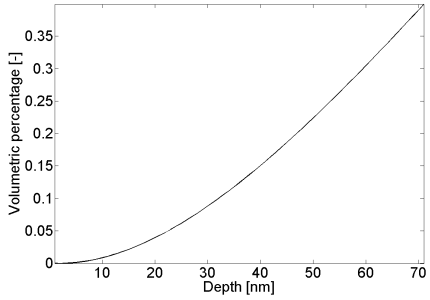


**c)**

**Figure 4-9:** Chemical composition of the chemical layer present in the system being studied**. a)** and **b)** XPS spectrum of the chemical layer present at the surface **c)** Volumetric percentage function.

For this purpose, the chemical composition of the chemical layer is needed for a given system. To determine this XPS is used, see for the result Figure 4-9-a. Here the result is presented for a boundary lubricated steel-steel contact with a normal pressure of around 150 *MPa* and a sliding speed of 1 *m/s*. Using this chemical composition as an input the volumetric content of the layer can be determined using the atomic diameters of the different components, of which the result is also presented in Figure 4-9-b.

In the system analyzed in Figure 4-9 the lubricant used was ZDDP-rich oil, this suggests that the mechanical properties are in the same range as given in Table 3-1 and the material behaves as given in Figure 4-7. Using the CGM contact model used in Paper C and the theory presented in Paper F the plastic strain in the thickness direction of the chemical layer $\varepsilon_{plzz}^{layer}$ can be computed. If this is then combined with the hypothesis presented in Figure 2-3 mild chemical wear can be modeled.

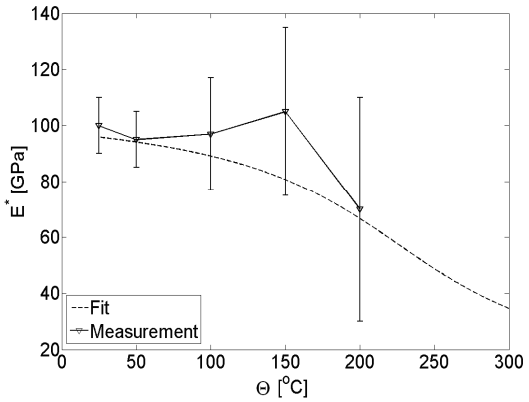


**Figure 4-10:** Equivalent Young's modulus $E^*$ as a function of the temperature, measurement data is reproduced from [8]**.**

However, if now sliding wear were to be modeled using only the contact model, an incremental step of only one element in the sliding direction is computed. This would imply significant computational times. However, as is shown in appended Paper C, this problem can be dealt with by setting the wear coefficient constant over one sliding increment. To do so, first the wear volume of a single situation is normalized by the characteristic length and rewritten to the wear height rather than the wear volume:

$$\frac{h_{inst}(x,y)}{l} = \frac{W_{wear}}{\Delta x \Delta y l} = \frac{W_{perc}(\varepsilon_{pl_{zz}}^{layer} h_{layer})\varepsilon_{pl_{zz}}^{layer} h_{layer}}{l} \tag{4-3}$$

Here $h_{inst}$ is the height loss due to contact situation calculated, $\Delta x$, $\Delta y$ the element size in respectively the $x$ and $y$ direction, $\varepsilon^{layer}{}_{plzz}$ the plastic strain in thickness direction of the reaction layer, $h_{layer}$ the thickness of the layer and $l$ the characteristic length it takes to detach the wear particle. It is assumed that for a wear particle to detach the average

length of the contact zone in direction of sliding needs to be slid. This can then be used as the wear rate expressed in profile height loss by multiplying it with the sliding increment giving:

$$h_{wear}(x,y) = \frac{h_{inst}(x,y)}{l}\Delta s \tag{4-4}$$

To validate this theory a mild wear test was performed using a CSM pin on disk tribometer. The sliding and stationary elements are a ball and disk of AISI 52100 with a hardness of 6.6 *GPa*. The surface topography of the elements is shown in Figure 4-11 and the test conditions in Table 4-3.

| Test conditions | |
|---|---|
| $F_N[N]$ | 10 |
| $V\ [m/s]$ | 0.005 |
| $\Theta_{env}\left[^{o}C\right]$ | 25 |
| $\mu\,[-]$ | 0.14 |
| Geometrical entities | |
| $R_{ball}\ [m]$ | $2\times10^{-3}$ |
| $R_{weartrack}\ [m]$ | $47\times10^{-3}$ |
| $R_{cylinder\ x}, R_{cylinder\ y}[m]$ | $4\times10^{-3}$ ,$26.67\times10^{-3}$ |
| Measurement results | |
| $k_{measured}^{ball}\left[mm^3/Nm\right]$ | $8\times10^{-9}$ |
| $k_{measured}^{cylinder}\left[mm^3/Nm\right]$ | $1.6\times10^{-8}$ |
| Calculation results | |
| $k_{calc}^{ball}\left[mm^3/Nm\right]$ | $4\times10^{-9}$ |
| $k_{calc}^{cylinder}\left[mm^3/Nm\right]$ | $9\times10^{-9}$ |

**Table 4-3:** Test conditions and results**.**

Under these very mild conditions the pressure in the contact will be under the threshold hardness of 2 *GPa* and thus the Young's modulus of the chemical reaction layer will be in the range of 40-45 *GPa*, while thermal effects can be neglected since the temperature rise in the contact will be less than one degree Celsius, see Figure 4-11-d. At this temperature the mechanical properties of the layer are not influenced significantly as can be concluded from Figure 4-10. For the hardness of the chemical layer a representative value is taken of 1 *GPa* due to the mild running conditions [61].

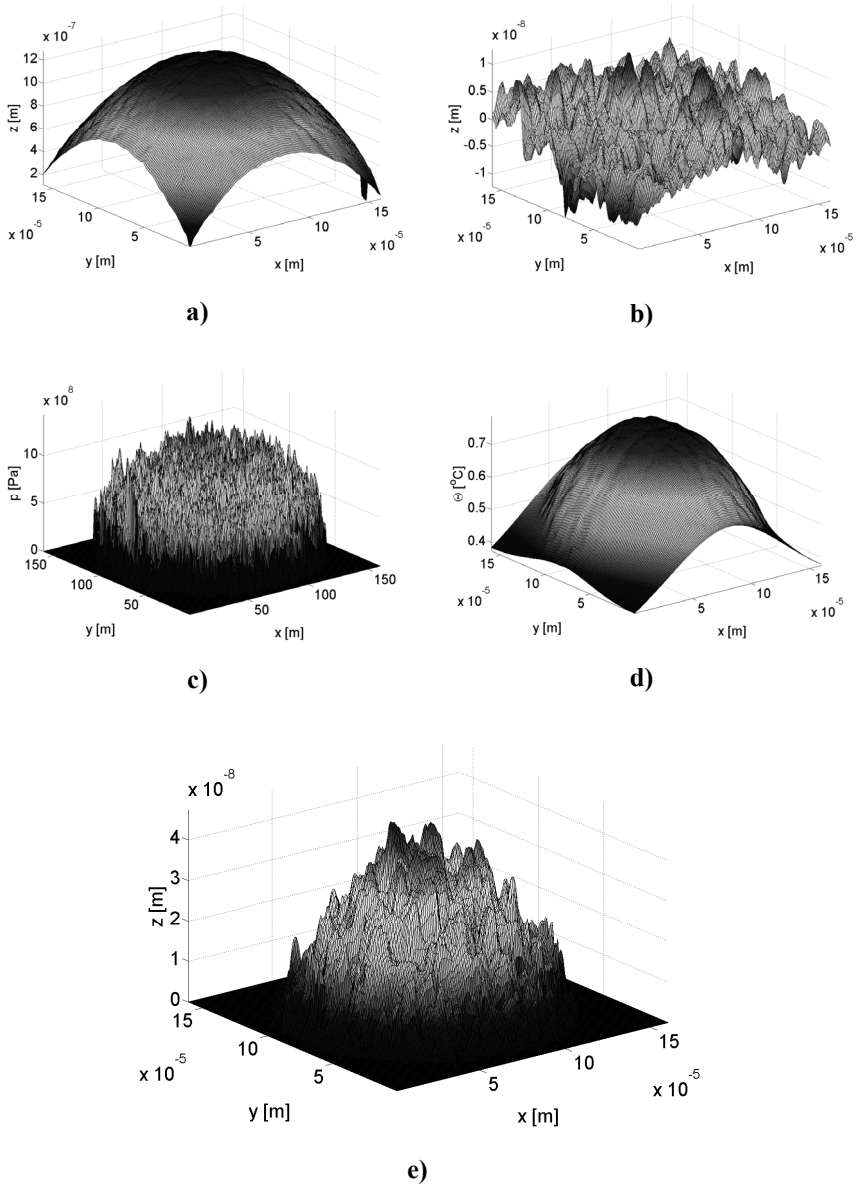


**Figure 4-11: a)** Surface topography of the ball and **b)** of the disk used during the experiments and simulations**. c)** Resulting pressure field and **d)** temperature field **e)** wear volume after 10 *m* of sliding**.**

Due to the very mild conditions it can be assumed that the main wear mechanism will be very mild wear by chemical removal through the mechanism suggested. This conclusion is also supported by the value of the specific wear rate resulting from the simulations and from the experiments, which are in good agreement with each other, see Table 4-3.

If now a system is taken which is already run-in, rather than a new system, as shown in Figure 4-12, the specific wear rate calculated is $9\times10^{-9}$ $mm^3/Nm$, while the measured specific wear rate is $1.6\times10^{-8}$ $mm^3/Nm$, which are both in the same range suggesting that the proposed model is capable of predicting mild wear under boundary lubricated conditions using values originating from measurements performed on comparable systems. However, the value of the calculated specific wear rate can be significantly improved if the exact properties of the chemical layer in the experimental system were known.

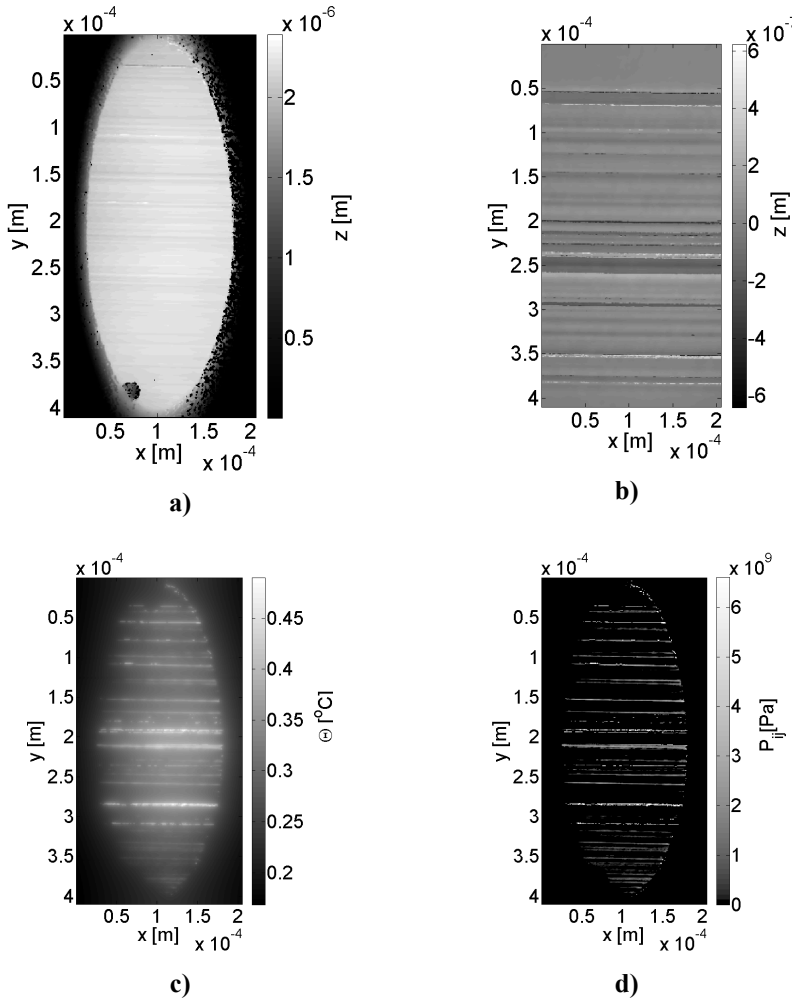


**Figure 4-12: a)** Surface profile of a cylinder run for 8 hours under the conditions given in Table 4-3**. b)** Counter surface topography **c)** Temperature field in the contact and **d)** Pressure field in the contact**.**

## 4.5. Wear diagram

As a next step the theory presented in the previous section will be combined with the theory discussed in chapter 1 and Paper B and C concerning the transition from mild wear to severe adhesive wear. The author would like to emphasize that this part of the thesis will not be validated by experiments yet and is added to show the practical implementation of the proposed models. For the simulations, surfaces are used without running in as are presented in Paper C (Figure 9), and values of the parameters and load and velocity are used as in that paper. The grid size is set to 240×240 elements since this has shown not to affect the accuracy of the calculations. The resulting "wear map" is presented in Figure 4-13. Here the effect of the temperature on the properties of the chemical layer becomes more pronounced as the curvature of the "iso-wear" lines have the same slope as the transition line, which is basically an iso-thermal line since it is created by a thermal threshold. As can be seen the values for the specific wear rate are in a realistic range for boundary lubricated contacts [73].

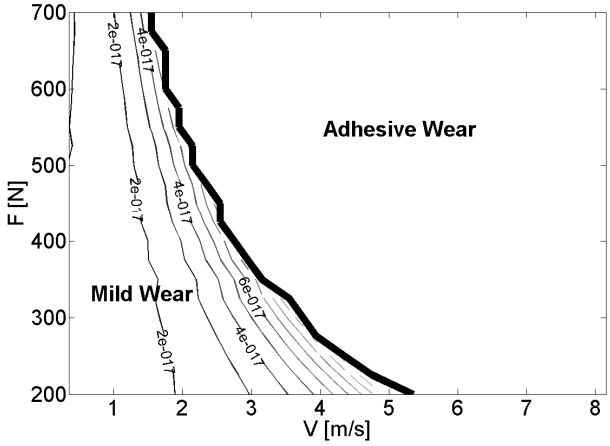


**Figure 4-13:** Wear map computed using the mild wear model combined with the transition model using the smooth-rough combination**.**

In Paper C the surfaces were a rough surface running against a smooth one ($Ra$=0.27 $\mu m$ vs. $Ra$=0.08 $\mu m$). To see how the roughness influences the wear map, i.e. transition from mild to severe wear as well as the wear rates within the mild wear regime, two additional simulations are done: one with a smooth-smooth combination and one with a rough-rough surface combination. The results are shown in Figure 4-14 and Figure 4-15 respectively. From these figures it can be concluded that the major effect of the surface roughness on the wear map is the location of the transition, rather than on the magnitude of the specific wear rate before the transition takes place. However, since in the current model the effect of the different contact conditions on the properties of the layer are not yet taken into account this conclusion should be interpreted with some care. For more examples on complete wear maps the reader is referred to appended Paper H.

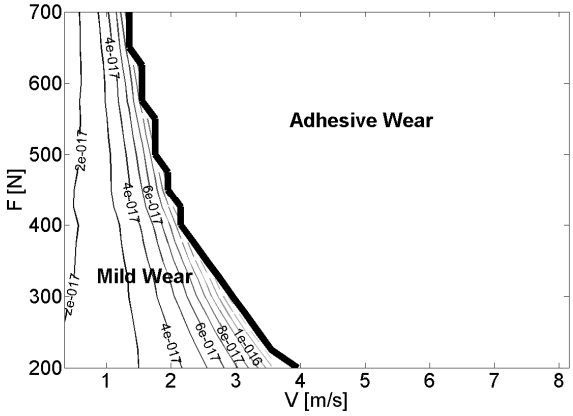


**Figure 4-14:** Wear map computed using the mild wear model combined with the transition model for the rough-rough surface combination**.**

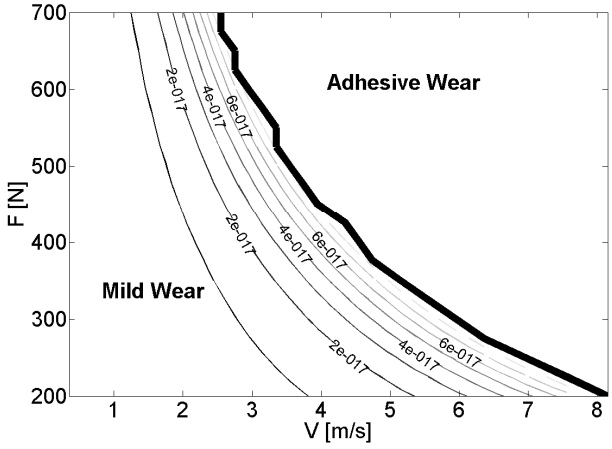


**Figure 4-15:** Wear map computed using the mild wear model combined with the transition model using the smooth-smooth surface combination**.**

# 5. Conclusions and Recommendations

In this thesis a first step is made in modeling three main phenomena in the wear of a surface: 1) the transition from mild to severe wear 2) running-in 3) steady state mild wear. The first is based upon a thermal threshold and yields very good coherence with the experimental results. The second is modeled using a Semi-Analytical-Contact code based upon the Boundary Integral Method and a wear criterion based on the maximum equivalent strain a material can handle. Combining this method with a model for the local coefficient of friction forms a running-in/wear model. The experimental validation of this model is recommended for future research, since in the current study the equipment needed for this was not available either at the university or industrial partners and thus a validation through general results found in the literature is done. The next step in the lifetime of a component is steady state wear. In this work a model based on observations done in boundary lubricated systems running under mild conditions is given, thereby completing the wear modeling to contain all cycles of the complete lifetime.

The main focus for future research should not only be on improving the wear models but also on a better understanding of the properties of the different layers in the system and especially the effect of the different running conditions on the properties and thickness of the layer formed, since it is shown that pressure and temperature have a pronounced effect on the properties of these layers (as discussed in sections 4.3 and 4.4). Within the current project attempts were made to obtain the different properties of the layers present in a model system under different running conditions. However, this task has not been completed due to its complex and costly nature. Therefore, representative values are taken from the literature; however for the model to become more general it is advised to put effort into the development of growth and material models for the chemical layer as well as the NC-layer, since this will make it feasible to predict the layers present in the system rather than measure them afterwards.

The growth model would also give more insight on the effect the temperature has on the diffusion of the chemical products into the Nano-Crystalline layer. Also, the effect the grain refinement has on the effective diffusion of the additive components is a subject which needs to be dealt with, since it is shown that the effective diffusion in NC-materials is higher due to the increase in grain boundary fraction, see for example [74-75]. These factors will increase the growth speed of the chemical layer and thus the protective capacity of the layer.

To validate the results of the models themselves a setup which can measure the roughness in a semi-online manner through a lubricant layer is needed, since cleaning the sample for each measurement will disturb the diffusion process and perhaps remove soft decomposed additive components which are the precursors of the chemical reaction layer. A confocal microscope with an adapted pin on disk setup would be a good option to do so.

# Appendix A : DC-FFT

In (semi-infinite) contact mechanics the main computational burden originates from the convolution between the pressure field and its influence matrix:

$$u(x,y) = \int\int p(x',y')K(x-x',y-y')dx'dy' \tag{A-1}$$

This convolution can be speed up greatly by doing in the frequency domain since:

$$\tilde{\tilde{u}}(\omega_1,\omega_2) = \tilde{\tilde{p}}(\omega_1,\omega_2)\cdot\tilde{\tilde{K}}(\omega_1,\omega_2) \tag{A-2}$$

However, if not enough care is taken a numerous amount of errors may occur with this operation. In this appendix a short introduction into the DC-FFT methods used in the results of this thesis are given.

There are main routes used in this thesis namely route 1 and 3 from reference [76], consisting of two different inputs:

1. The influence functions (usually Green functions) are known in the time/space domain.
2. The influence functions can be derived in the frequency domain rather than in the time domain. This will require an extra transformation as will be discussed shortly.

The mathematical proof of the methods discussed are left out for brevity and the interested reader is referred to [77]. First route 1 will be discussed.

Route 1 mainly consists of the following relatively simple steps:

1. Compute the influence coefficient $\{K_j\}_N$ (in the case of an asymmetric influence matrix compute $\{K_j\}_{2N}$
2. Wrap around order and zero padding of $\{K_j\}_N$ (see Figure A-1).
3. Apply FFT to $\{K_j\}_{2N}$ to get $K$ $\left\{\tilde{\tilde{K}}_j\right\}_{2N}$
4. Zero pad $\left\{P_j\right\}_{2N\ j=N+1:2N} = 0$ and FFT input pressure $\left\{P_j\right\}_N$ to $\left\{\tilde{\tilde{P}}_j\right\}_{2N}$
5. Obtain $\left\{\tilde{\tilde{u}}_j\right\}_{2N} = \left\{\tilde{\tilde{P}}_j\right\}_{2N}\left\{\tilde{\tilde{K}}_j\right\}_{2N}$
6. IFFT $\left\{\tilde{\tilde{u}}_j\right\}_{2N}$ and take solution $\left\{u_j\right\}_N = \left\{u_j\right\}_{2N\ j=1:N}$

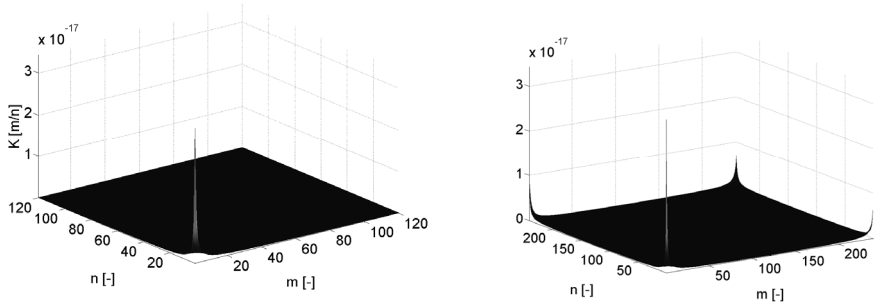


**a)** **b)**

**Figure A-1: a)** normal influence matrix (size 2Nx2M) b) wrap around influence matrix**.**

If however the influence coefficient are not known in the time/space domain the influence matrix is obtained through a Fourier analysis. One of the major issues here is to represent an infinite function representation $\tilde{h}(\omega)$ with a finite number of points without losing accuracy. For this purpose an anti aliasing method is used. Infinite function $\tilde{h}(\omega)$ is converted into a discrete series $K_j = h(t_j)\Delta$ by discretizing $\tilde{h}/\Delta$ into a series having $\gamma N/2$ complex members with an interval of $2\pi/(\gamma N\Delta)$ where $\gamma = 2:4:8....$ . This creates a series that spans between $0$ and the critical Nyquist frequency, $\omega_c = \pi/\Delta$. Here $N$ is thus used to create a denser mesh in the frequency domain while after IFFT the time domain in the range of $j = 1:N$ still corresponds to the domain of interest. However, by truncating the frequency at $\omega_c$ a conversion error occurs since the higher frequency information is lost. This can however also be compensated by mimicking the ailising behavior inherent to FT algorithms. If now the frequency domain is expended with a multiple of $\omega_c$ it is allowed to copy this back into the domain spanned from $0$ to $\omega_c$ thus including the high frequency domain and limiting the truncation error made through:

$$\tilde{\tilde{K}}_{s-r} = \tilde{\tilde{K}}_s \tag{A-3}$$

Here $s \in [(\gamma N/2-1), \gamma N-1]$ and $r = [\gamma N/2]$ enabling to copy the high frequency response (extended area in Figure A-2) into the domain of interest.

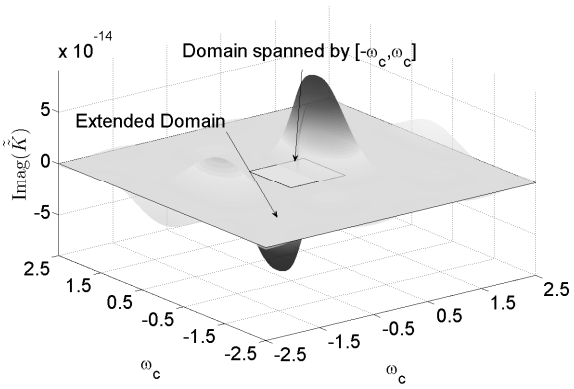


**Figure A-2:** The high frequency extended domain and the domain of interest (for a extension of $2\omega_c$).

The effect on the transformed signal is quite well visible in Figure A-3.

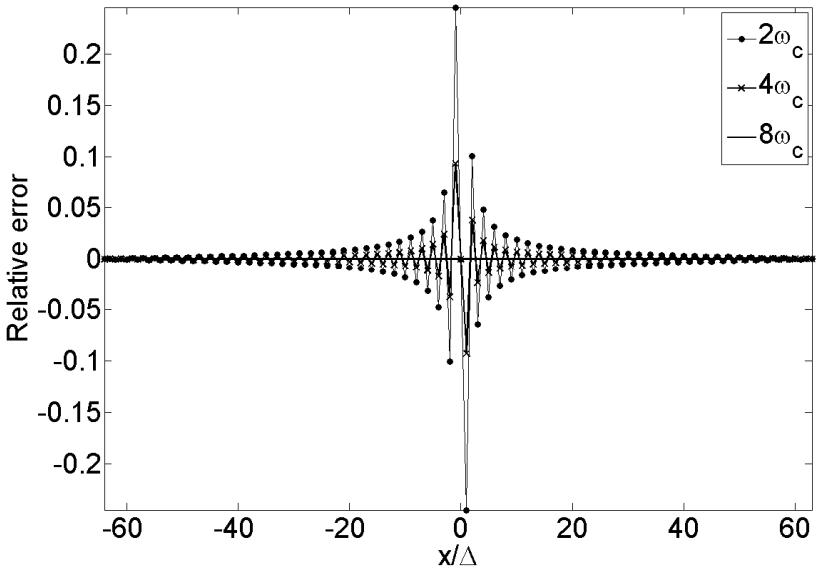


**Figure A-3:** Response function for the different domain extensions**.**

# Appendix B : Elastic contact Code

The elastic contact code is based upon the single loop CGM method first presented by Keer and Polonsky [78-79] and later on by Liu et al. [67, 76-77, 80-81]. In the later studies the multi summation method used to increase the computational performance of the contact code is replaced by the DC-FFT algorithm. At first the elastic contact code will be discussed shortly starting with the contact inequalities:

$$\sum_{(k,l)\in I_{discr}} D_{i-k,j-l}\, p_{kl} = h_{ij} + \alpha, \quad (i,j) \in I_c \tag{B-1}$$

$$p_{ij} > 0, \quad (i,j) \in I_c \tag{B-2}$$

$$\sum_{(k,l)\in I_{discr}} D_{i-k,j-l}\, p_{kl} \geq h_{ij} + \alpha, \quad (i,j) \notin I_c \tag{B-3}$$

With $h_{ij}$ the original surface separation, $\alpha$ the rigid body motion and $I_c$ all grid points in contact.

$$\Delta x \Delta y \sum_{(i,j)\in I_c} p_{ij} = \mathrm{F_n} \tag{B-4}$$

The inequalities stated will be solved using a CGM based iterative scheme. First the displacement of the current pressure guess is computed using the DC-FFT algorithm discussed in Appendix A and from this the current gap:

$$g_{ij} = -u_{ij} - h_{ij}, \quad (i,j) \in I_c \tag{B-5}$$

The average gap is obtained by:

$$\bar{g} = \frac{1}{N_c} \sum_{(k,l)\in I_c} g_{kl}$$
$$g_{ij} \leftarrow g_{ij} - \bar{g} \tag{B-6}$$

Here $N_c$ is the current number of elements in contact and $I_c$ are all grid points in the discretized region where $p_{ij} > 0$. For the new gap the sum is calculated:

$$G = \sum_{(i,j)\in I_c} g_{ij}^{\,2} \tag{B-7}$$

This value is then used to compute the new conjugate direction $t_{ij}$:

$$t_{ij} = g_{ij} + \delta(G/G_{old})t_{ij}, \quad (i,j) \in I_c \tag{B-8}$$

$$t_{ij} = 0, \quad (i,j) \notin I_c \tag{B-9}$$

The old value of $G$ is now stored for the new iteration $(G_{old} = G)$ and the convolution of $D_{ij}$ and $t_{ij}$ is computed for distribution in the multidimensional space of elemental pressures:

$$r_{ij} = \sum_{(k,l)\in I_{discr}} D_{i-k,j-l} t_{kl}, \quad (i,j) \in I_{discr} \tag{B-10}$$

$$\bar{r} = \frac{1}{N_c} \sum_{(k,l)\in I_c} r_{kl} \tag{B-11}$$

$$r_{ij} = r_{ij} - \bar{r}, \quad (i,j) \in I_{discr} \tag{B-12}$$

The size of the next iteration step is then computed:

$$\tau = \frac{\sum_{(i,j)\in I_c} g_{ij} t_{ij}}{\sum_{(i,j)\in I_c} r_{ij} t_{ij}} \tag{B-13}$$

The current pressure is stored for error computation:

$$p_{ij}^{\ old} = p_{ij}, \quad (i,j) \in I_{discr} \tag{B-14}$$

Now the pressure is updated:

$$p_{ij} = p_{ij} - \tau t_{ij}, \quad (i,j) \in I_c \tag{B-15}$$

Next the inequalities of eq. (B-2) is enforced setting all $p_{ij} < 0$ equal to $0$ after which the overlap is determined:

$$I_{ol} = \left\{(i,j) \in I_{disrc} : \quad p_{ij} = 0,\ g_{ij} < 0\right\} \tag{B-16}$$

If $I_{ol} = \varnothing$, then $\delta$ is set to unity otherwise to zero and the pressures at the overlap are corrected:

$$p_{ij} = p_{ij} - \tau g_{ij}, \quad (i,j) \in I_{ol} \tag{B-17}$$

Since $\tau > 0$ at every iteration all nodes in $I_{ol}$ will enter $I_c$ enforcing eq. (B-2). Next the current contact load is calculated and the error is estimated by enforcing eq. (B-4):

$$F_{it} = \Delta x \Delta y \sum_{(i,j) \in I_{discr}} p_{ij} \tag{B-18}$$

$$p_{ij} = \left(F_{it} / F_n\right) p_{ij}, \quad (i,j) \in I_{discr} \tag{B-19}$$

$$\varepsilon = \Delta x \Delta y F_n^{-1} \sum_{(i,j) \in I_{discr}} \left| p_{ij} - p_{ij}^{\ old} \right| \tag{B-20}$$

This iterative loop is repeated until $\varepsilon < \varepsilon_{set}$, which is set to $10^{-14}$. The contact model gives more realistic results by setting a maximum threshold to the contact pressure equal to the hardness of the material which is done in the same way as the restriction in eq. (B-2).

If now the pressure is known combined with the coefficient of friction the stress due to the normal pressure and surface traction can be calculated for the uncoated case the influence matrices for a uniform contact patch of size $2a \times 2b$ are known in the space-time domain and are [48]:

$$\sigma_{33}^{ij} = \frac{p}{2\pi} \begin{bmatrix} S_{33}^{ij}(x+a, y+b, z) - S_{33}^{ij}(x+a, y-b, z) \\ + S_{33}^{ij}(x-a, y-b, z) \\ - S_{33}^{ij}(x-a, y+b, z) \end{bmatrix} \tag{B-21}$$

With:

$$\begin{aligned} S_{33}^{11}(x,y,z) = 2\tan^{-1}\left(\frac{z^2 + y^2 - yR}{zx}\right) + \\ 2(1-2\nu)\tan^{-1}\left(\frac{R - y + z}{x}\right) \\ + \frac{(xyz)}{R(x^2 + z^2)} \end{aligned} \tag{B-22}$$

$$S_{33}^{22}(x,y,z) = 2\nu \tan^{-1}\left(\frac{z^2+y^2-yR}{zx}\right) + 2(1-2\nu)\tan^{-1}\left(\frac{R-x+z}{y}\right) + \frac{(xyz)}{R(y^2+z^2)} \tag{B-23}$$

$$S_{33}^{33}(x,y,z) = -\tan^{-1}\left(\frac{xy}{Rz}\right) + \frac{xy}{Rz} + \frac{xz}{R(R+y)} + \frac{yz}{R(R+x)} \tag{B-24}$$

$$S_{33}^{12}(x,y,z) = \frac{-z}{R} - (1-2\nu)\ln(R+z) \tag{B-25}$$

$$S_{33}^{13}(x,y,z) = \frac{-z^2}{R(R+y)} \tag{B-26}$$

$$S_{33}^{23}(x,y,z) = \frac{-z^2}{R(R+x)} \tag{B-27}$$

$$\sigma_{13}^{ij} = \frac{p}{2\pi}\begin{bmatrix} S_{13}^{ij}(x+a,y+b,z) \\ -S_{13}^{ij}(x+a,y-b,z) + S_{13}^{ij}(x-a,y-b,z) \\ -S_{13}^{ij}(x-a,y+b,z) \end{bmatrix} \tag{B-28}$$

$$S_{13}^{11}(x,y,z) = \frac{-z}{R}\left(1+\frac{yz-x^2}{(R+z)(R-y)}\right) + 2\nu\left(\frac{y}{(R+z)}\right) - 2\ln(R-y) \tag{B-29}$$

$$S_{13}^{22}(x,y,z) = \frac{-yz}{(R(R+z))} - 2\nu\left(\frac{y}{R+z} - 2\ln(R-y)\right) \tag{B-30}$$

$$S_{13}^{33}(x,y,z) = \frac{yz^2}{R(x^2+z^2)} \tag{B-31}$$

$$S_{13}^{12}(x,y,z) = \frac{-xz}{R(R+z)} - 2\nu\left(\frac{x}{R+z}\right) - \ln(R-x) \tag{B-32}$$

$$S_{13}^{13}(x,y,z) = \frac{xyz}{R(x^2+z^2)} + \tan^{-1}\left(\frac{z^2+y^2-yR}{xz}\right) \tag{B-33}$$

$$S_{13}^{23}(x,y,z) = \frac{-z}{R} \tag{B-34}$$

The total elastic stress state is defined as:

$$\sigma_{tot}^{ij} = \sigma_{13}^{ij} + \sigma_{33}^{ij} \tag{B-35}$$

For the surface with a single coating the equations for the stresses due to pressure and traction are not given in the time space domain but rather in the frequency domain. This is however not a problem but requires a different DC-FFT routine as discussed in Appendix A. The equations are [67]:

$$\begin{aligned}\tilde{\tilde{\sigma}}_{11}^{(r)} = &-m^2(D^{(r)}w_-^r + \overline{D}^{(r)}w_+^{(r)}) - 2im(2-\nu_{(r)})(B^{(r)}w_-^{(r)} + \overline{B}^{(r)}w_+^{(r)}) \\ &- 2\alpha\nu_{(r)}\left(-C^{(r)}w_-^{(r)} + \overline{C}^{(r)}w_+^{(r)}\right) \\ &- im^3 z_r \alpha^{-1}(B^{(r)}w_-^{(r)} - \overline{B}^{(r)}w_+^{(r)}) - z_{(r)}m^2(-C^{(r)}w_-^{(r)} + \overline{C}^{(r)}w_+^{(r)})\end{aligned} \tag{B-36}$$

$$\begin{aligned}\tilde{\tilde{\sigma}}_{22}^{(r)} = &-n^2(D^{(r)}w_-^r + \overline{D}^{(r)}w_+^{(r)}) - 2im\,\nu_{(r)}(B^{(r)}w_-^{(r)} + \overline{B}^{(r)}w_+^{(r)}) \\ &- 2\alpha\nu_{(r)}\left(-C^{(r)}w_-^{(r)} + \overline{C}^{(r)}w_+^{(r)}\right) \\ &- imn^2 z_r \alpha^{-1}(B^{(r)}w_-^{(r)} - \overline{B}^{(r)}w_+^{(r)}) \\ &- z_{(r)}n^2(C^{(r)}w_-^{(r)} + \overline{C}^{(r)}w_+^{(r)})\end{aligned} \tag{B-37}$$

$$\begin{aligned}\tilde{\tilde{\sigma}}_{33}^{(r)} = &\alpha^2(D^{(r)}w_-^r - \overline{D}^{(r)}w_+^{(r)}) + 2im(1-\nu_{(r)})(B^{(r)}w_-^{(r)} + \overline{B}^{(r)}w_+^{(r)}) \\ &- 2\alpha(1-\nu_{(r)})\left(-C^{(r)}w_-^{(r)} + \overline{C}^{(r)}w_+^{(r)}\right) \\ &- imz_r\alpha(B^{(r)}w_-^{(r)} - \overline{B}^{(r)}w_+^{(r)}) + z_{(r)}\alpha^2(C^{(r)}w_-^{(r)} + \overline{C}^{(r)}w_+^{(r)})\end{aligned} \tag{B-38}$$

$$\begin{aligned}\tilde{\tilde{\sigma}}_{12}^{(r)} = &-mn(D^{(r)}w_-^r + \overline{D}^{(r)}w_+^{(r)}) - 2in(1-\nu_{(r)})(B^{(r)}w_-^{(r)} + \overline{B}^{(r)}w_+^{(r)}) \\ &+ im^2 n z_r \alpha^{-1}(B^{(r)}w_-^{(r)} - \overline{B}^{(r)}w_+^{(r)}) - z_{(r)}nm(C^{(r)}w_-^{(r)} + \overline{C}^{(r)}w_+^{(r)})\end{aligned} \tag{B-39}$$

$$\begin{aligned}\tilde{\tilde{\sigma}}_{13}^{(r)} &= -im\alpha(D^{(r)}w_{-}^{r} - \overline{D}^{(r)}w_{+}^{(r)}) + \\ &\left(2\alpha(1-\nu_{(r)}) + m^2\alpha^{-1}\right)(B^{(r)}w_{-}^{(r)} - \overline{B}^{(r)}w_{+}^{(r)}) \\ &- im(1-2\nu_{(r)})\left(C^{(r)}w_{-}^{(r)} + \overline{C}^{(r)}w_{+}^{(r)}\right) \\ &- im^2 z_r(B^{(r)}w_{-}^{(r)} + \overline{B}^{(r)}w_{+}^{(r)}) + iz_{(r)}\alpha m(-C^{(r)}w_{-}^{(r)} + \overline{C}^{(r)}w_{+}^{(r)})\end{aligned} \tag{B-40}$$

$$\begin{aligned}\tilde{\tilde{\sigma}}_{23}^{(r)} &= -in\alpha(D^{(r)}w_{-}^{r} - \overline{D}^{(r)}w_{+}^{(r)}) + mn\alpha^{-1}(B^{(r)}w_{-}^{(r)} - \overline{B}^{(r)}w_{+}^{(r)}) \\ &- in(1-2\nu_{(r)})\left(C^{(r)}w_{-}^{(r)} + \overline{C}^{(r)}w_{+}^{(r)}\right) \\ &- mnz_r(B^{(r)}w_{-}^{(r)} + \overline{B}^{(r)}w_{+}^{(r)}) + inz_{(r)}\alpha(-C^{(r)}w_{-}^{(r)} + \overline{C}^{(r)}w_{+}^{(r)})\end{aligned} \tag{B-41}$$

$$\begin{aligned}2\mu_{(r)}u_3^{(r)} &= -\alpha(D^{(r)}w_{-}^{r} - \overline{D}^{(r)}w_{+}^{(r)}) + im\alpha^{-1}(B^{(r)}w_{-}^{(r)} - \overline{B}^{(r)}w_{+}^{(r)}) \\ &- (3-4\nu_{(r)})\left(C^{(r)}w_{-}^{(r)} + \overline{C}^{(r)}w_{+}^{(r)}\right) \\ &- imz_r(B^{(r)}w_{-}^{(r)} + \overline{B}^{(r)}w_{+}^{(r)}) + z_{(r)}\alpha(-C^{(r)}w_{-}^{(r)} + \overline{C}^{(r)}w_{+}^{(r)})\end{aligned} \tag{B-42}$$

Here the following expressions are used:

$$w_{+}^{(r)} = e^{\alpha z_r},\ w_{-}^{(r)} = e^{-\alpha z_r} \tag{B-43}$$

$$\theta^{-} = e^{-ah},\ \theta = e^{\alpha h} \tag{B-44}$$

$$\overline{\mu} = \mu_1 / \mu_2 \tag{B-45}$$

$$\overline{\nu} = (1-\nu_2)/(1-\nu_1) \tag{B-46}$$

$$\overline{B}^{(1)} = \beta_1(\overline{\mu} - 1)\theta^{-2} \tag{B-47}$$

$$B^{(1)} = \beta_1(\overline{\mu} + 1) \tag{B-48}$$

$$B^{(2)} = 2\beta_1\theta^{-1}/\overline{\nu} \tag{B-49}$$

$$\beta_1 = -\tilde{\tilde{s}} / \left[\left(2\alpha(1-\nu_1)\right)\left[(1+\overline{\mu}) + (1-\overline{\mu})\theta^{-2}\right]\right] \tag{B-50}$$

$$C^{(1)} = \gamma_3\theta^{-2}(1 - k\theta^{-2} - 2\alpha hk) - 2\gamma_2 + \lambda_2 - \lambda_1 \tag{B-51}$$

$$\overline{C}^{1} = \gamma_3\theta^{-2}k(\lambda_0\theta^{-2} + 2\alpha h\theta^{-2} - 1) \tag{B-52}$$

$$C^{(2)} = \theta^{-1}\left[C^{(1)}(1-\lambda_0) + (1-\overline{\mu})\gamma_1\right] \tag{B-53}$$

$$D^{(1)} = \left[\lambda_1 + \lambda_2 - (3-4\nu)C^{(1)} + \overline{C}^{(1)}\right]/(2\alpha) \tag{B-54}$$

$$\overline{D}^{(1)} = \left[\lambda_2 - \lambda_1 - C^{(1)} + (3-4\nu_1)\overline{C}^{(1)}\right]/(2\alpha) \tag{B-55}$$

$$D^{(2)} = -\theta^{-1}\begin{bmatrix} C^{(1)}(3-4\nu_2)(1-\lambda_0) + \gamma_3\left(\lambda_0\theta^{-2} + 2\alpha h\theta^{-2} - 1\right)(k-1) \\ +4(1-\nu_2)(\beta_2+\gamma_1) \end{bmatrix}/(2\alpha) \tag{B-56}$$

Here

$$\beta_2 = (2im\beta_1)/(\overline{\nu}\alpha) \tag{B-57}$$

$$\gamma_1 = \frac{(2\nu_2 - 1)\beta_2}{1 + (3-4\nu_2)\overline{\mu}} \tag{B-58}$$

$$\gamma_2 = \frac{\left[(\lambda_2 - \lambda_1)(\lambda_0 + 2\alpha h) + \lambda_1 + \lambda_2 - 2\lambda_4 + 4(1-\nu_2)(\overline{\mu}\gamma_1 + \beta_2)\right]\theta^{-2}}{2(\lambda_0\theta^{-2} - 1 + 2\alpha h\theta^{-2})} \tag{B-59}$$

$$\gamma_3 = \frac{\lambda_4 + \lambda_3 - \lambda_2 - \lambda_1 - (3-2\nu_2)\beta_2 + 2\alpha h(2\gamma_2 - \lambda_2 + \lambda_1)}{1 + \lambda_0 k\theta^{-4} - (\lambda_0 + k + 4\alpha^2 h^2 k)\theta^{-2}} \tag{B-60}$$

$$\lambda_1 = -im\alpha^{-1}(B^{(1)} - \overline{B}^{(1)}) \tag{B-61}$$

$$\lambda_2 = \left(-\tilde{\tilde{p}} - 2im(1-\nu_1)\left(B^{(1)} + \overline{B}^{(1)}\right)\right)/\alpha \tag{B-62}$$

$$\lambda_3 = 2im\beta_2\left[(1-\overline{\nu})/(\overline{\nu}\alpha) + h\overline{\mu}\right] \tag{B-63}$$

$$\lambda_4 = 2im\beta_2\left[2(1-\nu_2)(1-\overline{\mu})/(\overline{\nu}\alpha) + h\right] \tag{B-64}$$

$$\lambda_5 = imh\left(B^{(1)} - \overline{B}^{(1)}\theta^2\right) \tag{B-65}$$

$$\lambda_6 = 2im\beta_2\left[(\overline{\mu} - \overline{\nu})/(\overline{\nu}\alpha) + h\overline{\mu}\right] \tag{B-66}$$

$$\lambda_0 = 1 - \frac{4(1-\nu_1)}{1 + \overline{\mu}(3-4\nu_2)} \tag{B-67}$$

$$k = \frac{\overline{\mu} - 1}{\overline{\mu} + (3 - 4\nu_1)} \tag{B-68}$$

Here $r = 1$ refers to the coating and $r = 2$ refers to the bulk material, $\alpha = \sqrt{m^2 + n^2}$, $\tilde{\tilde{s}}$ and $\tilde{\tilde{p}}$ are the 2-D Fourier transformation of the pressure and traction on the surface, here normally the 2-D transform of a unit pulse function is used:

$$\tilde{\tilde{p}}, \tilde{\tilde{s}} = \frac{4\sin(0.5m\Delta_x)\sin(0.5n\Delta_y)}{mn} \tag{B-69}$$

Here $m$ and $n$ are the frequency counterparts of $\Delta_i$ in the frequency domain.

# Appendix C : Plastic Strain Influence matrix

The surface displacement due to a unit pressure put on a surface patch of size $2a \times 2b$ [82]:

$$D_{33}^{n} = \frac{1}{\pi E}\left\{\begin{array}{l}(x+a)\ln\left(\frac{(y+b)+\sqrt{(y+b)^2+(x+a)^2}}{(y-b)+\sqrt{(y-b)^2+(x+a)^2}}\right)+(y+b)\ln\left(\frac{(x+a)+\sqrt{(y+b)^2+(x+a)^2}}{(x-a)+\sqrt{(y+b)^2+(x-a)^2}}\right)+\\ (x-a)\ln\left(\frac{(y-b)+\sqrt{(y-b)^2+(x-a)^2}}{(y+b)+\sqrt{(y+b)^2+(x-a)^2}}\right)+(y-b)\ln\left(\frac{(x-a)+\sqrt{(y-b)^2+(x-a)^2}}{(x+a)+\sqrt{(y-b)^2+(x+a)^2}}\right)\end{array}\right\}$$

The surface displacement due to unit traction put on a surface patch of size $2a \times 2b$ [82]:

$$D_{31}^{n} = \frac{1-2\nu}{4\pi G}\left\{\begin{array}{l}(y+b)\ln\left(\frac{\sqrt{(x+a)^2+(y+b)^2}}{\sqrt{(x-a)^2+(y+b)^2}}\right)+(y-b)\ln\left(\frac{\sqrt{(x-a)^2+(y-b)^2}}{\sqrt{(x+a)^2+(y-b)^2}}\right)+\\ (x+a)\left(\arctan\frac{y+b}{x+a}-\arctan\frac{y-b}{x+a}\right)+(x-a)\left(\arctan\frac{y-b}{x-a}-\arctan\frac{y+b}{x-a}\right)\end{array}\right\}$$

Expressions for the surface displacement due to a volume element of size $2a \times 2b \times 2c$ with uniform strains inside the volume [49]:

$$K_{ij} = -\frac{1}{\pi}\left[\begin{array}{l}-2\varepsilon_{13}(R_{,133}-\phi_{,1})-2\varepsilon_{23}(R_{,233}-\phi_{,2})+2\varepsilon_{12}(D\psi_{,12}+R_{,123})\\ +\varepsilon_{11}(D\psi_{,11}+R_{,113})+\varepsilon_{22}(D\psi_{,22}+R_{,223})+\\ \varepsilon_{33}((2-3)\phi_{,3}+R_{,333})-2\nu\varepsilon_{ii}\phi_{3}\end{array}\right]\Bigg|_{-a}^{a}\Bigg|_{-b}^{b}\Bigg|_{-c}^{c} \qquad \text{(C-1)}$$

$$S_{233}^{elas}(x,y,z) = \frac{z^2 x}{R(y^2+z^2)} \qquad \text{(C-2)}$$

The stress influence vector can be split up into 2 parts: one for the stress inside the plastic volume $\Omega_p$ and one outside the volume. The stresses outside the plastic volume:

$$S_{ijkl}^{pl} = \nu f(\varepsilon_{ij})_{k,kmm}\delta_{ij} - f(\varepsilon_{ij})_{k,kij} + (1-\nu)(f(\varepsilon_{ij})_{i,kkj} + f(\varepsilon_{ij})_{j,kki})\Big|_{-a}^{a}\Big|_{-b}^{b}\Big|_{-c}^{c}$$

The stress inside the volume:

$$S_{ijkl}^{pl} = \nu f(\varepsilon_{ij})_{k,kmm}\delta_{ij} - f(\varepsilon_{ij})_{k,kij} + (1-\nu)(f(\varepsilon_{ij})_{i,kkj} + f(\varepsilon_{ij})_{j,kki}) - \mu 2\varepsilon_{ij} - \lambda\varepsilon_{kk}\delta_{ij}\Big|_{-a}^{a}\Big|_{-b}^{b}\Big|_{-c}^{c}$$

Here is $\delta_{ij}$ the kronecker delta and $\mu = \frac{E}{2(1+\nu)}$ with the following definition of the derivatives of $f_{ijkl}$:

$$f_{i,jj}/C = 2\varepsilon_{1i}(\phi^I{}_{,1} + \phi_{,1}) + 2\varepsilon_{2i}(\phi^I_{,2} + \phi_{,2}) + 2\varepsilon_{3i}(\phi^I_{,3} - \phi_{,3}) \quad (i = 1 \text{ or } 2) \tag{C-3}$$

$$f_{3,jj}/C = 2\varepsilon_{13}(\phi^I_{,1} + 4x_3 - 4R_{,133} + 3\phi_{,1}) + 2\varepsilon_{23}(\phi^I_{,2} + 4x_3\phi_{,23} - 4R_{,233} + 3\phi_{,2}) + 8\varepsilon_{12}(-x_3\phi_{,12} + R_{,123} + D\psi_{,12}) + 4\varepsilon_{11}(-x_3\phi_{,22} + R_{,113} + D\psi_{,11}) + 4\varepsilon_{22}(-x_3\phi_{,22} + R_{,223} + D\psi_{,22}) + 2\varepsilon_{33}(\phi^I_{,3} - 2x_3\phi_{,33} + 2R_{,333} - (5-4\nu)\phi_{,3}) - 8\nu\phi_{,3} \tag{C-4}$$

$$\begin{aligned} f_{m,jjm}/C = {} & 4\varepsilon_{13}(\phi^I_{,13} - 2R_{,1333} + 2x_3\phi_{,133} + 3\phi_{,13}) \\ & + 4\varepsilon_{23}(\phi^I_{,23} - 2R_{,2333} + 2x_3\phi_{233} + \phi_{,23}) \\ & + 4\varepsilon_{12}(\phi^I_{,12} + 2R_{,1233} - 2x_3\phi_{,123} + (1-4\nu)\phi_{,12}) \\ & + 2\varepsilon_{11}(\phi^I_{,11} + 2R_{,1133} - 2x_3\phi_{,113} + (1-4\nu)\phi_{,11}) \\ & + 2\varepsilon_{22}(\phi^I_{,22} + 2R_{,2233} - 2x_3\phi_{,223} + (1-4\nu)\phi_{,22}) \\ & + 2\varepsilon_{33}(\phi^I_{,33} + 2R_{,3333} - 2x_3\phi_{,333} - (7-4\nu)\phi_{,33}) \\ & - 8\nu\varepsilon_{ii}\phi_{,33} \end{aligned} \tag{C-5}$$

$$\begin{aligned} f_{j,j}/C = {} & 2\varepsilon_{13}(R^I_{,13} - (3-4\nu)R_{,13} + 4(1-\nu)x_3\phi_{,1} - 2x_3R_{,133} + 2x_3^2\phi_{,13}) \\ & + 2\varepsilon_{23}(R^I_{,23} - (3-4\nu)R_{,23} + 4(1-\nu)x_3\phi_{,2} - 2x_3R_{,233} + 2x_3^2\phi_{,23}) \\ & + 2\varepsilon_{12}(R^I_{,12} - (1-2D^2)R_{,12} + 4(1-\nu)D(x_3 + x_3^{'})\psi_{,12} + 2x_3R_{,123} - 2x_3^2\phi_{,12}) \\ & + \varepsilon_{11}(R^I_{,11} + (1-2D^2)R_{,11} + 4(1-\nu)D(x_3 + x_3^{'})\psi_{,11} + 2x_3R_{,113} - 2x_3^2\phi_{,11}) \\ & + \varepsilon_{22}(R^I_{,22} + (1-2D^2)R_{,22} + 4(1-\nu)D(x_3 + x_3^{'})\psi_{,22} + 2x_3R_{,2213} - 2x_3^2\phi_{,22}) \\ & + \varepsilon_{33}(R^I_{,33} + (3-4\nu)R_{,33} + 8(1-\nu)x_3\phi_{,3} - 4(1-\nu)D\phi + 2x_3R_{,333} - 2x_3^2\phi_{,33}) \\ & - 2\nu\varepsilon_{ii}(\phi^I + (3-4\nu)\phi + 2x_3\phi_{,3}) \end{aligned} \tag{C-6}$$

Here the functions $R, \psi, \phi$ are defined as:

$R = \sqrt{(x-x') + (y-y') + (z-z')}$, $\psi = \ln(R + \zeta_3)$ and $\phi = 1/R$.

The derivatives of this functions are given using $k \neq j \neq i$ and $\zeta_1 = x - x'$, $\zeta_2 = y - y'$, $\zeta_3 = z - z'$ (convolution/infinite space) or $\zeta_3 = z + z'$ (correlation/ halfspace) which is indicated by either a superscript $^I$ or absence of one:

$$\phi_{,k} = \zeta_j \ln[r+\zeta_l] + \zeta_l \ln[r+\zeta_j] - \zeta_k U_k$$

$$\phi_{,kl} = \ln[r+\zeta_j] \qquad \phi_{,kk} = -U_k \qquad \phi_{,kkk} = -\zeta_i V_l - \zeta_l V_i$$

$$\phi_{,kkl} = \zeta_k V_k \qquad \phi_{,123k} = \frac{-\zeta_k}{r^3} \qquad \phi_{,kkll} = -\zeta_k \zeta_l W_j$$

$$\phi_{,kkkk} = \zeta_l \zeta_k W_j + \zeta_k \zeta_j W_l \qquad \phi_{,kkkl} = V_j - \zeta_k^2 W_j$$

$$R_{,kkl} = \zeta_k \ln[r+\zeta_j] \qquad R_{,kkk} = \zeta_i \ln[r+\zeta_l] + \zeta_l \ln[r+\zeta_j] - 2\zeta_k U_k$$

$$R_{,123k} = \frac{\zeta_k}{r} \qquad R_{,kkkl} = \ln[r+\zeta_j] + \zeta_k^2 V_j \qquad R_{,kkll} = \zeta_k \zeta_l V_j$$

$$R_{,kkkk} = -\zeta_j \zeta_k V_l - \zeta_l \zeta_k V_j - 2U_k \qquad R_{,123kl} = \frac{-\zeta_k \zeta_l}{r^3}$$

For $\psi$ and $\zeta_3\psi$ the derivative with respect to $\zeta_3$ become $\phi$ and $(\psi + R_{,3})$ respectively so in the following only indices $k$ and $l$ are used which are both different and have the value of 1 or 2:

$$\psi_{,kk} = -\zeta_k \ln[r+\zeta_l] - 2\zeta_3 X_k \qquad \psi_{,12} = \zeta_3 \ln[r+\zeta_3] - r$$

$$\psi_{,kkk} = -2\ln[r+\zeta_l] - (\zeta_k^2 + \zeta_3^2)V_l - (\zeta_3 - r)\zeta_l V_3 \qquad \psi_{,kkl} = -\frac{\zeta_k}{r+\zeta_3}$$

$$4(\zeta_3\psi)_{,kkk} = 2\zeta_l \ln[r+\zeta_3] - \zeta_3(\zeta_k^2 + \zeta_3^2)V_l - \zeta_3\zeta_l(\zeta_3 - r)V_3 - 4\zeta_k U_k$$

$$2(\zeta_3\psi)_{,kkl} = \zeta_k \ln[r+\zeta_3] - \frac{\zeta_k\zeta_3}{r+\zeta_3} \qquad 2(\zeta_3\psi)_{,kkll} = \zeta_k\zeta_l V_3 + \frac{\zeta_k\zeta_l\zeta_3}{(r+\zeta_3)^2 r}$$

$$4(\zeta_3\psi)_{4,kkll} = V_3\zeta_l\zeta_k\left(\frac{\zeta_3}{r} - 2\right) + \zeta_3\zeta_k\left[\zeta_l(\zeta_3 - r)W_3 - 6V_l + (\zeta_k^2 + \zeta_3^2)W_l\right] - 4U_k$$

$$4(\zeta_3\psi)_{,kkkl} = 2\ln[r+\zeta_3] + (3\zeta_k^2 - 2\zeta_3^2)V_3 + \zeta_3\zeta_l^2(\zeta_3 - r)W_3 + \frac{\zeta_l^2 r + (\zeta_k^2 + \zeta_3^2)\zeta_3}{r^3} \qquad \text{(C-7)}$$

The different functions used in (C-7) are :

$$U_k = \tan^{-1}\left[\frac{\zeta_i \zeta_j}{\zeta_k r}\right] \tag{C-8}$$

$$V_k = \frac{1}{r(r+\zeta_k)} \tag{C-9}$$

$$W_k = \frac{2r+\zeta_k}{r^3(r+\zeta_k)^2} \tag{C-10}$$

$$X_k = \tan^{-1}\frac{\zeta_k}{(r+\zeta_l+\zeta_j)} \tag{C-11}$$

# References


[1] R. Stribeck, Die wesentlichen Eigenschaften der Gleit- und Rollenlager Zeitschrift des Vereins Deutscher Ingenieure. (1902) 7.

[2] D.J. Schipper, A.W.J.de Gee, Lubrication modes and the IRG transition diagram, Lubrication Science. 8 (1995) 27-35.

[3] M.van Drogen, The Transition to adhesive wear of Lubricated Concentrated Contacts, PhD Thesis, University of Twente www.tr.ctw.utwente.nl, 2005

[4] H. Blok, Seizure Delay Method for Determining the Protection Against scuffing Afforded by Extreme Pressure Lubricants SAE Journal. 44 (1939) 193-204.

[5] U. Olofsson, S. Andersson, S. Björklund, Simulation of mild wear in boundary lubricated spherical roller thrust bearings, Wear. 241 (2000) 180-185.

[6] P. Põdra, S. Andersson, Simulating sliding wear with finite element method, Tribology International. 32 (1999) 71-81.

[7] G.K. Sfantos, M.H. Aliabadi, Wear simulation using an incremental sliding Boundary Element Method, Wear. 260 (2006) 1119-1128.

[8] G. Pereira, D. Munoz-Paniagua, A. Lachenwitzer, M. Kasrai, P.R. Norton, T.W. Capehart, T.A. Perry, Y.-T. Cheng, A variable temperature mechanical analysis of ZDDP-derived antiwear films formed on 52100 steel, Wear. 262 (2007) 461-470.

[9] A. Voght, Tribological Reactions Layers in contacts. 2008, Bosh-CR: Schillerhohe.

[10] D. Godfrey, Boundary lubrication, Nasa Sp-118. (1968) 335-373.

[11] M.A. Nicholls, T. Do, P.R. Norton, M. Kasrai, G.M. Bancroft, Review of the lubrication of metallic surfaces by zinc dialkyl-dithiophosphates, Tribology International. 38 (2005) 15-39.

[12] M.Z. Huq, P.B. Aswath, R.L. Elsenbaumer, TEM studies of anti-wear films/wear particles generated under boundary conditions lubrication, Tribology International. 40 (2007) 111-116.

[13] H. So, Y.C. Lin, The theory of antiwear for ZDDP at elevated temperature in boundary lubrication condition, Wear. 177 (1994) 105-115.

[14] C. Minfray, J.M. Martin, T. Lubrecht, M. Belin, T.L. Mogne, M.P. Dowson, A novel experimental analysis of the rheology of ZDDP tribofilms, Tribology and Interface Engineering Series, Elsevier. 2003, pp. 807-817.

[15] N.J. Mosey, M.H. Muser, T.K. Woo, Molecular Mechanisms for the Functionality of Lubricant Additives, Science. 307 (2005) 1612-1615.

[16] N.J. Mosey, T.K. Woo, M. Kasrai, P.R. Norton, G.M. Bancroft, M.H. Müser, Interpretation of experiments on ZDDP anti-wear films through pressure-induced cross-linking, Tribology Letters. 24 (2006) 105-114.

[17] J. Tse, Y. Song, Z. Liu, Effects of Temperature and Pressure on ZDDP, Tribology Letters. 28 (2007) 45-49.

[18] K. Demmou, S. Bec, J.L. Loubet, Effect of hydrostatic pressure on the elastic properties of ZDTP tribofilms. Cornell University Library. (2007)
[19] V. Popov, E. Kroner, On the dynamic theory of elastoplastic medium with microstructure, Computational Materials Science. 16 (1999) 218-236.
[20] E. Arzt, Size effects in materials due to microstructural and dimensional constraints: a comparative review, Acta Materialia. 46 (1998) 5611-5626.
[21] M.A. Xinling, Simulation for surface self-nanocrystallization under shot peening, acta mechanica sinica. 19 (2002) 172-180.
[22] N.R. Tao, An investigation of surface nanocrystallization mechanism in Fe induced by surface mechinical attriation treatment, Acta Materialia. 50 (2002) 4603-4616.
[23] H.S. Kim, M.B. Bush, The effects of grain size and porosity on the elastic modulus of nanocrystalline materials, Nanostructured Materials. 11 (1999) 361-367.
[24] D. Shakhvorostov, B. Gleising, R. Büscher, W. Dudzinski, A. Fischer, M. Scherge, Microstructure of tribologically induced nanolayers produced at ultra-low wear rates, Wear. 263 (2007) 1259-1265.
[25] D. Shakhvorostov, K. Pohlmann, M. Scherge, Structure and mechanical properties of tribologically induced nanolayers, Wear. 260 (2006) 433-437.
[26] G. Baumann, Y. Zhong, H.J. Fecht, Comparison between nanophase formation during friction induced surface wear and mechanical attrition of a pearlitic steel, Nanostructured Materials. 7 (1996) 237-244.
[27] A.H. Chokshi, A.K. Mukherjee, T.G. Langdon, Superplasticity in advanced materials, Mater. Sci. Eng. R. 10 (1993) 237-274.
[28] A.H. Chokshi, A. Rosen, J. Karch, H. Gleiter, On the validity of the hall-petch relationship in nanocrystalline materials, Scripta Metallurgica. 23 (1989) 1679-1683.
[29] I. Garbar, Microstructural Changes in Surface Layers of Metal During Running-in Friction Processes, Meccanica. 36 (2001) 631-639.
[30] H. Hahn, P. Mondal, K.A. Padmanabhan, Plastic deformation of nanocrystalline materials, Nanostructured Materials. 9 (1997) 603-606.
[31] Y. Ivanisenko, R.K. Wunderlich, R.Z. Valiev, H.J. Fecht, Annealing behaviour of nanostructured carbon steel produced by severe plastic deformation, Scripta Materialia. 49 (2003) 947-952.
[32] D. Jia, Effects of nanocrystalline and ultrafine grain sizes on constitutive behavior and shear bands in iron, Acta Materialia. 51 (2003) 3495-3509.
[33] C.C. Koch, Y.S. Cho, Nanocrystals by high energy ball milling, Nanostructured Materials. 1 (1992) 207-212.
[34] V. Krstic, U. Erb, G. Palumbo, Effect of porosity on Young's modulus of nanocrystalline materials, Scripta Metallurgica et Materialia. 29 (1993) 1501-1504.
[35] X.Z. Liao, Y.H. Zhao, Y.T. Zhu, R.Z. Valiev, D.V. Gunderov, Grain-size effect on the deformation mechanisms of nanostructured copper processed by high-pressure torsion, Journal of Applied Physics. 96 (2004) 636-640.
[36] W. Lojkowski, Y. Millman, S.I. Chugunova, I.V. Goncharova, M. Djahanbakhsh, G. Burkle, H.J. Fecht, The mechanical properties of the nanocrystalline layer

on the surface of railway tracks, Materials Science and Engineering A. 303 (2001) 209-215.
[37] J. Schiotz, K.W. Jacobsen, A Maximum in the Strength of Nanocrystalline Copper, Science. 301 (2003) 1357-1359.
[38] J. Schiotz, F.D.D. Tolla, K.W. Jacobsen, Softening of nanocrystalline metals at very small grain sizes, Nature. 391 (1998) 561-563.
[39] C.A. Schuh, T.G. Nieh, T. Yamasaki, Hall-Petch breakdown manifested in abrasive wear resistance of nanocrystalline nickel, Scripta Materialia. 46 (2002) 735-740.
[40] Z.B. Wang, N.R. Tao, S. Li, W. Wang, G. Lui, J. Lu, K. Lu, Effect of surface nanocrystallization on friction and wear properties in low carbon steel, Material science and Engineering. 352 (2002) 114-119.
[41] J.R. Weertman, Hall-Petch strengthening in nanocrystalline metals, Mater. Sci. Eng. A. 166 (1993) 161-167.
[42] M. Reichelt, U. Gunst, T. Wolf, J. Mayer, H.F. Arlinghaus, P.W. Gold, Nanoindentation, TEM and ToF-SIMS studies of the tribological layer system of cylindrical roller thrust bearings lubricated with different oil additive formulations, Wear. 268 (2010) 1205-1213.
[43] A. Oila, S. Bull, Phase transformations associated with micropitting in rolling/sliding contacts, Journal of Materials Science. 40 (2005) 4767-4774.
[44] D. Nelias, V. Boucly, M. Brunet, Elastic-Plastic Contact Between Rough Surfaces: Proposal for a Wear or Running-in Model, Journal of Tribology. 128 (2006) 236-244.
[45] V. Boucly, Semi-Analytical Modeling of the Transient-Elastic-Plastic Contact and its Application to Asperity Collision, Wear and Running in of Surfaces, PhD Thesis, Lyon, 2008 p 203
[46] W.W. Chen, Q.J. Wang, Thermomechanical Analysis of Elastoplastic Bodies in a Sliding Spherical Contact and the Effects of Sliding Speed, Heat Partition, and Thermal Softening, Journal of Tribology. 130 (2008) 041402-10.
[47] C. Jacq, D. Nelias, G. Lormand, D. Girodin, Development of a Three-Dimensional Semi-Analytical Elastic-Plastic Contact Code, Journal of Tribology. 124 (2002) 653-667.
[48] D. Nelias, E. Antaluca, V. Boucly, S. Cretu, A Three-Dimensional Semianalytical Model for Elastic-Plastic Sliding Contacts, Journal of Tribology. 129 (2007) 761-771.
[49] S.B. Liu, Q. Wang, Elastic fields due to eigenstrains in a half-space, Journal of Applied Mechanics-Transactions of the Asme. 72 (2005) 871-878.
[50] J. Hol, Contact analysis of a 2d asperity in DIEKA. 2010.
[51] K.L. Johnson, Contact mechanics. Cambridge university Press, Cambridge, 1985
[52] M.A. Nicholls, P.R. Norton, G.M. Bancroft, M. Kasrai, T. Do, B.H. Frazer, G.D. Stasio, Nanometer scale chemomechanical characterizaton of antiwear films, Tribology Letters. 17 (2003) 205-336.
[53] Z. Zhang, Tribofilms generated from ZDDP and DDP on steel surfaces:Part I, Tribology Letters. 17 (2005) 211-220.
[54] J.P. Ye, S. Araki, M. Kano, Y. Yasuda, Nanometer-scale mechanical/structural properties of molybdenum dithiocarbamate and zinc dialkylsithiophosphate

tribofilms and friction reduction mechanism, Japanese Journal of Applied Physics Part 1-Regular Papers Brief Communications & Review Papers. 44 (2005) 5358-5361.
[55] J.M. Martin, C. Grossiord, T. Le Mogne, S. Bec, A. Tonck, The two-layer structure of zndtp tribofilms Part 1: AES, XPS and XANES analyses, Tribology International. 34 (2001) 523-530.
[56] M. Kasrai, S. Marina, B.G. Micheal, Y.E. S., R.P. Ray, X-ray adsorption study of the effect of calcium sulfonate on antiwear film formation generated from neutral and basic ZDDPs: Part 1 -Phosporus species, Tribology Transactions. 46 (2003) 434-442.
[57] M. Aktary, M.T. McDermott, G.A. Mc. Alpine, Morphology and nanomechanical properties of ZDDP antiwear films as a function of tribological contact time, Tribology Letters. 12 (2002) 155-162.
[58] M.A. Nicholls, G.M. Bancroft, P.R. Norton, M. Kasrai, G. De Stasio, B.H. Frazer, L.M. Wiese, Chemomechanical properties of antiwear films using X-ray absorption microscopy and nanoindentation techniques, Tribology Letters. 17 (2004) 245-259.
[59] J.P. Ye, M. Kano, Y. Yasuda, Evaluation of nanoscale friction depth distribution in ZDDP and MoDTC tribochemical reacted films using a nanoscratch method, Tribology Letters. 16 (2004) 107-112.
[60] H.B. Ji, M.A. Nicholls, P.R. Norton, M. Kasrai, T.W. Capehart, T.A. Perry, Y.T. Cheng, Zinc-dialkyl-dithiophosphate antiwear films: dependence on contact pressure and sliding speed, Wear. 258 (2005) 789-799.
[61] S. Bec, A. Tonck, J.M. Georges, R.C. Coy, J.C. Bell, G.W. Roper, Relationship between mechanical properties and structures of zinc dithiophosphate anti-wear films, Proceedings of the Royal Society of London Series a-Mathematical Physical and Engineering Sciences. 455 (1999) 4181-4203.
[62] K. Komvopoulos, V. Do, E.S. Yamaguchi, P.R. Ryason, Nanomechanical and nanotribological properties of an antiwear tribofilm produced from phosphorus-containing additives on boundary-lubricated steel surfaces, Journal of Tribology-Transactions of the Asme. 126 (2004) 775-780.
[63] O.L. Warren, Nanomechanical properties of films derived from zinc dialkyldithiophosphate, Tribology Letters. 4 (1998) 189-198.
[64] C. Minfray, J.M. Martin, C. Esnouf, T. Le Mogne, R. Kersting, B. Hagenhoff, A multi-technique approach of tribofilm characterisation, Thin Solid Films. 447 (2004) 272-277.
[65] G.M. Bancroft, M. Kasrai, M. Fuller, Z. Yin, K. Fyfe, K.H. Tan, Mechanisms of tribochemical film formation: stabilityof tribo- and thermally-generated ZDDP films, Tribology Letters. 3 (1997) 47-51.
[66] K. Topolovec-Miklozic, T. Forbus, H. Spikes, Film thickness and roughness of ZDDP antiwear films, Tribology Letters. 26 (2007) 161-171.
[67] S. Liu, Q. Wang, Studying Contact Stress Fields Caused by Surface Tractions With a Discrete Convolution and Fast Fourier Transform Algorithm, Journal of Tribology. 124 (2002) 36-45.
[68] J.M. Martin, Antiwear mechanisms of zinc dithiophosphate: a chemical hardness approach, Tribology Letters. 6 (1998) 1-8.

[69] M.A. Meyers, A. Mishra, D.J. Benson, Mechanical properties of nanocrystalline materials, Progress in Materials Science. 51 (2006) 427-556.
[70] X.H. Chen, J. Lu, L. Lu, K. Lu, Tensile properties of a nanocrystalline 316L austenitic stainless steel, Scripta Materialia. 52 (2005) 1039-1044.
[71] J. Rottler, M.O. Robbins, Yield conditions for deformation of amorphous polymer glasses, Physical Review E. 64 (2001) 051801.
[72] K. Demmou, S. Bec, J.-L. Loubet, J.-M. Martin, Temperature effects on mechanical properties of zinc dithiophosphate tribofilms, Tribology International. 39 (2006) 1558-1563.
[73] A. William Ruff, Friction and Wear Data Bank, Modern Tribology Handbook, Two Volume Set, CRC Press. 2000.
[74] I.V. Belova, G.E. Murch, Diffusion in nanocrystalline materials, Journal of Physics and Chemistry of Solids. 64 (2003) 873-878.
[75] C. Suryanarayana, C.C. Koch, Nanocrystalline materials – Current research and future directions, Hyperfine Interactions. 130 (2000) 5-44.
[76] S. Liu, Q. Wang, G. Liu, A versatile method of discrete convolution and FFT (DC-FFT) for contact analyses, Wear. 243 (2000) 101-111.
[77] S.B. Liu, Thermomechanical Contact Analyses of Rough Bodies, PhD Thesis, Northwestern University, 2001
[78] I.A. Polonsky, L.M. Keer, A numerical method for solving rough contact problems based on the multi-level multi-summation and conjugate gradient techniques, Wear. 231 (1999) 206-219.
[79] I.A. Polonsky, L.M. Keer, A Fast and Accurate Method for Numerical Analysis of Elastic Layered Contacts, Journal of Tribology. 122 (2000) 30-35.
[80] S. Liu, Q. Wang, A Three-Dimensional Thermomechanical Model of Contact Between Non-Conforming Rough Surfaces, Journal of Tribology. 123 (2001) 17-26.
[81] S. Liu, Q. Wang, Transient Thermoelastic Stress Fields in a Half-Space, Journal of Tribology. 125 (2003) 33-43.
[82] K. Willner, Fully Coupled Frictional Contact Using Elastic Halfspace Theory, Journal of Tribology. 130 (2008) 031405-8.

# Part II

**Paper A:** Transient Thermal Effects and Heat Partition in Sliding Contacts, R. Bosman and M.B. de Rooij, Journal of Tribology, 2010, Volume 132, Issue 2, (9 pages)

**Paper B:** Mild microscopic wear in the boundary lubrication regime, Materialwissenschaft und Werkstofftechnik, R. Bosman, 2010, Volume 41, Issue. 1, (4 pages).

**Paper C:** On the transition from mild to severe wear of lubricated, concentrated contacts: The IRG (OECD) transition diagram, R. Bosman and D.J. Schipper, Wear, 2010, Volume 269, Issue 7-8, (8 pages)

**Paper D:** Transition from mild to severe wear including running in effects, R. Bosman and D.J. Schipper, accepted for publication in Wear

**Paper E:** Running in of metallic surfaces in the boundary lubricated regime, R. Bosman, J. Hol and D.J. Schipper, resubmitted to Wear in revised form, 31-12-2010.

**Paper F:** Running in of systems protected by additive rich oils, R. Bosman and D.J. Schipper, accepted for publication in Tribology Letters.

**Paper G:** Mild Wear Prediction of Boundary Lubricated Contacts, R. Bosman and D.J. Schipper, Submitted to Tribology Letters, 20-10-2010

**Paper H:** Mild Wear Maps for Boundary Lubricated Contacts, R. Bosman and D.J. Schipper, submitted to Wear, 20-12-2010

Paper A

Transient Thermal Effects and Heat Partition in Sliding Contacts,
R. Bosman and M.B. de Rooij,
Journal of Tribology, 2010
Volume 132, Issue 2

# Transient Thermal Effects and Heat Partition in Sliding Contacts

R. Bosman and M.B. de Rooij
University of Twente, r.bosman@utwente.nl
Drienerlolaan 5
7500 AE Enschede

Published in: Journal of Tribology, 2010, Volume 132, Issue 2

***Abstract*** **In tribological applications, calculating the contact temperature between contacting surfaces makes it possible to estimate lubricant failure and effectiveness, material failure and other phenomena. The contact temperature can be divided into two scales: the macroscopic and the microscopic scale. In this article a semi analytical transient temperature model is presented which can be used at both scales. The general theory is presented here and used to calculate the contact temperature of a single micro and macro-contact. For the steady state situation, the results obtained are in good agreement with those found in literature. Further, it is shown that the simplification of modeling a micro-contact as an equivalent square uniform heat source to simplify the calculation of the maximum temperature is justified in the fully plastic regime. The partition is calculated by setting a continuity condition on the temperature field over the contact. From the results it can be concluded that at low sliding velocities the steady state assumption, which is often used for micro contacts, is correct. However, at higher sliding velocities, the micro contact is not in the steady state and transient calculation methods are advised.**

*Index Terms:* transient temperature, semi-analytical, flash temperature

## INTRODUCTION

In many applications, contacts become more highly stressed. One of the important reasons is the miniaturization, which results in an increasing mechanical and thermal load on machine elements. Further, there is a trend that tribological contacts are operating in the boundary lubrication regime. This results in an increasing demand for accurate calculation methods at the micro scale in the contact in order to predict thermal failure of e.g. boundary layers. As shown in [1], it is possible to predict lubrication failure using a thermal model. However, due to the multi scale level of thermal problems in contacts, the mutual influence of adjacent micro contacts, as well as the time dependent character of thermal phenomena, a precise estimation of the contact temperature is difficult. In this paper a general theory will be presented which can deal with multiple heat sources affecting each other. This paper will address some general topics like heat partition and the thermal behavior of micro contacts.

In recent years, a lot of modeling has been done in predicting the temperature of contacts [2-11]. One of the difficult aspects is the partition of heat generated in the contact. Some models simplify the problem by only taking into account gross influences [4, 11], or by setting the maximum temperatures equal at the interface [5, 8]. Others do not deal with partition at all [7] or, on the other extreme, deal with the partition in much detail [6, 12-15]

by stating that the temperature field needs to be continuous at the complete interface of the contacting bodies, using a partition factor which is a function of locations. Bos and Moes [16] developed a numerical model calculating the steady state temperature of a contact by integrating a Green function over the contact domain using multi-grid methods. They are able to calculate the partition factor at the complete interface of the contacting bodies. The steady state assumption can be overcome by using a transient solution of the temperature field, as done in [17]. In that study the transient solution of an equivalent square uniform heat source is used to predict the contacting temperature as well as the mutual thermal loading of different adjacent asperities. This thermal effect is modeled by averaging the total thermal load over the number of asperities in contact and thus disregarding the local effect of variation of distance between the asperities and load carried by the asperities. This approach is in agreement with the theory used in [18], where it is assumed that the distribution of the heat source does not affect the maximum temperature as long as the total amount of dissipated heat is the same. This model disregards the heterogeneous distribution of high asperities often seen in contacts and assumes that the contacting asperities are distributed evenly and close to each other. A global study of the effect that different micro contacts have on each other is conducted in [10]. In this study mutually influencing square heat sources are modeled using a model system instead of real contact geometries.

In this article, a transient temperature model will be presented. This model will be used to study the effect of multiple arbitrarily shaped heat sources. This model will be applied to a single asperity contact to validate the model. The general model will be discussed, starting with writing an arbitrary shaped heat source as the sum of uniform square heat sources. Then, this approach will be applied to a micro contact loaded with a Hertzian heat source. After that, a Hertzian heat source will be compared to a uniform heat source. Further, the behavior of contacts with small contact times as well as heat partition will be studied.

## TEMPERATURE FIELD DUE TO AN ARBITRARY SHAPED MOVING HEAT SOURCE

### Uniform square heat source

Assume an arbitrary shaped heat source, acting on the surface of a semi infinite body, which is insulated over the surface except for the infinite point the heat source is acting. Then, the transient temperature field can be written by Eq. (1) [19]. Here $x'$ is the target location expressed in the moving coordinate system, and $x''$ is the heat source location, see Figure 1.

$$\Theta(x',y,z,t)=\int_0^t\int_{-b}^{b}\int_{-a}^{a}\frac{1}{\tau^{3/2}}\frac{\varphi(x'',y')}{8(\pi\kappa)^{3/2}}e^{\frac{-((x'-x''+v\tau)^2+(y-y')^2+z^2)}{4\kappa\tau}}dx''dy'd\tau \qquad (1)$$

In this equation, $\Theta$ is the temperature rise at location ($x'$, $y$) due to a heat flux φ at location ($x''$, $y'$) moving with velocity $v$. Equation (1) can also be written in the form:

$$\Theta(x',y,z,t)=\int_0^t\int_{-b}^{b}\int_{-a}^{a}\varphi(x'',y')\,g(x''-x',y-y')\,dx''dy'd\tau \qquad (2)$$

Equation (2) can be recognized as a convolution integral. The function $g$ only needs to be evaluated over the relevant intervals of ($x''$-$x'$ ,$y$-$y'$) instead of every combination of ($x''$-$x'$, $y$-$y'$). Equation 1 has no analytical solution for practical expressions of $\varphi(x'',y')$. Therefore, a numerical solution is performed. Starting with the discretization of $\varphi(x'',y')$ by integrating over a small interval $x''=[x''-\Delta 0.5\Delta x''\ ,x''+0.5\Delta x'']$, $y'=[y'-0.5\Delta y',\ y'+0.5\Delta y']$ and dividing this by the area of the interval ($\Delta x''$, $\Delta y'$), creating a small uniform square heat flux at the location ($x''$, $y'$). Defining $k=x''/\Delta x''$ and $l=y'/\Delta y'$ gives a tensor $[\varphi_{kl}]$ defined as:

$$\varphi_{kl}=\int_{y_{kl}'-0.5\Delta y'}^{y_{kl}'+0.5\Delta y'}\int_{x_{kl}''-0.5\Delta x''}^{x_{kl}''+0.5\Delta x''}\varphi(x'',y')dx''dy' \qquad (3)$$

The problem can be simplified using the following transformation variables [9]:

$$\eta = \frac{x'-x''}{2\sqrt{\kappa\omega}} \qquad dx'' = -2\sqrt{\kappa\omega}\,d\eta \qquad \xi = \frac{y-y'}{2\sqrt{\kappa\omega}}$$

$$\lambda = \frac{z}{2\sqrt{\kappa\omega}} \qquad dy' = -2\sqrt{\kappa\omega}\,d\xi \qquad V_x' = \frac{V_x\omega}{2\sqrt{\kappa}}$$

$$\omega = \sqrt{\tau} \qquad q = \frac{\varphi}{\rho C_p} \qquad d\tau = 2\omega d\omega$$

$$m = \frac{x'}{\Delta x} \qquad n = \frac{y}{\Delta y}$$

$$\eta^0 = \frac{y'-(y''-\Delta y)}{2\sqrt{\kappa\omega}} \qquad \eta^1 = \frac{y'-(y''+\Delta y)}{2\sqrt{\kappa\omega}}$$

$$\xi^0 = \frac{x'-(x''-\Delta x)}{2\sqrt{\kappa\omega}} \qquad \xi^1 = \frac{x'-(x''+\Delta x)}{2\sqrt{\kappa\omega}}$$

Using these variables in Eq. (1) and assuming the heat source is constant in time, i.e. using the "transient continuous" case, the effect of every square heat source of tensor $q_{kl}$ at location $(x'', y')$ can be expressed as:

$$\Theta_{mn} = \frac{q_{kl}}{4\sqrt{\pi\kappa}\rho C_p} \int_0^{\sqrt{t}} e^{-\lambda_{mnkl}} \begin{pmatrix} erf\left(\xi^1_{klmn}\right) \\ -erf\left(\xi^0_{klmn}\right) \end{pmatrix} \begin{pmatrix} erf\left(\eta^1_{klmn} + V_x'\right) \\ -erf\left(\eta^0_{klmn} + V_x'\right) \end{pmatrix} d\omega \qquad (4)$$

It can be seen that the discretization of the heat source in place instead of time reduces the problem to an integral that only needs to be evaluated over 1 degree of freedom. The integration over ω in eq. (4) is done numerically using MATLAB. Even in steady state situations the integration over time is preferred, due to the reduction of integration over two variables to one variable.

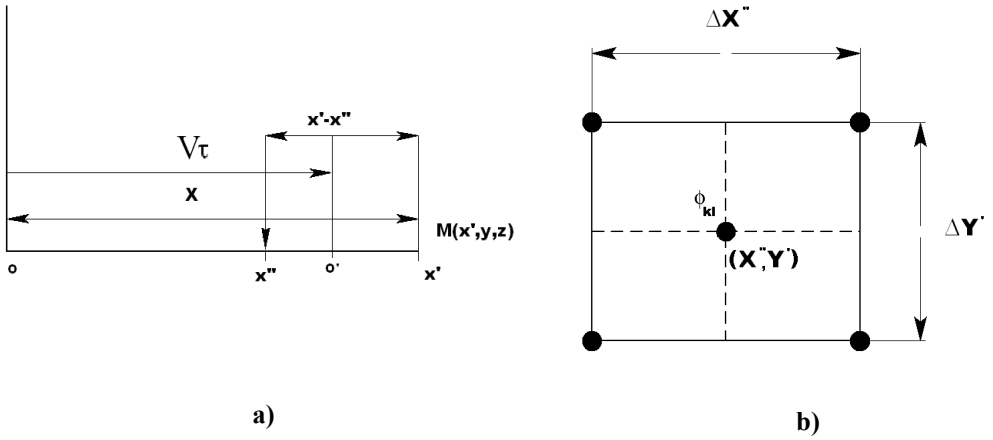


**Figure 1 :** Coordinate system **a)** Local coordinate system of the moving heat source **b)** Local coordinate system of a surface element [19].

### Discretization of the heat source

If the effect of heat source $\varphi_{kl}$ of size $\Delta x'', \Delta y'$ at location $(k\cdot\Delta x'', l\cdot\Delta y') = (x'', y')$ on location $(m\cdot\Delta x', n\cdot\Delta y) = (x', y)$ is defined as $M_{mnkl}$, it results in a fourth order tensor. The effect of the total heat source can be written as:

$$\Theta_{mn} = q_{kl} M_{klmn} \qquad (5)$$

When using an equidistant square grid, $M_{klmn}$ becomes a fourth order tensor of size $n^4$,

which is calculated using Eq. (4). $q_{kl}$ is a second order tensor which is calculated using Eq. (3). If the range of the indices of $m$ and $n$ are equal to $k$ and $l$ and looking closely at Eq. (3), convolution can be used to simplify the problem to a moving grid problem. This method is also described in [20]. The absolute distance between the source and the target area is the factor on which the $M_{klmn}$ is dependent. If now two new indices are defined:

$$w = \frac{x''-x}{\Delta x} \qquad s = \frac{y'-y}{\Delta y} \tag{6}$$

Then, a new effect tensor can be written that is dependent on $w$, $s$ and a "filter" $J_{wskl}$, which makes sure the correct effect is multiplied with the correct heat source stating:

$$\Theta_{kl} = q_{kl} J_{ws\,kl} M_{ws} \tag{7}$$

Here $M_{mnkl}$ is reduced to $M_{ws}$ which has only $4n^2$ elements. This is due to the fact that using a reference grid of two times the size of the grid size of interest, all values of $M_{ws}$ are present.

**Single elastic micro/macro contact**

Using the theory discussed above and the conditions given in Table 2, the temperature field cause by a single micro contact can be calculated. A single elastic contact can be modeled as a Hertzian contact resulting in a circular or elliptic contact zone with an elliptical pressure distribution [21]. It can be assumed that all heat is produced by friction and that the coefficient of friction is constant over the contact. Then, the heat source acting at the interface is $P(x,y)V\mu$. This gives the following expressions for contact size and heat source distribution:

$$(ab)^{\frac{1}{2}} = \left(\frac{3F_n R_e}{4E^*}\right)^{\frac{1}{3}} \tag{8}$$

$$q(x,y) = \frac{3\mu V F_n}{2\pi ab}\left(1 - \left(\frac{x}{a}\right)^2 - \left(\frac{y}{b}\right)^2\right)^{\frac{1}{2}} \tag{9}$$

| Operation Conditions | | | | |
|---|---|---|---|---|
| | | | Macro | Micro |
| Normal load | [$N$] | $F_N$ | 100 | 0.2 |
| Radius | [$m$] | $R_x$ | 0.005 | $5\times10^{-5}$ |

**Table 2:** Operation conditions.

| Material properties | | | | |
|---|---|---|---|---|
| | | | Body 1 | Body 2 |
| | | | AISI52100 hardened steel | $ZrO_2$ |
| Young's modulus | [$GPa$] | $E$ | 213 | 191 |
| Poisson ratio | | ν | 0.3 | 0.3 |
| Thermal conductivity | [$W/mK$] | $K$ | 45 | 2.5 |
| Specific heat | [$J/kg\ K$] | $c_p$ | 460 | 400 |
| Density | [$kg/m^3$] | ρ | 7880 | 6000 |

**Table 1:** Material properties [16].

This heat source can be discretized, resulting in a tensor $q_{kl}$ using Eq. (3) and $\varphi = q\rho C_p$. To validate the model described above, an example from [6] is reproduced and the results from the models are compared. In this example a zirconia ball, with a radius of 5 *mm*, is sliding against a steel plate. Using the material properties given in Table 1 and a normal load of100 *N*, this results in a contact radius of 0.15 *mm*. First, steady state conditions will be simulated by choosing the Fourier number ( $\Gamma$ ) greater than 100 [22].

$$\Gamma = \frac{\kappa t}{a^2} \tag{10}$$

The results are compared with results from [6] in Figure 2. It can be seen that the results are in agreement. In both calculations it is assumed that all the heat is conducted into the steel.

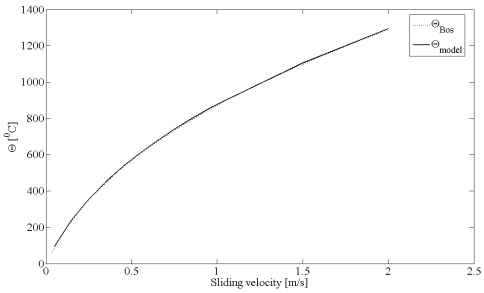


**Figure 2:** $\Theta_{model}$ is the maximum temperature calculated using the model presented in this paper and $\Theta_{bos}$ is the temperature calculated the theory presented in [6].

## PARTITION

In his postulate, Blok [5] uses global partitioning: for both contacting partners, only the maximum temperature needs to be the same. Using the theory presented in [16], the temperature fields of both surfaces are required to be the same at all points of contact. This will be called local partitioning and creates a continuous temperature field over the whole contact area. In the current work local partitioning will be used. This method is very suitable in combination with numerical methods as presented in this paper. So, at the interface, there are two conditions which need to be fulfilled [16]:

Continuity of both temperature fields ( $T_1(x,y,0,t) = T_2(x,y,0,t)$ )

The sum of both heat fluxes into the bodies needs to be equal to the total heat generated ( $\sum q_{kl}^1 + \sum q_{kl}^2 = \sum q_{kl}^{tot}$ )

If Eq. (7) is used for both bodies and it is stated that, at the interface, the temperature field needs to be continuous, it follows:

$$q_{kl}^1 F_{wskl}^1 M_{ws}^1 = q_{kl}^2 F_{wskl}^2 M_{ws}^2 \quad \text{at} \quad z_1 = z_2 = 0 \tag{11}$$

Adding condition 2 gives:

$$q_{kl}^1 = \frac{q_{kl} F_{wskl}^2 M_{ws}^2}{F_{wskl}^1 M_{ws}^1 + F_{wskl}^2 M_{ws}^2} \tag{12}$$

$$q_{kl}^2 = \frac{q_{kl} F_{wskl}^1 M_{ws}^1}{F_{wskl}^1 M_{ws}^1 + F_{wskl}^2 M_{ws}^2} \tag{13}$$

So the heat source can be divided into two heat sources, each acting on one of the two contacting bodies. Now a partition factor $\Phi_{kl}$ can be defined as:

$$\Phi_{kl} = \frac{q_{kl}^1}{q_{kl}} \tag{14}$$

Here, it should be noted that Eq. (11-14) does not imply values of $\Phi_{kl}$ to be in the range of [0-1] but rather in the range of $[-\infty, \infty]$, as discussed in [6]. If a range between [0-1] is taken, the circulation of heat, i.e. heat flowing between surfaces 1 and 2 with a net zero result, is excluded. However, there is a limitation in the way the partition is handled in the current model; since the heat source is

taken out of the integration over time in Eq. (4), the partition factor can no longer be a function of time is only a function of location, similar to [14].

To be able to take into account the effects a time dependent partition factor would have on the temperature field, prior knowledge of the partitioning would be required. This would imply an iterative approach in which for each iterative step Eq. (4) needs to be reevaluated making it very time consuming. Time dependent partitioning will therefore not be taken into account in the current study.

Now the same steady state problem, from section 2.3, of the zirconia ball sliding on a steel plate is studied including local partitioning. The assumption of a steady state situation is used to be able to compare the results given in the previous section by keeping the Fourier number ( $\Gamma$ ) above 100.

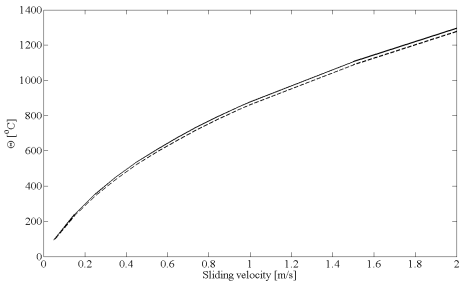


**Figure 3** Maximum contact temperature between a zirconia ball and a steel plate with contact conditions as in Figure 2. The dotted line is the temperature profile if heat is allowed to flow into the zirconia ball; the continuous line is without taking into account the heat flow into the zirconia ball.

In Figure 3 the maximum temperature of the steel plate is shown as a function of the sliding velocity. It is clearly seen that most of the produced heat is conducted into the steel plate. The complete temperature fields and partition factor at a velocity of 0.1 *m/s* are shown in Figure 4. From the results it can be seen that the solution fulfills both conditions, e.g. $T_1(x,y,0,t)=T_2(x,y,0,t)$ and $\Sigma q^1_{kl}+\Sigma q^2_{kl}=\Sigma q^{tot}_{kl}$.

**Effect of sliding velocity on heat partition**

To study the effect of the sliding velocity on the partition function and on temperature fields, two examples are given. The first example deals with the macroscopic scale and the second example with the microscopic scale. The important difference between the macroscopic and the microscopic scale is the size of the contact and its effect on the contact time. In both examples steel-steel contact situations will be studied. Operational conditions and material properties are given in Tables 1 and 2. In these examples, body 1 is kept stationary while the velocity of body 2 varies between 0.01-5 *m/s***,** i.e. a Peclet number between 0.2-120 at macroscopic level and [0.03-3.25] at microscopic level**.** In the calculations, both global as well as local partitioning will be used and the results will be compared.

**Macroscopic effect of sliding velocity on heat partition**

The results of both methods discussed above at macroscopic level are shown in Figure 5. In the figure, the centerline temperature field is divided by the maximum temperature at the given sliding velocity. As can be seen in Figure 5-c, using global partitioning gives results for the maximum temperature which are in very good agreement with the current partition model. However, using the global partitioning underestimates the amount of energy flowing into the moving body and gives a slightly different temperature profile, see Figure 5-a and 5-b. If only the maximum contact temperature is the point of interest, the use of a global partitioning factor is preferred due to its simplicity. If a more detailed analyses of the partition of heat is needed, local partitioning is preferred.

**Microscopic effect of sliding velocity on heat partition**

In the microscopic case, the effect of the sliding velocity on the temperature field is significantly reduced, as can be seen in Figure

6-a, due to the reduction of the Peclet number. The ratio of convection over diffusion is reduced and diffusion becomes the dominant factor, resulting in a more symmetrical temperature profile. The results of global and local partitioning are therefore closer to each other; however the total amount of heat flowing into the moving body is still underestimated.

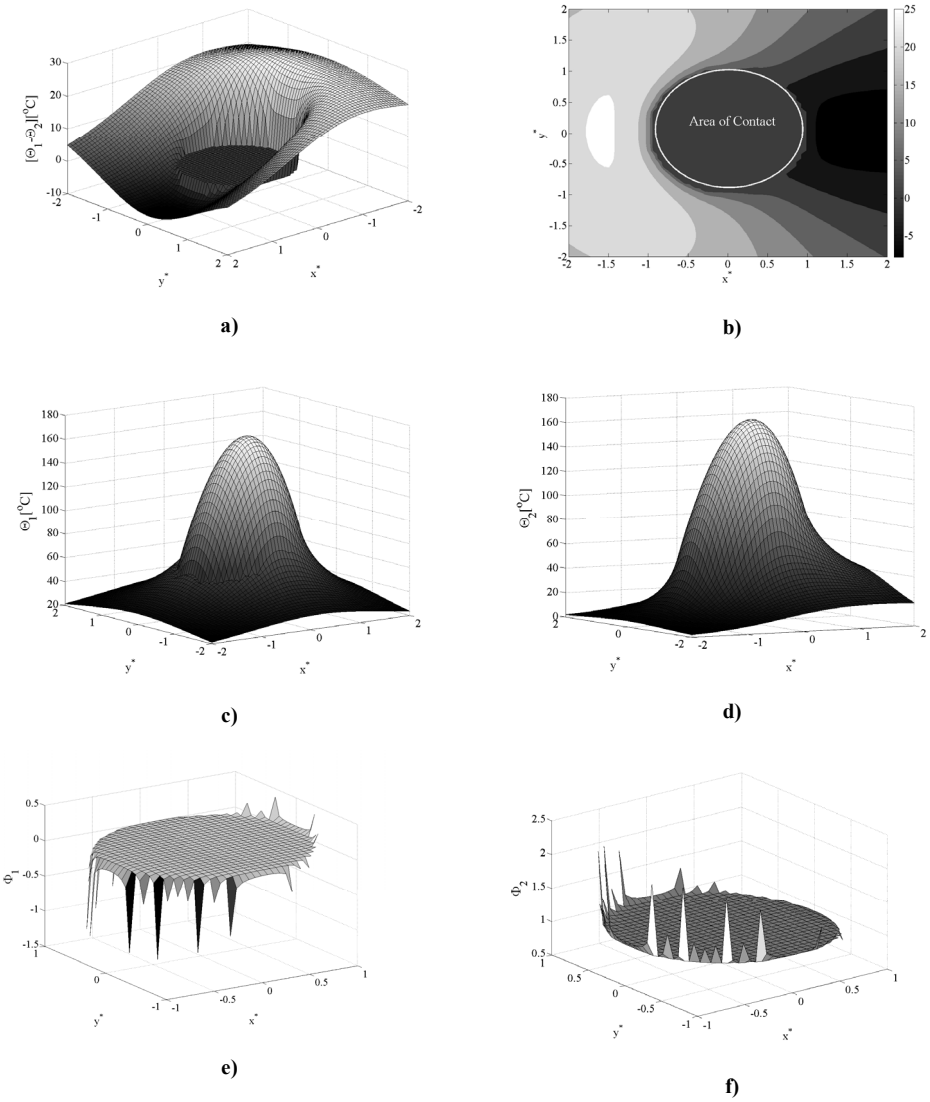


**Figure 4: a),b)** Temperature difference of the zirconia ball and steel plate **c)** Temperature of the zirconia ball **d)** Temperature of the steel plate **e**) Partition factor of the ball **f)** Partition factor of the steel plate.

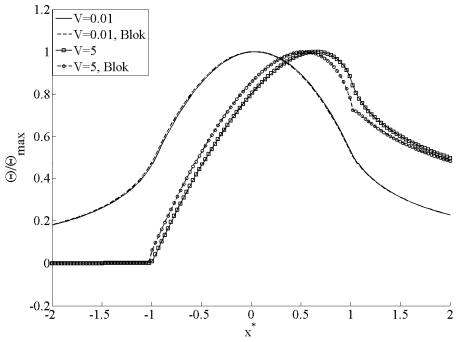


a)

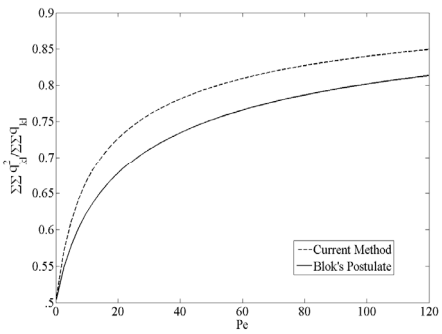


b)

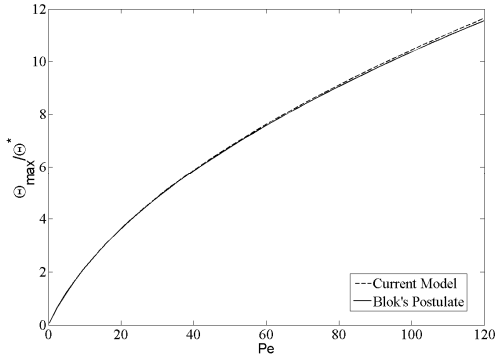


c)

**Figure 5: a)** Dimensionless temperature profiles of body 2 ($\Theta_{max}$ is the maximum temperature of the centerline profile at the given velocity) **b)** Total partition factor of body 2 (total amount of the generated heat flowing into body 2) **c)** Maximum temperature rise of body 2 divided by $\Theta^*$

## Effect of bulk temperature difference on heat partition

A difference in bulk temperature of body one and body two will affect the whole system. This temperature difference can be modeled by writing it as an equivalent heat source and incorporating it in Eq. (11) as an extra term.

$$q_{kl}^1 F_{wskl}^1 M_1^{ws} + \Theta^{1}{}_{kl}^{bulk} = q_{kl}^2 F_{wskl}^2 M_{wskl}^2 + \Theta^{2}{}_{kl}^{bulk} \quad (15)$$

Rewriting this gives:

$$q_{kl}^1 = \frac{q_{kl} F_{wskl}^2 M_{ws}^2 + \Theta_{kl}^{1\,bulk} - \Theta_{kl}^{21\,bulk}}{F_{wskl}^2 M_{ws}^2 + F_{wskl}^1 M_{ws}^1} \quad (16)$$

$$q_{kl}^2 = \frac{q_{kl} F_{wskl}^1 M_{ws}^1 + \Theta_{kl}^{2\,bulk} - \Theta_{kl}^{1\,bulk}}{F_{wskl}^1 M_{ws}^1 + F_{wskl}^2 M_{ws}^2} \quad (17)$$

Using the example of the zirconia ball sliding against the steel plate again and heating the plate to a steady temperature of 100 $^{o}$C the partition changes due to the bulk temperature difference (as expected), see Figure 7. More heat is conducted into the zirconia ball to compensate for the 100 $^{o}$C difference.

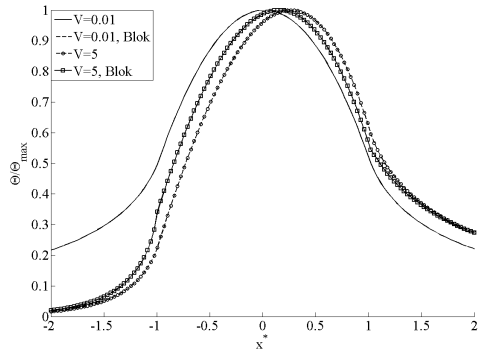


**a)**

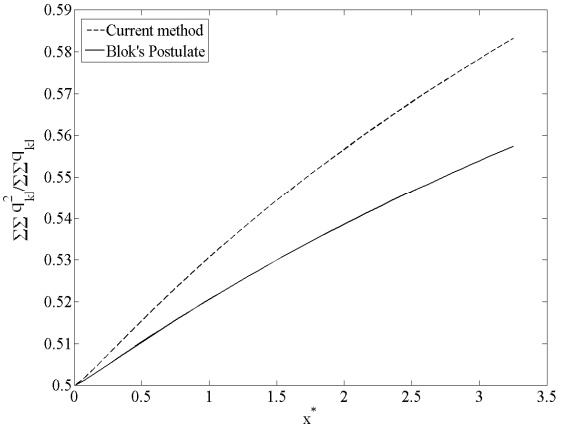


**b)**

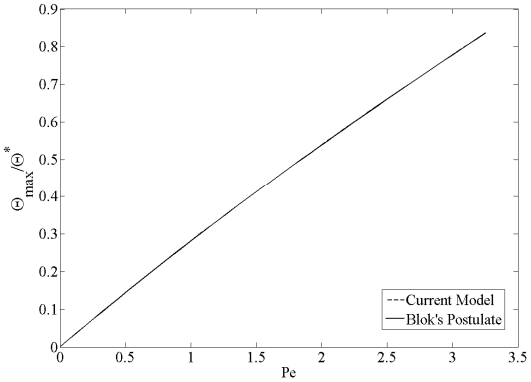


**c)**

**Figure 6: a)** Dimensionless temperature profiles of body 2 ($\Theta_{max}$ is the maximum temperature of the centerline profile at the given velocity) **b)** Total partition factor of body 2 (total amount of the generated heat flowing into body 2) **c)** Maximum temperature rise of body 2 divided by $\Theta^*$

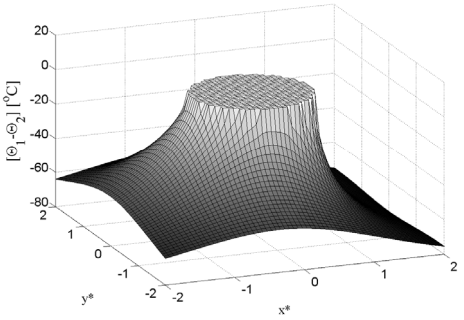


a)

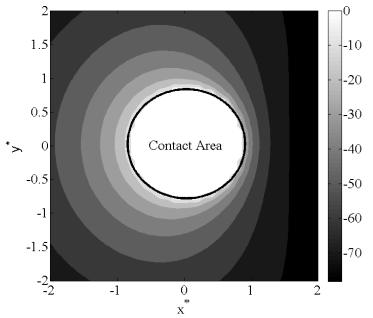


b)

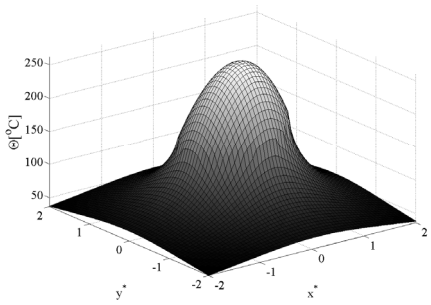


c)

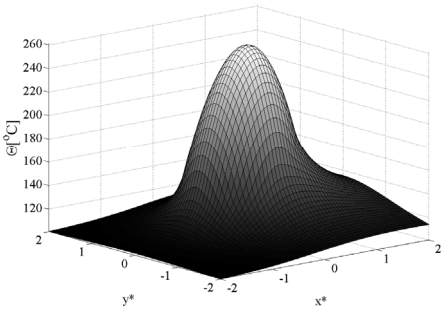


d)

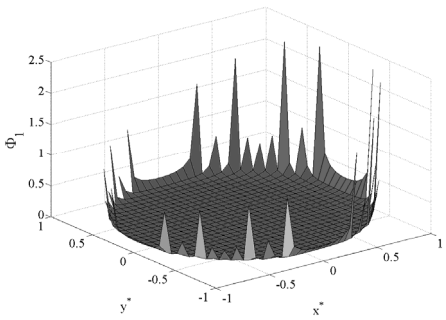


e)

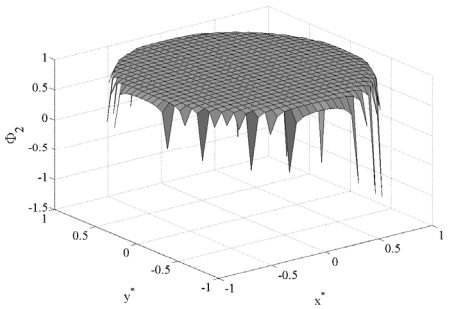


f)

**Figure 7: a),b)** Temperature difference of body 1 and body 2, **c)** Temperature of body 1, **d)** Temperature of body 2, **e**) Partition factor of body 1 and **f)** Partition factor of body 2. Conditions, see table 1 and $\Theta_{bulk}$ of the steel plate is 100°C higher than $\Theta_{bulk}$ of the zirconia ball

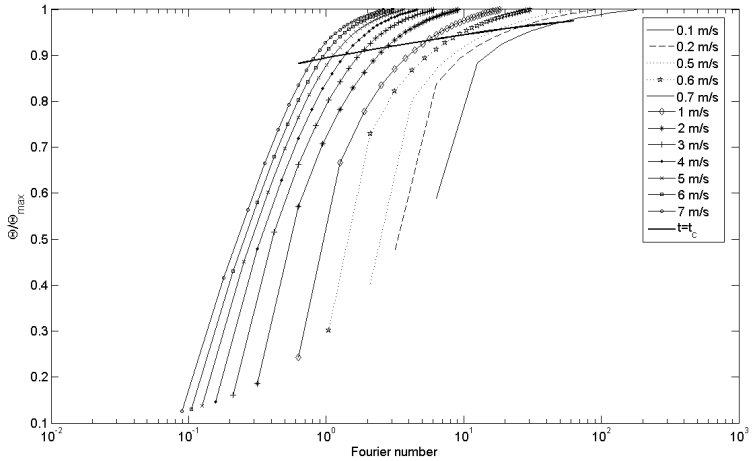


**Figure 8:** Contact temperature as a function of the Fourier number for a micro contact with a radius of contact of $4\times10^{-6}m$, normal load of 0.2 *N* and a coefficient of friction of 0.3 at a steel surface. The thick black line is the time at which contact is lost. Temperature is normalized to the maximum temperature of the cycle ($t=3t_c$).

### Time effect on contact temperature

For the macroscopic case, the steady state condition is valid for most contact cases. When two rough surfaces are sliding against each other on microscopic level, the contact situation is not constant. Asperities are sliding over each other and contact is made and lost. The duration of the contact is defined as:

$$t_c = \frac{2a}{v} \qquad (18)$$

where $a$ is the radius of the micro contact in the sliding direction, $v$ the sliding velocity and $t_c$ the time of contact. Assuming a contact pressure, the contact temperature can be calculated as a function of the Fourier number, see Figure 8. It is clearly seen that for higher contact velocities (e.g. low Fourier numbers) the quasi static temperature regime is not reached. For a micro-contact the assumption of a steady state temperature for a micro contact is therefore not as straightforward as it seems. Figure 8 shows also that the assumption that the quasi steady state is reached at Fourier numbers larger than 100, is correct.

The size of the heat affected area is predicted in Figure 9. Looking at the temperature profiles at different time increments ($t < t_c$) it is seen that the size of the heat affected zone is very restricted. This phenomenon is of interest if a smaller micro contact is neighboring a larger micro contact. The small micro contact already loses contact before the heat affected region of the large contact reaches the small microcontact. In this way, heat accumulation is reduced at the micro level and the contact temperature is reduced.

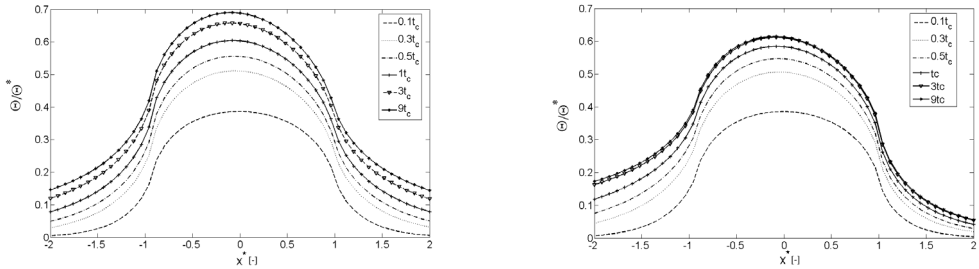


**Figure 9:** Temperature profile along the centerline ($y^*$=0) of **a)** body 1 and **b)** body 2. Sliding direction left to right with $Pe$≈0.8.

## Effect of the heat source distribution on the temperature

Transient contact temperature calculations [2, 3, 9, 10, 18] are often modeled using a uniform square heat source. Here, a single micro contact is studied in two situations: an elastically deforming contact with a Hertzian pressure profile and a fully plastic deforming micro contact with an elliptic shaped contact area. For the plastic case the contact pressure and contact area are calculated using a simple plastic contact model as discussed in [23].The results are obtained by keeping the load carried by the rectangular heat source equal to the one carried by the elliptic heat source while assuming for the plastic case a constant pressure over the microcontact with a value equal to the hardness. The ellipticity ($\psi$) is also set equal for the rectangular and elliptic case. The ellipticity ($\psi$) is varied while keeping $A_{con}$ constant. To be able to show the effect that the ellipticity has on the contact temperature, the results in Figure 10 are normalized by the maximum temperatures of the references cases. In the reference cases a round contact ($\psi = 1$) is used for both the elastic case as the plastic case ($\Theta_0$). The partitioning of heat is also dealt with in two different ways; for the elliptic shaped heat source, local partitioning is used and for the uniform rectangular heat source global partitioning is used. The reason is that for a prescribed uniform heat source local partitioning cannot be used since then the heat source would not have uniform shape anymore.

The results for the elastic case are given in Figure 10-a, showing that the simplification of a uniform rectangular heat source underestimates the maximum contact temperature by approximately 20 percent. In the plastic case, the temperature profile of the rectangular heat source corresponds well with the elliptic one, even though the partition is dealt with differently. It is also clearly shown that using an elliptic contact with its major axis orientated perpendicular to the sliding velocity reduces the contact temperature by more than 20 percent. In the plastic case, the temperature decrease by the orientation of the heat source is also seen.

## CONCLUSION

A thermal contact model is presented and validated using results from literature. It is shown that using global partitioning gives accurate results for the maximum contacting temperature. So using Blok's postulate is preferred over local partitioning if only the maximum temperature is of interest. Local partitioning is preferred if more detailed information about the temperature field and partitioning is needed. Local partioning is also preferred in modeling the maximum contact temperature as a combination of bulk and flash temperature. The reason is that the bulk temperature is typically a function of the location of the micro contact. This means that the temperature field needs to be calculated in detail [24].

The calculations also show that global partitioning, using Blok's postulate of equal maximum temperature of both contacting bodies, is justified for the plastic contact case characterized by a uniform pressure over the contact. However, in the case of elastically deforming contacts calculating the contact temperature using Blok's postulate gives an underestimation. Then, this approach is not sufficient to calculate the contact temperature at either macro or micro scale accurately. In these situations local partitioning is needed to calculate the temperature field. It is further shown that micro-contacts are thermally not always in a steady state situation and therefore the quasi-static assumption is not justified in every case. At low sliding velocities the micro contacts come near the stationary condition. At high sliding velocities the contact is still in the transient regime. Under these conditions, using a steady state model overestimates the contact temperature. It is shown by transient calculations that the assumption of a contact being is in the steady state if the Fourier number is higher than 100 is justified. Furthermore it is shown that the contact temperature is reduced by orienting an elliptic shaped contact area with the major axis perpendicular to the sliding direction.

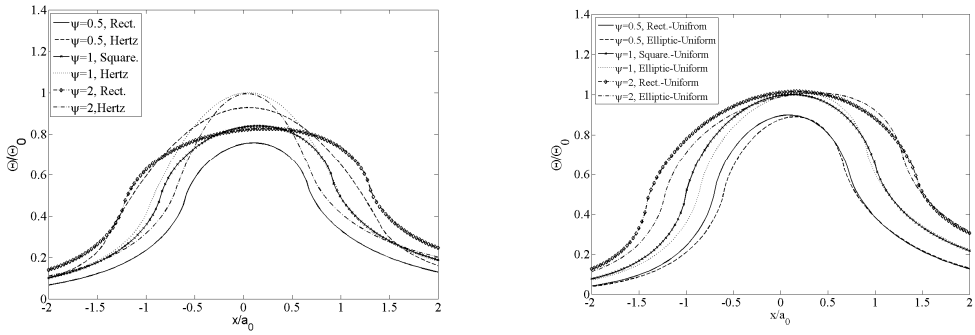


**a)** **b)**

**Figure 10:** Centerline temperature fields divided by the maximum temperature of the reference case ($\Theta_0$) as a function of x location on the center axis of the heat source **a)** elastic case **b)** plastic case. Sliding direction left to right with $Pe \approx [0.7–1.4]$ and $\Gamma \approx [2\text{-}4]$

## REFERENCES


[1] Drogen, M. van., 2005, "The Transition to Adhesive Wear of Lubricated Concentrated Contacts," Ph.D. thesis, Twente, Enschede.

[2] Abdel-Aal, H. A., 1997, "On the Distribution of Friction Induced Heat in the Dry Sliding of Metallic Solid Pairs," International Communications in Heat and Mass Transfer, 24(7), pp. 989-998.

[3] Abdel-Aal, H. A., 2001, "Thermal Compatibility of Dry Sliding Tribo-Specimens," Wear, 250, pp. 939-948.

[4] Ashby, M. F., 1991, "Temperature Maps of Frictional Heating in Dry Sliding," Tribology Transactions, 34(4), pp. 577-587.

[5] Blok, H., 1937, "Theoretical Study of Temperature Rise at Surfaces of Actual Contact under Oiliness Conditions," Proc. Inst. of Mechanical Engineers General Discussion of Lubrication, 2, pp. 222-235.

[6] Bos, J., 1995, "Frictional Heating of Tribological Contacts," Ph.D. thesis, University of Twente, Enschede.

[7] Hou, Z. B., 1999, "General Solutions for Stationary/Moving Plane Heat Source Problems in Manufacturing and Tribology," International Journal of Heat and Mass Transfer, 43, pp. 1679-1696.

[8] Tian, X., 1994, "Maximum and Average Flash Temperatures in Sliding Contacts," Journal of Tribology, 116, pp. 167-176.
[9] Vick, B., 2000, "Theoretical Surface Temperatures Generated from Sliding Contact of Pure Metallic Elements," Tribology International, 33 pp. 265-271.
[10] Vick, B., 2001, "A Basic Theoretical Study of the Temperature Rise in Sliding Contact with Multiple Contacts," Tribology International, 34(12), pp. 823-829.
[11] Wang, S., 1995, "A Fractal Theory of the Temperature Distribution at Elastic Contacts of Fast Sliding Surfaces," Journal of Tribology, 117, pp. 203-215.
[12] Cameron, A., Gordon, A. N., and Symm, G. T., 1965, "Contact Temperatures in Rolling/Sliding Surfaces," Proceedings of the Royal Society of London. Series A, Mathematical and Physical Sciences, 286(1404), pp. 45-61.
[13] Ling, F. F., Lai, W. Michael and Lucca, A., 2002, Fundamentals of Surface Mechanics, Mechanical Engineering Series, Springer-Verlag, New York.
[14] Gao, J., Lee, S. C., Ai, X., and Nixon, H., 2000, "An FFT-Based Transient Flash Temperature Model for General Three-Dimensional Rough Surface Contacts," Journal of Tribology, 122(3), pp. 519-523.
[15] Qiu, L., and Cheng, H. S., 1998, "Temperature Rise Simulation of Three-Dimensional Rough Surfaces in Mixed Lubricated Contact," Journal of Tribology, 120(2), pp. 310-318.
[16] Bos, J., and Moes, H., 1995, "Frictional Heating of Tribological Contacts," Journal of Tribology, 117(1), pp. 171-177.
[17] Abdel-Aal, H. A., 2003, "Efficiency of Thermal Energy Dissipation in Dry Rubbing," Wear, 255, pp. 348-364.
[18] Tian, X., and Kennedy, F. E., 1993, "Contact Surface Temperature Models for Finite Bodies in Dry Sliding and Boundary Lubricated Sliding," Journal of Tribology, 115, pp. 411-418.
[19] Carslaw, H. S., and Jaeger, J.C., 1959, Conduction of Heat in Solids, Clarendon press, Oxford.
[20] Ren, N., 1993, "Contact Simulation of Three-Dimensional Rough Surfaces Using Moving Grid Method.," Journal of Tribology, 115(4), pp. 597-601.
[21] Johnson, K. L., 1985, Contact Mechanics, Cambridge university Press, Cambridge.
[22] Gecim, B., 1985, "Transient Temperatures in the Vicinity of an Asperity Contact," Journal of Tribology, 107, pp. 333-342.
[23] Abbott, E. J., and Firestone, F. A., 1933, "Specific Surface Quality- a Method Based on Accurate Measurement and Comparison," Mechanical Engineering, 55, pp. 569 -572
[24] Bosman, R., 2008, "Mild Wear in the Boundary Lubricated Regime" accepted for publication in the proc. Friction, Wear and Wear Protection symposium, 2008, Aachen.

Paper B

Mild Microscopic Wear in the Boundary Lubrication Regime Materialwissenshaft und Werkstofftechniek,
R. Bosman,
2010, Volume 41, Issue 1

# Microscopic Mild Wear in the Boundary Lubricated Regime

R. Bosman
University of Twente, r.bosman@utwente.nl
Drienerlolaan 5
7500 AE Enschede

Published in: Materialwissenshaft und Werkstofftechniek,
Volume 41, issue 1.

*Abstract* - **The transition from a mild wear situation to a severe (adhesive) wear situation is of great interest to be able to design highly loaded concentrated contacts operating in the boundary lubricated regime. In this article a method is described to estimate this transition, based on a thermal criterion. It is stated that if a certain percentage of the contacting asperities transcends a critical temperature which is determined experimentally the transition from mild to severe wear takes place. The theory presented is validated with a model system and the results from experiments are is good agreement with the simulations.**

*Index Terms* – Wear transition, Boundary lubrication

## INTRODUCTION

The transition from mild wear to severe wear is of interest with respect to the load carrying capacity of lubricated contacts. Blok stated with his hypothesis that the transition is determined by the transcending of a critical temperature [1]. However, experimental results did not fit with model prediction very well. Probably, the thermal model used is not detailed enough to give a good representation of the real temperature field within the contact surface. Since the pioneering work of Blok a lot has changed. One of the mayor breakthroughs is the recognition of the effect of microscopic phenomena on the temperature field [2]. Blok did not take into account microscopic effects, but focused only on the macroscopic effects. He split up the complete temperature field into two domains: the overall bulk temperature and an instantaneous macro flash temperature, see Figure 1. However, in reality it is more likely that the highest temperature will occur at the microscopic contact between two roughness peaks (summits), as shown in Figure 1. Therefore, a new definition is made concerning the complete temperature field. Where $\Theta_{bulk}$ is the temperature of the environment, $\Theta_{macro}$ the macroscopic heating of the material (which Blok describes as the instantaneous flash temperature) and $\Theta_{micro}$ the temperature rise due to the microscopic contacts. The last can be split up into two parts. A part caused by the two summits in contact ($\Theta_{micro}$) and a part caused by the effect the surrounding micro contacts have on the summit ($\Theta_{microm}$) looked at. To calculate the temperature field to this level of detail, two things are needed: at first a contact model capable of calculating the area of contact and pressure distribution at every micro contact. Secondly, a thermal model capable of calculating the

microscopic (flash) temperature using the contact parameters as an input. Dealing with these subjects in the same order the article can be split up into roughly three major parts: 1) the contact model ; 2) the thermal model and 3) results.

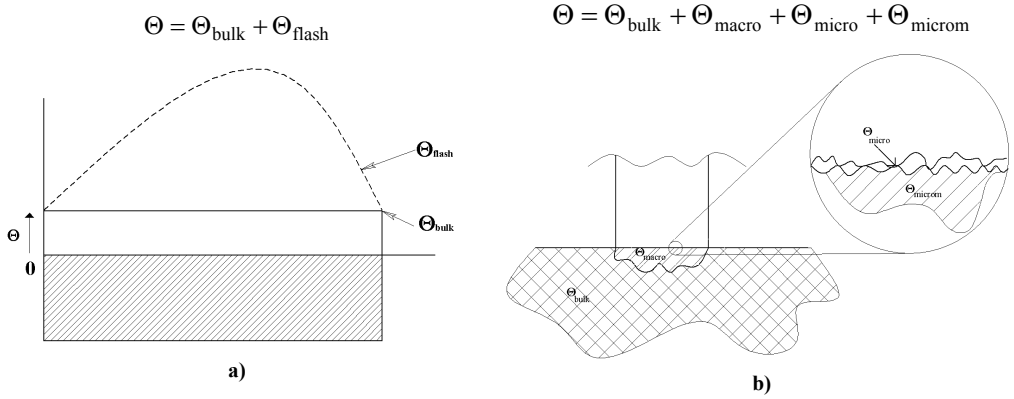


**Figure 1 a)** Temperature model used by Blok, **b)** temperature model used in this article.

## CONTACT MODEL

At macroscopic level the elastic contact can be calculated using Hertz. At the microscopic level the contact is calculated as follows: First a deterministic contact model is discussed, which can be used to calculate the pressure and contact area of every single summit. This model is based on an elastic-elastoplastic-plastic analytical contact model [4, 5]**.** As an input for this model the surface is characterized using a nine point summit model developed by Greenwood [6]. The contact between a flat and smooth surface against a rough one is schematically presented in Figure 2.

Depending on the indentation the asperity can be either in : 1) elastic; 2) elasto-plastic or 3) fully plastic contact [5]**.**

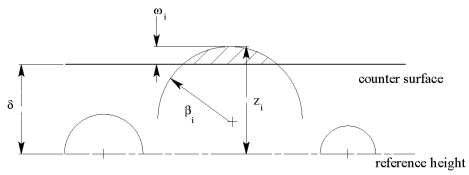


**Figure 2**: Surface representation as used in the contact model.

### Elastic contact

If a summit is deforming purely elastic the Hertz theory gives a very good approximation of the micro contact parameters [3].

$$\kappa_e = \frac{a_{x,e}}{a_{y,e}}, a'_{x,e} = \left(\frac{2\kappa_e \mathbf{E}(m)}{\pi}\right)^{1/3},$$
$$a'_{y,e} = \frac{a'_{x,e}}{\kappa_e} \qquad (1)$$
$$\text{and } \gamma_e = \frac{2\mathbf{K}(m)}{\pi a'_{y,e}}$$

Where:

$$a_{x,e} = a'_{x,e}\left(\frac{3F\beta'}{E'}\right)^{1/3} \text{ and}$$
$$a_{y,e} = a'_{e,y}\left(\frac{3F\beta'}{E'}\right)^{1/3} \qquad (2)$$

In which $F$ is the local load, $\beta'$ and $E'$ the reduced radius and equivalent modulus

respectively. The indentation, elastic contact area and load can now be defined as:

$$A_e = \pi a_{x,e} a_{y,e},$$
$$F_e(\omega) = \sqrt{\frac{8E'^2\beta'}{9}}\left(\frac{\omega}{\gamma_e}\right)^{3/2} \text{ and} \quad (3)$$
$$\omega = \gamma_e\left(\frac{9F^2}{8E'^2\beta'}\right)^{1/3}$$

**Plastic contact**

The full plastic contact situation results in a uniform pressure over the complete contact area with the same magnitude as the hardness of the material. The plastic contact area and reactive force as a function of the indentation become:

$$A_p = 2\pi\omega\sqrt{\beta_x\beta_y} \text{ and}$$
$$F_p(\omega) = 2\pi\omega H\sqrt{\beta_x\beta_y} \quad (4)$$

In which $\beta_x$ and $\beta_y$ are summit radii in *x* and *y* direction.

**Elasto-plastic contact**

According to Tabor the plastic deformation starts when the mean pressure is 0.4 times the hardness of the material [7]. The reactive force for summits in-between the elastic and full plastic regime as a function of the indentation is given by [2]:

$$A_{ep} = 2\pi\beta'\omega\frac{a'_{x,e}\,a'_{y,e}}{\gamma_e} + \left\{\begin{pmatrix} 2\pi\omega\sqrt{\beta'(\beta_x+\beta_y)} \\ -2\pi\beta'\omega\frac{a'_{x,e}\,a'_{y,e}}{\gamma_e}\end{pmatrix} \times\left[-2\left(\frac{\omega-\omega_e}{\omega_p-\omega_e}\right)^3+3\left(\frac{\omega-\omega_e}{\omega_p-\omega_e}\right)^2\right]\right\} \quad (5)$$

Using equation (5) and the expression for the mean pressure ( $p_{mean} = F / A_{ep}$ ):

$$p_{ep,mean} = H - H(1-k)\exp\left(-\left(\frac{dp_e}{d\omega}\right)_{\omega=\omega_e}\frac{\omega_p-\omega_e}{H(1-k)}\left(\frac{\omega-\omega_e}{\omega_p-\omega}\right)\right) \quad (6)$$

The reactive force becomes:

$$F_{ep}(\omega) = p_{ep,mean}(\omega)A_{ep}(\omega) \quad (7)$$

For all three contact situations the reactive force of every single summit can be calculated. Summarizing over all summits gives the total reactive force over the complete surface as a function of the indentation.

**TEMPERATURE MODEL**

The total temperature rise at the surface is defined as the sum of the environment ($\Theta_{bulk}$), macroscopic ($\Theta_{macro}$), micro-scopic temperature ($\Theta_{micro}$), which is divided into two parts. The effect of the interacting summits themselves ($\Theta_{micro}$) and the effect of the neighboring summits ($\Theta_{microm}$), see Figure 1. First a general solution is given after which all separate parts will be discussed.

**General Solution of the Temperature Field**

All heat generated at the surface by friction is assumed to be conducted into the contacting surfaces. This creates a heat source defined by:

$$Q(x,y) = \mu P(x,y)U \quad (8)$$

The motion is modeled by sliding the surface underneath the heat source. To do so a local grid is defined with its origin *0'* moving along the *x*-axis with velocity *U*. In

this coordinate system *x''* is the point were heat source *Q(x'',y')* is acting and the location M(*x' ,y)* is the target location. The temperature field of the complete moving heat source can now be determined [8]**:**

$$\Theta(x',y)=\int_{-a}^{a}\int_{-b}^{b}\int_{0}^{t}\frac{Q(x'',y')}{\rho C_{cp}8(\pi\kappa)^{3/2}}\frac{1}{\tau^{3/2}}\exp\left(-\frac{((x'-x''+U\tau)^2+(y-y')^2+z^2)}{4\kappa\tau}\right)dx''dy'd\tau \qquad (9)$$

However, in many cases there is no analytical solution to equation (9). In this paper the effect of the complete heat source is modeled using square heat sources of size $\Delta x'', \Delta y'$, which have effect $\mathrm{Eff}_{ij}$ on location *(x',y)* [8]:

$$\Theta(x',y)=q_{ij}\mathrm{Eff}_{ij} \qquad (10)$$

With $q_{ij}$ the local heat source at $x'', y'$ and $\mathrm{Eff}_{ij}$ the effect matrix for a location $x', y$, as given in [8]. If the domain of interest is discritizised with a similar grid as the one used for the heat source with the indexes *k* and *l* for the x' and y direction respectively, the temperature tensor becomes:

$$\Theta_{mn}=q_{ij}\mathrm{Eff}_{ijmn} \qquad (11)$$

During contact the temperature field needs to be continuous over both bodies in contact [9]. To fulfill this condition the following two restrictions can be set at the surface:

$${}^1\Theta(0,x,y)={}^2\Theta(0,x,y) \text{ and } {}^1q_{kl}+{}^2q_{kl}=q_{kl} \qquad (12)$$

Combining equations (11) and (12) results in:

$${}^1q_{kl}=q_{kl}\,{}^2\mathrm{Eff}_{klmn}({}^1\mathrm{Eff}_{klmn}+{}^2\mathrm{Eff}_{klmn})^{-1} \quad \text{and} \quad {}^2q_{kl}=q_{kl}\,{}^1\mathrm{Eff}_{klmn}({}^1\mathrm{Eff}_{klmn}+{}^2\mathrm{Eff}_{klmn})^{-1} \qquad (13)$$

The resulting temperature field at the surface of both contacting bodies becomes:

$${}^1\Theta_{mn}={}^1q_{kl}\,{}^1\mathrm{Eff}_{klmn} \text{ and } {}^2\Theta_{mn}={}^2q_{kl}\,{}^2\mathrm{Eff}_{klmn} \qquad (14)$$

**Macroscopic temperature field**

A method described in more detail in [10] is used to calculate the effect the macroscopic heat source has on the microscopic level. If it is assumed that the friction is constant over time, the total energy dissipated by friction is given by:

$$E=\int_{0}^{t}F_n\mu U dt \qquad (15)$$

The complete energy dissipated is now virtually split up into two parts. A macroscopic part and a microscopic part, where the macroscopic part represents the average energy dissipated over all the micro contacts during time interval $[0, t-\Delta t]$. Where $\Delta t_i=t_{i,c}=2R^{micro}_{i,x}/U$, with $R^{micro}{}_{i,x}$ the contact width of the micro contact in the *x*-direction and *U* the sliding velocity. Using the macroscopic pressure distribution the temperature field can be calculated.

**Microscopic temperature field**

The thermal energy left is dissipated during the short time of $[t-\Delta t, t]$, at the micro contacts. The microscopic temperature field is built up from two components, as

mentioned before. The temperature rise at the contact itself is calculated by using the general theory discussed in the section about the temperature field. The pressure distribution is given either by the elastic or plastic case. However, for the elasto-plastic case no complete pressure field is described. For this regime a threshold is set: if more then half of the contact is plastically deforming the heat source is modeled as a uniform one, else it is modeled as an elastic one. This is done to prevent an underestimation of the temperature field if a large part of the surface is still elastically deforming.

The temperature rise caused by the effect which the different micro heat sources have on each other can be calculated using a simplification of the problem**.** The heat sources surrounding the target summit are modeled as square, uniform heat sources in a tensor $q_{ij}^{surround}$. This is done by defining $\Delta x''$ and $\Delta y'$ as the equivalent length and width of the source, and replacing *x'* and *y* for the distance in *x* and *y* direction between source and target location respectively. The location of the micro contact inside the macroscopic contact area is defined, thus the effect the macroscopic heat source has on this location can be calculated as can the effect the different heat sources have on each other and the temperature rise within the micro-contact itself. Combining all these parts creates the complete temperature field at the surface.

## RESULTS

Using the theory discussed in the previous sections it is possible to calculate the complete temperature field of two contacting rough bodies at both macroscopic and microscopic level. This model is used to predict the transition from mild wear to severe wear using a critical temperature i.e. using Blok's original idea combined with a more detailed thermal model, see Figure 1. First a critical temperature needs to be defined. An experiment for doing so is discussed in [2, 12] and is also used here. In short the procedure is: perform a pin on disk test at very low velocity so there is negligible frictional heating and increasing the environmental temperature until scuffing occurs. For the oil used in the experiments this was 130 $^{o}$C. The experiments used to obtain a transition diagram from mild to severe wear are conducted in a different way. At a given velocity and load a specimen is pushed against its counter surface and the friction is measured. If the friction coefficient stays under 0.4 the test is a pass otherwise the contact is seen as a failure. For each test a new specimen is used to prevent running-in. The specimen used in the transition diagram tests where:

- Pin: Commercially available cylinder from a roller bearing of low alloyed chromium steel with a diameter of 4 mm with a load carrying length of 3.4 mm. The surface finish processes applied are grinding and polishing.
- Disk: The disk of diameter 150 mm is made of case hardening steel. The surface finish was grinding.

The parameters from the surface of the disk are presented in Table 1.

| $\bar{\beta}$ [m] | $\sigma$ [m] | $\eta$ [m$^{-2}$] |
|---|---|---|
| $4\times10^{-6}$ | $2\times10^{-7}$ | $6\times10^{10}$ |

**Table 1:** Statistical properties of the reference surface.

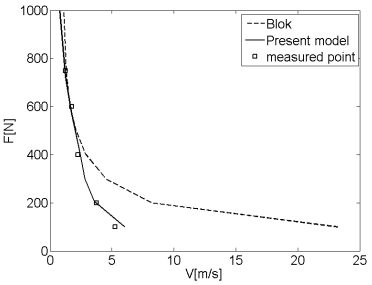


**Figure 3**: Transition diagram comparing the different models and measurements

Although a critical temperature is set a clear threshold for the transition form mild to severe wear is still needed. The threshold chosen is, the 10 percent failure criterion like in the bearing industry. Concrete this states that if the temperature of more than 10 percent of the summits in contact transcends the critical temperature the contact fails.
During testing the measured contact width did not concur with the calculated one using Hertz, even width a small correction for the roughness [13]. The reason for this is probably the mild wear already occurring after a few revolutions. To compensate for this a correction factor is introduced:

$$\zeta = \frac{R_{macro}}{R_{eq}} \qquad (16)$$

Where $R_{eq}$ is the radius of the macroscopic body (the pin) at which the contact width corresponds to the measured contact width. The average value of $\zeta$ following from the conducted tests was $\zeta = 8$. This value will be used for calculating the transition diagram, as shown in Figure 3: Using this value a good agreement is found between the calculated transition and the measurements. However, using Blok his original thermal model [14], with the correction as given by equation (16), the transition at low loads and high velocities is over estimated significantly.

## CONCLUSIONS

A new model capable of predicting the transition from mild to severe wear is presented. The model is based on a microscopic based thermal model in combination with a elasto-plastic deterministic contact model. Using this type of modeling the temperature field at the surface inside the contact can be calculated in detail. Combining this thermal model with Blok's hypothesis on the transition form mild to severe wear, that this is caused by transcending a critical temperature, good results are achieved.

## REFERENCES


1.Blok H., SAE Journal, 1939, 193-204.
2.Drogen van M., The Transition to adhesive wear of Lubricated Concentrated Contacts, PhD thesis, 2005, Twente: Enschede.
3.Hertz H., Journal für die reine und angewandte Mathematik, 1881, 16.
4.Zhao Y., Journal of Tribolgy, 2000,: 86-93.
5.Johnson K.L., Contact mechanics. 1985, Cambridge: Cambridge university Press.
6.Greenwood J.A., Proc. Soc. Lon. A, 1984, 133-157.
7.Tabor D., The hardness of Materials. 1951: Oxford University Press.
8.Carslaw H.S., Conduction of heat in solids. 1959, Oxford: Clarendon press.
9.Bos J., Frictional heating of tribological contacts, PhD thesis, 1995, University of Twente: Enschede. p. 137.
10.Bosman R., Thermal Boundary Element Method: Formulation and Application part-2. submitted to the Journal of Tribolgy, 2008.
11.Bosman R., Thermal Boundary Element Method Formulation and Application part-1 submitted to the Journal of Tribology, 2008.
12.Grew W.J.S. and A. Cameron, Proc. R. Soc. London, Series A327, 1972.
13.Gelinck E.R.M., Mixed Lubrication of Line Contacts, PhD Thesis,University of Twente. 1999: Enschede.
14.Blok H., Proc. Inst. of Mechanical Engineers General Discussion of Lubrication, 1937, 222-235.

Paper C

On the Transition from Mild to Severe Wear of Lubricated, Concentrated Contacts: The IRG-OECD Transition Diagram,

R. Bosman and D.J. Schipper,
Wear, 2010, Volume 269
Issue 7-8

# On the Transition from Mild to Severe Wear of Lubricated, Concentrated Contacts: the IRG (OECD) Transition Diagram

R. Bosman and D.J. Schipper
University of Twente, r.bosman@utwente.nl
Drienerlolaan 5
7500 AE Enschede
Published in: Wear, 2010, volume 269, issue 7-8

*Abstract* - **In this paper the transition from mild wear to severe wear of lubricated, concentrated contacts is dealt with. It is suggested that this transition is thermally induced. The transition from a mild wear to severe adhesive wear occurs when more then 10 percent of the surface transcends a predefined, critical temperature. A method for determining this critical temperature is presented. Using a BIM based numerical model including the local implementation of Archard's wear law, for the contact pressure and temperature the transition diagram for a model system is calculated and validated by experiments. The transition predicted by numerical calculations is in very good agreement with the experimental determined transition.**

*Index Terms* – Sliding wear, Thermal effects, Wear modeling

## NOMENCLATURE

| Roman Symbols | | |
|---|---|---|
| $C_p$ | $[J/kg^oC]$ | Specific heat |
| $D$, $D_{ij}$ | $\left[\frac{m}{Pa}\right]$ | Displacement Influence Coefficient/Tensor |
| $E$ | $[Pa]$ | Elastic Modulus |
| $F_n, F_{in}, F_{nMesh}$ | $[N]$ | Normal force total, incremental, local |
| $g_{ij}$ | $[m]$ | Gap |
| $h_{ij}$, $h(x,y)$ | $[m]$ | Separation/Separation tensor/height loss |
| $I_{discr}, I_c$ | [–] | Collection of grid points (all grid points/points in contact) |
| k | $[mm^3/Nm]$ | Specific wear rate |
| K | $[W/m^oC]$ | Thermal conductivity |
| $L$ | $[m]$ | Length |
| $N_c$ | [–] | Number of elements in contact |
| $p(x,y)$, $p_{ij}$ | $[Pa]$ | Pressure field/ tensor |
| $Ra$ | $\frac{1}{N}\sum\sum\left\|h_{ij}-\bar{h}_{ij}\right\|$ | Average roughness value |
| $r_{ij}$ | $[m^2/Pa]$ | Distribution in multidimensional space |
| $S$ | $[m]$ | Sliding distance |
| $t_{ij}$ | $[m]$ | Search direction |
| $t$ | $[s]$ | Time |
| $T(x,y)$, $T_{kl}$ | $[\Theta/Wm^2]$ | Thermal influence coefficient/tensor |

| | | |
|---|---|---|
| $u$ | $[m]$ | Surface displacement in normal direction |
| V | $[m/s]$ | Sliding velocity |
| $W$ | $[m^3]$ | Wear volume |
| $x, y$ | $[m]$ | Location of interest |
| $x', x'', y'$ | $[m]$ | Location of excitation |
| $\Delta x, \Delta y$ | $[m]$ | Element size |
| $\bar{x}_{ij}$ | $[-]$ | Average value of tensor |

| Greek symbols | | |
|---|---|---|
| $\varepsilon$, $\varepsilon_{set}$ | [-] | Relative error, preset relative error |
| $\Theta$ | $[^o C]$ | Temperature rise |
| $\kappa$ | $[K/\rho C_p]$ | Thermal diffusivity |
| $\mu$ | $[-]$ | Coefficient of friction |
| $\nu$ | $[-]$ | Poisson Ratio |
| $\rho$ | $[kg/m^3]$ | Specific density |
| $\tau$ | $[Pa/m]$ | Size of the iteration step |
| $\phi$ | $[-]$ | Partition factor |

**INTRODUCTION**

The last decade an increasing demand for smaller machines/components transmitting the same power or more is seen; hence the nominal contact pressures increase. Due to these increasing contact pressures components are operating in the boundary lubrication regime rather then in the full film or mixed lubrication regime. As a result the load is carried by the asperities rather than by the lubricant leaving the adsorbed/reacted boundary layers as the final protection against wear. To be able to design such a component in the most efficient way it is preferred to have beforehand knowledge at which nominal load and velocity the transition from mild wear to adhesive wear will take place. In the late 80's and early 90's the International Research Group on Wear of Engineering Materials did a lot of research on this topic, developing "IRG (OECD)" transition diagram [1], three different regions are distinguished as shown in Figure 1. These regions are distinguished on the bases of the recorded friction-time signals.

Regions I/II indicate the save region at which mild wear will occur. Regions III* and III indicate a region where temporary and respectively permanent severe wear will be present. In this study only the transition from region I/II to III* and I/II to III (thick line in Figure 1) will be studied, since it is assumed that after passing this transition enhanced wear will occur and the component has failed. Usually the transition diagram for a certain oil/system is based on experiments and lacks a predictive model or gives a relatively simple empirical relation [2-8]. However, it gives a good overview of the parameters influencing the transition to severe adhesive wear, the transition from mild to severe wear shifts to higher values for the load when for instance the viscosity is increased or the sample roughness is decreased. In this paper an attempt is made to predict the transition based on the postulate first made by Blok [9] and later on adapted by Lee and coworkers to include the presumed effect pressure has on the critical temperature [10-11]. Blok originally stated in the late 30's that the transition from mild to adhesive wear is a thermal phenomenon. Using this assumption the transition diagram is given a more predictive nature. The postulate states that if the contact temperature is higher than the critical temperature of the protective boundary layer, the layer will fail and the system will undergo severe adhesive wear. Blok did not succeed in defining a uniform critical temperature for a defined system. This is probably due to the lack of good thermal models at the time able to deal with contact temperatures in a sufficient degree of detail. Van Drogen [12] did succeed in defining a critical temperature for the transition from mild to severe wear using a thermal model taking into account the micro geometry. However, as discussed in that work the influence of wear is not to be neglected, and was taken into account

by adapting the macroscopic geometry by increasing the radius of the bodies in contact. In the current paper the Archard wear law is embedded in the contact model using the local pressure profile as an input. The modeling can be separated in three different parts: 1) Contact model, 2) thermal model and 3) Transition criterion. The different parts will be addressed in this order, starting with the contact model.

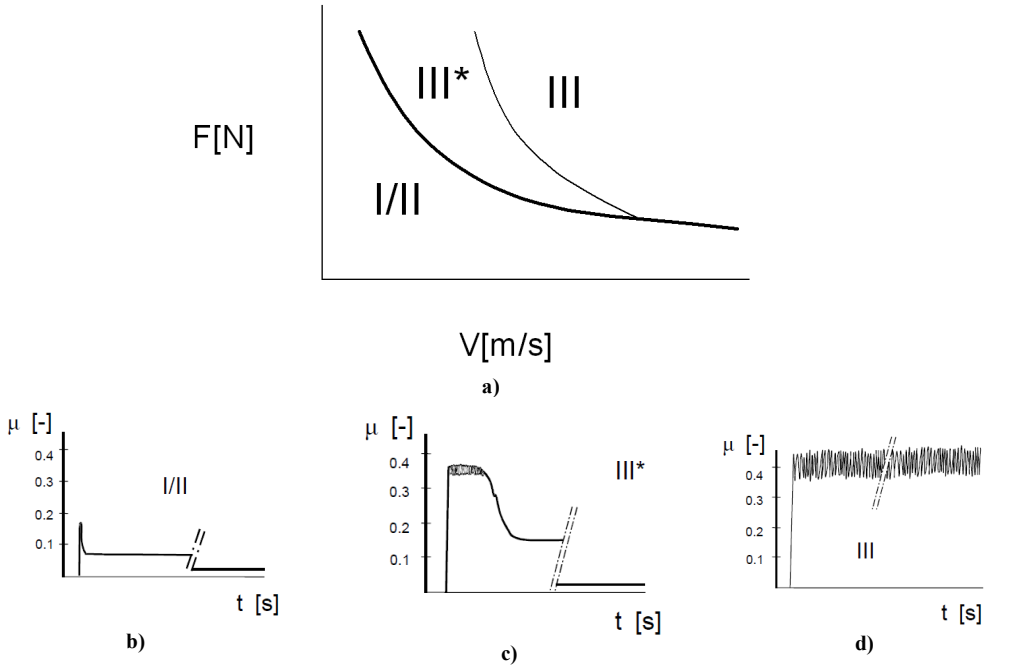


**Figure 1: a)** IRG transition diagram indicating regions I/II (mild wear) and III/III* (severe wear), **b)** Friction-time signal for wear region I/II, **c)** region III* and **d)** region III.

## CONTACT MODEL

The systems of interest in this study are boundary lubricated thus it is assumed that the contact load is carried by the asperities in contact rather then the lubricant as is assumed in [13]. This assumption makes it feasible to model the contact as a "dry" contact. The effect of the lubricant is only taken into account through a reduction in the coefficient of friction, e.g. the presence of the rather thin protective boundary layers. For dry contact the model used in this study is based on the single loop CGM fist discussed by Polonsky and Keer [14]. In their study a novel method is discussed capable of calculating the elastic contact of large meshes using the B(oundary) I(ntegral) M(ethod) in combination with a multi-level summation method. The efficiency of the model greatly depends on the reduction of iterative loops from two to one, namely only the approach (or rigid body motion) of the bodies relative to each other. Later this method is refined by Liu and Wang by replacing the multi-level summation method by a DC-FFT method, as discussed in [15], increasing the accuracy and calculation speed. This method is based on the basic assumptions that both bodies can be modeled as semi-infinite elastic half-spaces with homogenous properties throughout the bulk. The elastic displacement of the surface due to a pressure field $(p(x,y))$ can now be written as the convolution integral:

$$u(x,y) = -\iint D(x-x',y-y')\,p(x',y')\,dx'\,dy' \qquad (1)$$

The influence coefficient ($D(x\text{-}x',y\text{-}y')$) is given by the Boussinesq formula [16]:

$$D(x,y)=\left(\frac{1-\nu_1^{\,2}}{\pi E_1}+\frac{1-\nu_2^{\,2}}{\pi E_2}\right)\frac{1}{\sqrt{x^2+y^2}} \qquad (2)$$

Diskretizising eq. (1) gives at all points of interest ($I_{discr}$):

$$u_{ij}=\sum D_{i-k,j-l}\,p_{kl}, \quad (i,j)\in I_{discr} \qquad (3)$$

Equation (3) can be solved using the DC-FFT algorithm if the formula for the influence matrix is known. Where:

$$D_{ij}=\int_{-\frac{1}{2}\Delta x}^{\frac{1}{2}\Delta x}\int_{-\frac{1}{2}\Delta y}^{\frac{1}{2}\Delta y} D(x_i-x',y_j-y')dx'dy', \quad (i,j)\in I_{discr} \qquad (4)$$

The elastic contact problem can now be described by the following equations and inequalities (as discussed in [14]):

$$\sum_{(k,l)\in I_{discr}} D_{i-k,j-l}p_{kl}=h_{ij}+\alpha, \quad (i,j)\in I_c \qquad (5)$$

$$p_{ij}>0, \quad (i,j)\in I_c \qquad (6)$$

$$\sum_{(k,l)\in I_{discr}} D_{i-k,j-l}\,p_{kl}\geq h_{ij}+\alpha, \quad (i,j)\notin I_c \qquad (7)$$

With $h_{ij}$ the original surface separation, $\alpha$ the rigid body motion and $I_c$ all grid points in contact.

$$\Delta x\Delta y\sum_{(i,j)\in I_c} p_{ij}=\mathrm{F_n} \qquad (8)$$

Where $\Delta x$ and $\Delta y$ are the grid spacing and $F_n$ is the total normal force carried by the contact.

Using a CG based iteration method discussed next, the problem described is solved (for details the reader is referred to [14]). First the displacement of the current pressure guess is computed and from this the current gap:

$$g_{ij}=-u_{ij}-h_{ij}, \quad (i,j)\in I_c \qquad (9)$$

The average gap is obtained by:

$$\bar{g}=\frac{1}{N_c}\sum_{(k,l)\in I_c} g_{kl} \qquad (10)$$

$$g_{ij}\leftarrow g_{ij}-\bar{g}$$

Here $N_c$ is the current number of elements in contact and $I_c$ are all grid points in the diskretized region where $p_{ij}>0$. For the new gap the sum is calculated:

$$G=\sum_{(i,j)\in I_c} g_{ij}^{\,2} \qquad (11)$$

This value is then used to compute the new conjugate direction $t_{ij}$:

$$t_{ij}=g_{ij}+\delta(G/G_{old})t_{ij}, \quad (i,j)\in I_c \qquad (12)$$

$$t_{ij}=0, \quad (i,j)\notin I_c \qquad (13)$$

The old value of $G$ is now stored for the new iteration $G_{old}=G$ and the convolution of $D_{ij}$ and $t_{ij}$ is computed for distribution in the multidimensional space of elemental pressures:

$$r_{ij}=\sum_{(k,l)\in I_{discr}} D_{i-k,j-l}t_{kl}, \quad (i,j)\in I_{discr} \qquad (14)$$

$$\bar{r}=\frac{1}{N_c}\sum_{(k,l)\in I_c} r_{kl} \qquad (15)$$

$$r_{ij}=r_{ij}-\bar{r}, \quad (i,j)\in I_{discr} \qquad (16)$$

The size of the next iteration step is then computed:

$$\tau = \frac{\sum_{(i,j)\in I_c} g_{ij} t_{ij}}{\sum_{(i,j)\in I_c} r_{ij} t_{ij}} \tag{17}$$

The current pressure is stored for error computation:

$$p_{ij}^{\ old} = p_{ij}, \quad (i,j) \in I_{discr} \tag{18}$$

Now the pressure is updated:

$$p_{ij} = p_{ij} - \tau t_{ij}, \quad (i,j) \in I_c \tag{19}$$

Next the inequalities of eq. (6) is enforced setting all $p_{ij} < 0$ equal to $0$ after which the overlap is determined:

$$I_{ol} = \left\{ (i,j) \in I_{disrc} : p_{ij} = 0,\ g_{ij} < 0 \right\} \tag{20}$$

If $I_{ol} = \varnothing$, then $\delta$ is set to unity otherwise to zero and the pressures at the overlap are corrected:

$$p_{ij} = p_{ij} - \tau g_{ij}, \quad (i,j) \in I_{ol} \tag{21}$$

Since $\tau > 0$ at every iteration all nodes in $I_{ol}$ will enter $I_c$ enforcing eq. (6). Next the current contact load is calculated and the error is estimated by enforcing eq. (8):

$$F_{it} = \Delta x \Delta y \sum_{(i,j)\in I_{discr}} p_{ij} \tag{22}$$

$$p_{ij} = \left( F_{it} / F_n \right) p_{ij}, \quad (i,j) \in I_{discr} \tag{23}$$

$$\varepsilon = \Delta x \Delta y F_n^{-1} \sum_{(i,j)\in I_{discr}} \left| p_{ij} - p_{ij}^{\ old} \right| \tag{24}$$

This iterative loop is repeated until $\varepsilon < \varepsilon_{set}$, which is set to $10^{-14}$. The contact model gives more realistic results by setting a maximum threshold to the contact pressure equal to the hardness of the material which is done in the same way as the restriction in eq. (6).

To incorporate wear into the contact model a Archard's wear law [17], e.g. wear volume is proportional to the normal load, is applied at a local level. This method is used by many other authors either in combination with FEM or with BEM, see for example: [18-20]. This wear model states that the wear volume is proportional to the load applied and sliding distance through:

$$W = k F_n S \tag{25}$$

here $W$ is the volume loss, $k$ the specific wear rate and $S$ the sliding distance. This wear law can also be applied on a local level by replacing the local normal force $F_n$ by the local pressure times the element size. To obtain the loss in height this volume is then divided by the surface of one grid element. Replacing the total sliding distance by the incremental sliding distance ( $dS$ ) gives:

$$dh(x,y) = k p(x,y) dS \tag{26}$$

Here $dh(x,y)$ is the incremental height loss and $p(x,y)$ the local pressure field acting on the solid. Using the loop shown in Figure 3 an incremental loading and sliding wear model is realized. In the current study a line contact is used as a model system to validate the theory presented. To simulate this correctly a modification is made to the DC-FFT algorithm for the following reason. The numerical method suggested is limited in the number of elements used. Thus a balance needs to be found between taking into account enough detail of the surface geometry and calculation time. To reduce the number of elements in the

direction tangent to the sliding direction (e.g. the largest dimension of the contact) the periodic solution inherent to the FFT formulation is used.

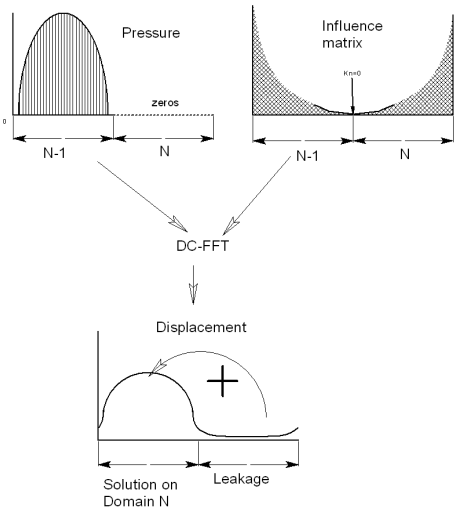


**Figure 2:** DC-FFT algorithm and leakage

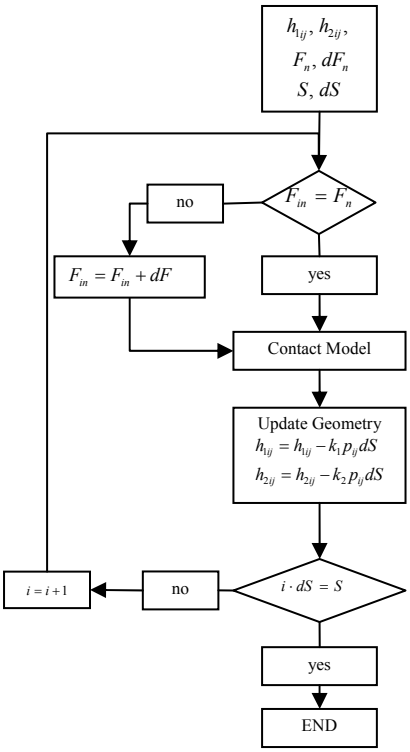


**Figure 3:** Incremental load/displacement loop

Normally the DC-FFT algorithm is formulated in such a way that it only takes the fist quadrant of the solution as a result of the convolution in the frequency domain, see [18] for details, as the solution in the time/space domain. This is done to compensate for leakage into the domain of interest. If now it is assumed that at both sides of the domain of interest a similar contact is situated (e.g. the contact is semi-periodical) the leakage normally removed can be used to mimic the line contact by adding this to the displacement in the domain of interest, see Figure 2. To validate this method an example is solved using 3 different methods: 1) Original DC-FFT method 2) DC-FFT with compensation 3) Hertzian theory. The example consists of a steel cylinder (with the elastic properties given in Table 3) with a radius of 8 mm pressed against a flat plate, resulting in a Hertzian line contact problem.

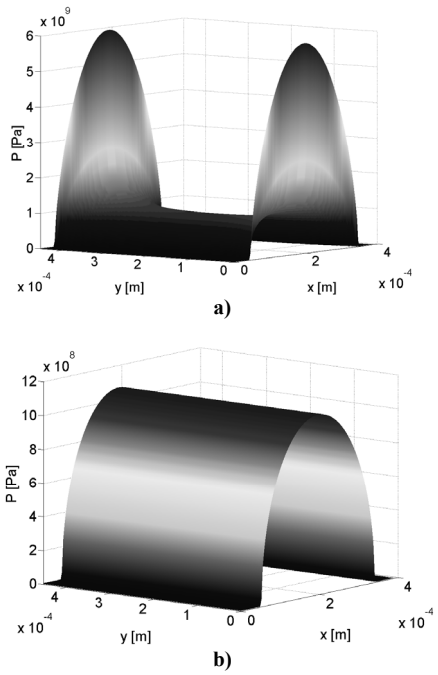


**Figure 4:** Pressure field calculated with **a)** original DC-FFT algorithm **b)** DC-FFT with compensation for line contact.

Solving the problem using the classical theory gives a maximum pressure of 1.01 GPa and a

semi-contact width of 0.14mm, which are in good agreement with the results obtained using DC-FFT algorithm with leakage compensation, shown in Figure 4. The "punch phenomenon" shown in the first figure is consistent for the solution of a pin with the finite length equal to the mesh size. However, this is not the case for the simulation done in this study where only part of the total length of the cylinder is used. For this reason the solution needs to be compensated for this as shown in the right figure. If the DC-FFT algorithm is used without leakage compensation for line contacts the solution is polluted with side effects as is shown in Figure 4.

## THERMAL MODEL

The thermal model used in this study is also based on the BIM method as discussed in [19]. One of the difficulties of using a thermal model is dealing with the heat partition to the contacting surfaces, which can be approached in different ways. One of the first who dealt with this problem is Blok [20]. This method gives good results for the maximum contact temperature of single contact calculations (e.g single asperity contact) as is discussed in [21]. However, for a more detailed study of the complete temperature field it is sensible to use a local partitioning method as discussed in [22] and is used in this work.

The temperature rise of a semi infinite body can be expressed in the convolution integral as eq. (1). Here the pressure field is exchanged for the heat source ( $q(x,y) = \mu V p(x,y)$ ), where it is assumed that the dissipated frictional energy is turned into heat, giving:

$$\Theta(x,y) = -\iint \frac{T(x-x',y-y',t)}{\mu V\, p(x',y')}\, dx'dy' \qquad (27)$$

Assuming the complete surface is insulated except for the infinite small element $\delta x'' \times \delta y'$, on which a uniform square heat source is acting, the influence matrix for a semi-infinite solid can be written as [23]:

$$T(x,y,t) = \int_0^t \frac{1}{\rho C_{cp} 8(\pi\kappa)^{3/2}\tau^{3/2}} \exp\left(-\frac{((x'-x''+U\tau)^2 + (y-y')^2)}{4\kappa\tau}\right) d\tau \qquad (28)$$

This can be rewritten for a heat source of finite size ( $\Delta x \times \Delta y$ ) using the following variables [24]:

$$\eta = \frac{x-x'}{2\sqrt{\kappa}\omega} \qquad dx' = -2\sqrt{\kappa}\omega d\eta$$

$$\xi = \frac{y-y'}{2\sqrt{\kappa}\omega} \qquad dy' = -2\sqrt{\kappa}\omega d\xi$$

$$V_x' = \frac{V_x\omega}{2\sqrt{\kappa}} \qquad \lambda = \frac{z}{2\sqrt{\kappa}\omega}$$

$$q = \frac{\varphi}{\rho C_p} \qquad \omega = \sqrt{\tau}$$

$$d\tau = 2\omega d\omega$$

$$\eta^0 = \frac{x''-(x''-0.5\Delta x'')}{2\sqrt{\kappa}\omega}$$

$$\eta^1 = \frac{x-(x''+0.5\Delta x'')}{2\sqrt{\kappa}\omega}$$

$$\xi^0 = \frac{y-(y'-0.5\Delta y)}{2\sqrt{\kappa}\omega}$$

$$\xi^1 = \frac{y-(y'+0.5\Delta y)}{2\sqrt{\kappa}\omega}$$

$$m = \frac{x'}{\Delta x} \qquad n = \frac{y}{\Delta y}$$

Giving:

$$T(x,y) = \frac{1}{4\sqrt{\pi\kappa}\rho C_p} \int_0^{\sqrt{t}} e^{-\lambda_{mnkl}} \begin{pmatrix} erf\left(\xi^1_{klmn}\right) \\ -erf\left(\xi^0_{klmn}\right) \end{pmatrix} \begin{pmatrix} erf\left(\eta^1_{klmn} + V_x'\right) \\ -erf\left(\eta^0_{klmn} + V_x'\right) \end{pmatrix} d\omega \qquad (29)$$

The surface temperature distribution can now be computed using eq. (29) and (27). However, the heat portioning still needs to be dealt with. This can be done by stating that the temperature fields needs to be continuous over the contact at all contact spots giving:

$$\sum_{(k,l)\in I_{discr}} T^1{}_{i-k,j-l}\phi_{kl}\mu V p_{kl} = \sum_{(k,l)\in I_{discr}} T^2{}_{i-k,j-l}(1-\phi_{kl})\mu V p_{kl} \qquad i,j \in I_c \tag{30}$$

The inequality described in eq. (30) containing the partition factor $(\phi)$ can be solved either directly or by using the CGM method. In this work the direct method is chosen since this requires less computational effort. This method requires the computation of the complete influence matrix $T_{i-k,\,j-l}$ for both bodies which is very memory inefficient, however no iterative loop is needed as is the case for the CGM method. For more details on the way partitioning is handled the interested reader is referred to [21], section 3.

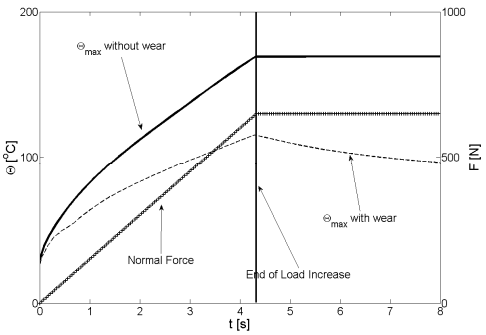


**Figure 5:** Calculated maximum temperature during loading of a "non-failure" contact using two different methods: one including wear ($\Theta_{wear}$) and one without ($\Theta$). Contact sliding at 1.25 m/s carrying a load of 600 N. The local specific wear rate is set at $1.2\text{x}10^{-6}$ mm$^3$/Nm.

The influence of incorporating wear in the contact model on the maximum contact temperature is clear in Figure 5. In this figure the maximum contact temperature is shown for a contact sliding at 1.25 m/s carrying a load of 600 N. The local specific wear rate is set at $1.2\text{x}10^{-6}$ mm$^3$/Nm. The temperature rise for the model including wear is not only lower but also more gradual and even decreases with increasing time when a constant load is applied. This is due to the fact that wear increases the contact area increasing the thermal conductivity of the total contact and thus lowering the maximum contact temperature.

## TRANSITION CRITERION

As discussed in the introduction Blok postulated that the transition from mild wear to severe wear is thermally induced. However, the temperature calculated along the measured transition using Blok's temperature model was not constant, [6, 12]. In [12] the thermal model is expanded to incorporate the flash temperature on asperity level which was not feasible at the time Blok did his work, since no suitable micro contact models where available at that time. In that work [12] it was shown that the transition from mild to adhesive wear can be predicted by a maximum temperature occurring at the asperity level interface using a asperity based contact model. The temperature criterion used is based on the failure of one single asperity, which may be discussed because the assumption made with respect to the asperity contact model, i.e. the asperities are represented as spheres of which the average temperature is calculated using the theory presented in [22] limits the detail of the model greatly. No distinction is made whether failure occurs at a small micro contact or a large micro contact. The influence of the number and size of failing asperities, i.e. the percentage of surface in contact that fails should be taken into account. Therefore, in the current work it is assumed a predefined percentage of the interface transcends the critical temperature at the transition from mild to severe wear.

As discussed before the critical temperature needs to be determined to predict the failure of

the lubricated contact. The procedure for obtaining this is discussed here briefly, for more details the reader is referred to [12]. An experimental method is used based on the theory of Grew and Cameron [25]. They suggested for determining the critical temperature for a boundary lubricated system using for instance a mineral oil a combination with non-reactive materials should be used to prevent chemo-sorbtion.

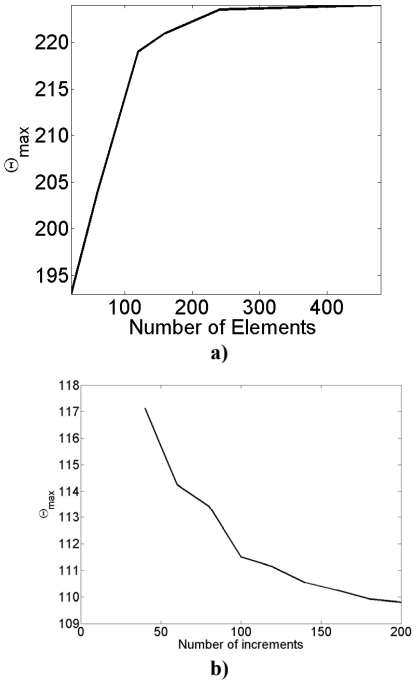


**Figure 6: a)** Maximum contact temperature as a function of the number of elements used**. b)** Maximum temperature as a function of the number of sliding increments used in the model**.**

This statement is based on the assumption that in a contact the temperature is build up from a steady state bulk temperature and a flash temperature. In this situation the flash temperature is of such short duration that the oil (surfactant) is desorbed before it is able to react with the surface preventing chemical reaction layers to form. Therefore, in their study austenitic stainless steel is used which also will be used in this study for determining the critical temperature of the boundary layer. To be able to determine this temperature a test in which as little as possible thermal energy is dissipated is conducted. The procedure consists of a polished stainless steel ball (Ra < 0.05 $\mu m$) with a radius of 10 mm pressed against a disk with a diameter of 40 mm using a constant normal force of 10 N sliding at a velocity of 0.065 m/s. This test is done on a standardized high temperature pin on disk machine. During the test the oil bath temperature is increased until the coefficient of friction "jumps" to a higher value (typically 0.4) as seen in Figure 7.

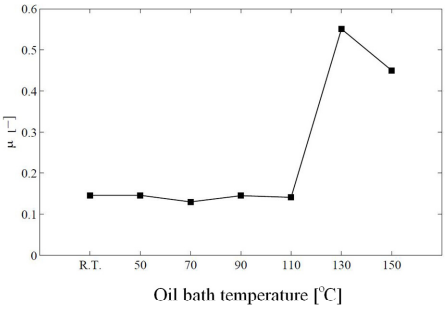


**Figure 7:** Typical friction signal of the test procedure for determining the critical temperature. Result shown is for an austenitic stainless steel ball and disk lubricated with highly refined mineral white oil [12].

Next, a series of experiments is conducted to determine the transition from mild to severe wear. For this a loading sequence needs to be chosen since the way a surface runs in determines greatly the outcome of the transition diagram as is discussed in [26]. For the current work the loading procedure used is one in which new contacting elements are used for every combination of load and sliding velocity. The contact elements consist of a stationary element and a sliding element (as in a normal pin on disk set up). First the sliding element (typically a disk) is speeded up to the preset sliding velocity at which point the stationary part is pressed onto it. This procedure is designed to minimize the effect of wear on the transition diagram. However, as will be shown in the next section even after a very small sliding interval wear already has a large influence on the contact.

To estimate the mild wear taking place before the transition from mild to severe wear occurs also an approximation is made of the contact area, this is done by optical microscopy of the mild worn surface of the test result closest to the transition from mild to severe wear. If the transition takes place at 750 N and 1.25 m/s the contact area is measured of the test result at a load of 750 N and the velocity prior to the transition velocity. This contact area is then used to estimate a value for the specific wear rate, which can be used in the contact calculations. These tests are preformed on a high load pin-on-disk setup designed in a previous study [12]. The main features of the designed pin-on-disk test rig are given in Table 1.

| Property | Range | Precision |
|---|---|---|
| Normal Force | 50-1000 [N] | 0.2% at full load-2N |
| Friction Force | 0-500 [N] | 0.05% at full load-0.025N |
| Sliding Velocity | 0.01-22 [m/s] | 0.05% at full load-0.01 [m/s] |
| Oil Temperature | $20-140\ [^oC]$ | $1\ [^oC]$ |

**Table 1:** Main features of the high load pin-on-disk setup.

Due to the non-infinite stiffness of the test rig the normal force signal will not be instantaneous as discussed before but will rather look like a linear loading sequence as shown in Figure 8. Here a typical loading sequence and additional friction signal are shown for a test resulting in adhesive failure of the contact. For the numerical modeling a linear curve fit is used as input for the normal force as given by the dashed line.

| $\rho$ $[kg/m^3]$ | Kinematic Viscosity $\nu_k[mm^2/s]$ | | Dynamic Viscosity $\eta_0[mPa\,s]$ | |
|---|---|---|---|---|
| $20\,^oC$ | 40 °C | 100 $^oC$ | 40 °C | 100 °C |
| 866 | 32 | 5 | 28 | 4 |

**Table 2:** Properties of the mineral oil used (Shell Ondina 32).

## RESULTS

To validate the theory described in this paper the transition of a cylindrical pin and a disk sliding under boundary lubrication conditions is calculated and determined experimentally. The oil used in this test is highly refined, light duty mineral white oil with the properties as presented in Table 2 This oil is chosen to assure that the main protection against severe wear is provided by a physical adsorbed layer, which has a relatively low critical temperature, see Figure 7.

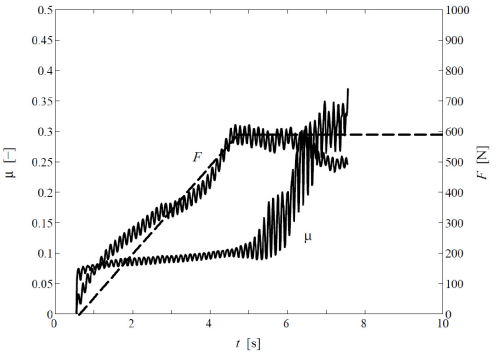


**Figure 8:** Typical friction and force measurement of a contact situation with direct failure. Solid line force measured and dashed line force used in the numerical model

First the experimental results, which were all conducted under room temperature and relative humidity between 40 and 50 percent, will be discussed after which the validation of the model is handled.

The critical temperature ($\Theta_{cr}$) is determined by the procedure described in the previous section. The material properties of the AISI 316 used for both contacting elements are presented in Table 3. Using a low load and sliding velocity it was assumed no frictional heating would occur. However, in practice a small increase of the surface temperature was noted and was calculated to be approximately within 15 degrees Celsius. This together with the result presented in Figure 7 gives an estimation of the critical temperature of 145 degree Celsius.

The next step is determining the transition diagram experimentally. For this purpose a disk with a diameter of 150 mm made of case hardened steel is used in combination with a case hardened cylindrical steel pin with radius 2 mm and length 3.4 mm, resulting in a line contact. The material parameters of the steel are given in Table 3.

| Material | $K\left[\frac{W}{m^o K}\right]$ | $\rho\left[\frac{kg}{m^3}\right]$ | $C_p\left[\frac{J}{kg^o K}\right]$ | $E[GPa]$ | $\nu[-]$ | $H[GPa]$ |
|---|---|---|---|---|---|---|
| AISI 316 | 17 | 7780 | 460 | 210 | 0.3 | 1.1 |
| AISI 52100 | 45 | 7800 | 470 | 210 | 0.3 | 6.6 |

**Table 3:** Material properties

The surface finish of the disk is grinding resulting in a *RA* value of 0.27 micron. The pin is grinded and polished so that its relative roughness can be neglected in comparison with the roughness of the disk, giving a rough-smooth surface contact. The transition is determined for the given system according to the procedure discussed in the previous section. The results of these measurements are given in Table 4. The influence of wear on the contact area is clear when comparing the measured contact width ($2b_{measured}$) with the contact width obtained through elastic perfect plastic calculation ($2b_{roughline}$).

| Transition points | | | | | |
|---|---|---|---|---|---|
| $F[N]$ | 750 | 600 | 400 | 200 | measured |
| $V[m/s]$ | 1.25 | 1.5 | 2.25 | 3.75 | |
| $\mu[-]$ | 0.103 | 0.100 | 0.091 | 0.094 | |
| $2b_{meas}[\mu m]$ | 348 | 364 | 354 | 384 | |
| $2b_{roughline}[\mu m]$ | 186 | 171 | 153 | 129 | Calculated |
| $rel.\ failure[-]$ | 10.9% | 8.7% | 12.1% | 11.7% | |
| $\Theta_{\max}[^0C]$ | 157 | 153 | 162 | 160 | |

**Table 4:** Measured transitions points and accompanying calculated values

From the measurements a system specific wear rate of $1.2 \times 10^{-6}$ $mm^3/Nm$ is obtained which is in the range of the values reported in literature for the system investigated [6-8, 27-29]. Since the wear track length on the disk is approximately 100 times the contact width it is assumed that the wear of the system is governed by the wear of the pin. Using the determined k value the contact pressure in time can be calculated.

For the prediction of the transition diagram only a part of the rough surface in contact is used. This part is chosen such that it gives a good representation of the complete surface in contact.The surface topography is measured by using an interference microscope with a resolution of 0.816 µm x 0.95 µm and a grid size of 480x780 pixels see Figure 9.

From this surface a 480x480 mesh is used which is then filtered to a 240x240 surface with a moving average filter to keep the computational time within limits (e.g. within 1 min for each contact calculation), since every load-sliding cycle is performed incrementally Since the length of the mesh used is only 0.456 mm and the real length of the pin used is 3.4 *mm* the force carried is normalized by the mesh length vs. the real length by using a normal force of:

$$F_{Nmesh} = F_n\left(\frac{L_{mesh}}{L_{contact}}\right) \tag{31}$$

The load rate applied to the cylindrical pin on disk contact is 150 N/s till the preset normal load is reached as is shown in Figure 8. During the test both the normal force and friction force are recorded to detect failure of the contact.If now the sliding and loading process is descritized in steps the increment for every load step can be determined in terms of sliding

increment (*dS*) and load increment (*dF*). Here only the time interval from onset of loading up to the point the maximum load is reached is descritized. Since in these tests during this period the highest contact temperature will occur, see Figure 5. To investigate the sensitivity of the method to the different numerical parameters (e.g. number of elements and number of increment steps) the results of different mesh sizes and increment steps were investigated.

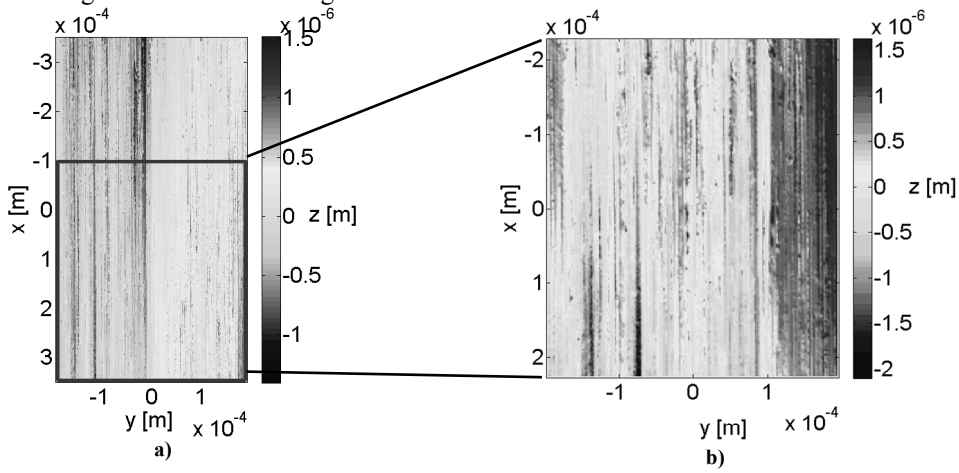


**Figure 9: a)** Measured disk **b)** Filtered part of the surface used for the calculations

Fist the number of elements is varied while keeping the load increment equal to 1. As the results in Figure 6 show increasing the number of elements from 240x240 to 480x480 has little to no effect on the temperature. The number of steps (100) is justified by comparing the results for the lowest sliding velocity and highest load varying the number of increment steps from 20 up to 200. From this analysis it follows that increasing the number of increment steps above 100 does not influence the temperature field. Using the theory discussed before it is now possible to calculate a transition diagram for the pin on disk system as a function of normal force and sliding velocity. The calculated maximum contact temperature and percentage of contact area above the critical temperature for the measured transition points are presented in Table 4 and visualized in Figure 10.From the results it can be concluded that the maximum temperature at the transition from mild to severe wear for the different load is constant and all are within a bandwidth of 10 degrees Celsius, suggesting that using a thermal failure criterion would give good results. However, the maximum contact temperatures are significantly higher (10 percent) than the critical temperature determined experimentally. The percentage of the surface which transcends the critical temperature determined experimentally is constant with an average value of approximately 10 percent.

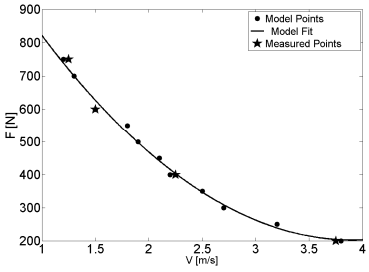


**Figure 10:** Transition diagram calculated and measured.

The results for the temperature and the relative surface failure presented in Table 4 are obtained using the coefficient of friction measured. To give a more predictive nature to the transition diagram during the calculations a coefficient of friction of 0.1 will be used. All measured values are in good agreement with this value. Also the average value of relative

surface failure is used as the failure criterion in the numerical calculations, and doing so gives good agreement between the measurements and calculations, as shown in Figure 10. Here it is seen that the calculated points deviate a little to the smooth line. This is due to the fact that to keep calculation times within realistic values (less than 4 hours) a coarse "grid" is used, e.g. the velocity interval is 0.1 m/s while the load is varied between 750 N and 200 N with an interval of 50 N. To validate if the model can also be applied for systems lubricated with fully formulated oils an attempt was made to determine the critical temperature of a commercial fully formulated CVT oil (oil A) with the properties as given in Table 5. However, it was found that the flash temperature of the base oil was lower than the critical temperature of the lubricant. For this reason it was experimentally impossible to determine the critical temperature of the oil A in the currently study. It was possible to determine the transition points for oil A on the high load setup. The tests where performed at room temperature (25 $^{o}C$) and elevated temperature (100 $^{o}C$). The latter is to show that indeed if the environmental temperature is raised the load carrying capacity is reduced due to the fact that the transition temperature is reached at lower load-speed combinations. The results of these tests are given in Table 6 with the corresponding maximum temperature ($\Theta_{max}$) and critical temperature at which more than 10 percent of the surface in contact has failed ($\Theta_{10\%}$). As can be seen the predicted transition temperature for the different points are within a small interval even for the elevated temperature tests. The results thus suggest that if one transition point is calculated this can be used to determine the critical temperature of the systems at all points.

| Density $\rho_d[kg/m^3]$ | Kinematic Viscosity $\nu_k[mm^2/s]$ | | Dynamic Viscosity $\eta_0[mPas]$ | |
|---|---|---|---|---|
| 25 °C | 40 °C | 100 °C | 40 °C | 100 °C |
| 862 | 40 | 9 | 35 | 7 |

**Table 5:** Properties of commercial oil A.

| Transition Points oil A | | | | | |
|---|---|---|---|---|---|
| | Room Temperature (25 °C) | | Elevated Temperature (100 °C) | | |
| $F[N]$ | 700 | 550 | 700 | 400 | measured |
| $V[m/s]$ | 3.25 | 5.75 | 1.25 | 1.88 | measured |
| $\mu[-]$ | 0.1 | 0.091 | 0.14 | 0.14 | measured |
| $2b_{meas}[\mu m]$ | 332 | 390 | 321 | 333 | measured |
| $\Theta_{10\%}[^{o}C]$ | 210 | 230 | 208 | 200 | Calc |

**Table 6:** Transition Points oil A

## CONCLUSIONS

In this study the temperature is calculated of a smooth cylinder on a rough disk at the transition from mild to severe wear using a contact model that incorporates wear. The results are used in combination with the hypothesis of Blok to predict the transition from mild to severe wear as a function of sliding velocity and normal force for a given system. The numerical models presented are obtained using a contact model and thermal model using adapted DC-FFT and CGM methods to calculate accurate temperature fields for boundary lubricated systems. In the contact model an incremental loading-sliding sequence is incorporated to be able to use Archard's wear model to include mild wear. Including wear gives more realistic results for the contact width and temperature in comparison with non-wear calculations. From the resulting temperature fields it is estimated that if 10 percent of the surface transcends a critical temperature, which is defined by a standardized protocol, the transition from mild to severe wear occurs. This assumption seems to be arbitrary; however this does not affect the efficiency of the model as long as it predicts a constant "failure percentage" for the transition from mild to severe wear. The relative surface failure criterion is preferred over the classical postulate of the maximum temperature originally stated by Blok. From the calculations in combination with experiments it followed that the maximum temperature at the transition points was significantly higher than the critical

temperature found experimentally. The theory presented is experimentally validated and the results from the simulations and experiments are in good agreement with each other.

## REFERENCES


[1] G. Salomon, Failure criteria in thin film lubrication The IRG program, Wear. 36 (1976) 1-6.

[2] S. Dizdar, Wear transition of a lubricated sliding steel contact as a function of surface texture anisotropy and formation of boundary layers, Wear. 237 (2000) 205-210.

[3] J. Sundh, U. Olofsson, Seizure mechanisms of wheel-rail contacts under lubricated conditions using a transient ball-on-disc test method, Tribology International. 41 867-874.

[4] S. Dizdar, S. Andersson, Influence of pre-formed boundary layers on wear transition in sliding lubricated contacts, Wear. 213 (1997) 117-122.

[5] S. Dizdar, S. Andersson, Influence of plastic deformation on seizure initiation in a lubricated sliding contact, Wear. 232 (1999) 151-156.

[6] A. Begelinger, A.W.J. De Gee, Failure of thin film lubrication -- A detailed study of the lubricant film breakdown mechanism, Wear. 77 (1982) 57-63.

[7] A. Begelinger, A.W.J. De Gee, Thin film lubrication of sliding point contacts of AISI 52100 steel, Wear. 28 (1974) 103-114.

[8] A. Begelinger, A.W.J. Gee de, Failure of Thin Film Lubrication The Effect of Running-In on the Load carrying Capacity of Thin-Film Lubricated Concentrated Contacts Journal of Lubrication Technology. 103 (1981) 103-111.

[9] H. Blok, Seizure Delay Method for Determining the Protection Against scuffing Afforded by Extreme Pressure Lubricants SAE Journal. 44 (1939) 193-204.

[10] S.C. Lee, H. Chen, Experimental Validation of Critical Temperature-Pressure Theory of Scuffing, Tribology Transactions. 38 (1995) 738 - 742.

[11] S.C. Lee, H.S. Cheng, Scuffing Theory Modeling and Experimental Correlations, Journal of Tribology. 113 (1991) 327-334.

[12] M. van Drogen, The Transition to adhesive wear of Lubricated Concentrated Contacts, PhD Thesis, University of Twente www.tr.ctw.utwente.nl, 2005 p 105

[13] A.A. Lubrecht, E. Ioannides, A Fast Solution of the Dry Contact Problem and the Associated Sub-Surface Stress Field, Using Multilevel Techniques, Journal of Tribology. 113 (1991) 128-133.

[14] I.A. Polonsky, L.M. Keer, A numerical method for solving rough contact problems based on the multi-level multi-summation and conjugate gradient techniques, Wear. 231 (1999) 206-219.

[15] S. Liu, Q. Wang, A Three-Dimensional Thermomechanical Model of Contact Between Non-Conforming Rough Surfaces, Journal of Tribology. 123 (2001) 17-26.

[16] K.L. Johnson, Contact mechanics. Cambridge university Press, Cambridge, 1985

[17] J.F. Archard, Contact and Rubbing of Flat Surfaces, Journal of Applied Physics. 24 (1953) 981-988.

[18] S. Liu, Q. Wang, G. Liu, A versatile method of discrete convolution and FFT (DC-FFT) for contact analyses, Wear. 243 (2000) 101-111.

[19] R. Bosman, M.B. de Rooij, Transient Thermal Effects and Heat Partition in Sliding Contacts, Journal of Tribology. 132 (2010) 021401.

[20] H. Blok, Theoretical study of Temperature Rise at Surfaces of Actual Contact under Oiliness Conditions, Proc. Inst. of Mechanical Engineers General

Discussion of Lubrication. 2 (1937) 222-235.
[21] R. Bosman, Mild microscopic wear in the boundary lubrication regimeGeringer mikroskopischer Verschleiß geschmierter Kontakte in Grenzflächen, Materialwissenschaft und Werkstofftechnik. 41 (2010) 29-32.
[22] J. Bos, H. Moes, Frictional Heating of Tribological Contacts, Journal of Tribology. 117 (1995) 171-177.
[23] H.S. Carslaw, Conduction of heat in solids. Clarendon press, Oxford, 1959
[24] B. Vick, Theoretical surface temperatures generated from sliding contact of pure metallic elements, Tribology International. 33 (2000) 265-271.
[25] W.J.S. Grew, A. Cameron, Thermodynamics of Boundary Lubrication and Scuffing, Proc. R. Soc. London, Series A327. (1972)
[26] D.J. Schipper, A.W.J. de Gee, Variations in the Procedure of Loading on the Load Carrying Capacity of Thin Film Lubricated Concentrated Contacts, in 4th International Tribolgy Conference, Austrib94. 1994: Australia. p. 105-112.
[27] A. Begelinger, A.W.J. De Gee, Boundary lubrication of sliding concentrated steel contacts, Wear. 22 (1972) 337-357.
[28] A. Begelinger, A.W.J. de Gee, Lubrication of sliding point contacts of AISI 52100 steel -- the influence of curvature, Wear. 36 (1976) 7-11.
[29] A. Begelinger, A.W.J. de Gee . Thin film lubrication of sliding point contacts formulation of a "collapse parameter". in Leeds/Lyon. 1977.

Paper D

Transition from Mild to Severe Wear
Including Running-in Effects,
R. Bosman and D.J. Schipper,
Accepted for publication in Wear
20-12-2010

# Transition from Mild to Severe Wear Including Running-in Effects

R. Bosman and D.J. Schipper
University of Twente, r.bosman@utwente.nl
Drienerlolaan 5
7500 AE Enschede

Accepted for publication in Wear 20/12/2010

*Abstract* - **In the current study a physical based threshold is used to calculate the transition from mild to severe wear. This threshold is formed by using a local coefficient of friction, which is split into two regimes: one low friction regime with a coefficient of friction of in the range of 0.1-0.15 and a high frictional regime in the range of 0.3-0.4. The transition from one to another is determined by the local transition of the predetermined critical contact temperature. To validate the model an experimental transition diagram is determined. The experimental results agree with the simulation for both the location of the transition as for the severity of the adhesive wear.**

*Index Terms* – Wear transition, Boundary lubrication

## INTRODUCTION

In general an engineer will prevent systems from running in the BL regime to avoid high friction and wear of these systems. However due to the increasing demand of smaller machine components transferring the same amount of power running under starved conditions is inevitable. In this type of systems one of the major failure mechanisms is severe adhesive wear. The transition from a mild wear situation (region I/II) to a severe (adhesive) wear (region III/III*) situation, as depicted in the IRG-OECD transition diagram Figure 1, is of great interest to prevent lubricated systems from this transition. In this article a model is discussed to predict this transition, based on a thermal criterion. This criterion was first introduced by Blok in the late thirties of the previous century [1]. It is stated that if the predefined critical contact temperature is exceeded the protective nature of the oil is abolished and severe adhesive wear will be the predominant wear mechanism, normally resulting in failure of the component. However, due to the thermal models available at that time Blok was not capable to define a uniform failure temperature for the different systems. The models Blok used were only capable of taking the macroscopic contact temperature into account, while the highest temperatures are present at the asperity contact level. Using a deterministic thermal model that takes into account the flash temperatures at the asperity level, van Drogen [2] was able to predict the transition from mild to severe wear in a more detailed manner. Since this method was based on an asperity contact model the influence the different asperities have on each other is not taken into account in both mechanical and thermal aspects. The latter is dealt with by Bosman [3] using a multi-scale thermal model, which increased the effectiveness of the model. However, during van Drogen's experiments mild wear was already present during short running time. To compensate for this the macroscopic radius of the geometry was increased to get better coherence between experiments and results.

This was later on adapted by Bosman and Schipper [4] by incorporating a linear variant of the well known linear wear law (Archard's wear law). However, in that study the coefficient of friction was taken as a global value even if local failure occurred. In the current study a different method will be used as will be discussed shortly.

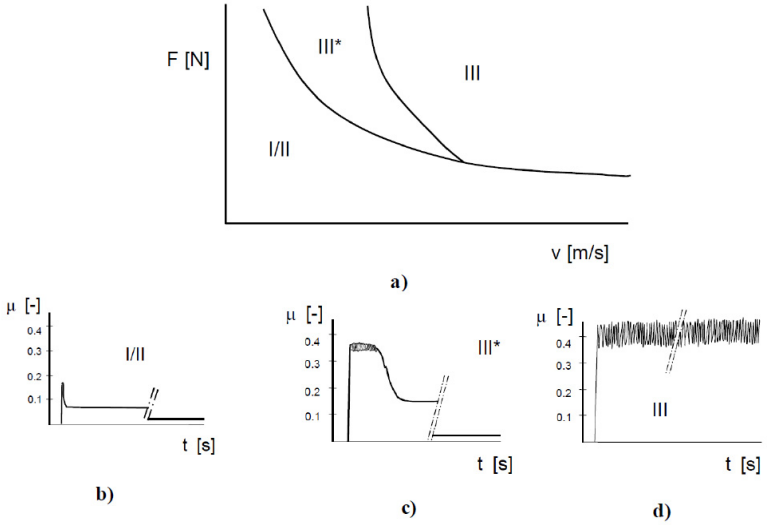


**Figure 1**: a) Transition diagram distinguishing three different regimes based on frictional signals: I/II mild wear regime with a typical coefficient of friction of 0.12 (b). III* Severe wear regime with transition to mild wearing regime (c) and III permanent severe wear regime (d).

## THEORY

In the current study it is assumed that the failure of the oil is a local phenomenon and can be used to represent the local value of the coefficient of friction. Two regimes are distinguished in the contact area: at first a low frictional regime, where the critical temperature is not exceeded and the local coefficient of friction is in the range of 0.1 (a value normally seen in run-in boundary lubricated systems). The second regime is created by the high frictional locations where the critical temperature is transcended and the lubricant fails to protect the surface against metal to metal contact. The friction coefficient is therefore of the order 0.4. The latter value is based on the overall coefficient of friction during macroscopic adhesion [5-10]. This local increase of dissipated energy will create a hot spot. The failing contact spots will increase the temperature not only at their own location but also in the nascent contact spots inducing an "avalanche" effect. There are then two possible scenarios : 1) the "avalanche" is damped after only a minor growth 2) the "avalanche" grows until the complete surface fails and macroscopic adhesion is seen. The greatest advantage of the current method to describe failure is that it is based on a physical hypothesis rather than the previous criterion used in [4], where it is shown that a predefined percentage of the surface is assumed to fail. This percentage is determined by a combined calculation/experimental procedure. While the current failure mechanism only uses the critical temperature as an experimentally determined value, of which the experiment will be discussed shortly. To calculate if the failure of the surface layers grows into a complete failure the next necessary step in the failure modeling is to estimate the severity of the local adhesive wear. Due to material removal the contact geometry changes and the contact area and pressure need to be adapted. This new situation either lowers the contact temperature or

increases the local temperature inducing more adhesion.

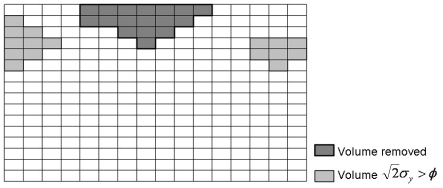


**Figure 2:** Schematic representation of the removal of the wear volume. As shown only the volume reaching the surface and where the stress state is outside the yield surface is removed.

A simplified version of the model suggested by Oila [11-12] for microscopic pitting is used. In these studies it is suggested that the wear particle formation in high carbon steels, which are often used in (tribological) applications, is associated with the plastic volume (light gray areas) formed underneath the surface and volumes that reach the surface (dark gray areas) as shown in Figure 2. The size of the plastic volume can be calculated by stating that this is the volume underneath the surface where the elastic stress state transcends the Von Mises yield criterion:

$$\sqrt{2}\sigma_y = \sqrt{\begin{matrix}(\sigma_{xx}-\sigma_{yy})^2 \\ +(\sigma_{yy}-\sigma_{zz})^2 \\ +(\sigma_{zz}-\sigma_{xx})^2 \\ +6\tau_{xy}^{\ 2}+6\tau_{xz}^{\ 2}+6\tau_{yz}\end{matrix}} \quad , \sqrt{2\sigma_y} \le \phi \qquad (1)$$

In which the $\sigma_{ij}$ are the different stress components, $\sigma_y$ is the yield stress and $\varphi$ the yield surface. This volume is then removed and the contact and thermal calculation is redone. However, due to the local increase of frictional energy the temperature will increase and as discussed before will cause more locations neighboring the initial point of failure to fail, therefore the calculation of the coefficient of friction is repeated again until a stable overall coefficient of friction is reached.

The locations at which the temperature is below the critical temperature however also experience wear in a mild wear manner. Currently this mild wear is modeled using the local interpretation of the well known Archard linear wear law. This method is used by many other authors either in combination with FEM or with BEM, see for example [13-14]:

$$dh(x,y) = kp(x,y)dS \qquad (2)$$

In which $dh$ is the local height loss during incremental sliding step $dS$ with pressure $p$ and specific wear coefficient $k$. Using this method the model predicts an increased conformity between the two contacting bodies lowering contact pressures and temperatures as clearly seen in Figure 3 (dashed line $\Theta_{wear}$), and thus creates a stable mild wear system. By including the increasing conformity of the two bodies the load carrying capacity of the system is increased due to running in under mild conditions as the temperature field is lowered. This effect is also observed in the study done by Schipper et al. [15]. This effect will be discussed more intensively in the results section of this article.

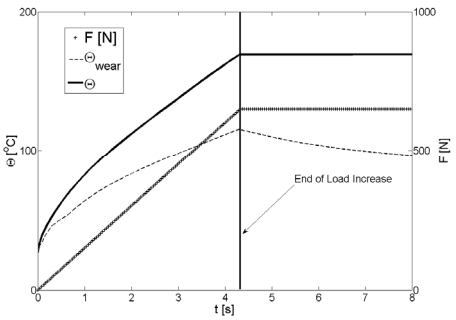


**Figure 3:** Maximum contact temperature as a function of rubbing time for the model incorporating mild wear ($\Theta_{wear}$) and no wear ($\Theta$).

## MODELING

To implement the theory presented above numerical modeling is needed: i.e. temperature and contact models are needed. The contact model which is used in the current model is a single loop CGM model first discussed by Polonsky and Keer [16]. This is build up from the contact inequalities:

$$h_{ij} = h_{ij} + \delta + u_{3ij}^{(1+2)}$$
$$h_{ij} \geq 0 \; then \; p_{ij} \geq 0 \qquad (3)$$
$$h_{ij} < 0 \; then \; p_{ij} = 0$$

In which $h_{ij}$ is the separation between the bodies in contact, $\delta$ is the rigid body motion and $u_{3ij}^{(1+2)}$ is the combined displacement of body 1 and body 2 due to the surface traction and pressure. These inequalities can be solved using the following iterative scheme (see for details [16]):

$$\mathbf{p}_{k+1} = \mathbf{p}_k - \frac{\mathbf{r}_k^T \mathbf{r}_k}{\mathbf{d}_k^T \mathbf{D}_{3i}^n \mathbf{d}_k} \mathbf{d}_k$$
$$\mathbf{r}_{k+1} = \mathbf{r}_k - \frac{\mathbf{r}_k^T \mathbf{r}_k}{\mathbf{d}_k^T \mathbf{D}_{3i}^n d_k} \mathbf{D}_{3i}^n$$
$$\mathbf{d}_{k+1} = -\mathbf{r}_{k+1} + \frac{\mathbf{r}_{k+1}^T \mathbf{r}_{k+1}}{\mathbf{r}_k^T \mathbf{r}_k}$$

In which **p** is the pressure tensor, **r** is the residual tensor, **d** the search direction and $\mathbf{D}_{3i}$ the influence matrix of the surface deflection for either pressure ($i$=3) or traction ($i$=1). In the original version the multi-grid method is used to compute the displacements as a function of the pressure and the directional steps for the CGM. This method is numerically quite complex and recently a more transparent and more accurate numerical method was discussed by Liu [17] which is called D(iscrete)-C(onvolution)-FFT. This method uses zero-padding to avoid the "leakage" which is the greatest source of error in the use of this type of algorithms. However, this "leakage" can also be used for modeling line contact situations by using the part of the solution normally seen as interference to mimic the effect neighboring contact zones will have on the target zone, as is clarified in Figure 4. To validate using this method a line contact using a pin with a radius of 8 *mm* pressed against a flat is modeled both using the Hertzian theory and the proposed model. From Hertz it follows that the maximum pressure is 1.01 *GPa* and the semi contact width is 0.14 *mm*, which is in very good coherence with the results presented in Figure 5 for the compensated case.

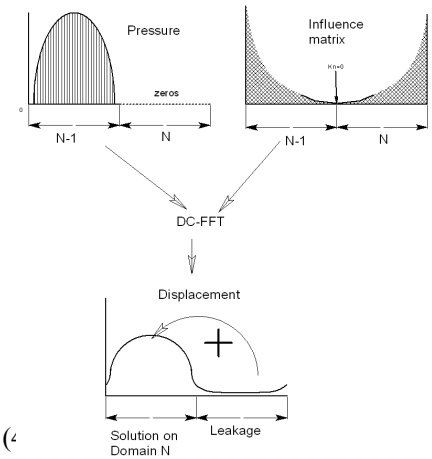


**Figure 4:** DC-FFT algorithm and leakage

As clearly can be seen if no compensation is used a "punch" effect occurs. Since the experimental validation of the current model is a line contact, e.g. cylinder-flat contact, this method will be very useful.

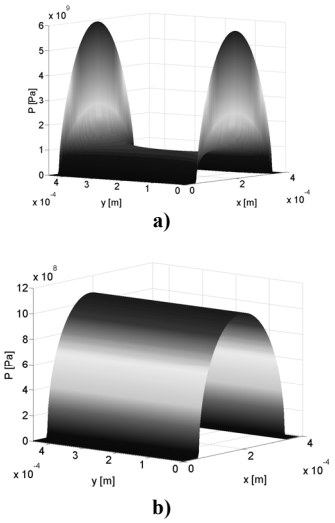


**Figure 5:** Pressure field calculated with **a)** original DC-FFT algorithm **b)** DC-FFT with compensation for line contact.

For the thermal model the model developed by Bosman and de Rooij [18] is used with a small adaption. Instead of using the direct solving method (i.e. matrix inverse method, combined with the moving grid method) discussed in [18] a non linear CGM method is used as discussed in [19]. The non-linear variant is used over the linear CGM since the influence matrix at high speeds is asymmetric for the thermal problem and thus convergence can significantly be speed up using the method proposed. The complete flow chart of the model is shown Figure 6

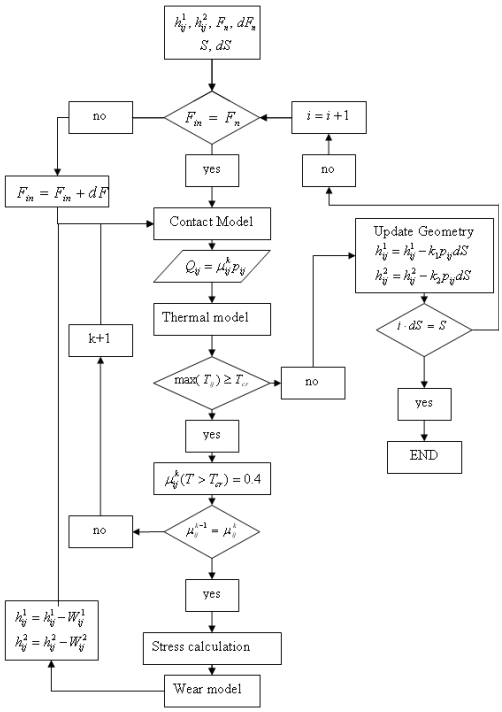


**Figure 6:** Incremental load/displacement loop including the wear and friction model.

## VALIDATION

To experimentally validate the theory discussed above 2 types of experiments are needed: 1) an experiment to get the critical temperature of a given lubricant 2) an experimental determined transition diagram. The first is conducted using a high temperature pin on disk setup. Using a stainless (AISI 316), of which the properties are presented in Table 1, steel ball with a radius of 10 *mm* and a mirror surface finish is pressed against a disk of the same material and surface finish with a diameter of 40 *mm* and 5 *mm* thick. The normal load used is 10 *N* with a low sliding velocity of 0.065 *m/s*. During the sliding of this contact the oil bath temperature is raised and the friction signal is monitored. If a sudden jump in the coefficient of friction is observed the oil bath temperature is a measure for the critical contact temperature for more details on these test the reader is referred to [2].For the validation two different oils were used for the discussed experiment: 1) light duty oil (oil A) 2) a fully formulated transmission oil (oil B). The properties of both of these oils are given in Table 2.

| | $K$ $\left[\frac{W}{m^oK}\right]$ | $\rho$ $\left[\frac{kg}{m^3}\right]$ | $C_p$ $\left[\frac{J}{kg^oK}\right]$ | $E$ $[GPa]$ | $\nu[-]$ | $H$ $[GPa]$ |
|---|---|---|---|---|---|---|
| AISI 316 | 17 | 7780 | 460 | 210 | 0.3 | 1.1 |
| AISI 52100 | 45 | 7800 | 470 | 210 | 0.3 | 6.6 |

**Table 1:** Material properties of the different steels.

During the experiments to determine the critical temperature of oil B it become clear that the flash temperature of the base oil was lower than the critical temperature of the additives. The base oil was already starting to burn while the coefficient of friction stayed at a low level. Therefore first all results will be discussed for the light duty oil. The critical temperature for oil A is relatively low and thus easy to determine. The critical temperature for the current oil was determined at 130 $^oC$ as concluded from Figure 7-a. Here the friction signal vs. the oil bath temperature of a low velocity and load sliding test is presented. During this test the oil bath temperature is increased until the coefficient of friction jumps to a higher value indicating failure of the lubricant. The experimental transition diagram is determined on a model system, composed of a cylinder on disk sliding test rig of which the main properties are given in Table 3. The

samples used in these test are cylindrical pins with a radius of 2 *mm* and a bearing length of 3.4 *mm* originating from a cylinder bearing and are made of AISI 52100, of which the properties are presented in Table 1, and have a CLA roughness of 70 *nm*.

| | Density $\rho_d$ $[kg/m^3]$ | Kinematic Viscosity $\nu_k$ $[mm^2/s]$ | | Dynamic Viscosity $\eta_0$ $[mPa\,s]$ | |
|---|---|---|---|---|---|
| $\Theta[^oC]$ | 25 | 40 | 100 | 40 | 100 |
| Oil A | 862 | 40 | 9 | 35 | 7 |
| Oil B | 866 | 32 | 5 | 28 | 4 |

**Table 2:** Properties of the oil A and oil B.

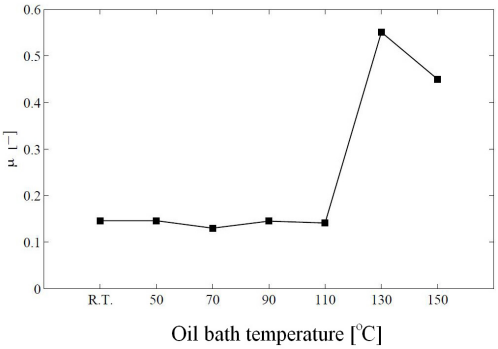


**Figure 7:** Coefficient of friction vs. oil bath temperature for oil A.

The disks used are hard turned AISI 52100 disk with a CLA roughness of 0.27 μm. The measurement protocol is as follows: 1) the disk is speed up to the preset speed. 2) the load is applied by pressing the cylinder onto the disk 3) if the coefficient of friction stays under 0.15 during one minute it is a pas else the test is noted as failed. The transition points which followed from the measurement using the light duty oil are depicted in Table 4 .A typical load vs. coefficient of friction is represented in Figure 12.In the case of the numerical model the roughness of the pin can be neglected due to the order of magnitude difference in CLA roughness between pin and disk. The roughness of the disk is modeled by using an interference microscope measurement of a representative disk. Since a new disk is used for every measurement one measured surface which is a good representation of all disks will be used in the calculations. The measurement is shown in Figure 8. Here both the rough interference measurement is shown and the one actually used during the calculations. In the calculation the element size is increased from 1x1 micron for the original measurement to 2x2 μm for the mesh used in the calculations. This is done using an average moving filter.

| Property | Range | Precision |
|---|---|---|
| Normal Force | 50-1000 [N] | 0.2% at full load-2N |
| Friction Force | 0-500 [N] | 0.05% at full load-0.025N |
| Sliding Velocity | 0.01-22 [m/s] | 0.05% at full load-0.01 [m/s] |
| Oil Temperature | $20-140\ [^oC]$ | $1\ [^oC]$ |

**Table 3:** Main features of the test rig used to determine the transition from mild to severe wear experimentally.

The effect of this simplification can be neglected as shown in Figure 9. Here it is also shown that using 150 increment steps to simulate the sliding motion and load application gives accurate results. Another conclusion which can be drawn from the experiments was that the adhesive wear was mainly build up from transfer of pin material to the disk as shown in Figure 11.

| Transition points | | | | |
|---|---|---|---|---|
| $F[N]$ | 750 | 600 | 400 | 200 |
| $V[m/s]$ | 1.25 | 1.5 | 2.25 | 3.75 |
| $\mu[-]$ | 0.103 | 0.100 | 0.091 | 0.094 |
| $V_{calc}[m/s]$ | 1.1 | 1.5 | 2.2 | 3.8 |

**Table 4:** Transition points for Oil A. The coefficient of friction is the measured friction during the measurement closest to the transition point (e.g. if the transition point was 750 N at 1.25 *m/s* the reported valued of μ is the one for a measurement at for example 750 N and 1 *m/s*).

This is probably mainly due to the higher roughness of the disk. In the modeling this

implies that the volume will only be removed from the pin rather than from the disk, as will be simulated. The transition velocity for the loads used in the experiments to determine the transition points are given in Table 4. As can be concluded from this table a good coherence between the model and experiments is seen. In Figure 10 a typical calculation result of a failed and of a mild wearing system are shown. Not only does the point of transition correspond very well, also the severity of the wear volume is approximately the same as the one shown in Figure 11 suggesting the model can not only be used to determine the point of transition but also the severity of the adhesive wear. Finally in Figure 13 are the results of Table 4 as well as some extra calculated model points for the normal loads of 300, 500 and 700 *N* respectively. The experimental results and calculations agree very well.

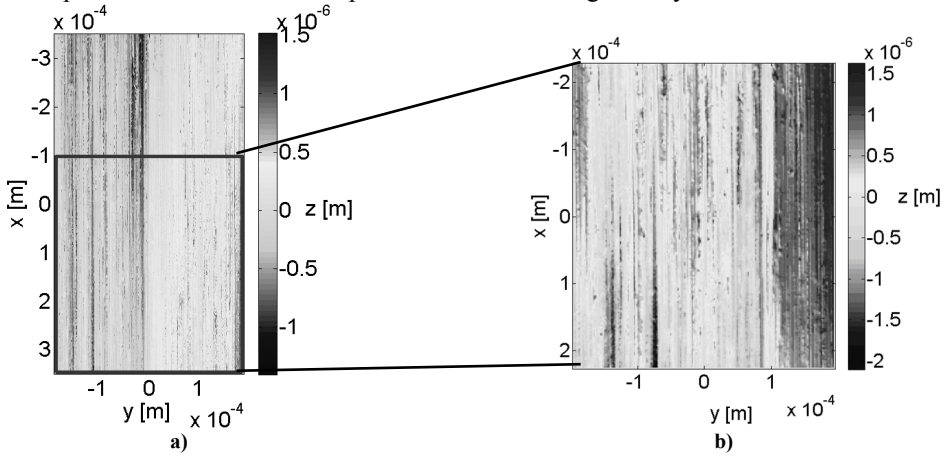


**Figure 8: a)** Measured disk **b)** Filtered part of the surface used for the calculations

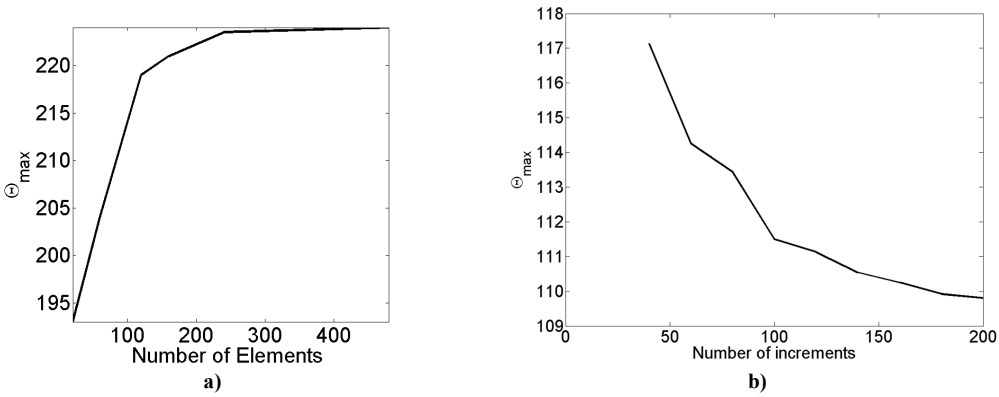


**Figure 9: a)** Maximum contact temperature as a function of the number of elements used. **b)** Maximum temperature as a function of the number of sliding increments used in the model**.**

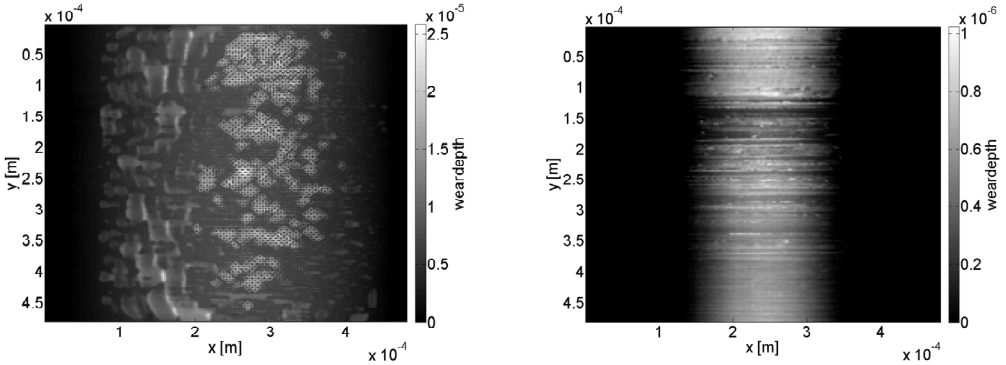


**a)** **b)**

**Figure 10**: Resulting wear volume a) severe wear occurred during the simulation normal force 750 *N* sliding velocity 1.1 *m/s* b) Only mild wear occurred during the simulation, normal force 750 *N* and sliding velocity 1.0 *m/s*.

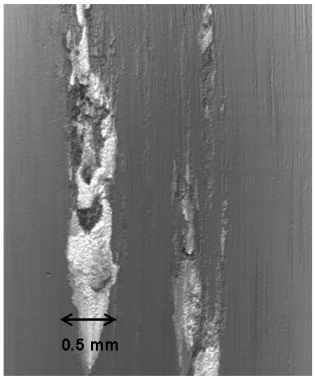


**Figure 11:** Typical interferometry measurement observed after adhesive failure on the disk. (height scale 0-40 µm)

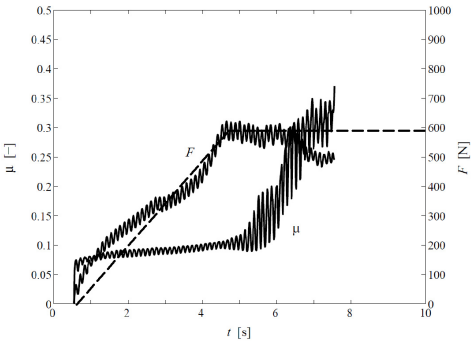


**Figure 12:** Typical friction and force measurement of a contact situation with direct failure. Solid line force measured and dashed line force used in the numerical model, van Drogen [2]

## CONCLUSION

In the current study a new method in calculating the transition from mild to severe wear is presented, which is based on the physical phenomenon of local failure of the oil. The failure is assumed to be caused by thermally overloading of the protective layers adsorbed onto the surface of the system. If locally the critical temperature is exceeded the coefficient of friction is raised, causing more energy to be dissipated, this either causes local failure or complete failure of the contact. Using this method a transition diagram is calculated and the results agree very well with the IRG experimental results.

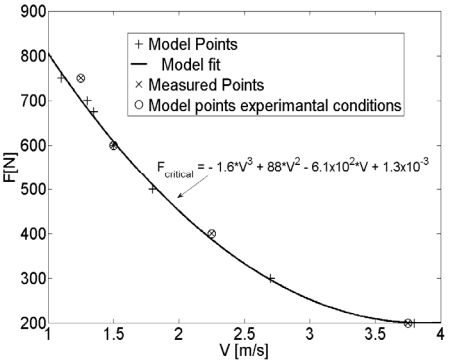


**Figure 13:** Transition diagram calculated using the presented theory, for the model system.

## REFERENCES


[1]H. Blok, Seizure Delay Method for Determining the Protection Against scuffing Afforded by Extreme Pressure Lubricants SAE Journal. 44 (1939) 193-204.

[2] M.van Drogen, The Transition to adhesive wear of Lubricated Concentrated Contacts, PhD Thesis, University of Twente www.tr.ctw.utwente.nl, 2005 p 105

[3] R. Bosman, Mild microscopic wear in the boundary lubrication regimeGeringer mikroskopischer Verschleiß geschmierter Kontakte in Grenzflächen, Materialwissenschaft und Werkstofftechnik. 41 (2010) 29-32.

[4] R. Bosman, D.J. Schipper, On the transition from mild to severe wear of lubricated, concentrated contacts: The IRG (OECD) transition diagram, Wear. In Press, Corrected Proof

[5] A. Begelinger, A.W.J. De Gee, Boundary lubrication of sliding concentrated steel contacts, Wear. 22 (1972) 337-357.

[6] A. Begelinger, A.W.J. De Gee, Thin film lubrication of sliding point contacts of AISI 52100 steel, Wear. 28 (1974) 103-114.

[7] A. Begelinger, A.W.J. De Gee, Lubrication of sliding point contacts of AISI 52100 steel -- the influence of curvature, Wear. 36 (1976) 7-11.

[8] A. Begelinger, A.W.J. De Gee, Failure of thin film lubrication -- A detailed study of the lubricant film breakdown mechanism, Wear. 77 (1982) 57-63.

[9] A. Begelinger, A.W.J. Gee de. Thin film lubrication of sliding point contacts formulation of a "collapse parameter". in Leeds/Lyon. 1977.

[10] A. Begelinger, A.W.J. Gee de, Failure of Thin Film Lubrication The Effect of Running-In on the Load carrying Capacity of Thin-Film Lubricated Concentrated Contacts Journal of Lubrication Technology. 103 (1981) 103-111.

[11] A. Oila, S. Bull, Phase transformations associated with micropitting in rolling/sliding contacts, Journal of Materials Science. 40 (2005) 4767-4774.

[12] A. Oila, S.J. Bull, Assessment of the factors influencing micropitting in rolling/sliding contacts, Wear. 258 (2005) 1510-1524.

[13] P. Põdra, S. Andersson, Simulating sliding wear with finite element method, Tribology International. 32 (1999) 71-81.

[14] G.K. Sfantos, M.H. Aliabadi, Wear simulation using an incremental sliding Boundary Element Method, Wear. 260 (2006) 1119-1128.

[15] D.J. Schipper, Steenhoven R.C, Gee de A.W.J. , Variations in the Procedure of Loading on the Load Carrying Capacity of Thin Film Lubricated Concentrated Contacts, in 4th International Tribolgy Conference, Austrib94. 1994: Australia. p. 105-112.

[16] I.A. Polonsky, L.M. Keer, A numerical method for solving rough contact problems based on the multi-level multi-summation and conjugate gradient techniques, Wear. 231 (1999) 206-219.

[17] S. Liu, Q. Wang, G. Liu, A versatile method of discrete convolution and FFT (DC-FFT) for contact analyses, Wear. 243 (2000) 101-111.

[18] R. Bosman, M.B.de Rooij, Transient Thermal Effects and Heat Partition in Sliding Contacts, Journal of Tribology. 132 (2010) 021401.

[19] W. Press, Numerical Recipes in C++: The Art of Scientific Computing. Cambridge University Press, 2002

Paper E

Running-in of Metallic Surfaces in the Boundary Lubrication Regime,
R. Bosman, J. Hol and D.J. Schipper,
Resubmitted to Wear in revised form
31-12-2010

# Running in of Metallic Surfaces in the Boundary Lubrication Regime

R. Bosman, J. Hol* and D.J. Schipper

University of Twente, r.bosman@utwente.nl
Drienerlolaan 5
7500 AE Enschede

* Materials innovation institute (M2i),
P.O. box 5008,
2600 GA Delft, the Netherlands

Resubmitted in revised form Wear 28/12/2010

*Abstract* - **During the running-in of surfaces a change in roughness takes place. The presented model predicts this change for concentrated contacts using an elasto-plastic contact model based on a semi-analytical-method recently developed. Combining this method with a local coefficient of friction, which is determined using a mechanical threshold on the protective nature of the lubricant, and a strain related failure to model the smoothening of surfaces protected by a lubricant, the surface topography can be calculated. Multiple examples using concentrated contacts are simulated using real engineering surfaces and realistic values for the properties of the chemical reaction layer as well as the Nano Crystalline layer present at and underneath the surface. The results obtained are realistic, indicating the usefulness of the developed method**

*Index Terms* – Running-in, Sliding wear, Boundary lubrication.

## INTRODUCTION

During the lifetime of components different stages of wear may occur such as: running-in, steady state wear. The first stage is the most dominant one determining the steady state wear rate of components in contact while lubricated with an additive containing lubricant. Some authors even suggest that the largest amount of material loss is present during running-in [1]. In the running-in stage the surface roughness changes due to plastic deformation of the surface asperities and local removal of material [2]. Through this process a system or process roughness is usually formed which will be maintained during the lifetime of the component if the operational conditions stay constant. However, if the system is overloaded in the running-in stage severe wear will take place and the system will not reach a steady state situation, e.g. the system will remain in a situation where only severe wear occurs without reaching a steady state mild wear situation. Already during this first stage of wear the protection provided by the lubricant plays a crucial role. In this paper the model first discussed by Bosman and Schipper in [3] will be used to model the removal of base material. Here the assumption is made that for a brittle material like high strength carbonized metals, often used in tribological applications a criterion based on critical strain can be used. The criterion contains a twofold of conditions: first a critical

strain needs to be transcended and secondly this volume needs to reach the surface as is depicted in Figure 1. To determine the location and magnitude of the plastic core two models are needed: an elasto-plastic contact solver and secondly a friction model capable of determining the local coefficient of friction; starting with a brief discussion on the contact solver used.

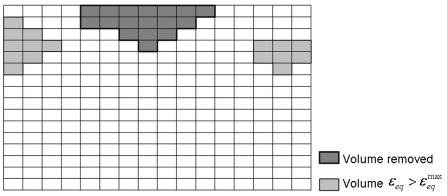


**Figure 1:** Graphical representation of the suggested wear criterion (dark gray is the volume removed, light gray is the volume transcending the maximum equivalent plastic strain) [3].

## CONTACT MODEL

The contact model used is based on the work first presented by Jacq et al. [4] and later on adapted by Nelias [5] to include sliding contacts. The complete model will not be discussed here and only a brief summary is given and the interested reader is referred to the dedicated literature for more details. In the current study the main theories which remain unchanged compared to the original code are summarized and briefly explained, while some parts which are altered are discussed in more detail. Starting with the reciprocal theory applied to a semi-infinite volume with boundary $\Gamma$ and volume $\Omega$. For this body different states are defined: an initial state with internal strains $(u, \varepsilon, \sigma, f_i)$ and a state for the time undefined: $(u_i^*, \varepsilon^*, \sigma^*, f_i^*)$. Using the reciprocal theory and the assumption that the second state is the one in which the surface is loaded by a unit pressure $p_i^*$ at the location $A$ gives:

$$u_3(A) = \underbrace{\int_{\Gamma_c} p_i\, u_{3i}^*(M,A)\, d\Gamma}_{u^e(A)} + \underbrace{\int_{\Omega} \varepsilon_{ij}^0(M)\, C_{ijkl}\, \varepsilon_{ij}^*(M,A)\, d\Omega}_{u^{pl}(A)} \quad (1)$$

Here $u^e(A)$ is the elastic surface displacement and by stating $\varepsilon_{ij}^0 = \varepsilon_{ij}^{pl}$, $U^{pl}(A)$ becomes the surface displacement due to the plastic strains inside volume Ω. The surface displacement of the body can now be expressed as a function of the contact pressure and the plastic strain. To calculate the plastic strains the subsurface stresses are needed. Using the reciprocal theory again and define a state $(u^{**}, \varepsilon^{**}, \sigma^{**}, f_k^{**})$, which can be seen as the state when a unit force is applied inside volume Ω at point B. This then results in:

$$\begin{aligned} u_k(B) = & \underbrace{\int_{\Gamma} u_{ki}^{**}(M,B)\, p_i(M)\, d\Gamma}_{u_k^e(B)} \\ & + \underbrace{\int_{\Omega} \varepsilon_{ij}^0(M)\, C_{ijkl}\, \varepsilon_{ij}^{**}(M,B)\, d\Omega}_{u_k^{pl}(B)} \end{aligned} \quad (2)$$

Here stating $\varepsilon_{ij}^0 = \varepsilon_{ij}^{pl}$ and only integrating over the volume where the plastic strains are not zero $\Omega = \Omega_{pl}$ the displacement field is written as a function of the elastic and the plastic strains. Using Hook's law:

$$\sigma_{ij}^{tot}(B) = C_{ijkl}\left[\begin{array}{l} \left(\frac{1}{2}\left(u_{k,l}^e(B) + u_{l,k}^e(B)\right)\right) \\ +\left(\frac{1}{2}\left(u_{k,l}^{pl} + u_{k,l}^{pl}\right) - \varepsilon_{kl}^{pl}\right) \end{array}\right] \quad (3)$$

Rewriting (3):

$$\sigma_{ij}^{tot}(B) = \sigma_{ij}^e(B) + \sigma_{ij}^{res}(B) \quad (4)$$

If now the unit pressure and unit force are replaced by complete pressure and force fields, a solution can be found for a complete rough contact situation, since the complete non linear response of the system can be calculated. This is done by discretization of the surface $\Gamma$ into surface elements $N_s$ of size $\Delta x \times \Delta y$ and the volume into elements $N_v$ of

size $\Delta x \times \Delta y \times \Delta z$. On the surface elements uniform pressures are acting and in the volume elements the strains inside each volume element are assumed to be uniform. Starting with the elastic surface displacement which then becomes the sum of the individual pressure patches:

$$u_3^{elas}(x,y) = \sum_{N=1}^{N=N_s} D_{3i}^{n}(x - x'_n, y - y'_n)\, p_i^n(x'_n, y'_n) \qquad (5)$$

Here $x_n$, $y_n$ are the coordinates of observation and $x'_n$, $y'_n$ are the coordinates of the center of the excitation patch $n$, the expressions of $D_{3i}^{n}$ are given in the appendix, where $i$ can have the value of 3 for the displacement due to normal force and 1 for the displacement due to traction. Next is the displacement due to the plastic strains $\varepsilon^{pl}_{ij}$. Using the assumption of uniform strains within the volume elements:

$$u_3^{pl}(x,y) = \sum_{n=1}^{N=N_v} D_{3i}^{pl}(x - x'_n, y - y'_n, z'_n)\, \varepsilon_{ij}^{p}(x'_n, y'_n, z'_n) \qquad (6)$$

Here $(x, y)$ is the location of the point of observation on the surface and $(x'_n, y'_n, z'_n)$ are the coordinates of the excitation volume $n$. The expressions for $D_{3i}^{pl}$ are given in the appendix. The stresses for the total system, given in eq. (4), can also be expressed in a summation form:

$$\sigma_{ij}^{tot}(x,y,z) = \sum_{n=1}^{N=N_s} S_{ijk}^{elas}(x - x'_n, y - y'_n, z - z'_n)\, p_k + \sum_{n=1}^{N=Nv} S_{ij}^{pl}((x - x'_n, y - y'_n, z - z'_n, z + z'_n), \varepsilon_{ij}^{pl}(x'_n, y'_n, z'_n)) \qquad (7)$$

Here the expressions for $S_{ij}^{elas}$ and $S_{ij}^{pl}$ for the different parts are given in the appendix, where the expression originally used in the code discussed in [4] and [5] are replaced by more efficient equations originating from [6]. Now the surface displacement and the stress inside the bulk material of an elastic half space with plastic strains inside the volume are described by equations can be used to model the contact of the elasto-plastic contact between two half spaces by using the model depicted in Figure 2.

One part will be discussed here in detail with respect to the plastic loop and the validation of the code. In the original code the Prandtl Reuss method is used to compute the plastic strains this is later on adapted by Nelias [5] to a return mapping algorithm to increase the efficiency of the code. The current model also uses a return mapping algorithm however in the current version the plastic loop is changed to a stress related one rather than strain. As can be seen in reference [4] the plasticity loop is stopped if convergence of the plastic strain is reached. However, the basis of the plasticity theory states that for a system to stay in the elastic regime the elastic stresses should be on the yield surface:

$$\phi \le 0 \qquad (8)$$

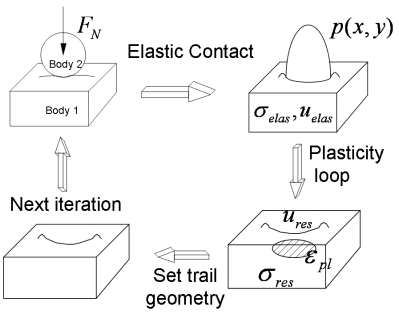


**Figure 2:** The iterative process of solving the elasto-plastic contact.

This is however not per definition satisfied if the convergence criterion used is based on the plastic strain inside the body. In the current model the plasticity loop used is depicted in Figure 3. This model is based on an elastic predictor plastic corrector scheme combined with the associated Drucker flow rule. This method is chosen over a plastic predictor elastic corrector scheme, since the strains in hard and brittle metals typically used in tribological systems are limited to a few percent.

Normally the return mapping uses strain as an input, which is then rewritten to a stress through Hook's law. However, since the elastic stress field for the elastic contact conditions can be calculated through the expression of $S^{elas}_{ij3}$ and $S^{elas}_{ij1}$ given in the appendix and the following expression:

$$\sigma_{ij}^{elas_{cont}} = pS_{ij3}^{elas_{cont}} + \mu pS_{ij1}^{elas_{cont}} \quad (9)$$

The elastic stress coming out of the elastic contact is used as the input stress state for the return mapping which is defined as:

$$\sigma_{ij_{n=0}}^{in} = \sigma_{ij}^{elas_{return}} = \sigma_{ij}^{elas_{cont}} - \sigma_{ij}^{cor} \quad (10)$$

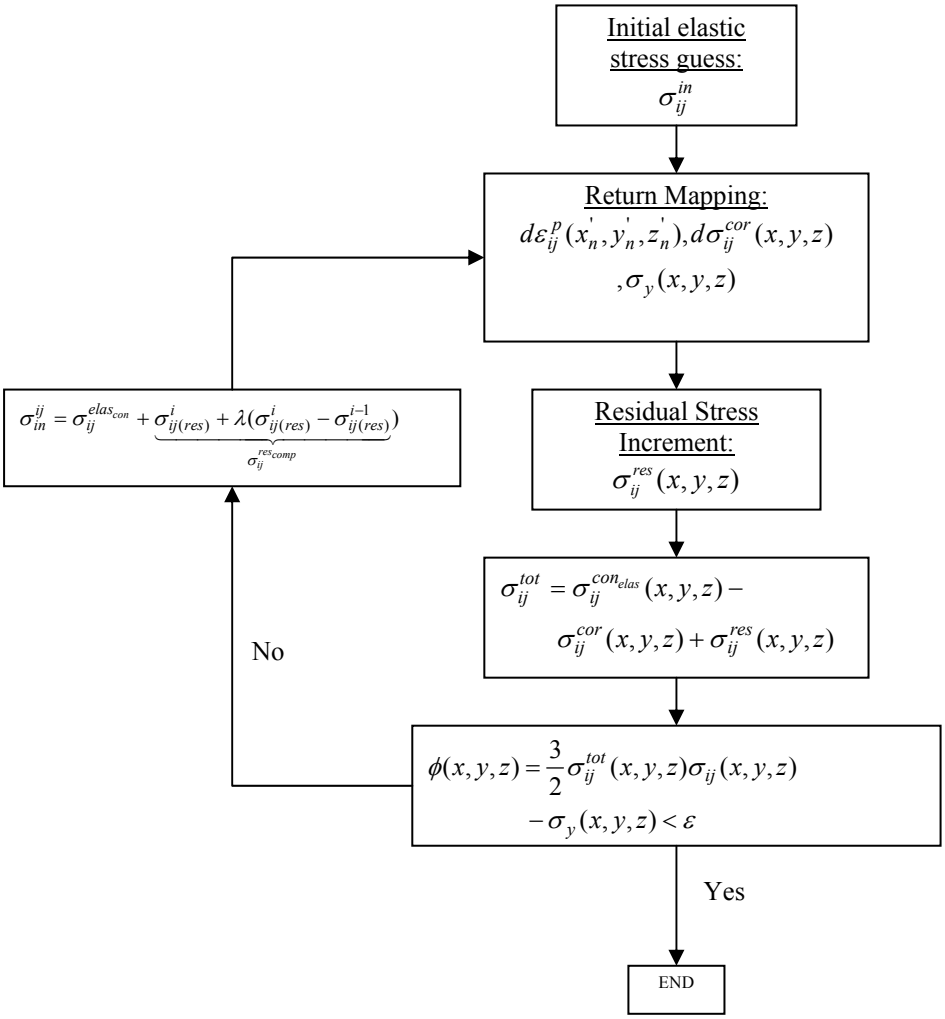


**Figure 3:** New "plasticity loop" based on the stress relaxation rather than on the relaxation of the plastic strain.

The stress coming out of the return algorithm will be on the yield surface. However, as the plastic strain will cause residual stresses the real stress state will be, see also eq (7):

$$\sigma_{ij}^{total} = \sigma_{ij}^{elas_{cont}} - \sigma_{ij}^{cor} + \sigma_{ij}^{res}(\varepsilon_{ij}^{p}) \quad (11)$$

This stress state will not be on the yield surface since the return mapping algorithm already

corrected the elastic stress state through the plastic corrector to be on the yield surface. For this reason the elastic guess going into the return mapping needs to be compensated in such a way that the stress the plastic corrector is adjusted so the complete stress state is on the yield surface again:

$$\sigma_{ij_{n+1}}^{in} = \sigma_{ij}^{elas_{con}} + \sigma_{ij}^{res_{comp}} \tag{12}$$

Here an iterative process, shown in Figure 3, is used to find the correct stress compensation such that the complete stress state is on the yield surface. To speed up the calculation of the plastic strain even more the compensation for the residual stress used in the first guess can be exchanged for the compensation of the previous iteration of the complete loop *(N-1)* in Figure 4. This method resembles the method used in [7] however the plasticity loop suggested in that study is not unconditionally stable and secondly only in their study only linear hardening laws are used to validate the model. To validate the new plasticity loop numerical analyses of a 2D asperity, done in the in-house FEM package DIEKA [8], are compared to a full 3D contact analysis using the code presented here. For the non linear hardening a Swift hardening law is used for the material behavior:

$$\sigma_{yield}(\varepsilon_{pl_{eq}}) = B(C + \varepsilon_{pl_{eq}} \cdot \alpha)^n \tag{13}$$

The parameters used are $B$ = 1280 *MPa*, $C$ = 4, $n$ = 0.095 and $\alpha$ is set to $10^6$, representing AISI 52100 steel. For the geometry in the simulation a 0.5 *mm* asperity is pressed against a rigid flat surface under a load ranging from 0.1 up to 600 times the critical load defined as [9]:

$$F_{critical} = (\pi\sigma_{yield})^3 \left(\frac{3R_{eq}}{E_{eq}}\right)^2 \tag{14}$$

Here $\sigma_{yield}$ is defined by eq. (13)**.** The results of this simulation are shown in Figure 5. From this figure it can be concluded that the SAM results concur very well with the FEM results. However, since the SAM model is based on small plastic deformations, e.g. the displacement field is not guaranteed to be continuous. Therefore there is a limitation to the use of the model regarding the maximum equivalent plastic strain allowed, as is shown in Figure 6. In this figure it becomes clear that up to an equivalent plastic strain of approximately 10 percent the SAM gives reliable values, after which the model starts diverging significantly from the FEM results.

## WEAR MODEL

As discussed in the introduction the contact regions within the model can be split up into two parts: regions where the oil protect the surface and unprotected areas. Both regimes have a different coefficient of friction with values in the range of 0.1 and 0.4 respectively. These values originate from measurements done in both the mild wear regime and the sever wear regime [10-11]. The transition from the one to the other is seen as a stepwise phenomenon, if the failure criterion of the layer is transcended the coefficient “jumps” to the higher value. For the mild wear situation it is first assumed that negligible wear will occur at these locations since the shearing will be located in the boundary layers formed on the steel surface and thus no bulk material will directly be removed. This corresponds well with real systems running under mild wear conditions since particles generated by this type of systems are mainly built up from chemical products which originated from the oil [12] and [13]. The severe, local wear is based on the brittle wear behavior of high strength carbon steels and is associated with a high coefficient of friction. The philosophy underlying the model presented here is introduced by Nelias in [14], using an overall coefficient of friction of 0.4. The wear model is found upon a recent study of Oila [15], who found that material removal was related to micro-cracks underneath the surface and was implemented in the current formulation by Bosman and Schipper [3], incorporating a local

coefficient of friction. To predict the formation of these micro-cracks a crack criterion is needed, which is currently set to a maximum equivalent plastic strain defined as:

$$\varepsilon_{eq}^{p} = \sqrt{\frac{2}{3}\varepsilon_{ij}^{p}\varepsilon_{ij}^{p}} \qquad (15)$$

It is then assumed that the crack runs along the line of the plastic volume both reaching the surface and transcending the critical strain value, creating a wear volume. In the current simulations it is assumed that the wear volume is removed in only one cycle directly after it is formed. Incorporating this threshold directly in the system creates very large wear rates since sharp edges will be created on the sides of the worn volume. To deal with this problem the volume removed is smoothened using a Savitzky–Golay smoothening filter [16]. This however introduces numerical artifacts, which can be used to fit the model for less and more ductile materials. This is left out in the discussion in [14] as will be done currently for brevity, but is discussed in detail in [17] and the reader is thus referred to this work for more detail on the smoothening. The complete wear model is shown schematically in Figure 4.

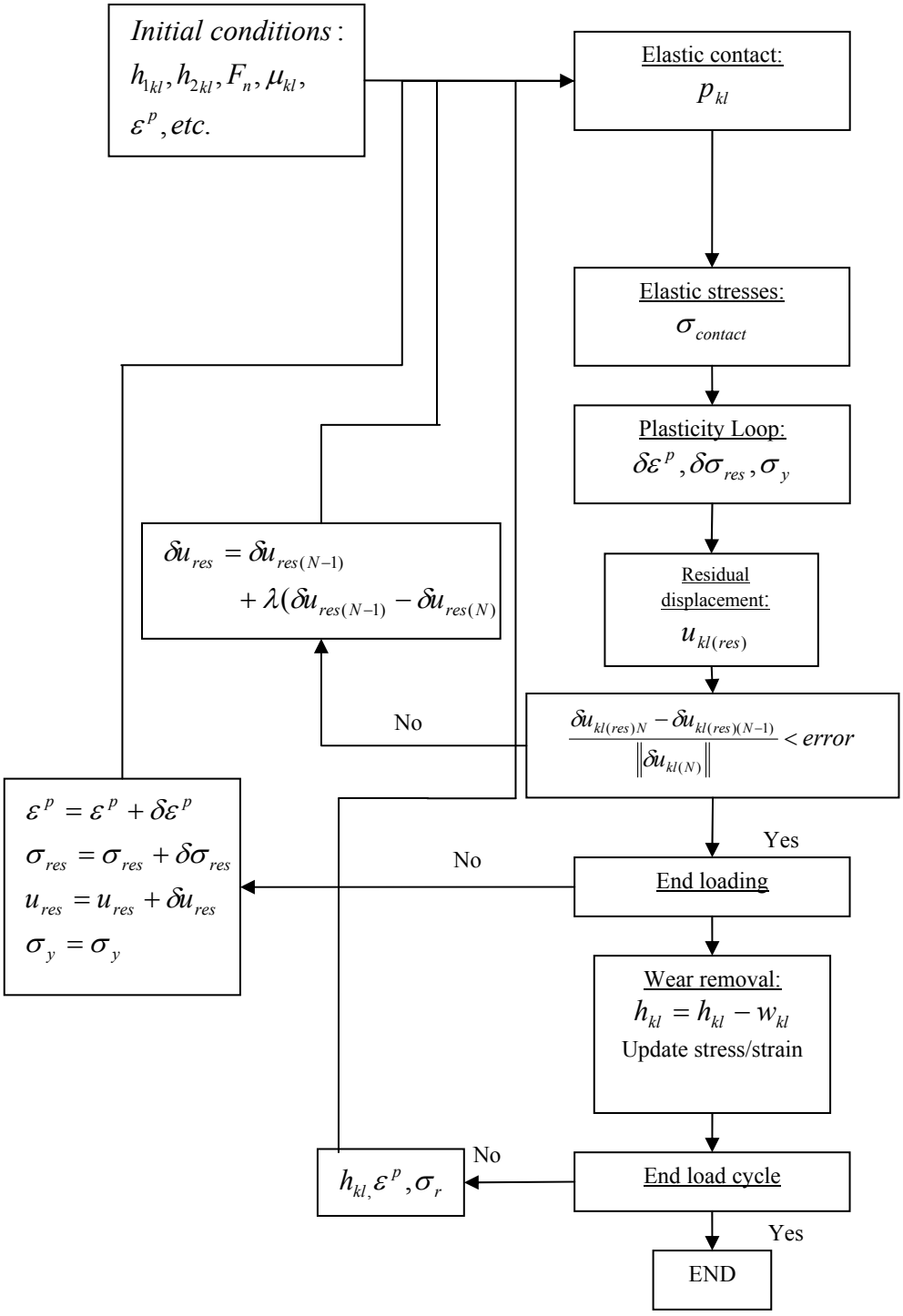


**Figure 4**: Flowchart of wear model

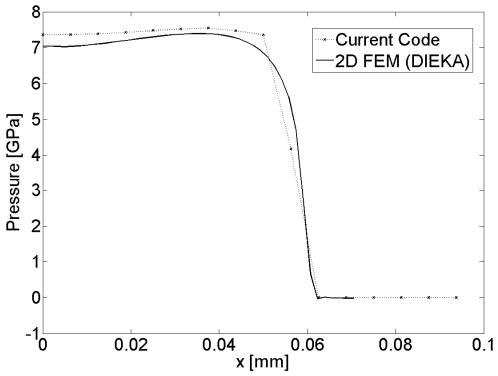


**a)**


**b)**

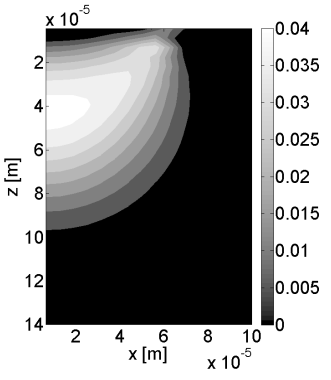


**c)**

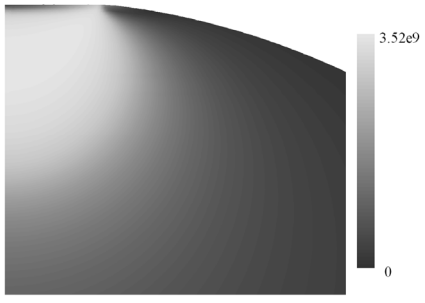


**d)**

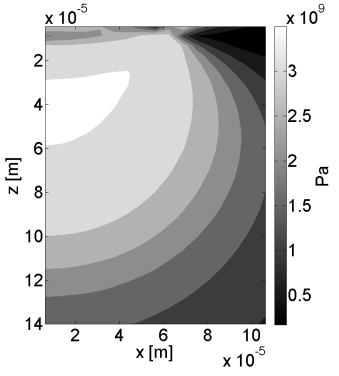


**e)**

**Figure 5 : a)** Normal pressure resulting from the calculation with the FEM package and SAM package at 100 times the critical load**. b)** Equivalent strain calculated using FEM. **c)** Equivalent strain calculated using SAM. **d)** Von Mises stress underneath the surface using FEM and **e)** SAM.

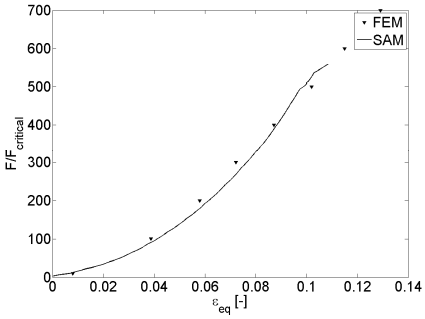


**Figure 6:** Equivalent plastic strain vs. normal load normalized with the critical load.

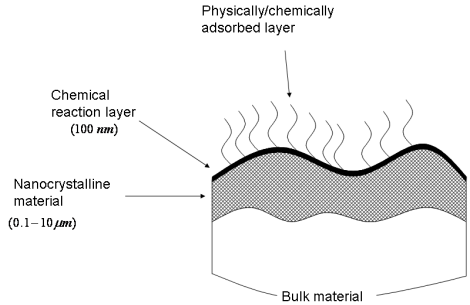


**Figure 7:** Layer built up for a fully formulated oil.

The next step is to formulate the criterion for failure of the boundary layers. First a representation of the boundary layer is given in Figure 7. Here the adsorbed layer is equivalent to a high viscous layer as reported in different studies and does not play a role in the anti-wear properties at severe conditions [18-19] and [20], which are typical for running-in situations. To model the boundary layer an assumption has to be made regarding the material model to be used for this layer, e.g. what kind of behavior will this layer have. Based on the work presented in [19] it is suggested that the chemical reacted boundary layers acts as a solid rather than a viscous fluid, this conclusion followed out of high frequency vibration viscosity measurements.

In this study the boundary layer is thus modeled as an elastic-plastic solid, where the transition from elastic to plastic is defined by the von Mises yield criterion as is used for the bulk material. The reference values in the current study are based on the ones presented in [21-37] and are set to an elasticity modulus of 80 GPa and a hardness of 2 GPa. Combining the properties of the layer with the limited thickness of the layer the effect this layer will have on the subsurface stress field and pressure in normal direction is very limited as is shown in [3] and the error made is less than 5%. A second conclusion which can be made from the analysis presented in this study is that the contact patches can be seen as individual contact patches and do not influence each other. For this reason it is sufficient to take the layer into account through the altering of the coefficient of friction. The model described before can visually be expressed as show in Figure 8, where the bulk material is protected by "wear-elements" which have in fact solely the purpose to indicate the coefficient of friction locally present.

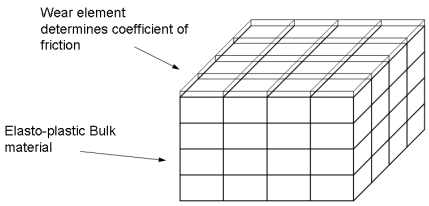


**Figure 8:** Visualization of the wear model as proposed.

The pressure criterion is based on the idea first presented in [38], where it is suggested the growth of tribo-chemical film protecting the surface must be larger than the removal rate of the lubricant to protect the surface against severe wear. Here it is assumed that the growth is diffusion based process and can be expressed as:

$$h_{growth}(t) = K_0\sqrt{t} \tag{16}$$

The different values of $K_0$ are given in Table 1. The amount of chemical layer removal is indicated by the plastic strain in the direction normal to the surface ( $\varepsilon_{zz}$ ). Due to its limited

thickness it is safe to assume all stresses do not vary through the thickness ( $\partial\sigma_{ij}/\partial z = 0$ ).

| Oil bath temperature $T\,[^{o}C]$ | Eff. Diffusion Coefficient $K_0\,[nm\,s^{-1/2}]$ |
|---|---|
| 50 | 2.451 |
| 100 | 3.644 |
| 150 | 4.620 |
| 200 | 4.916 |

**Table 1:** Effective diffusion coefficients measured in [38] at different oil bath temperatures at nominal contact pressures of 22 MPa.

To calculate the plastic strain the following simplification of the conditions the layer has to withstand are made. At the bottom side the layer is stretched by the strain of the bulk material, because it sticks to the bulk material and at the top side pressure and shear are acting on the surface of the layer. This results for the pre-strain in:

$$\sigma_{ii_{layer}}^{prestrain} = \frac{E_{layer}}{(1+\nu_{layer})}\varepsilon_{ii_{bulk}} + \frac{\nu_{layer}E_{layer}}{(1+\nu_{layer})(1-2\nu_{layer})} (\varepsilon_{ii_{bulk}} + \varepsilon_{jj_{bulk}} + \varepsilon_{kk_{bulk}}) \quad (17)$$

Where $i, j$ and $k$ can be $x, y$ or z. The external stresses at the top side are given by the normal load and the traction:

$$\sigma_{zz_{layer}} = \sigma_{zz_{layer}}^{prestrain} + P_{ij} \quad (18)$$

$$\sigma_{xz_{layer}} = \mu_{ij} : P_{ij} \quad (19)$$

Using these stress conditions the plastic strain can be calculated through a return mapping algorithm. The maximum plastic strain allowed in z direction is determined by the amount of growth gained every cycle. If now it is assumed that the layer only grows outside the apparent contact area the time of growth will be, see Figure 9:

$$t_{gr} = \frac{s_{track} - a}{|V_1 - V_2|} \quad (20)$$

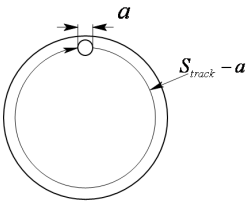


**Figure 9:** Relation between the track length, during which the chemical layer can renew and the contact area.

Here $t_{gr}$ is the time the layer is allowed to grow, $s_{track}$ is the wear track length, $a$ is the apparent contact with in sliding direction and $V_1/V_2$ are the sliding velocities of bodies one and two. The maximum amount of plastic strain allowed in the normal direction:

$$\varepsilon_{zz\max} = \frac{\sqrt{t_{gr}}K_0}{h_{balance}} \quad (21)$$

Here $h_{balance}$ is the layer thickness measured for a run in system, which is estimated at 100 *nm* [21-37]. The plastic strain of the chemical layer can be calculated using eqs. (17) and a return mapping algorithm.

## RESULTS

In this section the model discussed above will be applied to the different model systems to investigate how different parameters influence the running-in of contacts. Starting with the model systems presented in the different studies concerning the formation and properties of chemical layers [21-37]. In these studies only very mild wear is reported and thus it should follow from the model that only mild wear is present in the system. In the majority of the studies the specimens used where AISI 52100 steel cylinders with a diameter of 6 *mm*, which were used as received, without further specifying the roughness parameters. For these types of tests often roller bearing pins are used. The pins used in this type of bearings have a surface finish with an approximated CLA roughness value of 70 *nm* with a longitudinal

roughness orientation in sliding direction. The disk used in the tests listed are all polished using 3 $\mu m$ diamond paste resulting in a mirror finish surface with a CLA roughness varying between 7 and 10 *nm* Therefore, it is acceptable to regard the system as a rough/flat system and only the roughness of the cylinder will be taken into account during the simulations. The surface used for the polished cylinder is presented in Figure 10.

The next step is to setup a wear threshold for the "bulk" material. This will be done on the basis of three different material behaviors: 1) brittle like work hardening material behavior (common AISI 52100 2) ductile work hardening material 3) ductile soft NC material.

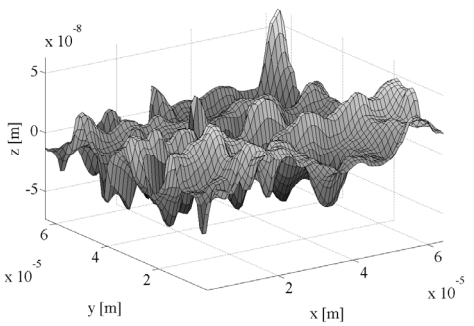


**Figure 10:** Surface profile of a polished bearing pin surface.

The more ductile material modeling is done to incorporate the NC layer in Figure 7. This layer is reported to have different material properties in the plastic regime than the bulk material, see for a more comprehensive review on the properties [3]. For the first material model a Swift hardening law is used to model the work hardening, which is shown in eq. (13). For the brittle work hardening material the parameters used are: $B$ = 1280 *MPa*, $C$=*4*, n=0.095 $\alpha$ is set $10^6$ and the maximum equivalent plastic strain: $\varepsilon_{pl_{eq}\max} = 0.2\%$. For the more ductile work hardening material $\alpha$ is changed to $10^5$ and the $\varepsilon_{pl_{eq}\max} = 2\%$. For both work hardening models the yield stress as a function of equivalent plastic strain are given in Figure 11. For the third model measurements done in [39] are used for the hardness (and thus the yield stress) as shown in Figure 12. And finally the maximum equivalent strain for this material is set to $\varepsilon_{pl_{eq}\max} = 5\%$. This value is based on theories presented in literature on NC materials [40]. If now the surface of the polished pin is used under the conditions given in the different studies, a dominantly mild wear situation should result from the simulations, as in the different studies only mild chemical wear is observed.

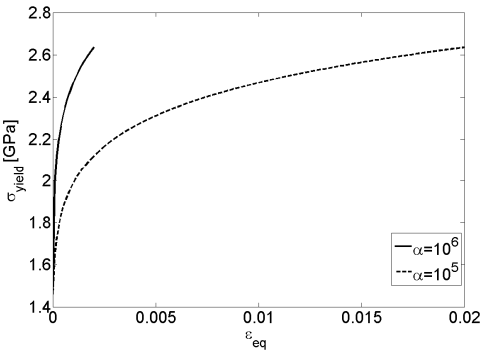


**Figure 11:** Yield stress as a function of the equivalent plastic strain for the material two different material models used.

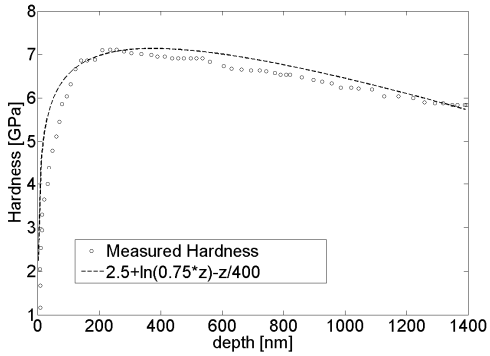


**Figure 12:** Hardness profile as a function of the depth from the surface for a system running under boundary lubrication and mild wear conditions conditions [39]**.**

To simulate this situation the following macroscopic settings are used: a load of 225 *N* is put on a pin with a diameter 6.2 *mm* and a length of 11 *mm*, resulting in a pressure of 500

*MPa* [25] with an average speed of 0.3 *m/s* and a track length of 14 mm at a temperature of 100 $^{o}C$ results in a growth rate of 1 *nm* per cycle approximately using the values of $K_0$ given in Table 1. Using a layer thickness of 100 *nm* this results in a maximum plastic indentation of the chemical layer of 1 percent using eq. (21). The normal pressure of 500 *MPa* is realized by putting a load of 1.6 *N* on the surface geometry presented in Figure 10. This load is applied in a linear increasing and decreasing signal as shown in Figure 13.

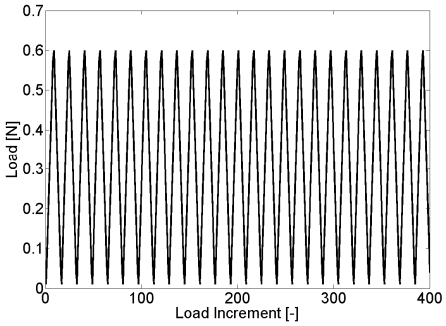


**Figure 13:** Loading sequence used for the calculations.

A load cycle refers to a complete increase and decrease of the normal load while a load step refers to one incremental load step. As mentioned before the simulation using the smooth surface should result in a predominately mild wear situation, which is the case for both the brittle and ductile material behavior, as no material is lost through direct material removal, however this does not exclude mild microscopic wear through chemical removal of bulk material as is discussed in [41]. However, for the NC material during the first few cycles a limited amount of wear is presented, as can be seen in Figure 15.If it is now assumed that the wear is limited to the rougher pin, since this in constant contact, and one cycle corresponds to the displacement of the grid size, is this case 64 $\mu$m an resulting specific wear rate as function of the load cycles can be calculated and is $2\times10^{-6}$ $mm^3/Nm$. Here also the coefficient of friction is presented and as can be seen both values are in good agreement with general values reported in general literature [42] validating the model as proposed, as well as the assumption that there is indeed a NC layer present in the first few microns present underneath the surface as is proposed in [3].

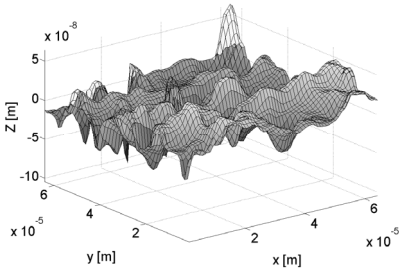


**Figure 14:** Worn surface using the smooth surface combined with the NC material model. Transparent surface is the worn part (compared with Figure 10).

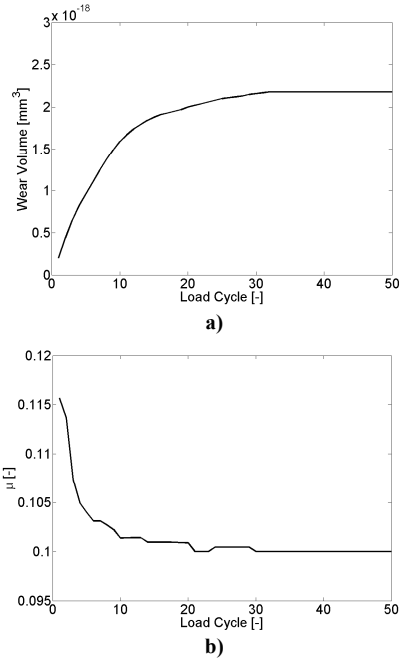


**Figure 15:a)** Wear volume vs. load cycle. **b)** Coefficient of friction vs. load cycle.

To investigate the influences of different parameters in the model under more severe wear conditions the smooth surface is replaced by a rough on in the simulation as is shown in Figure 16. As are the macroscopic contact conditions: a contact width of 300 $\mu m$ and total wear track of 314.5 *mm* (e.g. disk diameter of

100 *mm*) combined with a oil bath temperature of 100 $^{o}$ C and a sliding speed of 1 *m/s* are used. This gives a growth of the chemical layer of approximately 2 *nm* each contact cycle. Using an average chemical layer thickness of 100 *nm* results in $\varepsilon_{zzmax}$=2%, which will be used as the threshold for the frictional jump in the simulations following.. The nominal contact pressure for the contact simulations is reduced to approximately 150 *MPa* for the rough surface.

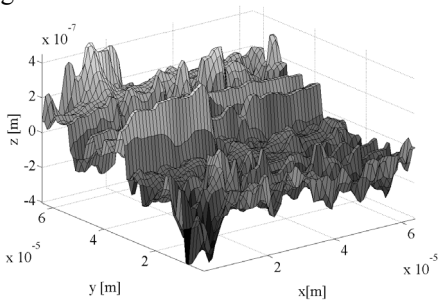


**Figure 16**: Surface profile of a hard turned disk surface.

In contradiction to the relatively smooth surface the rough surface undergoes severe wear and the surface roughness is significantly smoothened to a roughness close to the roughness of the polished pins at the load carrying locations as can be seen in Figure 17, even though the nominal contact pressure is a factor 3 lower. Comparing the results of the three different materials shown in Figure 18, it can be concluded that most material is lost in the first 5 cycles for the brittle material. As the surface roughness does not change after the first few cycles the coefficient of friction stays high. For the more ductile material and the NC material the wear volume is still increasing after 25 load cycles as is the coefficient of friction stabilizing. However, as can be concluded from the results a surface with a NC layer underneath is the most efficient in reducing the friction by lowering the surface roughness.

As the coefficient of friction for this material is already at a lower level as for the other materials while the volume loss is the least. This would be a situation that is most preferable in real engineering systems since the stress put on the bulk material is reduced as is the energy dissipated by the system. It can thus be concluded that the type of material present just underneath the surface has on very important influence on the way a system reacts to the stress put on it.

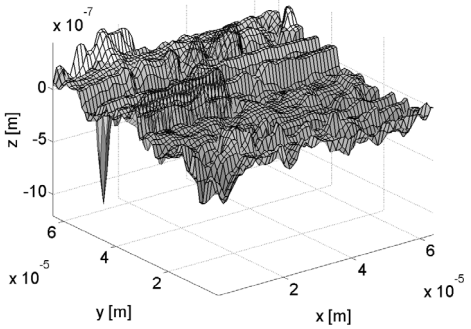


**Figure 17:** Representative result using the wear model combined with the rough surface and the brittle material behavior for a total of 25 load cylces. Transparent surface is the worn part compared to Figure 16.

A second conclusion is that the measured hardness curve on which the NC material is based is indeed the most efficient material concerning reduction in friction vs. wear volume. Therefore, to the authors opinion this is the most interesting material model and for the next simulation the main focus will be on this material model. A next step in modeling the running-in is extending the material model of the chemical layer with a pressure influence reported throughout literature [25, 43-45]. This effect is described in detail in [46]. Here a linear dependency of the Young's modulus on pressure is presented, after the pressure has passed a threshold as is presented in Figure 19.

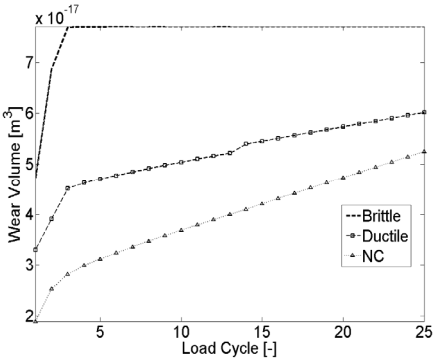


**a)**

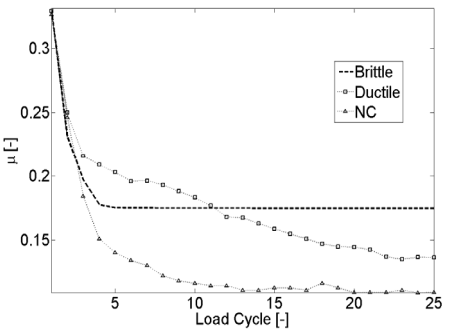


**b)**

**Figure 18: a)** Wear volume vs. load cycle for the three different material (Brittle, Ductile and N(ano)C(rystalline). **b)** Resulting coefficient of friction for the three different materials.

The material of the chemical layer is characterized as a polymer glass, yielding that the effect of the hydrostatic pressure on the yield stress can be assumed to be in the same range as for polymers, which can also be expressed as a linear function [47] of the hydrostatic pressure and is also a good representation of the curve given in [48]:

$$\sigma_{yield} = \sigma_{yield0} + \alpha \sigma_{hydro} \qquad (22)$$

Here $\sigma_{yield0}$ is the yield stress at zero hydrostatic pressure, which in the current case is estimated at 500 *MPa*. This is, however, only a rough estimation and in the future more research is needed since all the measured values for the yield stress of the chemical layer are indentation measurements and thus are measured under hydrostatic pressure.

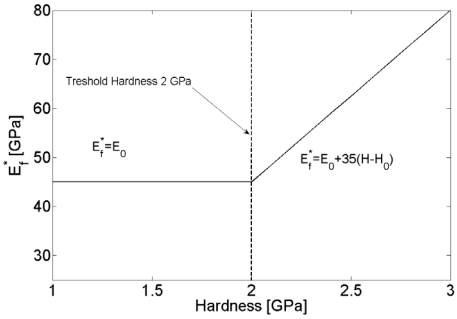


**Figure 19:** Young's Modulus of the chemical film as a function of the hardness $E=E_0+35(H-H_0)$ for $H>H_0$ e.g. the maximum pressure applied to it). Figure is reproduced using the data presented in [46]**.**

For the parameter α, in equation (22)**,** three different values (0.1, 0.2, 0.3) are used to see how this affects the wear behavior and frictional behavior of the system of both the smooth and rough surface. The results of these calculations (using the NC material underneath the surface) are presented in Figure 20 of the smooth surface and in Figure 21 for the rough surface. As for the smooth surface only the results for $\alpha = 0.1$ and 0.2 are presented, since for $\alpha = 0.3$ no wear was present at the surface and the coefficient of friction was at a constant value of 0.1. It is clearly seen that if the reference values of 80 *GPa* and a hardness of 2 *GPa* are used the layer provides better protection of the surface than pressure dependent layer properties. However, if the pressure dependency of the yield strength is increased above 0.3 the protection is better since no wear at all is present.

For the rough surface it can be concluded the effect of α is present in the first few cycles after which the effects is very limited for both the wear volume and the frictional signal. However, the main difference can be seen in the effect of increasing α from 0.2 to 0.3, as the slope of the wear curve also changes significantly, suggesting a better long term wear behavior, since less material is lost while the overall coefficient of friction is reduced to a low level.

For the smooth surface, however, the effect on the wear volume can be clearly seen in the first few cycles as the total wear volume is quite similar for the first 5 cycles after which the effect of $\alpha$ is quite well seen. As for the friction signal the level at which is stabilized is clearly influenced by the magnitude of $\alpha$. This would suggest that the influence of the hydrostatic pressure on the properties of the chemical reacted layer plays a significant role in the running-in of systems protected by these types of layers and more research on this topic is needed.

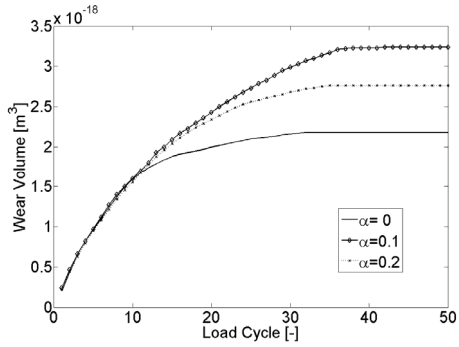


**a)**

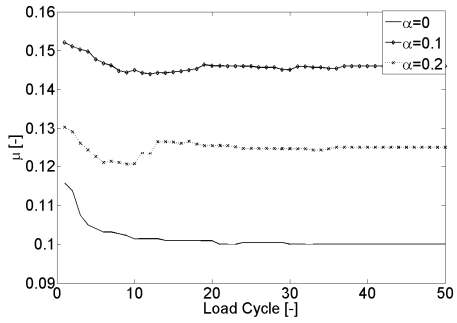


**b)**

**Figure 20: a)** Wear volume for the different values of $\alpha$. ($\alpha$=0 also indicates no pressure effect on the Young's modulus) **b)** coefficient of friction for the different values of $\alpha$.

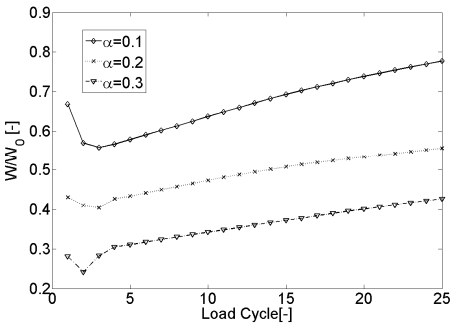


**a)**

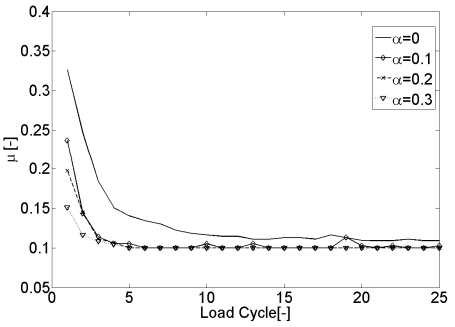


**b)**

**Figure 21:** a) Wear volume ($W$) normalized with the wear volume of $\alpha$=0 and no hydrostatic effect on the Youngs modulus ($W_0$) for the different values of $\alpha$ b) coefficient of friction for the different values of $\alpha$.

## CONCLUSIONS

In the current study a novel theory on the approach of running in of lubricated concentrated point contacts is presented based on the idea that the removal rate of the chemical products on the surface needs to be in balance for the oil to protect the surface sufficiently. To validate the model first a simulation of a relatively smooth surface is simulated. The results are in good agreement with values mentioned in literature validating the model. To investigate the effect different parameters in the system have on the running-in behavior of the surface three different material models and a rough and a smooth surface where used. This resulted in the conclusion that the material model based on measurements done on mild wearing results

yielded the most realist results as the chemical layer provided protection against severe wear within a few cycles, further validating the philosophy behind the model. However for the rough surface the chemical layer was not able to protect the complete surface suggesting a tougher layer should be present in a system with increased roughness. Finally the effect of the proposed "anvil" effect on the running-in of the surface is investigated. For the smooth surface the anvil effect had a significant influence on the amount of wear during running-in as well as on the level of the resulting stationary coefficient of friction. However, for the rough surface the influence of the "anvil" effect is only limited. As for a value of 0.1 it has only a limited effect on the running-in behavior, however as the value is increased to 0.3 the effect becomes significant as the slope of the wear volume decreases.

## NOMENCLATURE:

| Roman Symbols | | |
|---|---|---|
| $a$ | $[m]$ | Apparent contact width |
| $B$ | $[Pa]$ | Hardening coefficient |
| $C_{ijkl}$ | $[Pa]$ | Compliance matrix |
| $D$ | $[m/Pa]$ | Influence coefficient. surface deflection |
| $E$ | $[Pa]$ | Young's modulus |
| $h(x,y)$ | [m] | Surface height |
| $h$ | $[m]$ | Thickness |
| $k$ | $[mm^3/Nm]$ | Specific wear rate |
| $K$ | $[nm\ s^{-1/2}]$ | Eff. Diffusion Coefficient |
| $n$ | [-] | Hardening exponent |
| $s_{track}$ | $[m]$ | Wear track length |
| $S_{ijkl}$ | $[Pa]$ | Influence coefficient stress |
| $t$ | $[s]$ | Time |
| $T$ | $[^oC]$ | Temperature |
| $u$ | $[m]$ | Displacement |
| $V$ | $[m/s]$ | Sliding Velocity |
| $x,y,z$ | $[m]$ | Location observation point |
| $x',y',z'$ | $[m]$ | Location excitation point |
| w | $[m^3]$ | Wear volume |

| Greek Symbols | | |
|---|---|---|
| $\varepsilon_{ij},\varepsilon$ | [-] | Strain/error |
| $\phi$ | $[Pa]$ | Yield function |
| $\nu$ | [-] | Poisson ratio |
| $\sigma$ | $[Pa]$ | Stress |

| Sub/Super script | | |
|---|---|---|
| $elas$ | [-] | Elastic component |
| $pl$ | [-] | Plastic component |
| $eq$ | [-] | Equivalent |
| $ij$ | [-] | Dimension index |
| max | [-] | Maximum |
| $res$ | [-] | Residual |
| $y$ | [-] | Yield |

## APPENDIX

## Surface displacement coefficients due to pressure and shear

Surface displacement due to a unit pressure put on a surface patch of size $2a \times 2b$ [49]:

$$D_{33}^{n}=\frac{1}{\pi E}\left\{\begin{array}{l}(x+a)\ln\left(\frac{(y+b)+\sqrt{(y+b)^2+(x+a)^2}}{(y-b)+\sqrt{(y-b)^2+(x+a)^2}}\right)+(y+b)\ln\left(\frac{(x+a)+\sqrt{(y+b)^2+(x+a)^2}}{(x-a)+\sqrt{(y+b)^2+(x-a)^2}}\right)+\\(x-a)\ln\left(\frac{(y-b)+\sqrt{(y-b)^2+(x-a)^2}}{(y+b)+\sqrt{(y+b)^2+(x-a)^2}}\right)+(y-b)\ln\left(\frac{(x-a)+\sqrt{(y-b)^2+(x-a)^2}}{(x+a)+\sqrt{(y-b)^2+(x+a)^2}}\right)\end{array}\right\}$$

Surface displacement due to unit traction put on a surface patch of size $2a\times 2b$ [49]:

$$D_{31}^{n}=\frac{1-2\nu}{4\pi G}\left\{\begin{array}{l}(y+b)\ln\left(\frac{\sqrt{(x+a)^2+(y+b)^2}}{\sqrt{(x-a)^2+(y+b)^2}}\right)+(y-b)\ln\left(\frac{\sqrt{(x-a)^2+(y-b)^2}}{\sqrt{(x+a)^2+(y-b)^2}}\right)+\\(x+a)\left(\arctan\frac{y+b}{x+a}-\arctan\frac{y-b}{x+a}\right)+(x-a)\left(\arctan\frac{y-b}{x-a}-\arctan\frac{y+b}{x-a}\right)\end{array}\right\}$$

## Surface displacement coefficients due to plastic deformation underneath the surface

Expressions for the surface displacement due to a plastic volume of size $2a\times 2b\times 2c$ with uniform strains $\varepsilon_{ij}$ inside the volume [6]:

$$D_{ij}^{n_{pl}}=-\frac{1}{\pi}\left[\begin{array}{l}-2\varepsilon_{13}(R_{,133}-\phi_{,1})-2\varepsilon_{23}(R_{,233}-\phi_{,2})+2\varepsilon_{12}(D\psi_{,12}+R_{,123})\\+\varepsilon_{11}(D\psi_{,11}+R_{,113})+\varepsilon_{22}(D\psi_{,22}+R_{,223})+\\\varepsilon_{33}((2-3)\phi_{,3}+R_{,333})-2\nu\varepsilon_{ii}\phi_3\end{array}\right]\Bigg|_{-a}^{a}\Bigg|_{-b}^{b}\Bigg|_{-c}^{c} \tag{23}$$

## Stress coefficients due to Pressure and Traction on the surface

$$S_{113}^{elas}(x,y,z)=2\nu\tan^{-1}\left(\frac{z^2+y^2-Ry}{zx}\right)+2(1-\nu)\tan^{-1}\left(\frac{R-y+z}{x}\right)+\frac{xyz}{R(x^2+z^2)}$$

$$S_{223}^{elas}(x,y,z)=2\nu\tan^{-1}\left(\frac{z^2+y^2-Ry}{zx}\right)+2(1-\nu)\tan^{-1}\left(\frac{R-x+z}{y}\right)+\frac{xyz}{R(y^2+z^2)}$$

$$S_{333}^{elas}(x,y,z)=\tan^{-1}\left(\frac{z^2+y^2-Ry}{zx}\right)-\frac{xyz}{R}\left(\frac{1}{x^2+z^2}+\frac{1}{y^2+z^2}\right)$$

$$S_{123}^{elas}(x,y,z)=-\frac{z}{R}-(1-2\nu)\ln(R+z)$$

$$S_{133}^{elas}(x,y,z) = \frac{z^2 y}{R(x^2+z^2)}$$

$$S_{233}^{elas}(x,y,z) = \frac{z^2 x}{R(y^2+z^2)} \tag{24}$$

$$S_{111}^{elas}(x,y,z) = \frac{-z}{R}\left[1+\frac{yz-x^2}{(R+z)(R-y)}\right]+2\nu\left(\frac{y}{(R+z)}\right)-2\ln(R-y)$$

$$S_{221}^{elas}(x,y,z) = \frac{-yz}{(R(R+z))}-2\nu\left(\frac{y}{R+z}+\ln(R-y)\right)$$

$$S_{331}^{elas}(x,y,z) = \frac{xy^2 R}{R\left(x^2+z^2\right)}$$

$$S_{121}^{elas}(x,y,z) = \frac{-zx}{(R(R+z))}-2\nu\left(\frac{x}{(R+z)}\right)-\ln(R-x)$$

$$S_{131}^{elas}(x,y,z) = \frac{xyz}{R\left(x^2+y^2\right)}+\tan^{-1}\left(\frac{z^2+y^2-yR}{xz}\right)$$

$$S_{231}^{elas}(x,y,z) = \frac{-z}{R} \tag{25}$$

## Stress influence coefficients due to a plastic volume

The stress influence vector can be split up into 2 parts: one for the stress inside the plastic volume $\Omega_p$ and one outside the volume, starting with the stresses outside the volume

$$S_{ijkl}^{pl} = \nu f(\varepsilon_{ij})_{k,kmm}\delta_{ij} - f(\varepsilon_{ij})_{k,kij} + (1-\nu)(f(\varepsilon_{ij})_{i,kkj} + f(\varepsilon_{ij})_{j,kki})\Big|_{-a}^{a}\Big|_{-b}^{b}\Big|_{-c}^{c}$$

And for the stress inside the volume

$$S_{ijkl}^{pl} = \nu f(\varepsilon_{ij})_{k,kmm}\delta_{ij} - f(\varepsilon_{ij})_{k,kij} + (1-\nu)(f(\varepsilon_{ij})_{i,kkj} + f(\varepsilon_{ij})_{j,kki}) - \mu 2\varepsilon_{ij} - \lambda\varepsilon_{kk}\delta_{ij}\Big|_{-a}^{a}\Big|_{-b}^{b}\Big|_{-c}^{c}$$

Here $\delta_{ij}$ is the kronecker delta and $\mu = \frac{E}{2(1+\nu)}$ with the following definition of the derivatives of $f_{ijkl}$;

$$f_{i,jj}/C = 2\varepsilon_{1i}(\phi^I{}_{,1}+\phi_{,1}) + 2\varepsilon_{2i}(\phi^I_{,2}+\phi_{,2}) + 2\varepsilon_{3i}(\phi^I_{,3}-\phi_{,3}) \qquad (i = 1 \text{ or } 2) \tag{26}$$

$$
\begin{aligned}
f_{3,jj}/C &= 2\varepsilon_{13}(\phi^I_{,1}+4x_3-4R_{,133}+3\phi_{,1})+2\varepsilon_{23}(\phi^I_{,2}+4x_3\phi_{,23}-4R_{,233}+3\phi_{,2})\\
&+8\varepsilon_{12}(-x_3\phi_{,12}+R_{,123}+D\psi_{,12})+4\varepsilon_{11}(-x_3\phi_{,22}+R_{,113}+D\psi_{,11})+4\varepsilon_{22}(-x_3\phi_{,22}\\
&+R_{,223}+D\psi_{,22})+2\varepsilon_{33}(\phi^I_{,3}-2x_3\phi_{,33}+2R_{,333}-(5-4\nu)\phi_{,3})-8\nu\phi_{,3}
\end{aligned}
\tag{27}
$$

$$
\begin{aligned}
f_{m,jjm}/C &= 4\varepsilon_{13}(\phi^I_{,13}-2R_{,1333}+2x_3\phi_{,133}+3\phi_{,13})\\
&+4\varepsilon_{23}(\phi^I_{,23}-2R_{,2333}+2x_3\phi_{233}+\phi_{,23})\\
&+4\varepsilon_{12}(\phi^I_{,12}+2R_{,1233}-2x_3\phi_{,123}+(1-4\nu)\phi_{,12})\\
&+2\varepsilon_{11}(\phi^I_{,11}+2R_{,1133}-2x_3\phi_{,113}+(1-4\nu)\phi_{,11})\\
&+2\varepsilon_{22}(\phi^I_{,22}+2R_{,2233}-2x_3\phi_{,223}+(1-4\nu)\phi_{,22})\\
&+2\varepsilon_{33}(\phi^I_{,33}+2R_{,3333}-2x_3\phi_{,333}-(7-4\nu)\phi_{,33})\\
&-8\nu\varepsilon_{ii}\phi_{,33}
\end{aligned}
\tag{28}
$$

$$
\begin{aligned}
f_{j,j}/C &= 2\varepsilon_{13}(R^I_{,13}-(3-4\nu)R_{,13}+4(1-\nu)x_3\phi_{,1}-2x_3R_{,133}+2x_3^2\phi_{,13})\\
&+2\varepsilon_{23}(R^I_{,23}-(3-4\nu)R_{,23}+4(1-\nu)x_3\phi_{,2}-2x_3R_{,233}+2x_3^2\phi_{,23})\\
&+2\varepsilon_{12}(R^I_{,12}-(1-2D^2)R_{,12}+4(1-\nu)D(x_3+x_3^{'})\psi_{,12}+2x_3R_{,123}-2x_3^2\phi_{,12})\\
&+\varepsilon_{11}(R^I_{,11}+(1-2D^2)R_{,11}+4(1-\nu)D(x_3+x_3^{'})\psi_{,11}+2x_3R_{,113}-2x_3^2\phi_{,11})\\
&+\varepsilon_{22}(R^I_{,22}+(1-2D^2)R_{,22}+4(1-\nu)D(x_3+x_3^{'})\psi_{,22}+2x_3R_{,2213}-2x_3^2\phi_{,22})\\
&+\varepsilon_{33}(R^I_{,33}+(3-4\nu)R_{,33}+8(1-\nu)x_3\phi_{,3}-4(1-\nu)D\phi+2x_3R_{,333}-2x_3^2\phi_{,33})\\
&-2\nu\varepsilon_{ii}(\phi^I+(3-4\nu)\phi+2x_3\phi_{,3})
\end{aligned}
\tag{29}
$$

Here the functions $R,\psi,\phi$ are defined as $r=R=\sqrt{(x-x')+(y-y')+(z-z')},\psi=\ln(R+\zeta_3)$ and $\phi=\dfrac{1}{R}$. The derivatives of this functions are given using $k\neq j\neq i$ and $\zeta_1=x-x',\zeta_2=y-y',\zeta_3=z-z'$ (convolution/infinite space) or $\zeta_3=z+z'$ (correlation/ halfspace) which is indicated by either a superscript $^I$ or absence of one.:

$$
\begin{aligned}
&\phi_{,k}=\zeta_j\ln[r+\zeta_l]+\zeta_l\ln[r+\zeta_j]-\zeta_kU_k\\
&\phi_{,kl}=\ln[r+\zeta_j] \qquad \phi_{,kk}=-U_k \qquad \phi_{,kkk}=-\zeta_iV_l-\zeta_lV_i\\
&\phi_{,kkl}=\zeta_kV_k \qquad \phi_{,123k}=\frac{-\zeta_k}{r^3} \qquad \phi_{,kkll}=-\zeta_k\zeta_lW_j
\end{aligned}
$$

$$\phi_{,kkkk} = \zeta_l \zeta_k W_j + \zeta_k \zeta_j W_l \qquad \phi_{,kkkl} = V_j - \zeta_k^2 W_j$$

$$R_{,kkl} = \zeta_k \ln\left[r + \zeta_j\right] \qquad R_{,kkk} = \zeta_i \ln\left[r + \zeta_l\right] + \zeta_l \ln\left[r + \zeta_j\right] - 2\zeta_k U_k$$

$$R_{,123k} = \frac{\zeta_k}{r} \qquad R_{,kkkl} = \ln\left[r + \zeta_j\right] + \zeta_k^2 V_j \qquad R_{,kkll} = \zeta_k \zeta_l V_j$$

$$R_{,kkkk} = -\zeta_j \zeta_k V_l - \zeta_l \zeta_k V_j - 2U_k \qquad R_{,123kl} = \frac{-\zeta_k \zeta_l}{r^3}$$

For $\psi$ and $\zeta_3 \psi$ the derivative with respect to $\zeta_3$ become $\phi$ and $(\psi + R_{,3})$ respectively so in the following only indices $k$ and $l$ are used which are both different and have the value of 1 or 2:

$$\psi_{,kk} = -\zeta_k \ln\left[r + \zeta_l\right] - 2\zeta_3 X_k \qquad \psi_{,12} = \zeta_3 \ln\left[r + \zeta_3\right] - r$$

$$\psi_{,kkk} = -2\ln\left[r + \zeta_l\right] - (\zeta_k^2 + \zeta_3^2) V_l - (\zeta_3 - r)\zeta_l V_3 \qquad \psi_{,kkl} = -\frac{\zeta_k}{r + \zeta_3}$$

$$4(\zeta_3 \psi)_{,kkk} = 2\zeta_l \ln\left[r + \zeta_3\right] - \zeta_3(\zeta_k^2 + \zeta_3^2) V_l - \zeta_3 \zeta_l (\zeta_3 - r) V_3 - 4\zeta_k U_k$$

$$2(\zeta_3 \psi)_{,kkl} = \zeta_k \ln\left[r + \zeta_3\right] - \frac{\zeta_k \zeta_3}{r + \zeta_3} \qquad 2(\zeta_3 \psi)_{,kkll} = \zeta_k \zeta_l V_3 + \frac{\zeta_k \zeta_l \zeta_3}{(r + \zeta_3)^2 r}$$

$$4(\zeta_3 \psi)_{4,kkll} = V_3 \zeta_l \zeta_k \left(\frac{\zeta_3}{r} - 2\right) + \zeta_3 \zeta_k \left[\zeta_l (\zeta_3 - r) W_3 - 6V_l + (\zeta_k^2 + \zeta_3^2) W_l\right] - 4U_k$$

$$4(\zeta_3 \psi)_{,kkkl} = 2\ln\left[r + \zeta_3\right] + (3\zeta_k^2 - 2\zeta_3^2) V_3 + \zeta_3 \zeta_l^2 (\zeta_3 - r) W_3 + \frac{\zeta_l^2 r + (\zeta_k^2 + \zeta_3^2)\zeta_3}{r^3} \qquad (30)$$

The different functions used in (30) are :

$$U_k = \tan^{-1}\left[\frac{\zeta_i \zeta_j}{\zeta_k r}\right] \qquad (31)$$

$$V_k = \frac{1}{r(r + \zeta_k)} \qquad (32)$$

$$W_k = \frac{2r + \zeta_k}{r^3 (r + \zeta_k)^2} \qquad (33)$$

$$X_k = \tan^{-1} \frac{\zeta_k}{(r + \zeta_l + \zeta_j)} \qquad (34)$$

## REFERENCES


[1] H. So, R.C. Lin, The combined effects of ZDDP,surface texture and hardness on the running-in of ferrous metals, Tribology International,32 (1999) 143-153.

[2] I.M. Hutchings, Friction and Wear of Engineering Materials. Edward Arnold, Cambridge, 1992.

[3] R. Bosman, D.J. Schipper, Running-In of Systems Protected by Additive-Rich Oils, Tribology Letters. (2010) 1-20.

[4] C. Jacq, D. Nelias, G. Lormand, D. Girodin, Development of a Three-Dimensional Semi-Analytical Elastic-Plastic Contact Code, Journal of Tribology. 124 (2002) 653-667.

[5] D. Nelias, E. Antaluca, V. Boucly, S. Cretu, A Three-Dimensional Semianalytical Model for Elastic-Plastic Sliding Contacts, Journal of Tribology. 129 (2007) 761-771.

[6] S.B. Liu, Q. Wang, Elastic fields due to eigenstrains in a half-space, Journal of Applied Mechanics-Transactions of the ASME. 72 (2005) 871-878.

[7] Z.-J. Wang, W.-Z. Wang, Y.-Z. Hu, H. Wang, A Numerical Elastic–Plastic Contact Model for Rough Surfaces, Tribology Transactions, 53 (2010) 224-238.

[8] University of Twente, 2008; Available from: www.dieka.org.

[9] K.L. Johnson, Contact mechanics. Cambridge university Press, Cambridge, 1985.

[10] R. Bosman, D.J. Schipper, Running-In of Systems Protected by Additive-Rich Oils, Tribology Letters, (2010) 1-20.

[11] M.v. Drogen, The Transition to adhesive wear of Lubricated Concentrated Contacts, PhD Thesis, University of Twente www.tr.ctw.utwente.nl, 2005 p 105.

[12] M.Z. Huq, P.B. Aswath, R.L. Elsenbaumer, TEM studies of anti-wear films/wear particles generated under boundary conditions lubrication, Tribology International. 40 (2007) 111-116.

[13] C. Minfray, T. Le Mogne, J.-M. Martin, T. Onodera, S. Nara, S. Takahashi, H. Tsuboi, M. Koyama, A. Endou, H. Takaba, M. Kubo, C.A. Del Carpio, A. Miyamoto, Experimental and Molecular Dynamics Simulations of Tribochemical Reactions with ZDDP: Zinc Phosphate “Iron Oxide Reaction", Tribology Transactions, 51 (2008) 589 - 601.

[14] D. Nelias, V. Boucly, M. Brunet, Elastic-Plastic Contact Between Rough Surfaces: Proposal for a Wear or Running-in Model, Journal of Tribology. 128 (2006) 236-244.

[15] A. Oila, S.J. Bull, Assessment of the factors influencing micropitting in rolling/sliding contacts, Wear. 258 (2005) 1510-1524.

[16] W. Press, S. Teukolsky, W. Vetterling, B. Flannery, Numerical Recipes in C++: The Art of Scientific Computing. Cambridge University Press, 2002.

[17] V. Boucly, Semi-Analytical Modeling of the Transient-Elastic-Plastic Contact and its Application to Asperity Collision, Wear and Running in of Surfaces, PhD Thesis, Lyon, 2008 p 203.

[18] S. Bec, A. Tonck, J.M. Georges, G.W. Roper, Synergistic Effects of MoDTC and ZDTP on Frictional Behaviour of Tribofilms at the Nanometer Scale, Tribology Letters. 17 (2004) 797-809.

[19] C. Minfray, J.-M. Martin, M. Belin, T.L. Mogne, M.P.G.D. D. Dowson, A.A. Lubrecht, A novel experimental analysis of the rheology of ZDDP tribofilms, Tribology and Interface Engineering Series, Elsevier, 2003, pp. 807-817.

[20] A. Tonck, S. Bec, J.M. Georges, R.C. Coy, J.C. Bell, G.W. Roper, Structure and mechanical properties of ZDTP films in oil, Tribology Series, Elsevier, 1999, pp. 39-47.

[21] M.A. Nicholls, P.R. Norton, G.M. Bancroft, M. Kasrai, T. Do, B.H. Frazer, G.D. Stasio, Nanometer scale chemomechanical characterizaton of antiwear films, Tribology Letters, 17 (2003) 205-336.
[22] Z. Zhang, Tribofilms generated from ZDDP and DDP on steel surfaces: Part I, Tribology Letters, 17 (2005) 211-220.
[23] J.P. Ye, S. Araki, M. Kano, Y. Yasuda, Nanometer-scale mechanical/structural properties of molybdenum dithiocarbamate and zinc dialkylsithiophosphate tribofilms and friction reduction mechanism, Japanese Journal of Applied Physics Part 1-Regular Papers Brief Communications & Review Papers, 44 (2005) 5358-5361.
[24] J.M. Martin, C. Grossiord, T. Le Mogne, S. Bec, A. Tonck, The two-layer structure of zndtp tribofilms Part 1: AES, XPS and XANES analyses, Tribology International, 34 (2001) 523-530.
[25] M. Kasrai, S. Marina, B.G. Micheal, Y.E. S., Ray, X-ray adsorption study of the effect of calcium sulfonate on antiwear film formation generated from neutral and basic ZDDPs: Part 1 -Phosporus species, Tribology Transactions, 46 (2003) 434-442.
[26] M.A. Nicholls, T. Do, P.R. Norton, M. Kasrai, G.M. Bancroft, Review of the lubrication of metallic surfaces by zinc dialkyl-dithiophosphates, Tribology International, 38 (2005) 15-39.
[27] M. Aktary, M.T. McDermott, G.A. McAlpine, Morphology and nanomechanical properties of ZDDP antiwear films as a function of tribological contact time, Tribology Letters, 12 (2002) 155-162.
[28] M.A. Nicholls, G.M. Bancroft, P.R. Norton, M. Kasrai, G. De Stasio, B.H. Frazer, L.M. Wiese, Chemomechanical properties of antiwear films using X-ray absorption microscopy and nanoindentation techniques, Tribology Letters, 17 (2004) 245-259.
[29] J.P. Ye, M. Kano, Y. Yasuda, Evaluation of nanoscale friction depth distribution in ZDDP and MoDTC tribochemical reacted films using a nanoscratch method, Tribology Letters. 16 (2004) 107-112.
[30] H.B. Ji, M.A. Nicholls, P.R. Norton, M. Kasrai, T.W. Capehart, T.A. Perry, Y.T. Cheng, Zinc-dialkyl-dithiophosphate antiwear films: dependence on contact pressure and sliding speed, Wear. 258 (2005) 789-799.
[31] S. Bec, A. Tonck, J.M. Georges, R.C. Coy, J.C. Bell, G.W. Roper, Relationship between mechanical properties and structures of zinc dithiophosphate anti-wear films, Proceedings of the Royal Society of London Series A-Mathematical Physical and Engineering Sciences. 455 (1999) 4181-4203.
[32] K. Komvopoulos, V. Do, E.S. Yamaguchi, P.R. Ryason, Nanomechanical and nanotribological properties of an antiwear tribofilm produced from phosphorus-containing additives on boundary-lubricated steel surfaces, Journal of Tribology-Transactions of the ASME. 126 (2004) 775-780.
[33] O.L. Warren, Nanomechanical properties of films derived from zinc dialkyldithiophosphate, Tribology Letters. 4 (1998) 189-198.
[34] C. Minfray, J.M. Martin, C. Esnouf, T. Le Mogne, R. Kersting, B. Hagenhoff, A multi-technique approach of tribofilm characterisation, Thin Solid Films. 447 (2004) 272-277.
[35] G. Pereira, A varialbe temperature mechanical analysis of ZDDP-derived antiwear films formed on 52100 steel, Wear (2006) 461-470.
[36] G.M. Bancroft, M. Kasrai, M. Fuller, Z. Yin, K. Fyfe, K.H. Tan, Mechanisms

of tribochemical film formation: stabilityof tribo- and thermally-generated ZDDP films, Tribology Letters. 3 (1997) 47-51.
[37] K. Topolovec-Miklozic, T. Forbus, H. Spikes, Film thickness and roughness of ZDDP antiwear films, Tribology Letters. 26 (2007) 161-171.
[38] H. So, Y.C. Lin, The theory of antiwear for ZDDP at elevated temperature in boundary lubrication condition, Wear. 177 (1994) 105-115.
[39] D. Shakhvorostov, B. Gleising, R. Büscher, W. Dudzinski, A. Fischer, M. Scherge, Microstructure of tribologically induced nanolayers produced at ultra-low wear rates, Wear. 263 (2007) 1259-1265.
[40] M.A. Meyers, A. Mishra, D.J. Benson, Mechanical properties of nanocrystalline materials, Progress in Materials Science. 51 (2006) 427-556.
[41] R. Bosman, D.J. Schipper, Mild Wear Prediction of Boundary Lubricated Contacts, Tribology Letters. Submitted (2010)
[42] A. William Ruff, Friction and Wear Data Bank, Modern Tribology Handbook, Two Volume Set, CRC Press. 2000.
[43] N.J. Mosey, M.H. Muser, T.K. Woo, Molecular Mechanisms for the Functionality of Lubricant Additives, Science. 307 (2005) 1612-1615.
[44] N.J. Mosey, T.K. Woo, M. Kasrai, P.R. Norton, G.M. Bancroft, M.H. Müser, Interpretation of experiments on ZDDP anti-wear films through pressure-induced cross-linking, Tribology Letters. 24 (2006) 105-114.
[45] J. Tse, Y. Song, Z. Liu, Effects of Temperature and Pressure on ZDDP, Tribology Letters. 28 (2007) 45-49.
[46] K. Demmou, S. Bec, J.L. Loubet (2007) Effect of hydrostatic pressure on the elastic properties of ZDTP tribofilms. Cornell University Library.
[47] J. Rottler, M.O. Robbins, Yield conditions for deformation of amorphous polymer glasses, Physical Review E. 64 (2001) 051801.
[48] K. Demmou, S. Bec, J.-L. Loubet, J.-M. Martin, Temperature effects on mechanical properties of zinc dithiophosphate tribofilms, Tribology International. 39 (2006) 1558-1563.
[49] K. Willner, Fully Coupled Frictional Contact Using Elastic Halfspace Theory, Journal of Tribology. 130 (2008) 031405-8.

Paper F

Running-in of Systems Protected by Additive Rich Oils,
R. Bosman and D.J. Schipper,
Article in press: Tribology Letters

# Running-in of Systems Protected by Additive Rich Oils

R. Bosman and D.J. Schipper
University of Twente, r.bosman@utwente.nl
Drienerlolaan 5
7500 AE Enschede

Accepted for publication in Tribology Letters

**Abstract - Recent research on mild wearing systems running under boundary lubrication conditions focus more and more on the role of the nano-crystalline layer present at the surface of the components in contact. This layer has a typical thickness of a few tenths of nano-meters up to a few microns depending on the operational conditions. The role of this layer with respect to wear is however still unclear as well as its mechanical behavior. In the current work a first step is made in incorporating this type of layer into a wear model. Using an elasto-plastic semi-analytical-method the effect of different material behavior reported through out current literature for the nano-crystalline layer on wear is studied. From the results it can be concluded that the effect of this mechanically altered layer has an important influence on the wear of the system, especially during the initial phase of running.**

*Index Terms* – Wear transition, Boundary lubrication

## INTRODUCTION

The wear of components is of great interest to industry and society and therefore a lot of research is conducted on this topic. The publications range from developed (pragmatic) wear equations to written descriptions about the wear of certain systems, for a review the reader is referred to the paper of Meng [1]. As can be concluded from this article many different equations are used and still one of the most commonly used is the Archard/Holm equation [2], where it is assumed that the wear is linear related to the sliding distance and normal load. Currently this model is most often used, or a derivative of it, enabling it to be incorporated within a numerical method such as BIM and FEM, see for example [3-5]. This type of models yield good results if the appropriate specific wear coefficient is used and appropriate care is taken in chosen the right incremental steps for the sliding distance and load. However, it does not give insight into the wear mechanism behind material removal. The driving force behind the wear of materials is still a topic which is researched intensively in literature. The research is currently focusing more towards the micro/nano-level, as it is becoming clearer that the friction and wear in systems is determined in the first few nanometers/micrometers underneath the surface. Looking at systems operating in boundary lubrication conditions extensive grain refinement down to tenths of nanometer is seen near the surface and different plastic material properties can be expected through the Hall-Petch relationship and the inverse Hall-Petch relationship [6-7], e.g. material hardening or softening respectively. Both of these theories are based upon physical hypotheses. The alleged mechanism behind the Hall-Petch relationship is the pile up of dislocations/grain refinement; e.g. dislocation density increase.

Since in coarse grain material the main plasticity mechanism is dislocation diffusion, the energy needed for this increases and thus the material is hardened. However, if the grain size is reduced to a level at which every crystal can only contain a very limited number of dislocations no pile up occurs and thus hardening due to grain refinement/dislocation pile up is limited. If now the grain size is reduced further a different type of plasticity mechanism is suggested; grain boundary slip rather than dislocation diffusion [8], e.g. the grains themselves are not deforming but the lattice as a total and grains start slipping over each other. This mechanism would promote super plasticity at relatively low temperatures, suggesting that a softer and more ductile layer is formed at the surface preventing the brittle and hard (sub-surface) bulk material from yielding. Other authors however claim an increase of hardness towards the surface [9], suggesting that the Hall-Petch relationship still holds even at sub-micron grain sizes. Both of these theories are consistent with theoretical and experimental studies performed at N(ano)-C(rystalline) materials [10-17]. The influence of this gradual increase and/or decrease of the yield stress on wear are currently not treated in a theoretical manner. In this article a first step to include the NC-layer, which are observed in experiments performed, is taken. The formation of this layer will not be dealt with, and it is assumed that the layer is stable after running-in conditions [18] having a constant thickness and grain size.

The wear model used in the current study was first discussed by Nelias [19] based on a semi-analytical elasto-plastic contact code. The SAM code was first developed by Jacq [20] and later on adapted to include friction by Nelias [21]. In the latter study it is stated that there is a threshold equivalent plastic strain at which the material will start tearing. The formed crack will then grow towards the surface enclosing a volume which will form a wear particle. This method is used successfully to study two academic situations for a smooth surface with a high load and a lowly loaded isotropic rough surface [19]. In both situations an overall coefficient of friction of 0.4 is assumed. It was shown that during the first contact cycles the surface can either run in (smoothening of the rough surface) or run out (roughening of the smooth surface). In the current model a similar approach is used, however a local coefficient of friction based on the effectiveness of the lubricant to protect the surface is used.

It is suggested that a lubricated system running under boundary lubrication conditions can be modeled according to Figure 1; with a system consisting of three layers [22]. The top layer is a physically/chemically adsorbed layer forming the first line of defense against high friction and extensive wear and is meant to provide protection under mild conditions. This layer is adsorbed on a harder thin chemically reaction layer, which is however still softer than the bulk material or the NC-layer. The chemical layer is typically built up from oxides formed on the surface and chemical products originating from the additives present in the oil, which have reacted with the oxide on the surface forming a complex structure which typically consists of an amorphous glass type of material. Underneath this layer a metallurgical altered NC-layer exists, which is formed through high strain rates under high hydrostatic pressures. This layer is the final line of defense protecting the less ductile bulk material against tearing. The current model will focus mainly on the role of the chemical reacted layer and NC-layer. The wear model will be based upon a SAM model and will be discussed briefly followed by a short discussion on the material model used for the NC-layer and finally the concept of the complete wear model will be discussed after which two examples will be shown, demonstrating the practical application of the current model.

## CONTACT MODEL

The system built up in Figure 1 may suggest that a layered contact model is needed. However, through some well educated

simplifications this is not necessary. First the chemical reacted layer, which is very thin in comparison with the contact patch size used in the current study, will be neglected in the normal direction (e.g. the direction in which the normal load is applied). The chemical layer in systems operating under conditions studied is approximately 100 nm thick and has a Young's modulus of 80 GPa, as shown in Table 1. The data used for the micro geometry are interference microscope measurements with a lateral resolution of 1 micron. To estimate the exact effect of the layer on the stress state and contact pressure the interference microscopy measurement shown in Figure 2 is used combined with the theory presented in [23]. In Figure 3 the resulting stress and pressure field for the elastic calculations are shown using the input parameters given in Table 1. Here the overall coefficient of friction is set to 0.1, which is the value used for the situation where the oil provides sufficient protection as will be discussed in the next section.

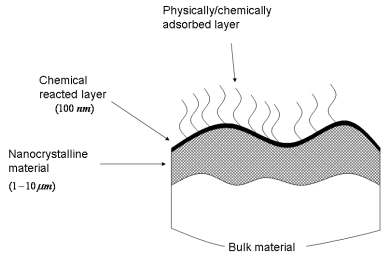


**Figure 1:** Layers present at the surface of a run in system. The top layer is a physically/chemically adsorbed layer which only withstands very mild operational conditions. The second layer is a chemical layer which is a mixture of oxides and chemical products of the lubricant. The third layer is a Nano-Crystalline layer formed at the top of the bulk material by severe plastic deformation under large hydrostatic pressure.

The normal load is set to 0.6 N, at this value the maximum pressure is in the range of the hardness of the bulk material and thus will give a realistic contact situation. As can clearly be seen the effect of the layer on both the stress-state in the bulk material as the normal pressure is less than 5 percent. This justifies the simplification suggested before. In the tangent (sliding direction) the dominant influence of the chemical layer will be on the coefficient of friction. If the chemical layer is sufficient in protecting the surface the main shearing will be located in the chemical layer and thus lowering the coefficient of friction. This subject will be discussed in more detail in the next section which deals with the local nature of the coefficient of friction.

| Input Parameter | Value |
|---|---|
| $E_{coating}$ | 80 [$GPa$] |
| $E_{substrate}$ | 210 [$GPa$] |
| $\nu_{coating}$ | 0.3[-] |
| $\nu_{substrate}$ | 0.3[-] |
| $F_N$ | 0.6 [N] |
| $\mu$ | 0.1 [-] |
| $h_{coating}$ | 100 [$nm$] |

**Table 1:** Input parameters layered calculation.

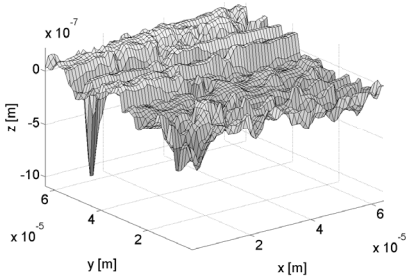


**Figure 2:** Interference microscopy measurement used in the layered calculations.

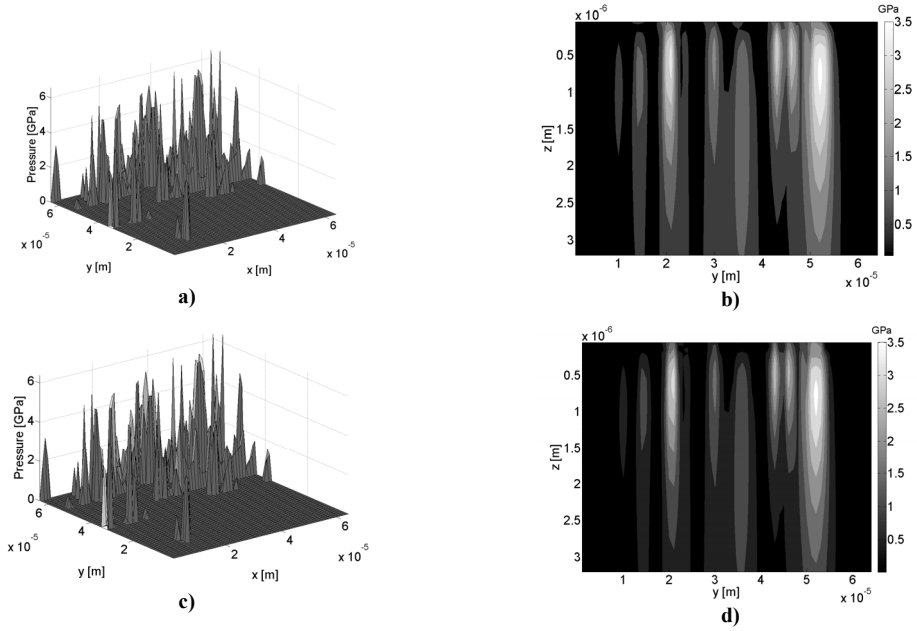


**Figure 3:** Pressure profile for **a)** coated surface $p_{max}$=6.4 *GPa*) and **c)** uncoated surface ($p_{max}$=6.5 *GPa*).Von Mises stress underneath the surface, maximum von Mises stress **b)** coated material $\sigma_{vm}^{max}$=3.5 *GPa* **d)** and uncoated material $\sigma_{vm}^{max}$=3.55 *GPa*

The behavior of the NC-layer can be split up into two parts: 1) Elastic or 2) Plastic. For the elastic part the assumption can be made that the properties of the NC-layer with negligible porosity do not change down to a crystal size of 20 nm, which originates from a study by Kim [24], see Figure 4.

The average grain size reported in literature for tribologically induced NC layers at steel surfaces are in the range 20 nm and higher, see for example [7, 9], thus for the elastic part a model without layers can be used for the simulations regarding steel-like materials. This enables the use of the SAM model discussed in [21] with only a small adaptation, since the plastic part is calculated separately and then imposed on the elastic bulk through the use of eigen-strains. For the exact code the interested reader is referred to the dedicated literature about the SAM model in [20-21, 25], where the model is dealt with in detail.

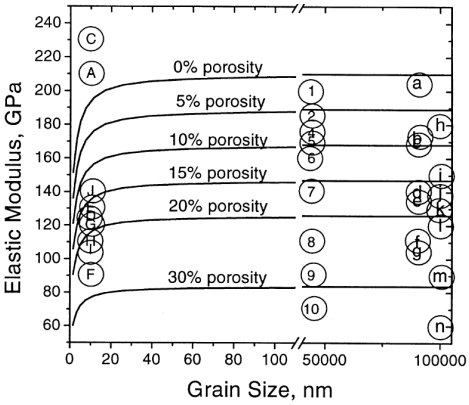


**Figure 4:** Elasitic modulus of steel as a function of porosity and grain size [24].

The version of the code used in the current study slightly differs from the one dealt with in this literature since the convergence of the plasticity loop is over the stress rather than over the strain which is dealt with in more detail in [26]. Only a short overview of the most important parts of the code and the ones

that are adapted are presented here. Starting with the reciprocal theory applied to a semi-infinite volume with boundary $\Gamma$ and volume $\Omega$. For this body different states are defined: an initial state with internal strains $(u, \varepsilon, \sigma, f_i)$ and a state for the time undefined: $(u_i^*, \varepsilon^*, \sigma^*, f_i^*)$. Using the reciprocal theory and the assumption that the second state is the one in which the surface is loaded by a unit pressure $p_i^*$ at the location $A$ gives:

$$u_3(A) = \underbrace{\int_{\Gamma_c} p_i \, u_{3i}^*(M, A)\, d\Gamma}_{u^e(A)} + \underbrace{\int_{\Omega} \varepsilon_{ij}^0(M)\, C_{ijkl} \varepsilon_{ij}^*(M, A)\, d\Omega}_{u^{pl}(A)} \quad (1)$$

Here $u^e(A)$ is the elastic surface displacement and by stating $\varepsilon_{ij}^0 = \varepsilon_{ij}^{pl}$, $u^{pl}(A)$ becomes the surface displacement due to the plastic strains inside volume $\Omega$. The surface displacement of the body can now be expressed as a function of the contact pressure and the plastic strain. To calculate the plastic strains the subsurface stresses are needed. Using the reciprocal theory again and define a state $(u^{**}, \varepsilon^{**}, \sigma^{**}, f_k^{**})$, which can be seen as the state when a unit force is applied inside volume $\Omega$ at point B. This then results in:

$$u_k(B) = \underbrace{\int_{\Gamma} u_{ki}^{**}(M, B)\, p_i(M) d\Gamma}_{u_k^e(B)} + \underbrace{\int_{\Omega} \varepsilon_{ij}^0(M)\, C_{ijkl} \varepsilon_{ij}^{**}(M, A)\, d\Omega}_{u_k^{pl}(B)} \quad (2)$$

Here stating $\varepsilon_{ij}^0 = \varepsilon_{ij}^{pl}$ and only integrating over the volume where the plastic strains are not zero $\Omega = \Omega_{pl}$ the displacement field is written as a function of the elastic and the plastic strains. Using Hook's law:

$$\sigma_{ij}^{tot}(B) = C_{ijkl} \left[ \begin{array}{l} \left( \frac{1}{2} \left( u_{k,l}^e(B) + u_{l,k}^e(B) \right) \right) \\ + \left( \frac{1}{2} \left( u_{k,l}^{pl} + u_{k,l}^{pl} \right) - \varepsilon_{kl}^{pl} \right) \end{array} \right] \quad (3)$$

Rewriting (3):

$$\sigma_{ij}^{tot}(B) = \sigma_{ij}^e(B) + \sigma_{ij}^{res}(B) \quad (4)$$

If now the unit pressure and unit force are replaced by the complete pressure and force fields, a solution can be found for a complete rough contact situation. This is done by descrization of the surface $\Gamma$ into surface elements $N_s$ of size $\Delta x \times \Delta y$ and the volume into elements $N_v$ of size $\Delta x \times \Delta y \times \Delta z$. On which at the surface uniform pressures are acting and in the volume the strains inside each volume element are uniform. Starting with the elastic surface displacement which then becomes the sum of the individual pressure patches:

$$u_3^e(x, y) = \sum_{n=1}^{N=N_s} D_{3i}^n(x - x'_n, y - y'_n)\, p_i^n(x'_n, y'_n) \quad (5)$$

Here $x_n$ ,$y_n$ are the coordinates of observation and $x'_n$, $y'_n$ are the coordinates of the center of the excitation patch *n*, the expressions of $D^n_{3i}$ are given in the appendix, where $i$ can have the value of 3 for the displacement due to normal force and 1 for the displacement due to traction. Next is the displacement due to the plastic strains $\varepsilon^p_{ij}$. Using the assumption of uniform strains within the volume elements:

$$u_3^{pl}(x,y) = \sum_{n=1}^{N=N_v} K_{ij}^{pl}(x-x'_n, y-y'_n, z'_n) \\ \varepsilon_{ij}^{p}(x'_n, y'_n, z'_n) \quad (6)$$

Here ($x$, $y$) is the location of the point of observation on the surface and ($x'_n$, $y'_n$, $z'_n$) are the coordinates of the excitation volume $n$. The expression for $K^{pl}_{3i}$ is given in the appendix.

The stresses for the total system, given in eq. (3), can also be expressed in a summation form:

$$\sigma_{ij}^{tot}(x,y,z) = \sum_{n=1}^{N=N_v} S_{ijk}^{elas}(x-x'_n, y-y'_n, z-z'_n)p_k + \\ \sum_{n=1}^{N=Nv} S_{ij}^{pl}((x-x'_n, y-y'_n, z-z'_n, z+z'_n), \\ \varepsilon_{ij}^{pl}(x'_n, y'_n, z'_n)) \quad (7)$$

Here the expressions for $S_{ij}^{elas}$ and $S_{ij}^{pl}$ for the different parts are given in the appendix, where the expression originally used in the code discussed in [20] and [21] are replaced by more efficient equations originating from [27].Now the surface displacement and the stress inside the bulk material of an elastic half space with plastic strains inside the volume are described by equations it can be used to model the contact of the elasto-plastic contact between two half spaces by using the model depicted Figure 5 of which the flow chart is shown in Figure 6.

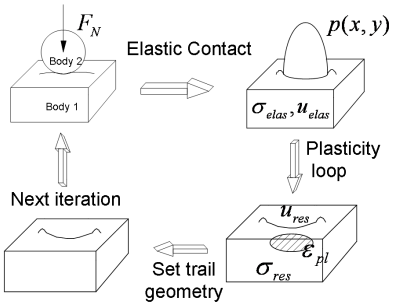


**Figure 5:** The iterative process of solving the elasto-plastic contact.

One part will be discussed here in detail with respect to the plastic loop and the validation of the code. In the original code the Prandtl Reuss method is used to compute the plastic strains this is later on adapted by Nelias [21] to a return mapping algorithm to increase the efficiency of the code. The current model also uses a return mapping algorithm however in the current version the plastic loop is changed to a stress related one rather than strain. As can be seen in reference [20] the plasticity loop is stopped if convergence of the plastic strain is reached. However, the basis of the plasticity theory states that for a system to stay in the elastic regime the elastic stresses should be on the yield surface:

$$\sigma_{ij} \leq \phi \quad (8)$$

This is however not per definition satisfied if the convergence criterion used is based on the plastic strain inside the body. In the current model the plasticity loop used is depicted in Figure 7. Here the yield surface is defined by the von Mises yield criterion and the loop is stopped if the stress state in the complete meshed volume is either within the yield surface or within the predefined error outside the yield surface. Also the iteration on the stress rather than on the strain ensures that the plasticity loop stays stable, since the return mapping algorithm is unconditionally stable. To validate the new plasticity loop the examples given in [21] Figure 5 are reproduced and the results are presented in Figure 8. It can be concluded that the current code gives approximately the same results for the low friction situation and slightly better results for the high friction situation. However, the results of the SAM code will not correspond completely with the FEM solution since the tangential displacement are taken into account in a decoupled method in the SAM code while in the FEM code they are coupled. Now the complete surface displacement and stress state can be calculated the contact problem stated as:

$$h(x,y) = h(x,y) + \delta + u_3^{(1+2)}(x,y) \\ h(x,y) \geq 0 \ then \ p(x,y) \geq 0 \quad (9) \\ h(x,y) < 0 \ then \ p(x,y) = 0$$

The inequalities stated by eq. (9) can be solved using the CGM method [28]:

$$\begin{aligned}\mathbf{p}_{k+1} &= \mathbf{p}_k - \frac{\mathbf{r}_k^T \mathbf{r}_k}{\mathbf{d}_k^T \mathbf{D}_{3i}^n \mathbf{d}_k} \mathbf{d}_k \\ \mathbf{r}_{k+1} &= \mathbf{r}_k - \frac{\mathbf{r}_k^T \mathbf{r}_k}{\mathbf{d}_k^T \mathbf{D}_{3i}^n d_k} \mathbf{D}_{3i}^n \\ \mathbf{d}_{k+1} &= -\mathbf{r}_{k+1} + \frac{\mathbf{r}_{k+1}^T \mathbf{r}_{k+1}}{\mathbf{r}_k^T \mathbf{r}_k}\end{aligned} \tag{10}$$

The above method is the elastic loop in Figure 6.

## MATERIAL MODEL

The NC-layer is included in the contact model by using a different model for the yield stress and hardening behavior for the fist few elements in depth direction. However, the exact value of the plastic properties of the first few hundred nm underneath the surface is currently still not fully defined due to lack of understanding of the NC-layer. In literature the different authors have different opinions since different measured values are found for the hardness of the materials near the surface as a result of crystalline changes due to tribological/ mechanical interaction or artificially created NC-layers (see for example [10-12][23-26]). Therefore, in the current paper the exact numerical data will not be the point of particular interest nor will the origin of the layer be. The focus will be on the effect the different yield behaviors have on the wear modeling. This approach gives the opportunity to make a clear distinguishing between the two main theories which both will be dealt with.

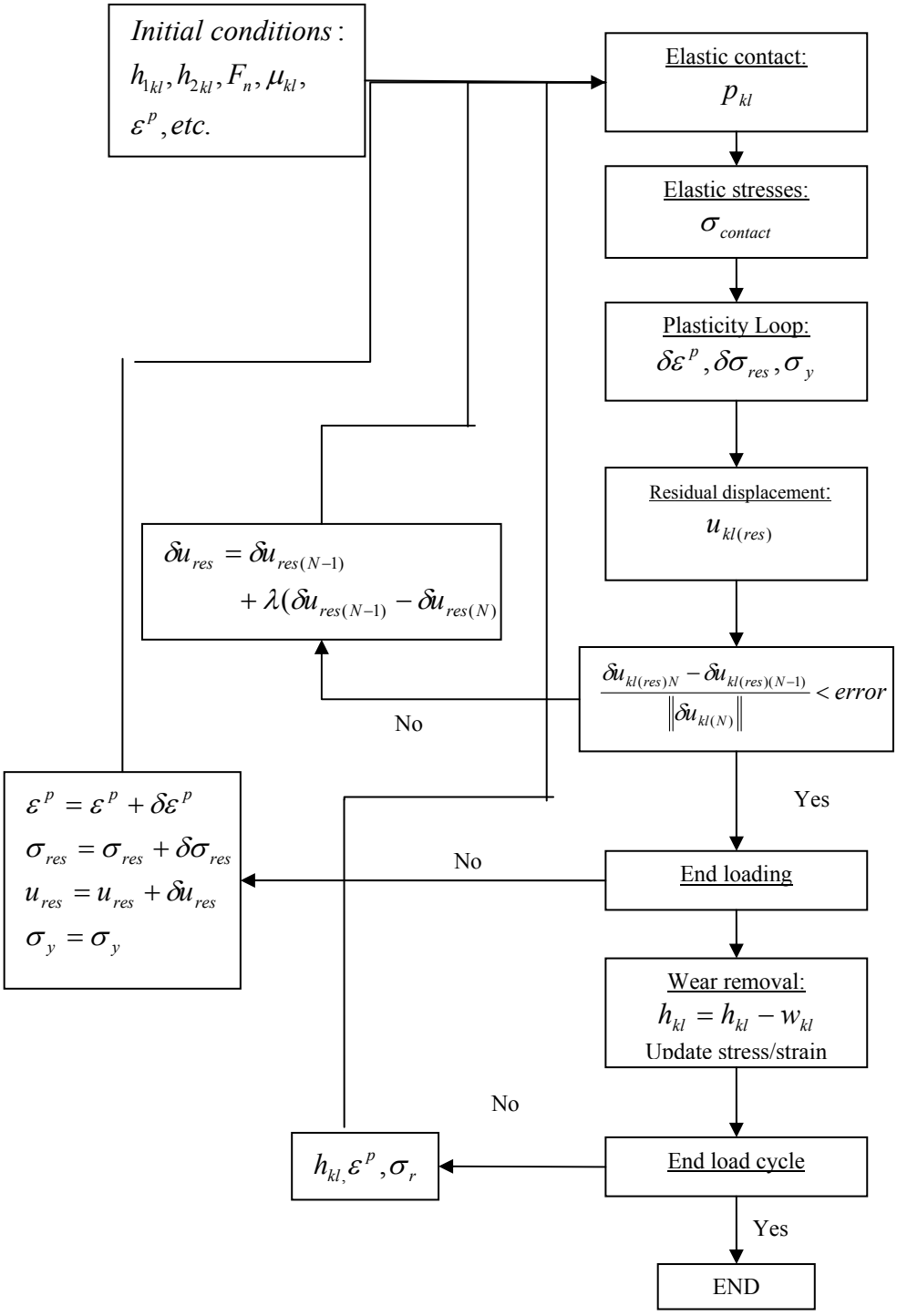


**Figure 6:** Flowchart of wear model

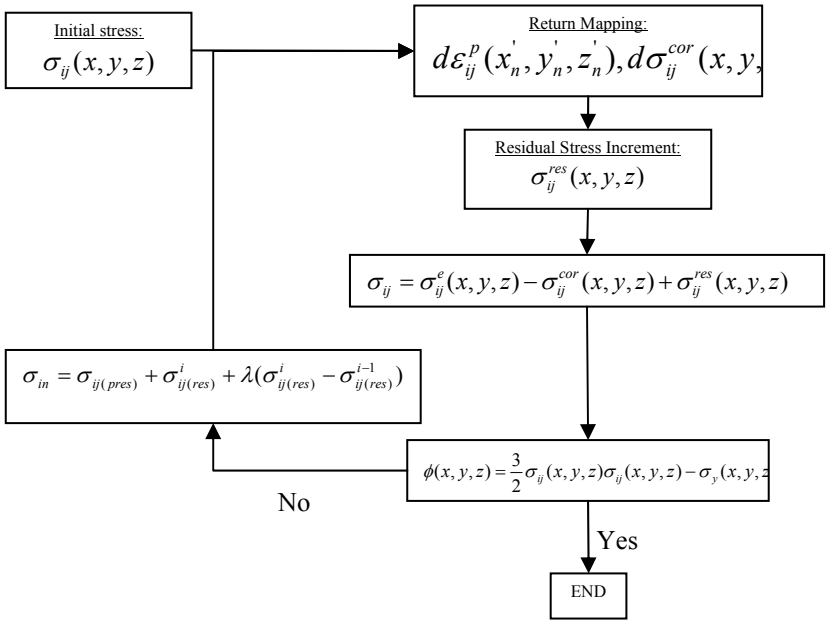


**Figure 7:** New "plasticity loop" based on the stress relaxation rather than on the relaxation of the plastic strain.

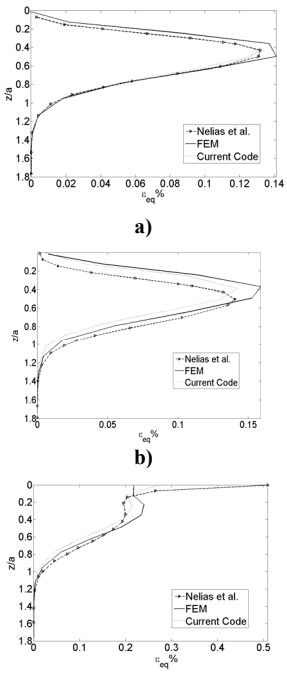


**a)**

**b)**

**c)**

**Figure 8:** Equivalent plastic strain for the elasto-plastic solutions given in [21] compared with the current code and FEM results **a)** for the frictionless case **b)** cof=0.2 **c)** cof=0.4

The first one is that the NC-layer only exhibits hardening: introducing a hard surface layer capable of withstanding the high local pressures present at the peaks of the asperities, resulting in a hardness profile shown in Figure 9-a. The second theory states that the NC-layer formed has a gradual increase/decrease curve and thus has a very ductile nature. This will prevent high shear strains in the bulk material preventing the forming of cracks in the bulk material while the NC-layer accommodates the required plastic strain. The hardness profiles resulting from this theory are presented in Figure 9-b. These curves are reproduced from measurements presented in [6]. The three curves represented: curve A originates from a new sampled after polishing, curve B from a mild wear test and curve C from a failed (high wearing) system. These three curves are mainly of interest to see if the change seen from hardness profile A to curve B has a positive effect in the simulations, since this is the profile created and thus favored by a system with low wear.

## FRICTION MODEL

The next step is to formulate a criterion for the failure of the boundary layers so the local coefficient of friction can be determined. The coefficient of friction will be split into two regimes: high local coefficient of friction by metal to metal contact and a low coefficient of friction where the main shearing is located in the chemical reaction layer.

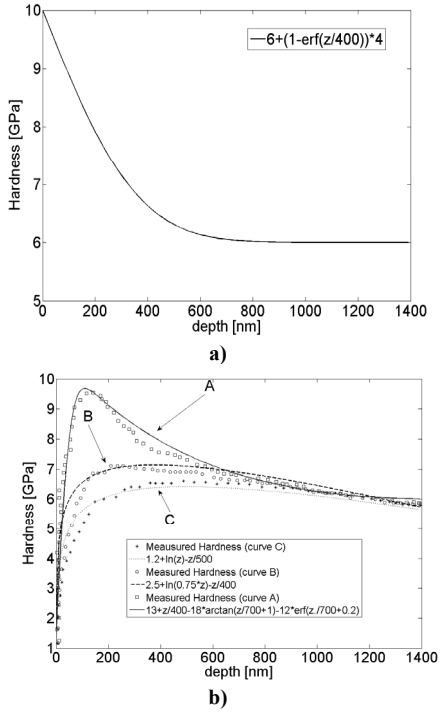


**Figure 9:** Hardness profile according to measurements presented in literature. **a)** Increasing hardness towards the surface. **b)** Different hardness profiles for curve A polished surface, curve B mild wearing surface and curve C for a severe wearing surface [7].

The defined regimes have different coefficients of friction in the range of 0.1 and 0.4 for protected and unprotected areas respectively. The transition from the one to the other is seen as a stepwise phenomenon, if the failure criterion of the layer is transcended the coefficient of friction "jumps" to the higher value. A representation of the boundary layer is given in Figure 1. Here the adsorbed layer is equivalent to the high viscous layer reported in different studies and does not play a role in the anti-wear properties at severe conditions [31-33], which are typical for run-in situations. To model the chemically reaction layer an assumption has to be made regarding the material model to be used for this layer, e.g. what kind of behavior this layer has. Based on the work presented in [29] it is suggested that the chemical reacted boundary layers acts as a solid rather than a viscous fluid. In this study the boundary layer is thus modeled as an elastic-plastic solid, where the transition from elastic to plastic is defined by the von Mises yield criterion as is used for the bulk material. The properties of this layer are based on averaging the properties given from the different studies presented in Table 2. The main properties determined from this table are the thickness of the layer estimated at 100 nm and the Young's modulus of the layer of 80 GPa. The yield stress of the surface layer is not very well defined in the different studies and ranges from 2 GPa up to 6 GPa. However, if the layer thickness is estimated at 100 nm the indentation depth is not to exceed 10 nm for the hardness measurement. This is not the case for the measurements reporting 6 GPa and to the authors opinion the hardness of the NC-layer/bulk material is influencing the measurement significantly and this results in a unrealistic high hardness. For this reason the simulations are done with a chemical layer with a hardness of 2 GPa, which results in a yield stress of approximately 0.7 GPa.

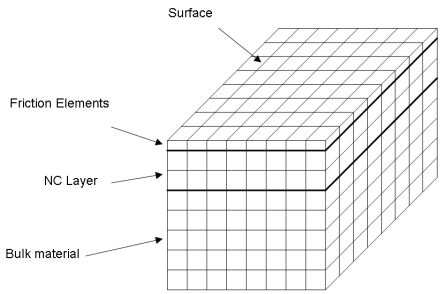


**Figure 10:** Representation of the wear model built up.

| Ref. # | $P_n$ [MPa] | $V$ $[m/s]$ | $T_{bath}$ $[C^o]$ | $t_{layer}$ $[nm]$ | $E_{layer}$ [GPa] |
|---|---|---|---|---|---|
| [30] | 504 | 0.3 | 100 | 115 | 85-75 |
| [31] | 504 | 0.3 | 100 | 60-120 | - |
| [32] | 700 | 0.03 | 83 | 40-100 | - |
| [33] | 700 | - | 83 | 100 | - |
| [34] | 500 | ~0.3 | 100 | 30-60 | - |
| [35] | - | - | - | 100 | 81 |
| [36] | 400 | ~0.3 | 100 | 70 | 96 |
| [37] | 500 | ~0.3 | 100 | 300 | 120-90 |
| [38] | ~300-500 | 0.03 | 83 | <100 | 130 |
| [39] | 10-50 | 0.25-0.55 | 100 | <100 | |
| [40] | 360 | - | 100 | 140 | 90 |
| [41] | ~425 | 0.34 | 100 | 160> | 122.7 |
| [42] | 590 | ~0.3 | 100 | ~160 | 81 |
| [43] | 600 | 0.01 | 80 | <60 | - |
| [44] | 135 | ~0.35 | 100 | 60-180 | 90-120 |
| [45] | 300 | ~0.3 | 100 | 30-60 | - |
| [46] | 950 | 0.1 | 100 | 120 | - |

**Table 2:** Results for thickness and Young's modulus for the chemical reacted layer retrieved from literature resulting from rubbing experiments in ZDDP rich oils.

The model described before can visually be expressed as show in Figure 10, where the bulk material is protected by "friction-elements", representing the chemical layer, which currently have the sole purpose to indicate the coefficient of friction locally present, under which the NC material is located.

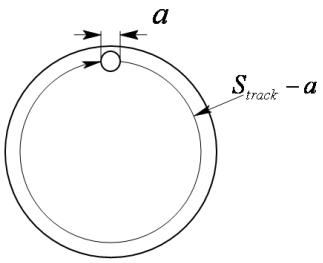


**Figure 11:** Wear track vs. apparent contact area

The pressure criterion is based on the idea first presented in [47] and [48], where it is suggested the growth of tribo-chemical film protecting the surface must be greater then the removal rate for the lubricant to protect the surface against severe wear. Here it is assumed that the growth is diffusion based process and can be expressed as:

$$h_{growth}(t) = K_0\sqrt{t} \tag{11}$$

, the different values of $K_0$ are given in Table 3. The nominal pressure is lower than the system studied however since it is assumed that the growth of the layer will take place outside the contact area the main factor influencing the growth rate will be the temperature of the oil.

| Oil bath temperature $T\ [^oC]$ | Eff. Diffusion Coefficient $K_0\ [nm\ s^{-1/2}]$ |
|---|---|
| 50 | 2.451 |
| 100 | 3.644 |
| 150 | 4.620 |
| 200 | 4.916 |

**Table 3:** Effective diffusion coefficients measured in [47] at different oil bath temperatures at nominal contact pressures of 22 MPa.

The amount the chemical layer removal is indicated by the plastic strain in the direction normal to the surface ($\varepsilon_{zz}^{layer}$). Due to its limited thickness it is safe to assume all stresses do not vary through the thickness of the layer ($\partial\sigma_{ij}/\partial z = 0$), e.g. the plain stress state. To calculate the plastic strain the following simplification of the conditions the layer has to withstand are made. From the bulk side the layer is stretched by the strain of the bulk material, because it sticks to the bulk material (no slip condition between layer and bulk material) and at the top the pressure and shear is put on the surface of the layer. This results for the pre-strain in:

$$\sigma_{ii_{layer}} = \frac{E_{layer}}{2(1+\nu_{layer})}\varepsilon_{ii_{bulk}} + \frac{\nu_{layer}E_{layer}}{(1+\nu_{layer})(1-2\nu_{layer})} (\varepsilon_{ii_{bulk}} + \varepsilon_{jj_{bulk}} + \varepsilon_{kk_{bulk}}) \quad (12)$$

Where $i, j$ and $k$ can be $x, y$ or z and the external pressures from the top side are given by the normal load and the traction:

$$\sigma_{zz_{layer}} = \sigma_{zz_{layer}} + P \quad (13)$$

$$\sigma_{xz_{layer}} = \mu P \quad (14)$$

Using these stress conditions the plastic strain can be calculated. The maximum plastic strain allowed in normal direction is determined by the amount of growth gained every cycle. This is done to satisfy the chemical balance which is needed for the protection:

$$\dot{X}(t) \geq \dot{W}(t) \quad (15)$$

Here $\dot{X}(t)$ is the growth rate of the chemical film and $\dot{W}(t)$ is the wear rate. If now the growth rate is expressed per cycle and it is assumed the layer only grows outside the apparent contact area the time of growth will be, see Figure 11:

$$t_{gr} = \frac{s_{track} - a}{|V_1 - V_2|} \quad (16)$$

The maximum amount of plastic strain allowed in the normal direction over the thickness of the layer per contact cycle can be expressed as:

$$\varepsilon_{zz\max}^{layer} = \frac{\sqrt{t_{gr}}K_0}{h_{balance}} \quad (17)$$

Here $h_{balance}$ is the layer thickness measured for a system, see Table 2.

## WEAR MODEL

In the current model the coefficient of friction is determined locally as discussed in the previous section by assuming the protection of the lubricant is limited to preset contact conditions, e.g. a maximum amount of chemical film that is allowed to be removed each contact cycle given by eq. (17). As for the coefficient of friction also the wear can be thought of as a twofold mechanism: local severe wear and local mild wear. For the mild wear (protected) situation it is first assumed that negligible wear will occur at these locations since the shearing will be located in the boundary layers formed on the steel surface and thus no bulk material will directly be removed. This corresponds well with real systems running in mild conditions since particles generated by this type of systems are mainly built up from chemical products which originated from the chemicals present in the oil [48-49].

The severe wear is based on the brittle wear behavior of high strength carbon steels and is associated with a high coefficient of friction. The train of thought in the wear model used here is introduced by Nelias in [19]. The wear model is found upon a recent study of Oila [49], who stated that micro-pitting was related to micro-cracks underneath the surface. To predict the formation of these micro-cracks a crack criterion is needed, which is currently simulated as a maximum equivalent plastic strain. It is then assumed that the crack runs along the line of the plastic volume both reaching the surface and transcending the critical strain value, creating a wear volume. In the current simulations it is assumed that the wear volume is removed in only one cycle directly after it is formed. Incorporating this threshold directly in the system creates very large wear since sharp edges will be created on the sides of the worn volume. To deal with this problem the volume removed is smoothened

using a Savitzky–Golay smoothing filter. This however introduces numerical artifacts, which can be used to modify the model for less or more ductile materials. This is left out in the discussion in [19] as will be done currently for brevity, but is discussed in detail in [50] and the reader is thus referred to this work for more details on the smoothening. The complete wear model is schematically shown in Figure 6. To reduce the effect of the element size on the wear volume an interpolation is used to determine the wear depth, again for more details the reader is referred to [50].

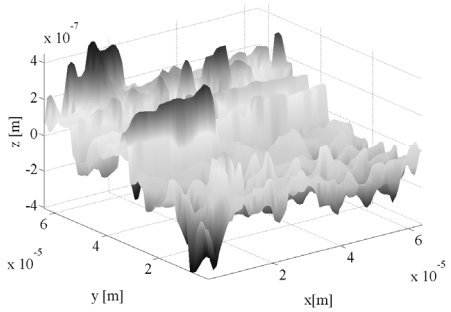


**Figure 12:** Surface profile of the surface used in the simulations: a relatively rough, hard turned surface.

## RESULTS

Using the methods discussed above a set of examples will be calculated, using a relatively rough surface of a hard turned pin (Figure 12). This surface is measured using an inter-reference microscope with a lateral resolution of 1 micron and a depth resolution of 1 nm. The $Ra$ value of the surface is 0.270 $\mu m$. Using the values of $K_0$ given in Table 3, a contact width of 300 $\mu m$, total wear track of 314.15 *mm* (e.g. track radius of 50 *mm*), a oil bath temperature of 100 $^oC$ and a sliding speed of 1 *m/s* gives a growth of the chemical layer of 2.04 *nm* for each cycle. Using an average chemical layer thickness of 100 *nm* results in $\varepsilon_{zz\,\max}^{layer} = 2\%$, which will be used in the current simulations. The nominal contact pressure for the contact simulations is kept at approximately 150 *MPa* (a normal load of maximal 0.6 N). This load is applied in a linear increasing and decreasing signal while a Coulomb friction law is used to simulate a quasi-sliding situation. A load cycle refers to a complete increase and decrease of the normal load while a load step refers to one incremental load step.

The next step is setting up a threshold for the equivalent plastic strain at which the bulk material and NC material will tear. Here two different material models will be evaluated, one for the base material and one for the NC-layer. The base material is represented by a failure strain given in [19] of 0.2 % equivalent strain. For the NC-layer a higher equivalent strain will be used in the range of 2%. In reality this value might be much higher since in literature super plasticity is reported for some types of NC material. The reason for the adaptation of the material model is to give show the effect of a more ductile soft layer at the surface as would be formed by the tribosystem through the reduction of the grain size in the form of a NC-layer underneath the surface [8, 51]. For the work hardening of both materials a Swift hardening law combined with a isotropic hardening model is used:

$$\sigma_{yield}(\varepsilon_{pl_{eq}}) = B(C + \varepsilon_{pl_{eq}} \cdot \alpha)^n \qquad (18)$$

The parameters used are $B$=1780, $C$=4, and n=0.095. If $\alpha$ is set to $10^6$ the material model represents AISI 52100, which is a highly work hardening material with very limited plastic strain $\varepsilon_{pl_{eq}\,\max} = 0.2\%$.

### Simulation Results

For the brittle bulk material model the results are presented in Figure 13. Here it can be seen that the mean wear takes place in the first 6 load cycles and then is reduced to only mild wear, see Figure 13-c and d. This suggests very good wear resistance, however looking at the friction coefficient it can be seen the coefficient of friction remains at a relatively high level (0.17), due to the fact that the surface stays relatively rough and the oil can not provide sufficient protection at all contact

locations. If the friction level remains at this high value more energy will be dissipated and thus available for inducing wear which is not wanted in a system. The efficiency of the system itself will also be reduced by the higher frictional level. However, since mild wear is currently not modeled the exact influence of the higher friction level is difficult to quantify. However, higher friction levels induce higher contact temperatures and a more tribologically stressed system. As the removal rate of the chemical layer is higher it can be suggested that the wear level of this type of system will be increased by a more corrosive wear mechanism. In the second calculation example the material model curve A is used see Figure 9. The results of the simulation are given in Figure 14 and it can be concluded that the wear volume here is increasing in a linear manner after it is stabilized after the first load cycles. This suggests that the surface is still smoothening (running-in) after 25 cycles. This is also represented in a lowering of the overall coefficient of friction. This suggests that the surface roughness is reduced more than when bulk material would be present at the surface instead of the NC layer, which reduces the stress put on the chemical protective layer. The effect of a NC-layer on top of the bulk material would in this case be isolating the plastic core into the surface material ensuring that material removal will result in a smoothening of the surface and thus local pressure reduction, which will reduce wear on the larger time scale. At first sight the presence of a NC-layer with the properties of material curve A would not be beneficial; however with respect to the lifetime of the component it will be. Especially if the ductility would be increased due to super plasticity, however this concept is not fully understood in NC materials yet and is thus left out of the discussion for this moment.

Calculation of the frictional and wear behavior using curve B or curve C (which is very close to curve B) as the material model for the NC layer one finds that the effect of roughness reduction is even more pronounced, see Figure 15, and the system and the overall fictional level is reduced even further for the complete contact, e.g. the oil is capable of protecting the complete system. To the authors opinion this is the system strived for by nature, since the least amount of energy is dissipated through frictional losses. However, as can be concluded from the figure the wear volume is still increasing linearly after 25 cycles while the complete surface is protected by the chemical layer which is most probably due to the very strictly chosen $\varepsilon_{pl_{eq}\max} = 2\%$ for the NC-material. In literature both high and low equivalent strain values are reported for the NC-layer. For this purpose a simulation is run where the maximum equivalent strain is increased to $\varepsilon_{pl_{eq}\max} = 5\%$, the results of which are presented in Figure 16. The effect of increasing the strain is mainly limited to the first 5 cycles after which the slope of the wear volume increase is stabilized at the same value as for the simulations run with an equivalent strain of $\varepsilon_{pl_{eq}\max} = 2\%$.

If the hardness curve showing only hardening within the NC layer is used, the results for the calculations are given in Figure 17. The wear volume is in the same range as for the bulk material model, with the difference that the wear is still slowly increasing after 25 cycles, suggesting a slowly smoothening surface. This effect will lower the local pressure put on the protecting layer, decreasing the overall coefficient of friction. This mechanism would very well be the most beneficial for the system since the removal rate is low compared to the ones obtained using a soft ductile NC layer and the while still effectively reducing the local pressure by roughness reduction, resulting in mild running conditions and as a result a low wearing system without a large volume loss of material.

## CONCLUSIONS

A wear model is presented which is based on the hypothesis that a system which wears under mild oxidative conditions is protected by a surface layer of which the removal and grow

rate are in balance. The values used as an input for this model are taken from literature and are therefore realistic values. To investigate the effect the different material properties of the NC layer, reported throughout literature, has on the wear of this type of system 3 different material behaviors are included in the model. From the results it can be concluded that the presence of a NC-layer has a great influence on the wear behavior and frictional behavior of the system. The most beneficial would be a NC layer with increased hardness towards the surface while also presenting a slight increase of ductility (maximum equivalent strain set at 2 percent). The real properties of the NC layer are still unclear yet and future research on this will hopefully give a better insight into the properties and origin of this important layer.

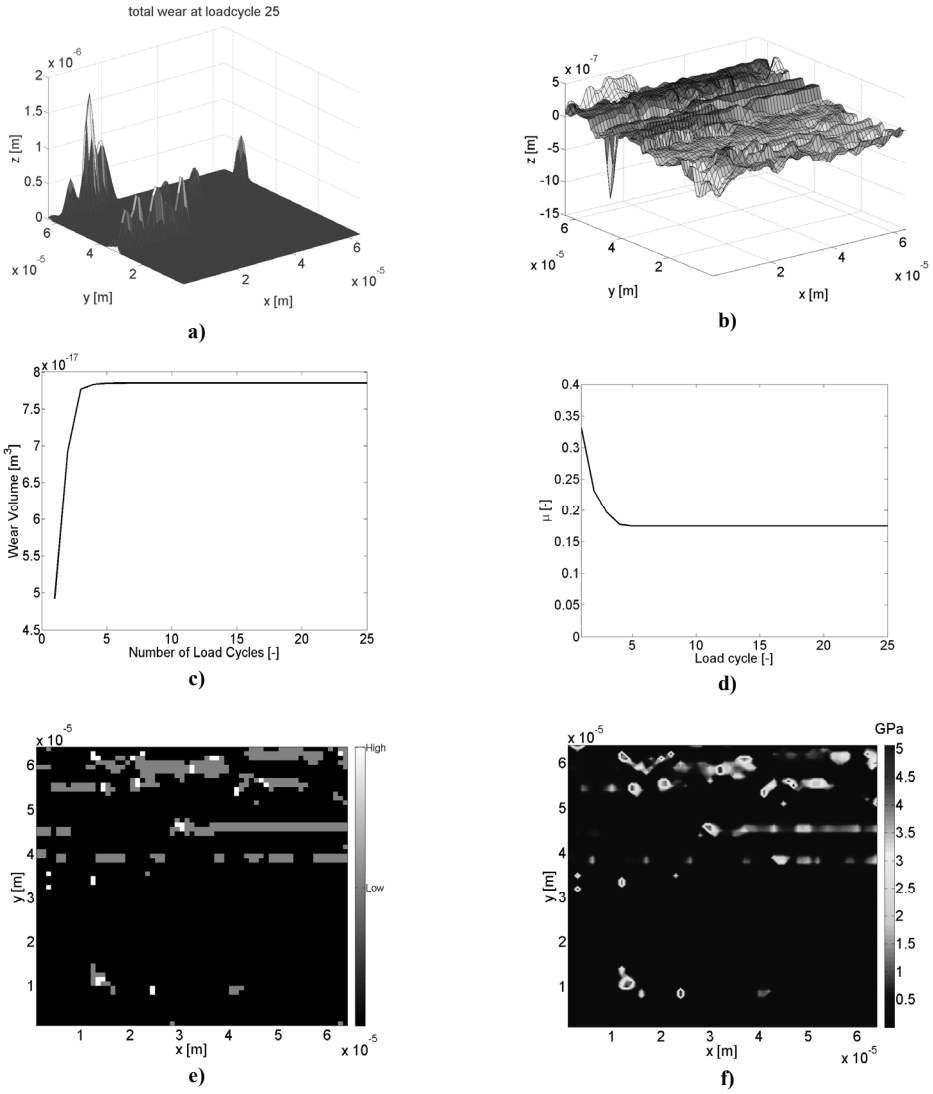


**Figure 13:** Results for the simulation with bulk material properties **a)** wear volume after 25 cycles **b)** original surface geometry (transparent) vs. worn surface (solid) **c)** Wear volume as a function of load cycle **d)** Coefficient of friction vs. load cycle **e)** Local coefficient of friction at cycle 25 (black no contact, white high friction, gray low friction. f**)** Pressure field.

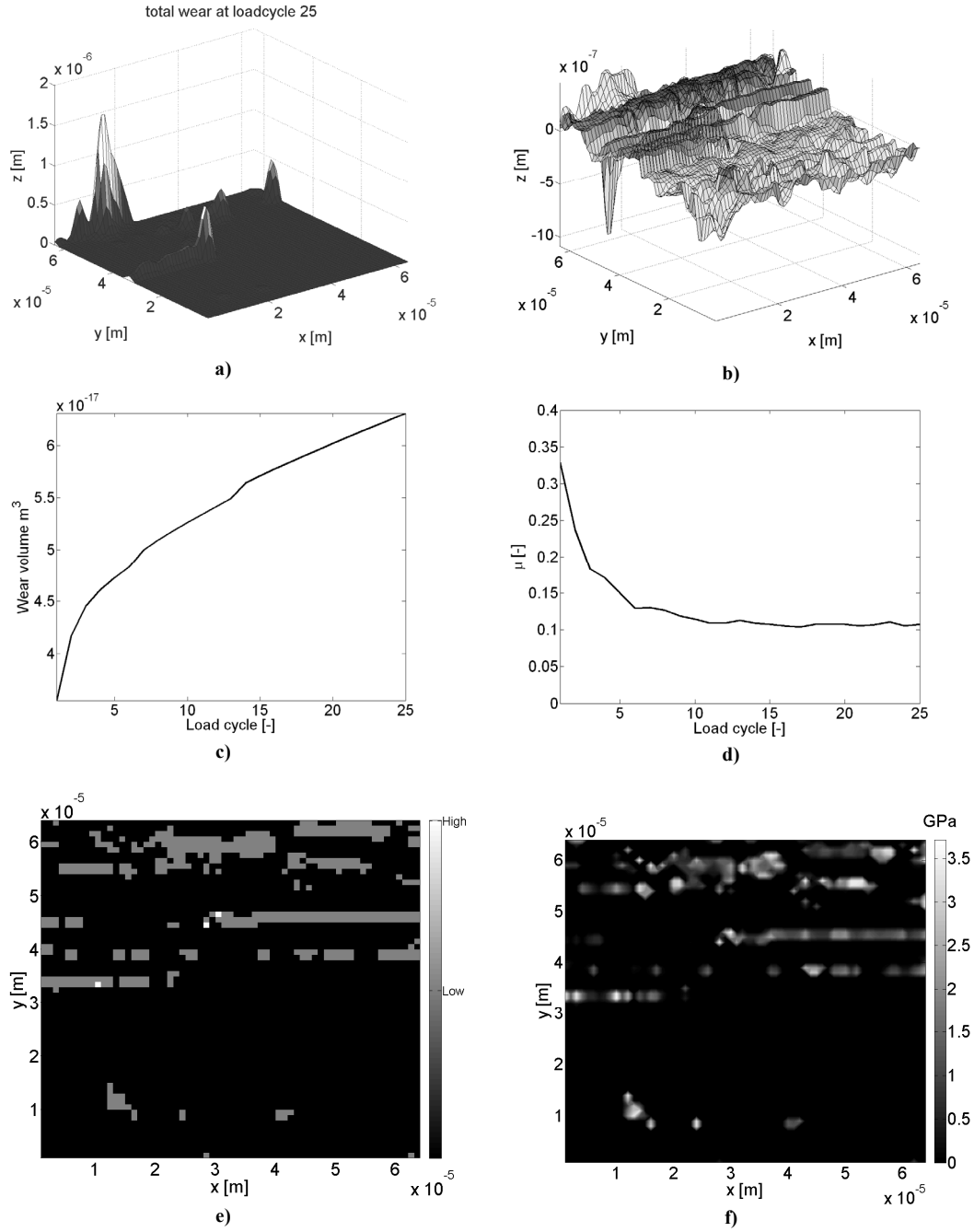


**Figure 14:** Results for the simulation with material curve A: **a)** wear volume after 25 cycles **b)** original surface geometry (transparent) vs. worn surface (solid) **c)** Wear volume as a function of load cycle **d)** Coefficient of friction vs. load cycle **e)** Local coefficient of friction at cycle 25 (black no contact, white high friction, gray low friction. **f)** Pressure field.

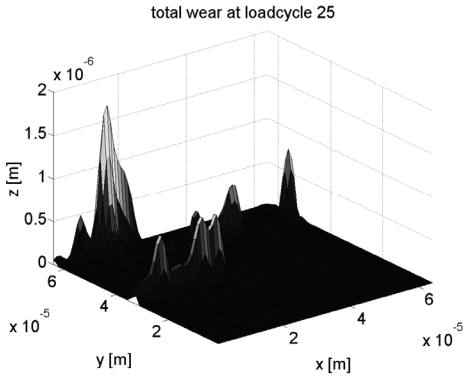


a)

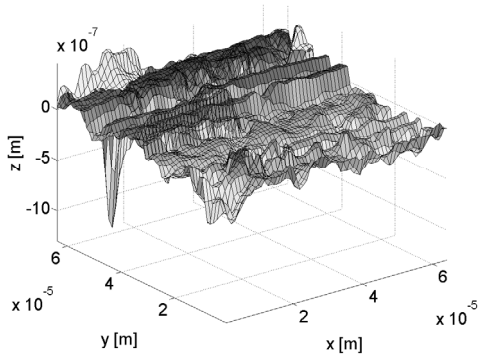


b)

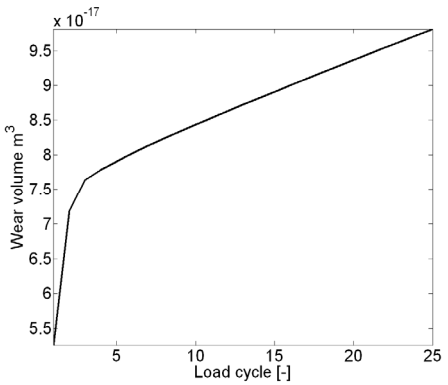


c)

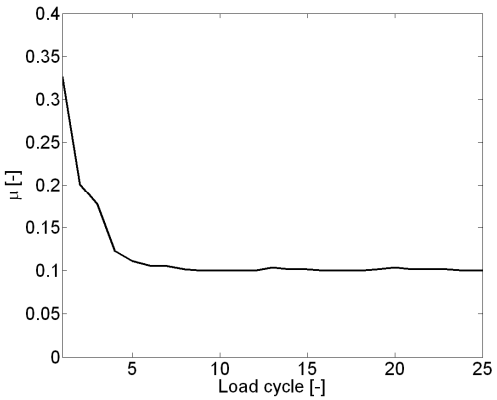


d)

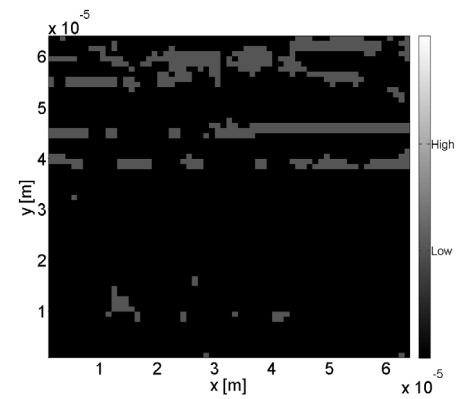


e)

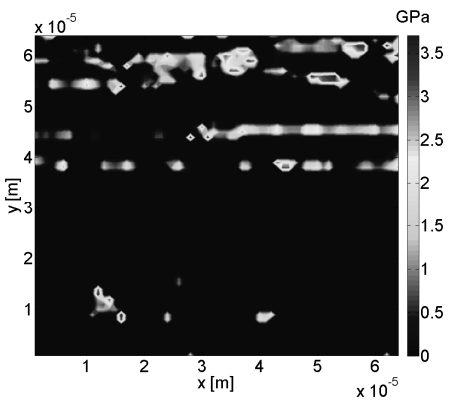


f)

**Figure 15:** Results for the simulation with material curve B/C **a)** wear volume after 25 cycles **b)** original surface geometry (transparent) vs. worn surface (solid) **c)** Wear volume as a function of load cycle **d)** Coefficient of friction vs. load cycle **e)** Local coefficient of friction at cycle 25 (black no contact, white high friction, gray low friction. **f)** Pressure field.

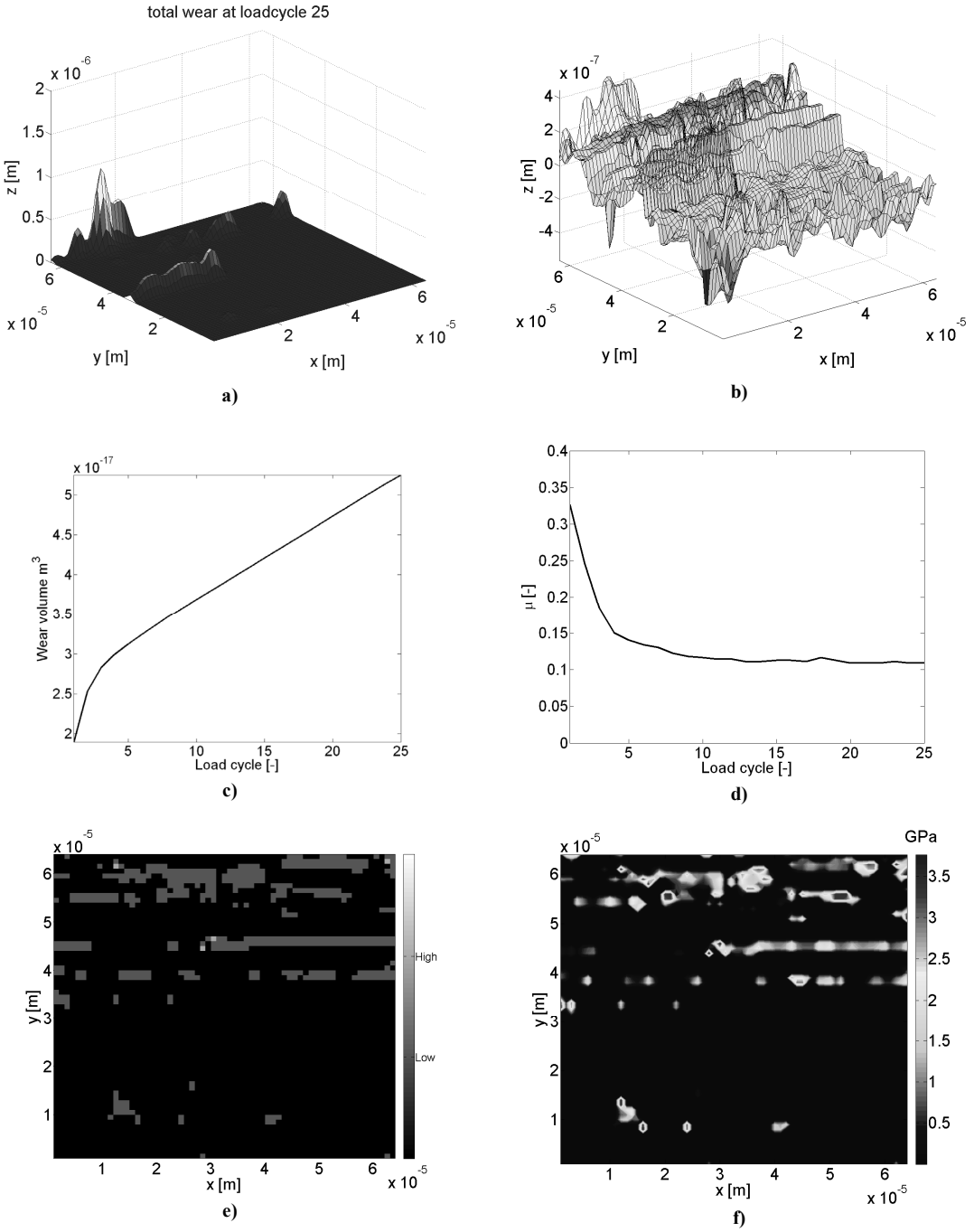


**Figure 16:** Results for the simulation with material curve B with $\varepsilon_{pmax}$ **a)** wear volume after 25 cycles **b)** original surface geometry (transparent) vs. worn surface (solid) **c)** Wear volume as a function of load cycle **d)** Coefficient of friction vs. load cycle **e)** Local coefficient of friction at cycle 25 (black no contact, white high friction, gray low friction. **f)** Pressure field..

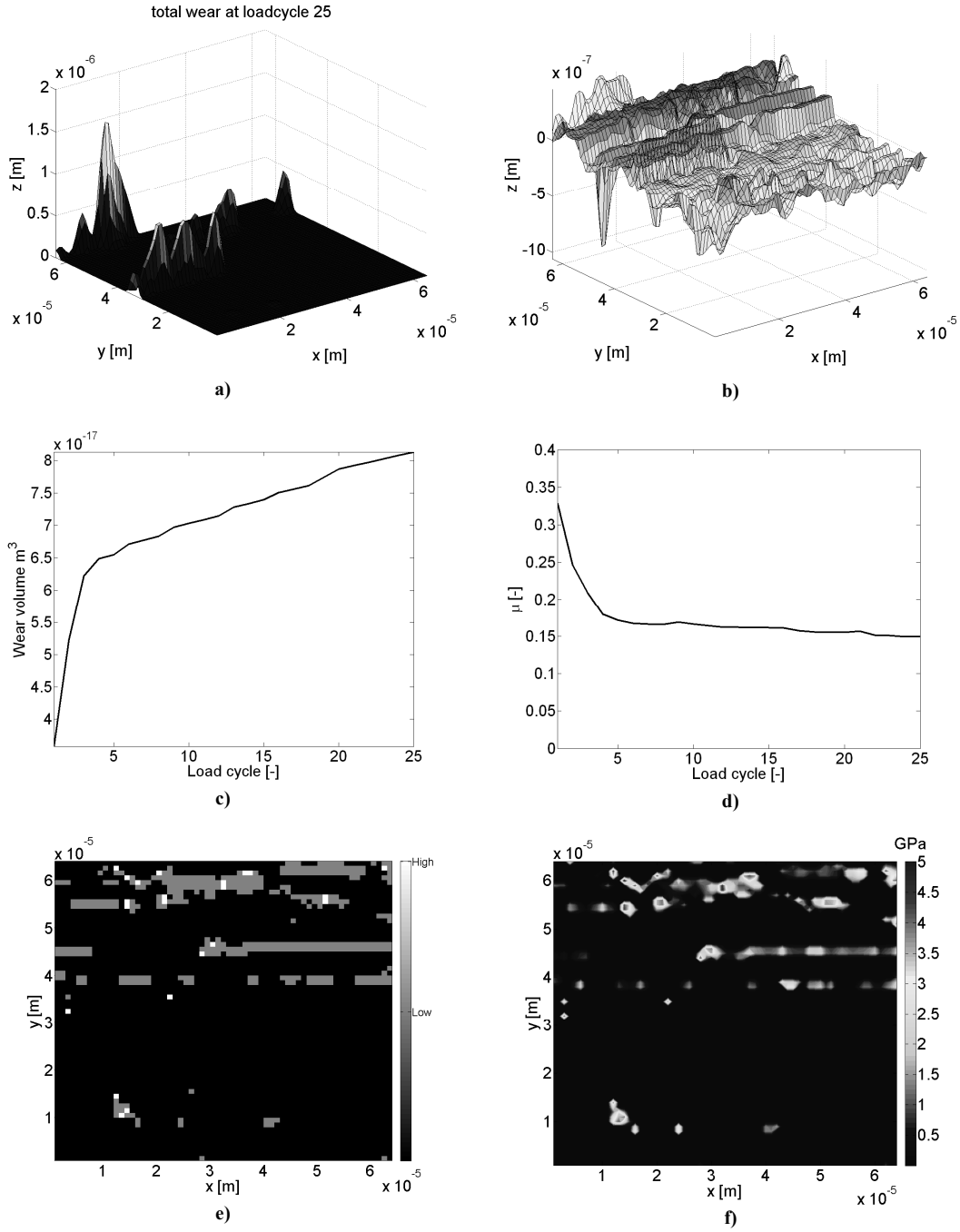


**Figure 17:** Results for the simulation with only hardening towards the surface **a)** wear volume after 25 cycles **b)** original surface geometry (transparent) vs. worn surface (solid) **c)** Wear volume as a function of load cycle **d)** Coefficient of friction vs. load cycle **e)** Local coefficient of friction at cycle 25 (black no contact, white high friction, gray low friction. **f)** Pressure field.

**APPENDIX**

## Surface displacement coefficients

The surface displacement due to a unit pressure put on a surface patch of size $2a \times 2b$ [52]:

$$D_{33}^{n} = \frac{1}{\pi E}\left\{\begin{array}{l}(x+a)\ln\left(\frac{(y+b)+\sqrt{(y+b)^2+(x+a)^2}}{(y-b)+\sqrt{(y-b)^2+(x+a)^2}}\right)+(y+b)\ln\left(\frac{(x+a)+\sqrt{(y+b)^2+(x+a)^2}}{(x-a)+\sqrt{(y+b)^2+(x-a)^2}}\right)+\\ (x-a)\ln\left(\frac{(y-b)+\sqrt{(y-b)^2+(x-a)^2}}{(y+b)+\sqrt{(y+b)^2+(x-a)^2}}\right)+(y-b)\ln\left(\frac{(x-a)+\sqrt{(y-b)^2+(x-a)^2}}{(x+a)+\sqrt{(y-b)^2+(x+a)^2}}\right)\end{array}\right\}$$

The surface displacement due to unit traction put on a surface patch of size $2a \times 2b$ [52]:

$$D_{31}^{n} = \frac{1-2\nu}{4\pi G}\left\{\begin{array}{l}(y+b)\ln\left(\frac{\sqrt{(x+a)^2+(y+b)^2}}{\sqrt{(x-a)^2+(y+b)^2}}\right)+(y-b)\ln\left(\frac{\sqrt{(x-a)^2+(y-b)^2}}{\sqrt{(x+a)^2+(y-b)^2}}\right)+\\ (x+a)\left(\arctan\frac{y+b}{x+a}-\arctan\frac{y-b}{x+a}\right)+(x-a)\left(\arctan\frac{y-b}{x-a}-\arctan\frac{y+b}{x-a}\right)\end{array}\right\}$$

Expressions for the surface displacement due to a volume element of size $2a \times 2b \times 2c$ with uniform strains inside the volume [27]:

$$K_{ij} = -\frac{1}{\pi}\left[\begin{array}{l}-2\varepsilon_{13}(R_{,133}-\phi_{,1})-2\varepsilon_{23}(R_{,233}-\phi_{,2})+2\varepsilon_{12}(D\psi_{,12}+R_{,123})\\ +\varepsilon_{11}(D\psi_{,11}+R_{,113})+\varepsilon_{22}(D\psi_{,22}+R_{,223})+\\ \varepsilon_{33}((2-3)\phi_{,3}+R_{,333})-2\nu\varepsilon_{ii}\phi_{3}\end{array}\right]\Bigg|_{-a}^{a}\Bigg|_{-b}^{b}\Bigg|_{-}^{c} \qquad (19)$$

$$S_{113}^{elas}(x,y,z) = 2\nu\tan^{-1}\left(\frac{z^2+y^2-Ry}{zx}\right)+2(1-\nu)\tan^{-1}\left(\frac{R-y+z}{x}\right)+\frac{xyz}{R(x^2+z^2)}$$

$$S_{223}^{elas}(x,y,z) = 2\nu\tan^{-1}\left(\frac{z^2+y^2-Ry}{zx}\right)+2(1-\nu)\tan^{-1}\left(\frac{R-x+z}{y}\right)+\frac{xyz}{R(y^2+z^2)}$$

$$S_{333}^{elas}(x,y,z) = \tan^{-1}\left(\frac{z^2+y^2-Ry}{zx}\right)-\frac{xyz}{R}\left(\frac{1}{x^2+z^2}+\frac{1}{y^2+z^2}\right)$$

$$S_{123}^{elas}(x,y,z) = -\frac{z}{R}-(1-2\nu)\ln(R+z)$$

$$S_{133}^{elas}(x,y,z) = \frac{z^2 y}{R(x^2+z^2)}$$
$$S_{233}^{elas}(x,y,z) = \frac{z^2 x}{R(y^2+z^2)} \tag{20}$$

$$S_{111}^{elas}(x,y,z) = \frac{-z}{R}\left[1+\frac{yz-x^2}{(R+z)(R-y)}\right]+2\nu\left(\frac{y}{(R+z)}\right)-2\ln(R-y)$$
$$S_{221}^{elas}(x,y,z) = \frac{-yz}{(R(R+z))}-2\nu\left(\frac{y}{R+z}+\ln(R-y)\right)$$
$$S_{331}^{elas}(x,y,z) = \frac{xy^2 R}{R\left(x^2+z^2\right)}$$
$$S_{121}^{elas}(x,y,z) = \frac{-zx}{(R(R+z))}-2\nu\left(\frac{x}{(R+z)}\right)-\ln(R-x)$$
$$S_{131}^{elas}(x,y,z) = \frac{xyz}{R\left(x^2+y^2\right)}+\tan^{-1}\left(\frac{z^2+y^2-yR}{xz}\right)$$
$$S_{231}^{elas}(x,y,z) = \frac{-z}{R} \tag{21}$$

The stress influence vector can be split up into 2 parts: one for the stress inside the plastic volume $\Omega_p$ and one outside the volume. The stresses outside the plastic volume:

$$S_{ijkl}^{pl} = \nu f(\varepsilon_{ij})_{k,kmm}\delta_{ij} - f(\varepsilon_{ij})_{k,kij} + (1-\nu)(f(\varepsilon_{ij})_{i,kkj} + f(\varepsilon_{ij})_{j,kki})\Big|_{-a}^{a}\Big|_{-b}^{b}\Big|_{-c}^{c}$$

The stress inside the volume:

$$S_{ijkl}^{pl} = \nu f(\varepsilon_{ij})_{k,kmm}\delta_{ij} - f(\varepsilon_{ij})_{k,kij} + (1-\nu)(f(\varepsilon_{ij})_{i,kkj} + f(\varepsilon_{ij})_{j,kki}) - \mu 2\varepsilon_{ij} - \lambda\varepsilon_{kk}\delta_{ij}\Big|_{-a}^{a}\Big|_{-b}^{b}\Big|_{-c}^{c}$$

Here is $\delta_{ij}$ the kronecker delta and $\mu = \frac{E}{2(1+\nu)}$ with the following definition of the derivatives of $f_{ijkl}$:

$$f_{i,jj}/C = 2\varepsilon_{1i}(\phi^I{}_{,1}+\phi_{,1}) + 2\varepsilon_{2i}(\phi^I_{,2}+\phi_{,2}) + 2\varepsilon_{3i}(\phi^I_{,3}-\phi_{,3}) \quad (i = 1 \text{ or } 2) \tag{22}$$

$$
\begin{aligned}
f_{3,jj}/C &= 2\varepsilon_{13}(\phi^I_{,1} + 4x_3 - 4R_{,133} + 3\phi_{,1}) + 2\varepsilon_{23}(\phi^I_{,2} + 4x_3\phi_{,23} - 4R_{,233} + 3\phi_{,2}) \\
&+ 8\varepsilon_{12}(-x_3\phi_{,12} + R_{,123} + D\psi_{,12}) + 4\varepsilon_{11}(-x_3\phi_{,22} + R_{,113} + D\psi_{,11}) + 4\varepsilon_{22}(-x_3\phi_{,22} \\
&+ R_{,223} + D\psi_{,22}) + 2\varepsilon_{33}(\phi^I_{,3} - 2x_3\phi_{,33} + 2R_{,333} - (5-4\nu)\phi_{,3}) - 8\nu\phi_{,3}
\end{aligned} \tag{23}
$$

$$
\begin{aligned}
f_{m,jjm}/C &= 4\varepsilon_{13}(\phi^I_{,13} - 2R_{,1333} + 2x_3\phi_{,133} + 3\phi_{,13}) \\
&+ 4\varepsilon_{23}(\phi^I_{,23} - 2R_{,2333} + 2x_3\phi_{233} + \phi_{,23}) \\
&+ 4\varepsilon_{12}(\phi^I_{,12} + 2R_{,1233} - 2x_3\phi_{123} + (1-4\nu)\phi_{,12}) \\
&+ 2\varepsilon_{11}(\phi^I_{,11} + 2R_{,1133} - 2x_3\phi_{,113} + (1-4\nu)\phi_{,11}) \\
&+ 2\varepsilon_{22}(\phi^I_{,22} + 2R_{,2233} - 2x_3\phi_{,223} + (1-4\nu)\phi_{,22}) \\
&+ 2\varepsilon_{33}(\phi^I_{,33} + 2R_{,3333} - 2x_3\phi_{,333} - (7-4\nu)\phi_{,33}) \\
&- 8\nu\varepsilon_{ii}\phi_{,33}
\end{aligned} \tag{24}
$$

$$
\begin{aligned}
f_{j,j}/C &= 2\varepsilon_{13}(R^I_{,13} - (3-4\nu)R_{,13} + 4(1-\nu)x_3\phi_{,1} - 2x_3R_{,133} + 2x_3^2\phi_{,13}) \\
&+ 2\varepsilon_{23}(R^I_{,23} - (3-4\nu)R_{,23} + 4(1-\nu)x_3\phi_{,2} - 2x_3R_{,233} + 2x_3^2\phi_{,23}) \\
&+ 2\varepsilon_{12}(R^I_{,12} - (1-2D^2)R_{,12} + 4(1-\nu)D(x_3 + x_3')\psi_{,12} + 2x_3R_{,123} - 2x_3^2\phi_{,12}) \\
&+ \varepsilon_{11}(R^I_{,11} + (1-2D^2)R_{,11} + 4(1-\nu)D(x_3 + x_3')\psi_{,11} + 2x_3R_{,113} - 2x_3^2\phi_{,11}) \\
&+ \varepsilon_{22}(R^I_{,22} + (1-2D^2)R_{,22} + 4(1-\nu)D(x_3 + x_3')\psi_{,22} + 2x_3R_{,2213} - 2x_3^2\phi_{,22}) \\
&+ \varepsilon_{33}(R^I_{,33} + (3-4\nu)R_{,33} + 8(1-\nu)x_3\phi_{,3} - 4(1-\nu)D\phi + 2x_3R_{,333} - 2x_3^2\phi_{,33}) \\
&- 2\nu\varepsilon_{ii}(\phi^I + (3-4\nu)\phi + 2x_3\phi_{,3})
\end{aligned} \tag{25}
$$

Here the functions $R, \psi, \phi$ are defined as $R = \sqrt{(x-x') + (y-y') + (z-z')}$, $\psi = \ln(R + \zeta_3)$ and $\phi = 1/R$. The derivatives of this functions are given using $k \neq j \neq i$ and $\zeta_1 = x - x'$, $\zeta_2 = y - y'$, $\zeta_3 = z - z'$ (convolution/infinite space) or $\zeta_3 = z + z'$ (correlation/ halfspace) which is indicated by either a superscript $^I$ or absence of one:

$$
\begin{aligned}
&\phi_{,k} = \zeta_j \ln\lfloor r + \zeta_l \rfloor + \zeta_l \ln\lfloor r + \zeta_j \rfloor - \zeta_k U_k \\
&\phi_{,kl} = \ln\lfloor r + \zeta_j \rfloor \qquad \phi_{,kk} = -U_k \qquad \phi_{,kkk} = -\zeta_i V_l - \zeta_l V_i \\
&\phi_{,kkl} = \zeta_k V_k \qquad \phi_{,123k} = \frac{-\zeta_k}{r^3} \qquad \phi_{,kkll} = -\zeta_k\zeta_l W_j \\
&\phi_{,kkkk} = \zeta_l\zeta_k W_j + \zeta_k\zeta_j W_l \qquad \phi_{,kkkl} = V_j - \zeta_k^2 W_j
\end{aligned}
$$

$$R_{,kkl} = \zeta_k \ln\left[r+\zeta_j\right] \qquad R_{,kkk} = \zeta_i \ln\left[r+\zeta_l\right] + \zeta_l \ln\left[r+\zeta_j\right] - 2\zeta_k U_k$$

$$R_{,123k} = \frac{\zeta_k}{r} \qquad R_{,kkkl} = \ln\left[r+\zeta_j\right] + \zeta_k^2 V_j \qquad R_{,kkll} = \zeta_k \zeta_l V_j$$

$$R_{,kkkk} = -\zeta_j \zeta_k V_l - \zeta_l \zeta_k V_j - 2U_k \qquad R_{,123kl} = \frac{-\zeta_k \zeta_l}{r^3}$$

For $\psi$ and $\zeta_3\psi$ the derivative with respect to $\zeta_3$ become $\phi$ and $(\psi + R_{,3})$ respectively so in the following only indices $k$ and $l$ are used which are both different and have the value of 1 or 2:

$$\psi_{,kk} = -\zeta_k \ln\left[r+\zeta_l\right] - 2\zeta_3 X_k \qquad \psi_{,12} = \zeta_3 \ln\left[r+\zeta_3\right] - r$$

$$\psi_{,kkk} = -2\ln\left[r+\zeta_l\right] - (\zeta_k^2 + \zeta_3^2)V_l - (\zeta_3 - r)\zeta_l V_3 \qquad \psi_{,kkl} = -\frac{\zeta_k}{r+\zeta_3}$$

$$4(\zeta_3\psi)_{,kkk} = 2\zeta_l \ln\left[r+\zeta_3\right] - \zeta_3(\zeta_k^2 + \zeta_3^2)V_l - \zeta_3\zeta_l(\zeta_3 - r)V_3 - 4\zeta_k U_k$$

$$2(\zeta_3\psi)_{,kkl} = \zeta_k \ln\left[r+\zeta_3\right] - \frac{\zeta_k\zeta_3}{r+\zeta_3} \qquad 2(\zeta_3\psi)_{,kkll} = \zeta_k\zeta_l V_3 + \frac{\zeta_k\zeta_l\zeta_3}{(r+\zeta_3)^2 r}$$

$$4(\zeta_3\psi)_{4,kkll} = V_3\zeta_l\zeta_k\left(\frac{\zeta_3}{r} - 2\right) + \zeta_3\zeta_k\left[\zeta_l(\zeta_3 - r)W_3 - 6V_l + (\zeta_k^2 + \zeta_3^2)W_l\right]$$

$$4(\zeta_3\psi)_{,kkkl} = 2\ln\left[r+\zeta_3\right] + (3\zeta_k^2 - 2\zeta_3^2)V_3 + \zeta_3\zeta_l^2(\zeta_3 - r)W_3 + \frac{\zeta_l^2 r + (\zeta_k^2 +}{r^3} \qquad (26)$$

The different functions used in (26) are :

$$U_k = \tan^{-1}\left[\frac{\zeta_i\zeta_j}{\zeta_k r}\right] \qquad (27)$$

$$V_k = \frac{1}{r(r+\zeta_k)} \qquad (28)$$

$$W_k = \frac{2r+\zeta_k}{r^3(r+\zeta_k)^2} \qquad (29)$$

$$X_k = \tan^{-1}\frac{\zeta_k}{(r+\zeta_l+\zeta_j)} \qquad (30)$$

## REFERENCES


[1] H.C. Meng, K.C. Ludema: Wear models and predictive equations: their form and content. Wear. 181-183 443-457 (1995).

[2] J.F. Archard: Contact and Rubbing of Flat Surfaces. Journal of Applied Physics. 24 981-988 (1953).

[3] P. Põdra, S. Andersson: Simulating sliding wear with finite element method. Tribology International. 32 71-81 (1999).

[4] U. Olofsson, S. Andersson, S. Björklund: Simulation of mild wear in boundary lubricated spherical roller thrust bearings. Wear. 241 180-185 (2000).

[5] G.K. Sfantos, M.H. Aliabadi: Wear simulation using an incremental sliding Boundary Element Method. Wear. 260 1119-1128 (2006).

[6] D. Shakhvorostov, K. Pohlmann, M. Scherge: Structure and mechanical properties of tribologically induced nanolayers. Wear. 260 433-437 (2006).

[7] D. Shakhvorostov, B. Gleising, R. Büscher, W. Dudzinski, A. Fischer, M. Scherge: Microstructure of tribologically induced nanolayers produced at ultra-low wear rates. Wear. 263 1259-1265 (2007).

[8] H. Hahn, P. Mondal, K.A. Padmanabhan: Plastic deformation of nanocrystalline materials. Nanostructured Materials. 9 603-606 (1997).

[9] H. Kato, M. Sasase, N. Suiya: Friction-induced ultra-fine and nanocrystalline structures on metal surfaces in dry sliding. Tribology International. 43 925-928 (2009).

[10] L. Lu, M.L. Sui, K. Lu: Superplastic Extensibility of Nanocrystalline Copper at Room Temperature. Science. 287 1463-1466 (2000).

[11] J. Schiotz, F.D.D. Tolla, K.W. Jacobsen: Softening of nanocrystalline metals at very small grain sizes. Nature. 391 561-563 (1998).

[12] J. Schiotz, K.W. Jacobsen: A Maximum in the Strength of Nanocrystalline Copper. Science. 301 1357-1359 (2003).

[13] L. Lu, S.X. Li, K. Lu: An abnormal strain rate effect on tensile behavior in nanocrystalline copper. Scripta Materialia. 45 1163-1169 (2001).

[14] Z.B. Wang, N.R. Tao, S. Li, W. Wang, G. Lui, J. Lu, K. Lu: Effect of surface nanocrystallization on friction and wear properties in low carbon steel. Material science and Engineering. 352 114-119 (2002).

[15] Y. Wang, T. Lei, J. Liu: Tribo-metallographic behavior of high carbon steels in dry sliding: III. Dynamic microstructural changes and wear. Wear. 231 20-37 (1999).

[16] X.H. Chen, J. Lu, L. Lu, K. Lu: Tensile properties of a nanocrystalline 316L austenitic stainless steel. Scripta Materialia. 52 1039-1044 (2005).

[17] M. Umemoto: Nanocrystallization of steels by severe plastic deformation. Materials Transactions. 44 1900-1911 (2003).

[18] I. Garbar: Microstructural Changes in Surface Layers of Metal During Running-in Friction Processes. Meccanica. 36 631-639 (2001).

[19] D. Nelias, V. Boucly, M. Brunet: Elastic-Plastic Contact Between Rough Surfaces: Proposal for a Wear or Running-in Model. Journal of Tribology. 128 236-244 (2006).

[20] C. Jacq, D. Nelias, G. Lormand, D. Girodin: Development of a Three-Dimensional Semi-Analytical Elastic-Plastic Contact Code. Journal of Tribology. 124 653-667 (2002).

[21] D. Nelias, E. Antaluca, V. Boucly, S. Cretu: A Three-Dimensional Semianalytical Model for Elastic-Plastic Sliding Contacts. Journal of Tribology. 129 761-771 (2007).

[22] D. Godfrey: Boundary lubrication. Nasa Sp-118. 335-373 (1968).
[23] S. Liu, Q. Wang: Studying Contact Stress Fields Caused by Surface Tractions With a Discrete Convolution and Fast Fourier Transform Algorithm. Journal of Tribology. 124 36-45 (2002).
[24] H.S. Kim, M.B. Bush: The effects of grain size and porosity on the elastic modulus of nanocrystalline materials. Nanostructured Materials. 11 361-367 (1999).
[25] F. Wang, L.M. Keer: Numerical Simulation for Three Dimensional Elastic-Plastic Contact With Hardening Behavior. Journal of Tribology. 127 494-502 (2005).
[26] R. Bosman, D.J. Schipper: Running in of metallic surfaces in the boundary lubricated regime. Wear. Submitted (2010).
[27] S.B. Liu, Q. Wang: Elastic fields due to eigenstrains in a half-space. Journal of Applied Mechanics-Transactions of the Asme. 72 871-878 (2005).
[28] I.A. Polonsky, L.M. Keer: A numerical method for solving rough contact problems based on the multi-level multi-summation and conjugate gradient techniques. Wear. 231 206-219 (1999).
[29] C. Minfray, J.-M. Martin, T. Lubrecht, M. Belin, T.L. Mogne, M.P.G.D. D. Dowson, A.A. Lubrecht, A novel experimental analysis of the rheology of ZDDP tribofilms, Tribology and Interface Engineering Series, Elsevier. 2003, pp. 807-817.
[30] M.A. Nicholls, P.R. Norton, G.M. Bancroft, M. Kasrai, T. Do, B.H. Frazer, G.D. Stasio: Nanometer scale chemomechanical characterizaton of antiwear films. Tribology Letters. 17 205-336 (2003).
[31] Z. Zhang: Tribofilms generated from ZDDP and DDP on steel surfaces:Part I. Tribology Letters. 17 211-220 (2005).
[32] J.P. Ye, S. Araki, M. Kano, Y. Yasuda: Nanometer-scale mechanical/structural properties of molybdenum dithiocarbamate and zinc dialkylsithiophosphate tribofilms and friction reduction mechanism. Japanese Journal of Applied Physics Part 1-Regular Papers Brief Communications & Review Papers. 44 5358-5361 (2005).
[33] J.M. Martin, C. Grossiord, T. Le Mogne, S. Bec, A. Tonck: The two-layer structure of zndtp tribofilms Part 1: AES, XPS and XANES analyses. Tribology International. 34 523-530 (2001).
[34] M. Kasrai, S. Marina, B.G. Micheal, Y.E. S., R.P. Ray: X-ray adsorption study of the effect of calcium sulfonate on antiwear film formation generated from neutral and basic ZDDPs: Part 1 -Phosporus species. Tribology Transactions. 46 434-442 (2003).
[35] M.A. Nicholls, T. Do, P.R. Norton, M. Kasrai, G.M. Bancroft: Review of the lubrication of metallic surfaces by zinc dialkyl-dithiophosphates. Tribology International. 38 15-39 (2005).
[36] M. Aktary, M.T. McDermott, G.A. McAlpine: Morphology and nanomechanical properties of ZDDP antiwear films as a function of tribological contact time. Tribology Letters. 12 155-162 (2002).
[37] M.A. Nicholls, G.M. Bancroft, P.R. Norton, M. Kasrai, G. De Stasio, B.H. Frazer, L.M. Wiese: Chemomechanical properties of antiwear films using X-ray absorption microscopy and nanoindentation techniques. Tribology Letters. 17 245-259 (2004).
[38] J.P. Ye, M. Kano, Y. Yasuda: Evaluation of nanoscale friction depth distribution in ZDDP and MoDTC tribochemical reacted films using a nanoscratch method. Tribology Letters. 16 107-112 (2004).

[39] H.B. Ji, M.A. Nicholls, P.R. Norton, M. Kasrai, T.W. Capehart, T.A. Perry, Y.T. Cheng: Zinc-dialkyl-dithiophosphate antiwear films: dependence on contact pressure and sliding speed. Wear. 258 789-799 (2005).
[40] S. Bec, A. Tonck, J.M. Georges, R.C. Coy, J.C. Bell, G.W. Roper: Relationship between mechanical properties and structures of zinc dithiophosphate anti-wear films. Proceedings of the Royal Society of London Series a-Mathematical Physical and Engineering Sciences. 455 4181-4203 (1999).
[41] K. Komvopoulos, V. Do, E.S. Yamaguchi, P.R. Ryason: Nanomechanical and nanotribological properties of an antiwear tribofilm produced from phosphorus-containing additives on boundary-lubricated steel surfaces. Journal of Tribology-Transactions of the Asme. 126 775-780 (2004).
[42] O.L. Warren: Nanomechanical properties of films derived from zinc dialkyldithiophosphate. Tribology Letters. 4 189-198 (1998).
[43] C. Minfray, J.M. Martin, C. Esnouf, T. Le Mogne, R. Kersting, B. Hagenhoff: A multi-technique approach of tribofilm characterisation. Thin Solid Films. 447 272-277 (2004).
[44] G. Pereira, D. Munoz-Paniagua, A. Lachenwitzer, M. Kasrai, P.R. Norton, T.W. Capehart, T.A. Perry, Y.-T. Cheng: A variable temperature mechanical analysis of ZDDP-derived antiwear films formed on 52100 steel. Wear. 262 461-470 (2007).
[45] G.M. Bancroft, M. Kasrai, M. Fuller, Z. Yin, K. Fyfe, K.H. Tan: Mechanisms of tribochemical film formation: stabilityof tribo- and thermally-generated ZDDP films. Tribology Letters. 3 47-51 (1997).
[46] K. Topolovec-Miklozic, T. Forbus, H. Spikes: Film thickness and roughness of ZDDP antiwear films. Tribology Letters. 26 161-171 (2007).
[47] H. So, Y.C. Lin: The theory of antiwear for ZDDP at elevated temperature in boundary lubrication condition. Wear. 177 105-115 (1994).
[48] E.C. Cutiongco, Y.-W. Chung: Prediction of Scuffing Failure Based on Competitive Kinetics of Oxide Formation and Removal: Application to Lubricated Sliding of AISI 52100 Steel on Steel. Tribology Transactions. 37 622 - 628 (1994).
[49] A. Oila, S.J. Bull: Assessment of the factors influencing micropitting in rolling/sliding contacts. Wear. 258 1510-1524 (2005).
[50] V. Boucly, Semi-Analytical Modeling of the Transient-Elastic-Plastic Contact and its Application to Asperity Collision, Wear and Running in of Surfaces, PhD Thesis, Lyon, 2008 p 203
[51] R.D. Evans: Transmission Electron Microscopy of Boundary-Lubricated Bearing Surfaces. Part:II Mineral Oil Lubricant with Sulfur and Phosphorus-Containing Gear Oil Additives. Tribology Trasnsactions. 48 299-307 (2005).
[52] K. Willner: Fully Coupled Frictional Contact Using Elastic Halfspace Theory. Journal of Tribology. 130 031405-8 (2008).

Paper G

Mild Wear Prediction of Boundary Lubricated Contacts,
R. Bosman and D.J. Schipper,
Submitted to Tribology Letters,
20-10-2010

# Mild Wear Prediction of Boundary Lubricated Contacts

R. Bosman and D.J. Schipper
University of Twente, r.bosman@utwente.nl
Drienerlolaan 5
7500 AE Enschede

Submitted to Tribology Letters 26/10/2010

*Abstract* - **In this paper a wear model is introduced for the mild wear present in boundary lubricated systems protected by additive rich lubricants. The model is based on the hypothesis that the mild wear is mainly originating from the removal of the sacrificial layer formed by a chemical reaction between the base material and the additive packages present in the lubricant. By removing a part of this layer the chemical balance of the system is disturbed and the system will try to restore the balance for which it uses base material. In this study mechanical properties reported throughout literature are included into the wear model based on observed phenomena for this type of systems. The model is validated by model experiments and the results are in very good agreement, suggesting that the model is able to simulate wear having a predictive nature, rather than on empirical based relationships as Archard's linear wear model. Also a proposal is made to include the transition from mild to severe wear into the model creating a complete wear map.**

*Index Terms* Mild Wear, Boundary lubrication, Wear Transition

## INTRODUCTION

Wear is a topic that received a lot of attention in the past decades, however still the most commonly used wear model is the linear wear law of Archard [1]. To model wear in more detail Archard's original model is combined with numerical methods to obtain the local variation in contact conditions and wear see for example [2-4], however the basic principle is the same. And as an input these methods use empirical determined values, which are determined for one combination of bodies, lubricant and a limited load and velocity range and thus lack a predictive nature as there is no descriptive nature in the treatment of wear. In this study a hypothesis for a wear model based on observed phenomena in mild wearing boundary lubricated systems is suggested. This lubrication region is of increasing importance since more and more systems are running under starved conditions due to the increasing demand for smaller, efficient components. To optimize systems running under these conditions without loss of lifetime it is of crucial importance to understand the wear mechanism dominant in these systems and what kind of mechanical principle is causing the wear. Therefore this article discusses a general hypothesis how to deal with mild (oxidative) wear in boundary lubricated systems lubricated by additive rich oils and

running under mild conditions, which is applicable in a very wide range of applications and conditions. The philosophy behind the model is: the protection provided by the additive package originates from the chemical deposit/reaction it leaves on the surface, which acts as a sacrificial layer and is typically an amorphous glassy type of layer [5]. This layer is in chemical balance, which is than disturbed by mechanical removal of a part of the layer. To restore the chemical balance base material is used. A commonly used additive is ZDDP, which is used as an anti-wear agent in most engine lubricants. Due to the fact that the environmental regulations are becoming more restrictive concerning phosphorous and sulphur containing additives [6] the usage of ZDDP is restricted more and more. This results in the fact that a lot of research is currently done in understanding the mechanism behind the excellent anti-wear properties of this additive [7-22] to eventually produce a more environment friendly additive with the same excellent wear protection like ZDDP. These studies give a good overview of the film formed by this specific additive package, however up to now only little of this information is indeed used to model mild wear present in systems lubricated using a lubricant containing ZDDP.

## THEORY

The model discussed here is based on some basic assumptions made in [23], where it is assumed that an boundary lubricated system's main protection mechanism is the chemical reaction layer on top of the surface in a system schematically depicted in Figure 1. If it is now assumed that for only mild wear to take place it is necessary that the shearing, which is needed for the accommodation of the velocity difference between the two contacting bodies, is located mainly in the chemically/physically adsorbed layer as well as the chemical reaction layer a first step in modeling mild wear can be made. This assumption concurs very well with TEM studies done on particles originating from systems running under mild conditions in the boundary lubrication regime see for example [9]. Here the thickness of the wear particles is less than the overall thickness of the chemical layer and the main components of the wear particles are chemical products originating from the additive packages present in the lubricant, rather than from wear particles "broken" out of the surface supporting the suggested wear mechanism proposed here. For a schematically representation of the hypothesis see Figure 2. At the instant of first contact is it assumed that the system is chemical balanced, after which the amount of plasticity in the thickness direction of the layer is assumed to be the thickness decrease due to contact. As mentioned before, for the lubricant to protect the surface the growth rate of the chemical layer should be larger than the removal rate:

$$\dot{X} \geq \dot{W} \tag{1}$$

In this paper only the removal rate $\dot{W}$ will be discussed and it is assumed that the growth rate is of such a magnitude it satisfies eq. (1) and thus the system is in a mild wear situation**.** To calculate the volume removed during wear a removal model needs to be formulated. This will be done on the basic assumptions discussed in studies [23-24], which will shortly be repeated here for brevity and the interested reader is referred to the indicated references for details. First the representation of the system is given in Figure 1, which suggests modeling of a layered system is required, however this is not necessary if the right assumptions are made. First a general impression is given of the mechanical properties of the chemical reaction layer. In typical systems this layer has only a limited thickness 100 *nm* and is reasonably tough $E$=80 *GPa*, see Table 1. These properties combined with the input micro geometry/surface roughness used in this paper, which are interference microscopy measurements with a lateral resolution in the range of 1 micron, it can be concluded that the influence of the chemical layer in the normal direction can be neglected [23]. The major

effect of the chemical reaction layer on the tribological system is lowering of the coefficient of friction. This ensures that plasticity is confined deep inside the bulk material rather than reaching the surface. The model thus assumes that the "environmental" conditions the chemical layer has to withstand, e.g. which mechanical and thermal stress the layer is put to is determined by the properties of the bulk material.

The contact model used is a CGM based elasto-plastic single loop model first used by Keer and Polonsky [25], here the numerical efficiency was improved using the Multi-Grid Multi-Summation method. The MGMS method was later on replaced by Liu and Wang [26] with the DC-FFT algorithms not only decreasing the computational burden and improving accuracy, but most of all making the algorithm more comprehensive. The thermal model used is the model discussed in [27] with the adaption of interchanging the direct matrix inversion method combined with the moving grid method to solve the thermal inequality with the same numerical schemes as used for the contact solver rendering it possible to use larger grids without memory problems.

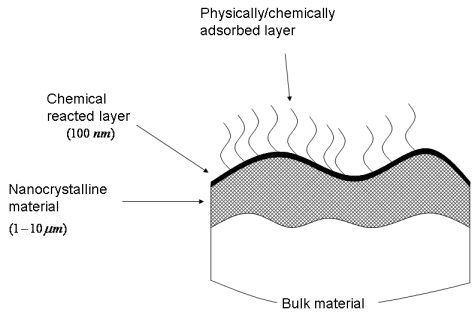


**Figure 1:** Layers present at the surface of a run in system. The top layer is a physically/chemically adsorbed layer which only withstands very mild operational conditions. The second layer is a chemical layer which is a mixture of oxides and chemical products of the lubricant. The third layer is a Nano-Crystalline layer formed at the top of the bulk material by severe plastic deformation under large hydrostatic pressure.

From the contact simulation the stresses and displacements at the surface of the bulk material are known. The chemical layer is formed by the additives which reacted with the surface material and thus it can be assumed that the layer is mechanically bonded to the surface. Therefore a non-slip condition at the interface between the base material and the chemical reaction layer is assumed. Due to the very limited thickness of the layer, the layer is in the plain stress condition. Using these assumptions and the strain at the surface of the bulk material the stresses put on the chemical layer by the deformation of the bulk material can be expressed:

$$\sigma_{ii_{layer}} = \frac{E_{layer}}{(1+\nu_{layer})}\varepsilon_{ii_{bulk}} + \frac{\nu_{layer}E_{layer}}{(1+\nu_{layer})(1-2\nu_{layer})} (\varepsilon_{ii_{bulk}} + \varepsilon_{jj_{bulk}} + \varepsilon_{kk_{bulk}}) \quad (2)$$

The stress put on the layer by the "environment" are the stress and shear due to the contact conditions giving:

$$\sigma_{zz_{layer}} = \sigma_{zz_{layer}} + p \quad (3)$$

$$\sigma_{xz_{layer}} = \mu\, p \quad (4)$$

Using these conditions the plastic yield of the layer can be calculated using a return mapping algorithm.

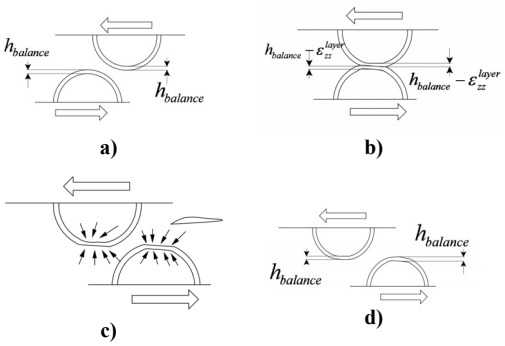


**Figure 2: a)** Asperities come into contact **b)** Part of the chemical layer is sheared of **c)** Removed film is build up again from bulk and additives **d)** The geometry is changed and wear has occurred.

Now the contact conditions can be determined, the response of the chemical layer to these conditions is known if the mechanical properties of the layer are evaluated. To retrieve these parameters a wide literature research was done on the properties of the chemical reaction layer and a short summary is given in Table 1.

| Ref. # | $p$ $[MPa]$ | $V$ $[m/s]$ | $T_{bath}$ $[^oC]$ | $h_{balance}$ $[nm]$ | $E_{ridge}$ $[GPa]$ | $E_{valley}$ $[GPa]$ |
|---|---|---|---|---|---|---|
| [28] | 504 | 0.3 | 100 | 115 | 85-75 | 25-30 |
| [22] | 504 | 0.3 | 100 | 60-120 | - | - |
| [29] | 700 | 0.03 | 83 | 40-100 | - | - |
| [13] | 700 | - | 83 | 100 | - | - |
| [11] | 500 | ~0.3 | 100 | 30-60 | - | - |
| [30] | - | - | - | 100 | 81 | 25 |
| [7] | 400 | ~0.3 | 100 | 70 | 96 | - |
| [31] | 500 | ~0.3 | 100 | 300 | 120-90 | - |
| [32] | ~300 -500 | 0.03 | 83 | <100 | 130 | - |
| [10] | 10-50 | 0.25-55 | 100 | <100 | | - |
| [5] | 360 | - | 100 | 140 | 90 | - |
| [33] | ~425 | 0.34 | 100 | 160> | 122.7 | - |
| [21] | 590 | ~0.3 | 100 | ~160 | 81 | 36 |
| [15] | 600 | 0.01 | 80 | <60 | - | - |
| [34] | 135 | ~0.35 | 100 | 60-180 | 90-120 | |
| [35] | 300 | ~0.3 | 100 | 30-60 | - | - |
| [20] | 950 | 0.1 | 100 | 120 | - | - |

**Table 1:** Results for thickness and Young's modulus for the chemical reaction layer retrieved from literature resulting from rubbing experiments in ZDDP rich oils.

Table 1 gives a good first representation of the properties of a tribo-chemical layer present in a run in system, however there are some important effects missing. At first the effect of the hydrostatic pressure on the properties will be discussed followed by the effect of the temperature. The effect of the normal pressure on the Young's modulus is depicted in Figure 3. After a threshold pressure of 2 *GPa* the equivalent modulus of the layer shows a linear increase with a slope of 35. Also the hardness is influenced by the effect of the normal pressure put on the film, however the exact value is hard to obtain and in the results section a first estimation will be made.

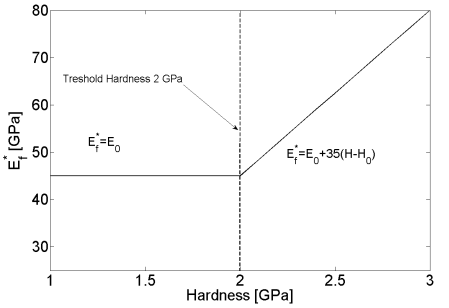


**Figure 3:** Young's Modulus of the chemical film as a function of the hardness ($E=E_0+35(H-H_0)$ for $H>H_0$), e.g. the maximum pressure applied to it. Figure is reproduced using the data presented in [36].

A second effect is the effect temperature has on the mechanical properties [18, 37]. In both studies it is shown that the influence of the temperature on the equivalent modulus is limited up to temperatures in the range of 100 $^oC$, as shown in Figure 4. However, in [37] a more pronounced temperature effect on the hardness is reported. Here it is reported that at 80 $^oC$ the hardness is already reduced to half of the value measured at 24 $^oC$ for low indentation depths. The typical "indentation" during the wear process is also in the range of a few nano-meters, suggesting this behavior is typical during the wear process. For this reason an arctan function is used as depicted in Figure 5 for the yield stress as a function of the temperature.

The volume which will be removed from the chemical layer during wear can be calculated using the contact solver combined with the assumptions made and mechanical properties of the chemical layer. It needs to be defined what the amount of base material inside this

volume is. To do so the first step is to get the chemical composition of the layer as a function of the depth.

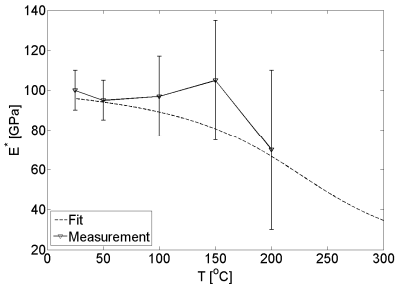


**Figure 4:** Equivalent Young's modulus $E^*$ as a function of the temperature, measurement data is reproduced from [18].

Different XPS studies where investigated [13, 15, 38-39] and from these measurements it can be concluded that the different conditions do not effect the iron concentration vs. depth profile significantly. For the current study the profiles originating from [39] are used, see Figure 6-a. As discussed earlier the structure of the film is amorphous suggesting a random molecule orientation and this enables the use of the atomic radius of the different molecules to calculate the volumetric percentage of iron as a function of depth from the XPS signal, see Figure 6-b, which then can be used to calculate the amount of iron removed, which is fitted by the function:

$$W_{perc}(\delta) = \frac{\begin{array}{c} 4.5\times10^{19}\delta^4 - 2.83\times10^{13}\delta^3 \\ +1.75\times10^{-7}\delta^2 + 0.001\delta \end{array}}{h_{balance}} \qquad (5)$$

Here $\delta=\varepsilon^l_{plzz}h_{baance}$ is the plastic penetration depth of the layer, in which $\varepsilon^l_{plzz}$ is the plastic strain in the chemical reaction layer in thickness direction and $h_{balance}$ is the thickness of the layer at which the system is in chemical balance. The next step is defining the "wear cycle" to estimate the rate the film is removed. For doing so either a characteristic length or time is needed. Here a length is chosen so that the wear loss parameter becomes dimensionless:

$$\begin{aligned} K_{wear}(x,y) &= \frac{h_{inst}(x,y)}{l} = \frac{W_{wear}}{\Delta x\Delta y l} \\ &= \frac{W_{perc}(\varepsilon^l_{plzz}h_{balance})\varepsilon^l_{plzz}h_{balance}}{l} \end{aligned} \qquad (6)$$

Here $W_{perc}(x)$ is the percentage volumetric wear function presented in Figure 6, $\Delta x$ and $\Delta y$ are the element sizes in $x/y$ direction and $l$ is a characteristic wear length to be determined. If it is now assumed that for the system to wear volume $W_{wear}$ the contact needs to be lost and then regained, e.g. the contact needs to be "opened" for the wear particle to detach, the average micro-contact length in direction of sliding can be used as the characteristic length $l$.

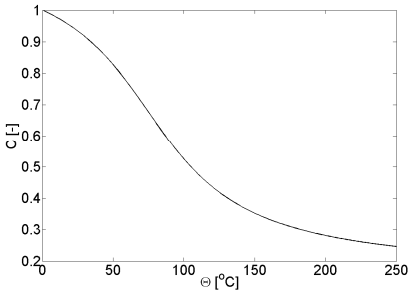


**Figure 5:** Proposed compensation factor C [-]as a function of the temperature for the yield stress of the chemical reaction layer.

However, this would also imply that the sliding increment step would be of the same size yielding large computational times for longer sliding distances. To increase the numerical effectiveness the specific wear coefficient is calculated from eq. (6) and set constant over one sliding increment, as it is shown in [40] that this does not effect the results if the increment is chosen correctly:

$$k(x,y) = \frac{K(x,y)}{p(x,y)} \qquad (7)$$

Giving the height loss for each increment:

$$\begin{aligned} &h_{increment}(x,y) = \\ &k(x,y)p(x,y)\Delta s = K(x,y)\Delta s \end{aligned} \qquad (8)$$

## RESULTS

To validate the proposed wear model two different tests where preformed and reproduced in simulations: first a new smooth ball and disk are used and secondly a barreled shaped specimen with a disk (elliptical contact) are simulated. The interference microscopy of the smooth new ball and disk are presented in Figure 7-a and b. The ball, disk and barrel shaped roller originate from roller bearings and are made of AISI-52100. The material parameters and geometrical entities and are presented in Table 2 and Table 3.

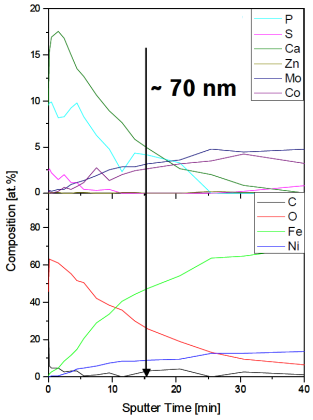


**a)**

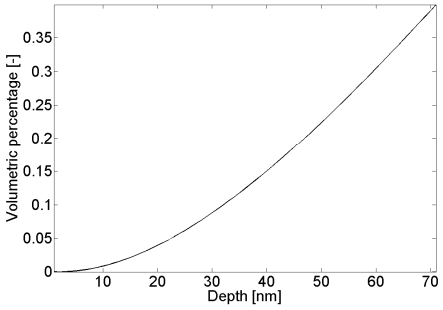


**b)**

**Figure 6:** Chemical composition of chemical reaction layer with a thickness of 70 *nm*. **a)** XPS profile and **b)** volume percentage of iron as a function of the depth.

The first test is done using the new ball and disk on a CSM standard ball on disk setup under very mild conditions, $F_n$=10 $N$ and $V$=0.005 *m/s* , using an commercially available ZDDP rich lubricant of which some properties are given in Table 4 [41]. The test was run for half an hour after which the specific wear rate was determined.

| | Disk[SKF] | Ball | Spherical roller |
|---|---|---|---|
| Material | AISI 52100 | AISI 52100 | AISI 52100 |
| $D\,[mm]$ | $D_{in}=15$ $D_{ext}=47$ | 10 | $D_x=8$ $D_y=53.2$ |
| $F_n\,[N]$ | 10 | | |
| $V\,[m/s]$ | 0.005 | | |
| $\Theta_{env}\,[^oC]$ | 25 | | |

**Table 2:** Geometrical entities and test conditions.

Under the given conditions it is safe to assume that the main wear mechanism will be very mild oxidational wear. The measured coefficient of friction in this situation is 0.134 conforming that indeed the contact is indeed running under boundary lubricated conditions. The normal pressure in the test was under the threshold value of 2 *GPa* and thus the equivalent modulus of the film will be in the range of 35-40 *GPa*, since the "anvil effect" is not triggered at this pressure. The temperature rise inside the contact is less then one degree Celsius as shown in Figure 7-d, e.g. the reference hardness of 1 *GPa* [5] can be used for the chemical layer, since the contact conditions are very mild.

| | $K$ $\left[\frac{W}{mK}\right]$ | $\rho$ $\left[\frac{kg}{m^3}\right]$ | $C_p$ $\left[\frac{J}{kgK}\right]$ | $E$ $[GPa]$ | $\nu$ $[-]$ | $H$ $[GPa]$ |
|---|---|---|---|---|---|---|
| AISI 52100 | 45 | 7800 | 470 | 210 | 0.3 | 6.6 |
| Case hardened steel | 45 | 7700 | 467 | 210 | 0.3 | 6 |

**Table 3:** Material parameters

The measured specific wear rate during the test was found to be 8x10$^{-9}$ $mm^3N^{-1}m^{-1}$. If the same sliding distance is modeled using 100 increment steps and the layer thickness ($h_{balance}$) is set to 70 *nm*, as measured for this

type of system, the specific wear rate calculated is $4x10^{-9}$ $mm^3N^{-1}m^{-1}$, which is determined using the calculated wear profile shown in Figure 7-e. This value is in the same range as the measured one, indicating the proposed wear model is capable of determining the specific wear rate for mild wearing point contacts.

| Density $\rho_d$ $[kg/m^3]$ | Kinematic Viscosity $\nu_k[mm^2/s]$ | | Dynamic Viscosity $\eta_0[mPa\,s]$ | |
|---|---|---|---|---|
| 25 °C | 40 °C | 100 °C | 40 °C | 100 °C |
| 862 | 40 | 9 | 35 | 7 |

**Table 4:** Properties of commercial oil

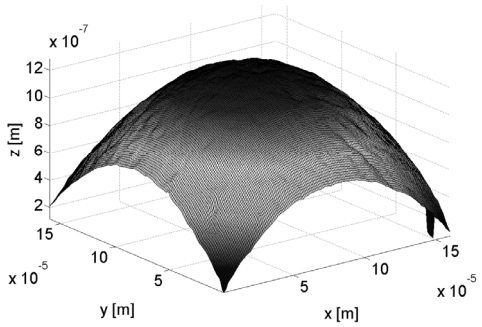


**a)**

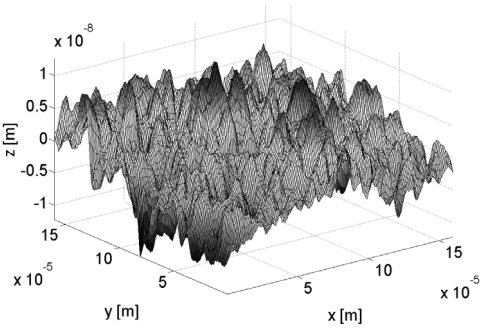


**b)**

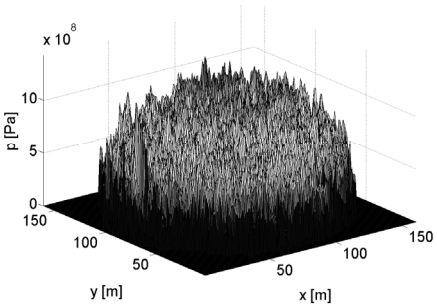


**c)**

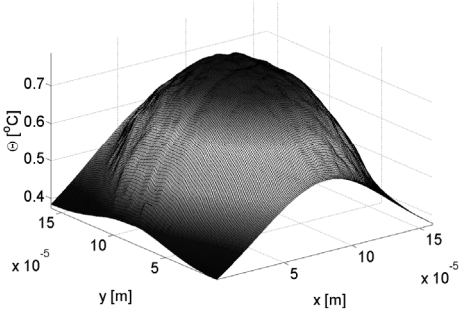


**d)**

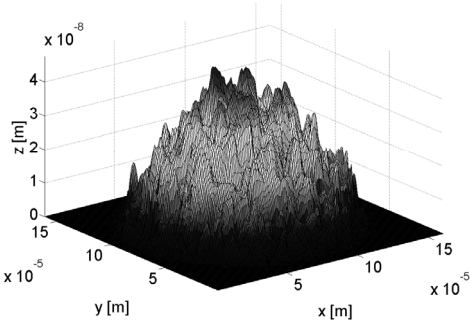


**e)**

**Figure 7: a)** Surface topography of the ball and **b)** of the disk used in during the experiments and simulations. **c)** Resulting pressure field and **d)** temperature field. **e)** Wear volume after $10\ m$ of sliding.

The next step is to determine the specific wear rate of the run in elliptical contact of which the surface geometry is presented in Figure 8-a. The run in procedure is the same as for the ball. However, in the roller-disk combination the roughness of the roller used is significantly higher than the ball used in the previous test. This is also quite well represented by the clear roughening of the disk inside the wear track as shown in Figure 8-b. The roughening, e.g. running-out, of the disk is currently not incorporated in the model since the responsible mechanism will be plowing. Due to this increase in roughness it is clearly shown in Figure 8-d that the pressure exceeds the threshold value of 2 *GPa* and the anvil effect needs to taken into consideration. However, as discussed in the modeling part of the paper not only the equivalent modus is a function of the pressure above the threshold but also the hardness starts to be effected by the pressure, as can be seen in Fig. 4 in [37]. To compensate for this effect the yield strength is defined as:

$$\sigma_y(x,y) = \sigma_{y0} + \alpha p(x,y) \quad for\ p(x,y) > p_{tresh} \qquad (9)$$

In the simulation the threshold pressure is set to 2 *GPa*, e.g. equal to the threshold for the Young's modulus and $\alpha = 0.1$, which is in a realistic range for amorphous polymer glasses [42]. Using these values the calculated specific wear rate calculated becomes $9x10^{-9}mm^3Nm^{-1}$ for a sliding distance of 1 *m* while the measured one is $1.6x10^{-8}mm^3Nm^{-1}$. As for the smooth ball-disk combination both calculated and measured values are in close range with each other, using values readily obtained either from experiments or dedicated literature.

## WEAR MAP

To increase the potential of the model even further it can be combined with the theory presented in [40], where the transition from mild to severe wear is discussed. The hypothesis presented in this study states that if more than 10 percent of the contacting surfaces transcend a predefined critical temperature severe adhesive wear will occur. In principle this theory is inline with the current model, which states that the chemical layer softens under the influence of increasing temperature.

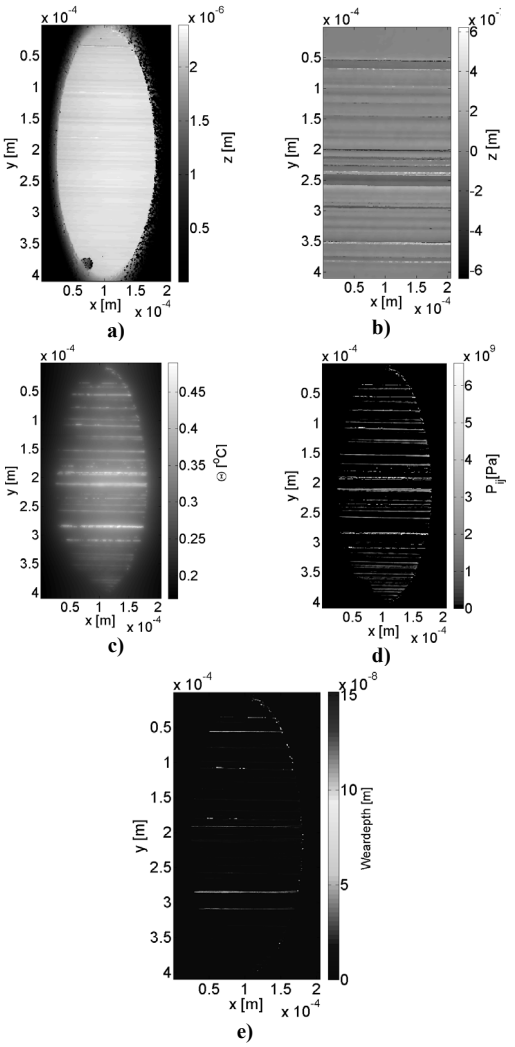


**Figure 8: a)** Surface profile of a roller run for 8 hours under the conditions given in Table **2**. **b)** Counter surface topography. **c)** Temperature field in the contact and **d)** Pressure field in the contact. **e)** Resulting wear depth.

If now the temperature is increased to far the chemical layer will not be able to protect the surface against metal to metal contact and local adhesive wear will occur, increasing the temperature in the contact even further introducing complete failure of the whole

contact. Using this hypothesis an *F-V* failure diagram can be constructed as depicted in Figure 10, which can now be extended by "iso-$k$" lines using the model presented in this paper. To do so the input geometries from the previous study are used, see Figure 9 for the disk surface topography. The counter surface is a cylindrical pin with a length effective contact length of 3.4 *mm* and a radius of 2 *mm* with a smooth surface creating a line contact situation. The disk is a hard turned disk made of case hardened steel, for the material parameters see Table 3.

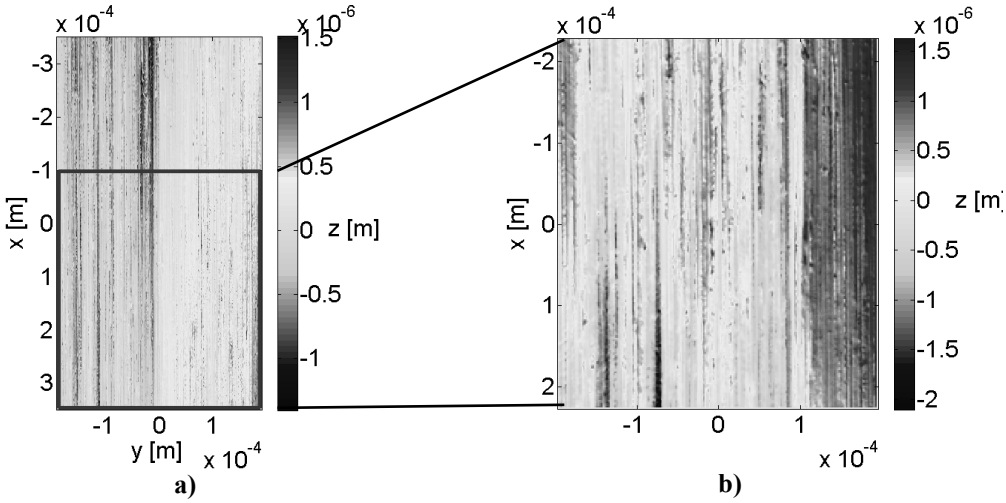


**Figure 9: a)** Measured disk **b)** Filtered part of the surface used for the calculations

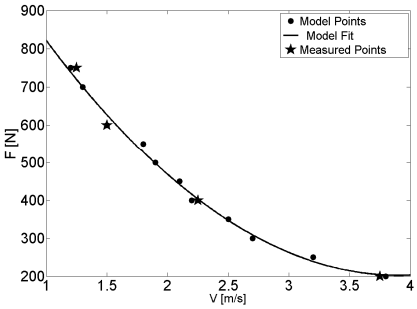


**Figure 10:** Failure diagram for a boundary lubricated contact, reproduced from [40]

To reduce calculation time without a significant loss of accuracy the surface is reduced to a 240×240 grid using an average moving filter as discussed in [40]. If the new surface is used of both cylinder and disk and it is assumed the load is put on instantaneously the resulting calculated wear diagram is depicted in Figure 11. This wear diagram shows realistic values for a boundary lubricated contact, however the validation of this diagram is a subject of further research and the authors would like to emphasize that the wear diagram presented here is to show the potential of the model. Further research on the effect the different operational conditions have on the chemical layer is needed to improve the wear diagram. Also the running-in under these conditions needs to be modeled using for example a model as discussed in [23]. To show the effect a change in roughness has the simulation is also run with a smooth pin and smooth disk combination as well as a rough-rough combination of which the results are shown in Figure 11. Here it is clearly shown that the change in roughness has a limited effect on the specific wear rate. However, the effect of the roughness change on the location of the transition line from mild to severe wear is pronounced.

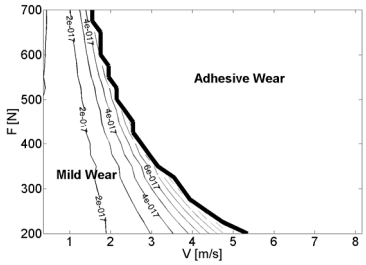


a)

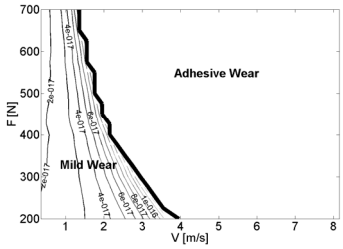


b)

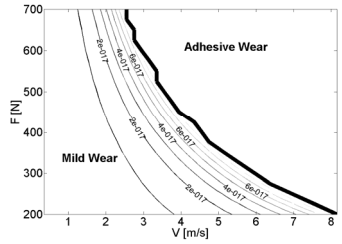


c)

**Figure 11:** Wearmap for the combination of a rough disk an smooth pin **b)** Wearmap for the combination of a rough disk and rough pin (Ra=0.27) **c)** Wearmap if both the disk and pin are assumed to be smooth (Ra=0.08 microns)

## CONCLUSION

In this paper a model for mild wearing systems is proposed which is based on physical properties and phenomena observed in boundary lubricated systems. A general model is proposed and to validate the model two model tests were conducted to validate the model. The numerical results concur very well with the experiments validating the model. One of the next steps in modeling wear of this type would be including a growth model for the additive layer, this would not only include the thickness of the layer, but also the effect the different additives have on the properties of the chemical layer. In this way in the near future it might become possible to predict the lifetime of a component without the need to do countless wear experiments over a wide range of contact conditions. As an example of a theoretical wear diagram is presented of a model system consisting of a smooth cylinder sliding over a rough disk. In this simulation the hypothesis that the transition from mild to severe wear is a thermal one is used to set the regime in which the mild wear model is valid is used. The results are not validated and this is a next step in the current research project, however the potential of the model in which both the mild wear model and the transition prediction is combined is shown.

## REFERENCES

[1] J.F. Archard, Contact and Rubbing of Flat Surfaces, Journal of Applied Physics. 24 (1953) 981-988.

[2] P. Põdra, S. Andersson, Simulating sliding wear with finite element method, Tribology International. 32 (1999) 71-81.

[3] U. Olofsson, S. Andersson, S. Björklund, Simulation of mild wear in boundary lubricated spherical roller thrust bearings, Wear. 241 (2000) 180-185.

[4] G.K. Sfantos, M.H. Aliabadi, Wear simulation using an incremental sliding Boundary Element Method, Wear. 260 (2006) 1119-1128.

[5] S. Bec, A. Tonck, J.M. Georges, R.C. Coy, J.C. Bell, G.W. Roper, Relationship between mechanical properties and structures of zinc dithiophosphate anti-wear films, Proceedings of the Royal Society of London Series a-Mathematical Physical and Engineering Sciences. 455 (1999) 4181-4203.

[6] H. Spikes, The History and Mechanisms of ZDDP, Tribology Letters. 17 (2004) 469-489.

[7] M. Aktary, M.T. McDermott, G.A. McAlpine, Morphology and nanomechanical properties of ZDDP

antiwear films as a function of tribological contact time, Tribology Letters. 12 (2002) 155-162.
[8] S. Bec, A. Tonck, J.M. Georges, G.W. Roper, Synergistic Effects of MoDTC and ZDTP on Frictional Behaviour of Tribofilms at the Nanometer Scale, Tribology Letters. 17 (2004) 797-809.
[9] M.Z. Huq, P.B. Aswath, R.L. Elsenbaumer, TEM studies of anti-wear films/wear particles generated under boundary conditions lubrication, Tribology International. 40 (2007) 111-116.
[10] H.B. Ji, M.A. Nicholls, P.R. Norton, M. Kasrai, T.W. Capehart, T.A. Perry, Y.T. Cheng, Zinc-dialkyl-dithiophosphate antiwear films: dependence on contact pressure and sliding speed, Wear. 258 (2005) 789-799.
[11] M. Kasrai, S. Marina, B.G. Micheal, Y.E. S., R.P. Ray, X-ray adsorption study of the effect of calcium sulfonate on antiwear film formation generated from neutral and basic ZDDPs: Part 1 -Phosporus species, Tribology Transactions. 46 (2003) 434-442.
[12] Y.-R. Li, G. Pereira, A. Lachenwitzer, M. Kasrai, P. Norton, X-Ray Absorption Spectroscopy and Morphology Study on Antiwear Films Derived from ZDDP Under Different Sliding Frequencies, Tribology Letters. 27 (2007) 245-253.
[13] J.M. Martin, C. Grossiord, T. Le Mogne, S. Bec, A. Tonck, The two-layer structure of zndtp tribofilms Part 1: AES, XPS and XANES analyses, Tribology International. 34 (2001) 523-530.
[14] C. Minfray, T. Le Mogne, J.-M. Martin, T. Onodera, S. Nara, S. Takahashi, H. Tsuboi, M. Koyama, A. Endou, H. Takaba, M. Kubo, C.A. Del Carpio, A. Miyamoto, Experimental and Molecular Dynamics Simulations of Tribochemical Reactions with ZDDP: Zinc Phosphateâ€“Iron Oxide Reaction, Tribology Transactions. 51 (2008) 589 - 601.
[15] C. Minfray, J.M. Martin, C. Esnouf, T. Le Mogne, R. Kersting, B. Hagenhoff, A multi-technique approach of tribofilm characterisation, Thin Solid Films. 447 (2004) 272-277.
[16] C. Minfray, J.-M. Martin, T. Lubrecht, M. Belin, T.L. Mogne, M.P.G.D. D. Dowson, A.A. Lubrecht, A novel experimental analysis of the rheology of ZDDP tribofilms, Tribology and Interface Engineering Series, Elsevier. 2003, pp. 807-817.
[17] N.J. Mosey, T.K. Woo, M. Kasrai, P.R. Norton, G.M. Bancroft, M.H. Müser, Interpretation of experiments on ZDDP anti-wear films through pressure-induced cross-linking, Tribology Letters. 24 (2006) 105-114.
[18] G. Pereira, D. Munoz-Paniagua, A. Lachenwitzer, M. Kasrai, P.R. Norton, T.W. Capehart, T.A. Perry, Y.-T. Cheng, A variable temperature mechanical analysis of ZDDP-derived antiwear films formed on 52100 steel, Wear. 262 (2007) 461-470.
[19] A. Tonck, S. Bec, J.M. Georges, R.C. Coy, J.C. Bell, G.W. Roper, Structure and mechanical properties of ZDTP films in oil, Tribology Series, Elsevier. 1999, pp. 39-47.
[20] K. Topolovec-Miklozic, T. Forbus, H. Spikes, Film thickness and roughness of ZDDP antiwear films, Tribology Letters. 26 (2007) 161-171.
[21] O.L. Warren, Nanomechanical properties of films derived from zinc dialkyldithiophosphate, Tribology Letters. 4 (1998) 189-198.
[22] Z. Zhang, Tribofilms generated from ZDDP and DDP on steel surfaces:Part I, Tribology Letters. 17 (2005) 211-220.
[23] R. Bosman, D.J. Schipper, Running in of systems protected by additive rich oils, Tribology Letters. In Production (2010)

[24] R. Bosman, D.J. Schipper, Running in of metallic surfaces in the boundary lubricated regime, Wear. Submitted (2010)
[25] I.A. Polonsky, L.M. Keer, A numerical method for solving rough contact problems based on the multi-level multi-summation and conjugate gradient techniques, Wear. 231 (1999) 206-219.
[26] S. Liu, Q. Wang, A Three-Dimensional Thermomechanical Model of Contact Between Non-Conforming Rough Surfaces, Journal of Tribology. 123 (2001) 17-26.
[27] R. Bosman, M.B.d. Rooij, Transient Thermal Effects and Heat Partition in Sliding Contacts, Journal of Tribology. 132 (2010) 021401.
[28] M.A. Nicholls, P.R. Norton, G.M. Bancroft, M. Kasrai, T. Do, B.H. Frazer, G.D. Stasio, Nanometer scale chemomechanical characterizaton of antiwear films, Tribology Letters. 17 (2003) 205-336.
[29] J.P. Ye, S. Araki, M. Kano, Y. Yasuda, Nanometer-scale mechanical/structural properties of molybdenum dithiocarbamate and zinc dialkylsithiophosphate tribofilms and friction reduction mechanism, Japanese Journal of Applied Physics Part 1-Regular Papers Brief Communications & Review Papers. 44 (2005) 5358-5361.
[30] M.A. Nicholls, T. Do, P.R. Norton, M. Kasrai, G.M. Bancroft, Review of the lubrication of metallic surfaces by zinc dialkyl-dithiophosphates, Tribology International. 38 (2005) 15-39.
[31] M.A. Nicholls, G.M. Bancroft, P.R. Norton, M. Kasrai, G. De Stasio, B.H. Frazer, L.M. Wiese, Chemomechanical properties of antiwear films using X-ray absorption microscopy and nanoindentation techniques, Tribology Letters. 17 (2004) 245-259.
[32] J.P. Ye, M. Kano, Y. Yasuda, Evaluation of nanoscale friction depth distribution in ZDDP and MoDTC tribochemical reacted films using a nanoscratch method, Tribology Letters. 16 (2004) 107-112.
[33] K. Komvopoulos, V. Do, E.S. Yamaguchi, P.R. Ryason, Nanomechanical and nanotribological properties of an antiwear tribofilm produced from phosphorus-containing additives on boundary-lubricated steel surfaces, Journal of Tribology-Transactions of the Asme. 126 (2004) 775-780.
[34] G. Pereira, A varialbe temperature mechanical analysis of ZDDP-derived antiwear films formed on 52100 steel, Wear
(2006) 461-470.
[35] G.M. Bancroft, M. Kasrai, M. Fuller, Z. Yin, K. Fyfe, K.H. Tan, Mechanisms of tribochemical film formation: stabilityof tribo- and thermally-generated ZDDP films, Tribology Letters. 3 (1997) 47-51.
[36] K. Demmou, S. Bec, J.L. Loubet (2007) *Effect of hydrostatic pressure on the elastic properties of ZDTP tribofilms*. Cornell University Library.
[37] K. Demmou, S. Bec, J.-L. Loubet, J.-M. Martin, Temperature effects on mechanical properties of zinc dithiophosphate tribofilms, Tribology International. 39 (2006) 1558-1563.
[38] C. Minfray, J.M. Martin, M.I. De Barros, T.L. Mogne, R. Kersting, B. Hagenhoff, Chemistry of ZDDP Tribofilm by ToF-SIMS, Tribology Letters. 17 (2004) 351-357.
[39] A. Voght, *Tribological Reactions Layers in CVT contacts*. 2008, Bosh-CR: Schillerhohe.
[40] R. Bosman, D.J. Schipper, On the transition from mild to severe wear of lubricated, concentrated contacts: The IRG (OECD) transition diagram, Wear. 269 (2010) 581-589.

[41] I. Cracoanu, Effect of Macroscopic Wear on the Friction in Lubricated Concentrated Contacts, PhD Thesis, University of Twente (www.tr.ctw.utwente.nl), 2010 p

[42] J. Rottler, ouml, rg, M.O. Robbins, Yield conditions for deformation of amorphous polymer glasses, Physical Review E. 64 (2001) 051801.

# Mild Wear Maps for Boundary Lubricated Contacts

R. Bosman and D.J. Schipper

Submitted to Wear 20-12-2010

Paper H

# Mild Wear Maps for Boundary Lubricated Contacts

R. Bosman and D.J. Schipper
University of Twente, r.bosman@utwente.nl
Drienerlolaan 5
7500 AE Enschede

Submitted to Wear 20/12/2010

*Abstract* - **In this study a model capable of predicting a mild wear map for boundary lubricated contacts is presented and validated using model experiments. The model is based on the hypothesis that for an additive to protect the surface against severe wear a balance between the growth and removal rate of the chemical layer present at the surface needs to be obtained. The simulations are in good agreement with the experimental results. It can thus be concluded that the wear model presented can be seen as a first step in the complete wear modeling of boundary lubricated contacts.**

*Index Terms* – Wear transition, Boundary lubrication

## INTRODUCTION

Wear in engineering systems is a problem from a scientific and engineering point of view but. Since, for most maintenance operations the machinery needs to be stopped and production is thus delayed. This is in contrast with the increasing demand for smaller more efficient machinery, since it is most profitable to prevent wear by running in the (Elastic) Hydrodynamic Lubrication regime in which no solid-solid contact is occurring. However, if machine components are becoming smaller while carrying the same load the nominal contact pressure increases forcing the components to run in the Boundary Lubrication regime, in which wear is significantly increased compared to the (E)HL regime [1]. To deal with this problem the lifetime and reliability of a component has to be estimated while running under BL conditions. However, before these steps can be made the type of wear present in the system needs to be determined. For the component to run without failure severe (adhesive) wear needs to be avoided at all time. Therefore, in this article both mild wear, e.g. life time estimation, and the transition to severe wear, e.g. instantaneous failure, are dealt with. The latter is modeled using the theory first suggested by Blok in the late thirties [2], who stated that the transition from mild to severe adhesive wear in BL contacts is caused by transcending a critical predefined temperature. However, Blok was not capable of defining a uniform critical temperature for a given combination of lubricant and base material, even for a given system in which only the load and velocity are varied. This was mainly due to the fact that at his time there were no microscopic models available for neither the mechanical nor the thermal calculation. Van Drogen [3] was as one of the first able to identify a uniform critical temperature for a given system and lubricant. Van Drogen [3] was as one of the first able to identify a uniform critical temperature for a given system and lubricant. However, there was one main shortcoming in this model: mild wear was not included. To validate the model a test setup was designed to apply the load instantaneously, however as this is physically impossible the

result was a setup which applied the load at a rate of approximately 150 *N/s* as depicted in Figure 1.

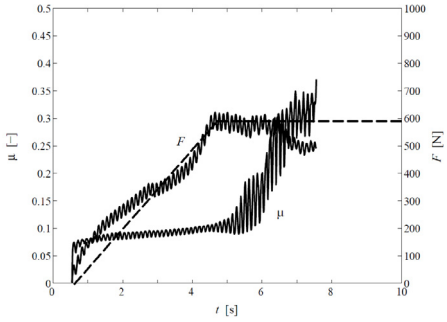


**Figure 1:** Typical friction and force measurement of a contact situation with direct failure. Solid line force measured and dashed line force used in the numerical model

This implies that before the full load is reached already several meters are slid and mild wear occurred which changes the contact geometry. The wear was first dealt with by both van Drogen and Bosman [4] by adapting the macroscopic contact dimensions so the calculated contact radius matches the measured one. This model yielded rather good results; although the change in micro-geometry is not included. To deal with this problem Bosman used a BEM based contact and temperature model combined with the linear wear law of Holm/Archard to include mild wear [5]. This resulted in an improvement in predicting the transition from mild to severe wear. By doing so a simple wear map was created: a mild wear regime with a constant specific wear rate on one side of the transition line and on the other side a severe wear regime where the contact fails as is shown in Figure 2.

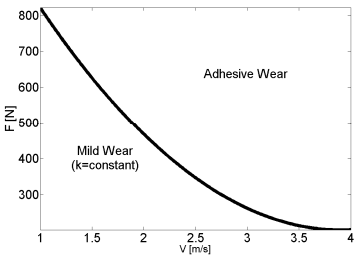


**Figure 2:** Simple transition diagram, in the mild wear regime the specific wear rate is constant.

However, in real engineering applications the specific wear rate of systems operating in the mild wear regime will not be constant under the different conditions and this issue needs to be dealt with to complete the wear map. In this paper the transition predicted by the thermal threshold is used to identify the regime where the mild wear model presented here is valid, while the mild wear model itself determines the specific wear rate under the different operating conditions.

## THEORY

As discussed in the introduction a mild wear model will be discussed, however first some basic assumption are discussed starting with the application regime of the model, which is the boundary lubrication regime in which the system is running under tribo-chemical wear conditions. In this regime typically chemical products in the lubricant react with the surface material to protect the surface against severe wear by introducing a sacrificial layer of chemical products [6]. This layer is supported by a Nano-crystalline layer, which is formed by large plastic deformation under high strain rates and hydrostatic pressure [7-10], forming the complete system schematically presented in Figure 3. The sacrificial nature of the chemical reaction layer is supported by TEM studies done on wear particles generated by these types of systems running under mild wear conditions [11-12], in these studies the wear particle thickness was typically an order lower than the thickness of the chemical reaction layer present at the surface of the system.

A second conclusion may be drawn from these studies: mild (corrosive) wear originates from shearing off the chemical products formed by the additive package through reaction with base material rather than by direct base material removal. This would imply that if the removal rate of the chemical reaction layer can be evaluated the wear rate of a system can be estimated, making it feasible to estimate the wear rate of a given system.

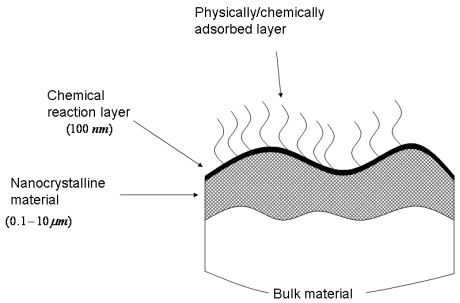


**Figure 3:** Layers present in a run-in system. The top layer is a physically/chemically adsorbed layer which only withstands very mild conditions. The second layer is a chemical layer which is a mixture of oxides and chemical products of the lubricant. The third layer is a Nano-crystalline layer formed at the top of the bulk material by severe plastic deformation under large hydrostatic pressure.

This assumption is then combined with the statement that for a lubricant to protect the system against severe (adhesive) wear the removal rate $\dot{W}$ needs to be lower than the growth rate $\dot{X}$ giving [13]:

$$\dot{X} \geq \dot{W} \tag{1}$$

This seems in contrast with the thermal transition criterion and eq. (1), however as explained shortly the mechanical properties of the chemical reaction layer are greatly influenced by the temperature, and it is therefore assumed for this moment that if the critical temperature is reached the mechanical properties of the chemical reaction layer are degenerated so severely it is not able to protect the surface any more. Since no growth model is discussed in this paper it is assumed the growth rate is high enough to fulfill eq. (1) for the complete surface, e.g. the system is running under mild conditions. If this condition would not be fulfilled the authors would like to point the reader towards an alternative model presented in [13]. In this study a model is discussed which runs in the surface towards a balanced wear condition. This is done through direct material removal. This mechanism, however, is not the scope of the current study.

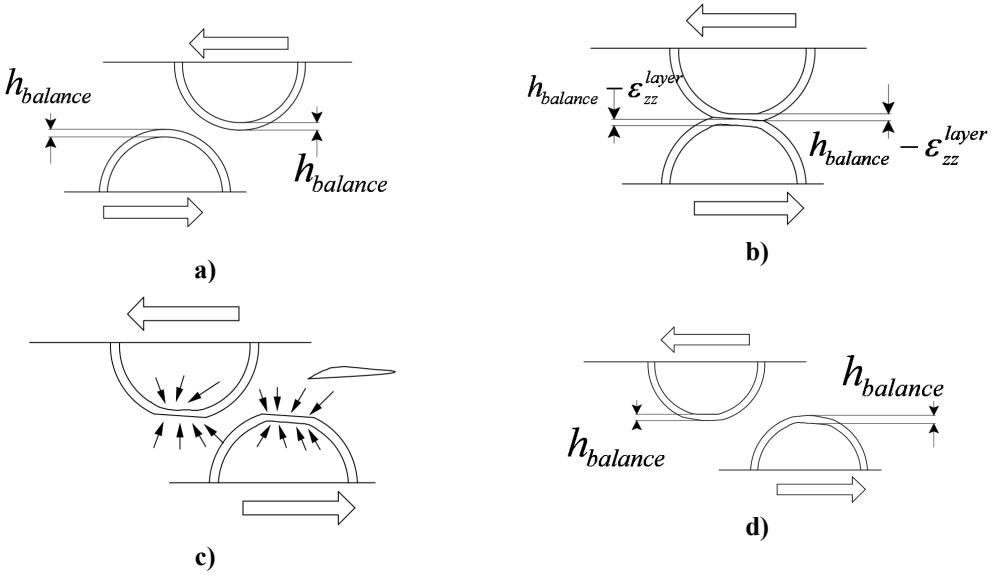


**Figure 4:** Asperities come into contact **b)** Part of the chemical layer is sheared off **c)** Removed film is built up again from bulk and additives **d)** The geometry is changed and wear has occurred.

If it is now considered that the plastic indentation of the chemical reaction layer is a good indication for the volume removed from the chemical layer due to contact, see Figure 4, the removed volume can be calculated. At the first instance of contact the surface is covered with a layer of which the thickness is determined by the chemical balance in the system. Upon contact the layer is stressed and might start yielding, reducing its thickness. When contact is lost the system will restore the layer thickness. By doing so it will use base material for the reaction needed, because the layer is built up from both base material and chemical products originating from the additive packages.

To determine the thickness "loss" of the layer a few simplifications will be made. First the representative values of the chemical reaction layer are obtained. This is done by comparing the different studies done on boundary lubricated contacts lubricated by additive rich lubricants. In this literature study the main focus was on ZDDP/DDP rich lubricants, since the use of these additives is becoming more and more restrictive due to environmental rules, resulting in an increase of the information about properties and wear preventing mechanism of these types of additives.

Using the results from [6, 14-28] the values for the chemical reacted layers are set to: $E$=80 *GPa,*ν=*0.3* , and $h_{balance}$=100 *nm*. If these values are combined with the fact that in the simulations presented in this paper typically the input geometries are interference microscopy measurements with a minimum lateral resolution of $1\mu m \times 1\mu m$ used it is shown in [29] that the effect of the chemical reaction layer on the used contact conditions is very limited (less than 3%). Therefore, the effect of the layer is only accounted for in the simulations by lowering the coefficient of friction, while modeling an un-layered system in normal direction. This can be interpreted as follows: the bulk material is determining the environment which the chemical layer needs to prevail, while the properties of the layer itself determine the amount of wear under the given conditions.

To complete the model the plastic strains in the layer need to be determined. A start in this is made with the statement that the layer will act as a solid rather than a liquid, as is suggested in [30]. The next step is determining the stresses in the layer, which then will be used to determine the final plastic yield inside the layer. The thickness of the layer is very limited which leads to the following assumptions; first the layer is in a plain stress conditions and secondly the different contact patches do not interact with each other. If now the non-slip and full adherence conditions are used at the interface of the layer the pre-stress put on the layer by the bulk material can be expressed as [31]:

$$\sigma_{ii_{layer}} = \frac{E_{layer}}{(1+\nu_{layer})}\varepsilon_{ii_{bulk}} + \frac{\nu_{layer}E_{layer}}{(1+\nu_{layer})(1-2\nu_{layer})}(\varepsilon_{ii_{bulk}} + \varepsilon_{jj_{bulk}} + \varepsilon_{kk_{bulk}}) \quad (2)$$

And the stress put on the layer by the "environment" becomes:

$$\sigma_{zz_{layer}} = \sigma_{zz_{layer}} + p \quad (3)$$

$$\sigma_{xz_{layer}} = \mu\, p \quad (4)$$

Combining eq. (2-4) the total stress state of the layer is defined and a return mapping algorithm combined with a von Mises yield criterion can be used to compute the plastic strains of the layer. However, for the return algorithm to work a yield stress needs to be determined. The hardness of the layer is estimated between 1 and 2 *GPa* and dependent on the running conditions [23]. A second

aspect that is in need of attention is the effect temperature has on the properties of the chemical layer. This is discussed in [30] and [31], where the first study mainly focuses on the elastic properties up to a temperature of 200 $^oC$ and the latter focuses both on the hardness and elastic properties only for a limited range of temperature up to 80 $^oC$. For the elastic properties ($E$) it followed out of both studies that the effect up to a temperature of around 100 $^oC$ is very limited and can be represented by the curve given in Figure 5. However, the effect on the hardness was more pronounced, especially for low indentation depths as will be case in the low wear situation [12]. For this reason the slope and "transition point" in Figure 5 are altered to increase the influence of the temperature on the yield strength.

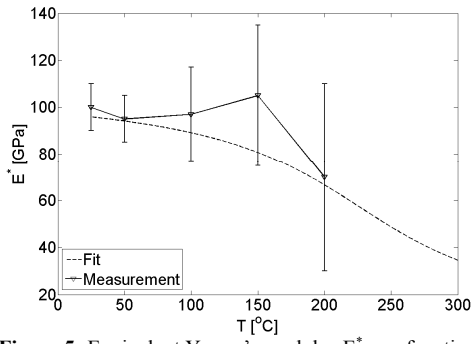


**Figure 5:** Equivalent Young's modulus $E^*$ as a function of the temperature, measurement data is reproduced from [30].

A second "external" effect on the properties of the chemical layer is the hardening through hydrostatic pressure called the "Anvil Effect" [34], which effect often seen in indentation done in soft amorphous glassy films supported by harder substrates. For the film derived from a ZDDP containing lubricant this effect starts at a threshold pressure of 2 GPa and runs linearly with a slope of 35 as shown in Figure 6. However in the current version a maximum is set at 120 GPa, since it is unlikely the film will obtain a increase further than this as it is the maximum measured value reported in the studied literature. For the hardness the same slope as a function of the indentation depth is seen, suggesting a similar behavior. Using the rule of thump $H=2.8\sigma_{yield}$ would render the yield strength as a function of the normal pressure:

$$\sigma_{yield}^{layer} = \sigma_{yield\,0}^{layer} + \alpha p \quad \text{for } p > p_{tresh} \qquad (5)$$

In this case the value of $\alpha$ would be in the range of 0.1, which is a realistic value also seen in amorphous polymers [35].

Next is to define the contact model and thermal model. The contact model currently used is a single loop CGM model first discussed by Polonsky and Keer [36] and later on adapted by Liu et al. [37] to facilitate the DC-FFT algorithm, improving the accuracy while reducing computational times significantly. For the thermal calculations a similar code is used, based upon the theory presented in [38], with the minor adaptation that instead of the direct solver (matrix inversion) method combined with the moving grid method used in the original code the CGM method is used to solve the thermal inequalities.

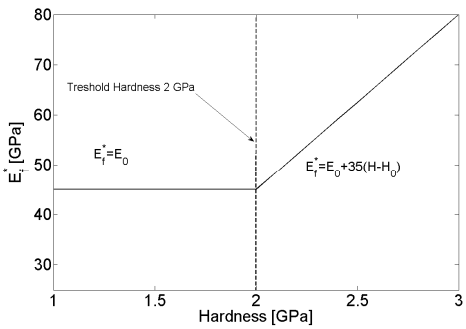


**Figure 6:** Young's Modulus of the chemical film as a function of the hardness ($E=E_o35(H-H_0)$ for $H > H_0$) (e.g. the maximum pressure applied to it). Figure is reproduced using the data presented in [32].

If now the contact pressure and displacement of the surface are determined the plastic strain of the chemical layer can be determined, of which only a certain percentage is reacted base material. To obtain a good approximation of

the actual amount, XPS can be used to get an average compound as a function of sputter depth curve as shown in Figure 7. This measurement originates from [39] and yields comparable results as given in [17, 23]. This suggests that different conditions only have a limited effect on the concentration of base material inside the tribo-chemical layer. If now the atomic percentage is used combined with the atomic radius of the different atoms present in the film a good estimation can be made of the volumetric percentage of base material present in the film. This method is indeed allowed since the film has an amorphous structure and thus the atomic radius gives a good representation of the size of the different atoms. The resulting function for the volumetric percentage is:

$$W_{perc}(\delta) = \frac{4.5\times10^{19}\delta^4 - 2.83\times10^{13}\delta^3 + 1.75\times10^{-7}\delta^2 + 0.001\delta}{h_{balance}} \quad (6)$$

Here $W_{perc}$ is the volumetric percentage base material, $\delta$ the plastic indentation of the chemical layer, $h_{balance}$ the layer thickness at which the system is in chemical balance.
For the systems used in this article is was found that the average film thickness was around 70 *nm* and the resulting volumetric percentage curve for this particular system is given in Figure 7-b. Now the volume loss can be calculated for each contact situation.

However, for each contact calculation this is then only done for one contact instance. This would yield that to calculate a reasonable sliding distance the computational times will be in the range of days. To solve this problem first the wear rate is determined using a characteristic length

$$K_{wear}(x,y) = \frac{h_{inst}(x,y)}{l} = \frac{W_{perc}(\varepsilon^{l}_{plzz} h_{balance})}{\frac{W_{wear}}{\Delta x \Delta y l} = \frac{\varepsilon^{l}_{plzz} h_{balance}}{l}} \quad (7)$$

Here $K_{wear}$ is the dimensionless wear parameter, $h_{inst}$ the height los for a single contact instance, $\varepsilon^{l}_{plzz}$ the plastic strain of the chemical layer in thickness direction and $l$ the characteristic contact length. This can then be rewritten to a specific wear rate:

$$k(x,y) = \frac{K(x,y)}{p(x,y)} \quad (8)$$

Which can be used to determine the profile change for each sliding increment:

$$h_{increment}(x,y) = k(x,y)p(x,y)\Delta s = K(x,y)\Delta s \quad (9)$$

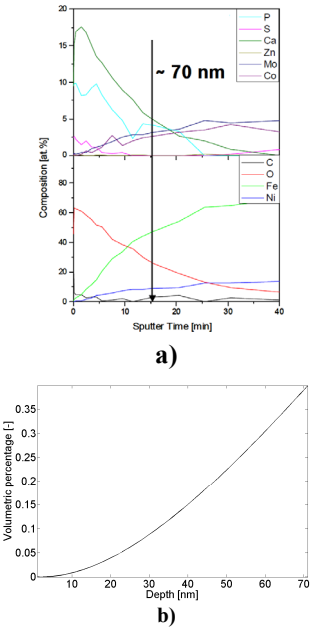


**Figure 7:** Chemical composition of the chemical layer present in the system being studied.

## RESULTS

In the first example a smooth ball sliding on a smooth disk is modeled. Both bodies are made of AISI 52100 steel, of which the material parameters are given in Table 2. The surface geometries of both bodies are shown in Figure 8-a and b. The load and speed used in the simulation under mild conditions is 10 *N* combined with a sliding velocity of 0.005 *m/s* as the other parameter of the test are given in Table 1. These conditions not only prevent "severe" wear from occurring it also limits both the contact pressure and temperature so they are in a range where the "Anvil Effect" and thermal effects are not present yet, as shown in Figure 8-c and d and offer a change to validate the model using reference value, reducing the change of using wrong values for the different parameters influencing wear. If now the contact is slid for half an hour for both the simulation and the experiment the resulting specific wear rate for the test becomes $8\times10^{-9}$ $mm^3/Nm$ and for the simulation $4\times10^{-9}$ $mm^3/Nm$ which are in very good agreement with each other. The next step is validating the model for an elliptical contact surface that has been run-in for 4 hours. The running-in procedure is as the normal running conditions. However, during running in it was shown that the surface run-out, rather than running in. As can be seen in Figure 9. As the disk started with the same surface roughness as shown in Figure 7 it can quite clearly be seen that both the disk and the roller are roughened during running. Since this process most certainly contains abrasive/ plowing wear it is currently not included in the model. Therefore, only the mild chemical wear is modeled, which is assumed to be the main wear mechanism after running-in. Since the pressure is increased to a level above 2 *GPa* the "Anvil Effect" needs to be considered for the simulations using the roller. As can be seen from the results presented in Table 1 the simulations and results concur quite well, validating the model.

| Test conditions | |
|---|---|
| $F_n\,[N]$ | 10 |
| $V\,[m/s]$ | 0.005 |
| $\Theta_{env}\left[^oC\right]$ | 25 |
| $\mu\,[-]$ | 0.14 |
| Geometrical entities | |
| $R_{ball}\,[m]$ | $2\times10^{-3}$ |
| $R_{weartrack}\,[m]$ | $47\times10^{-3}$ |
| $R_{cylinder\,x}, R_{cylinder\,y}[m]$ | $4\times10^{-3}$ , $26.67\times10^{-3}$ |
| Measurement results | |
| $k^{ball}_{measured}\left[mm^3/Nm\right]$ | $8\times10^{-9}$ |
| $k^{cylinder}_{measured}\left[mm^3/Nm\right]$ | $1.6\times10^{-8}$ |
| Calculation results | |
| $k^{ball}_{calc}\left[mm^3/Nm\right]$ | $4\times10^{-9}$ |
| $k^{cylinder}_{calc}\left[mm^3/Nm\right]$ | $9\times10^{-9}$ |

**Table 1**: Values used in the mild wear test and simulations.

| Material | $K\left[\frac{W}{mK}\right]$ | $\rho\left[\frac{kg}{m^3}\right]$ | $C_p\left[\frac{J}{kgK}\right]$ | $E[GPa]$ | $\nu[-]$ | $H[GPa]$ |
|---|---|---|---|---|---|---|
| AISI 52100 | 45 | 7800 | 470 | 210 | 0.3 | 6.6 |
| Case hardened steel | 45 | 7700 | 467 | 210 | 0.3 | 6 |

**Table 2:** Material parameters.

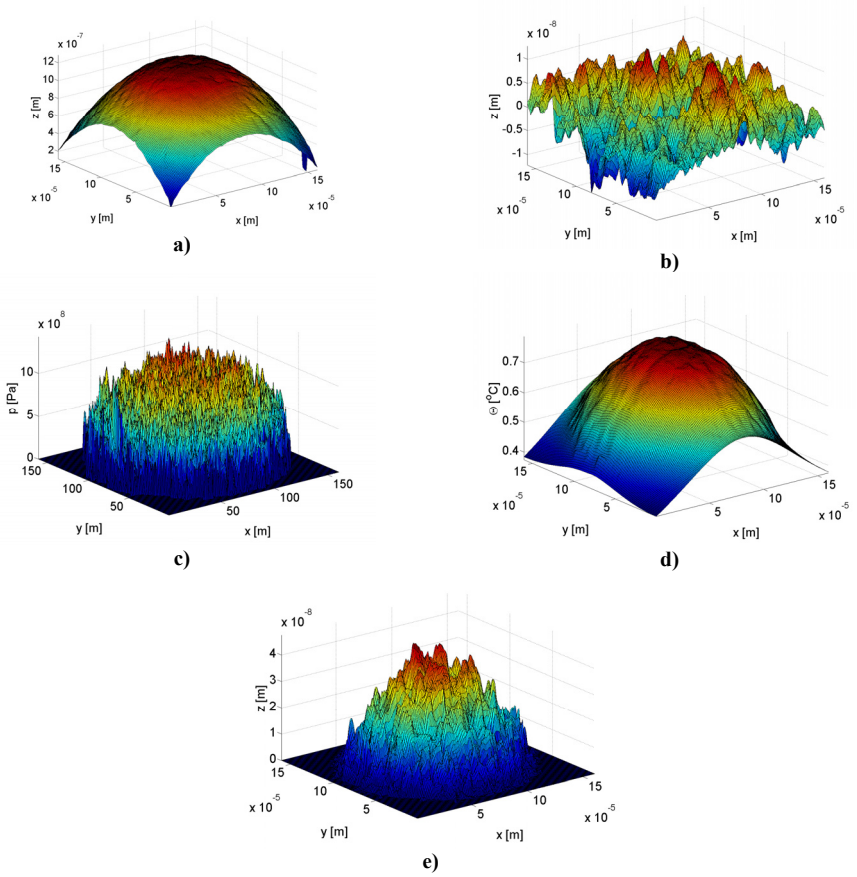


**Figure 8: a)** Surface topography of the ball and **b)** of the disk used during the experiments and simulations. **c)** Resulting pressure field and **d)** temperature field **e) w**ear volume after 10 *m* of sliding.

Next step is validating the thermal effects on the properties of the chemical layer as proposed. This will be done using measurements presented earlier in [5] of a polished cylinder combined with a hard turned disk. The disk is made of AISI 52100 steel of which the properties are given in Table 2 as are the properties of the case hardened steel for the disk. To validate the model under the most hostile circumstances the measurement point close to the transition point is used as a wear reference and the transition point itself is also predicted to validate the combination of the here proposed wear model in combination with the transition model. However, from the measurement results originating from [3] it can be concluded that not all tests where conducted under boundary lubrication conditions. As for the 400 $N$ measurement the coefficient of friction is in the mixed lubrication regime rather than in the boundary lubrication regime, as shown in Table 3.

From the measured transition points combined with thermal analyses done in earlier studies a critical temperature of around 200 $^{o}C$ was obtained for the lubricant [5]. Using this critical temperature, combined with a mesh of 240x240 elements and 150 sliding increments the transition points calculated are close to the

ones measured. If the wear widths close to the transition points, shown in Figure 10, are compared for the different load ands velocities it becomes quite clear that there are some differences in the value, however they are in the same range indicating the usefulness of the current model.

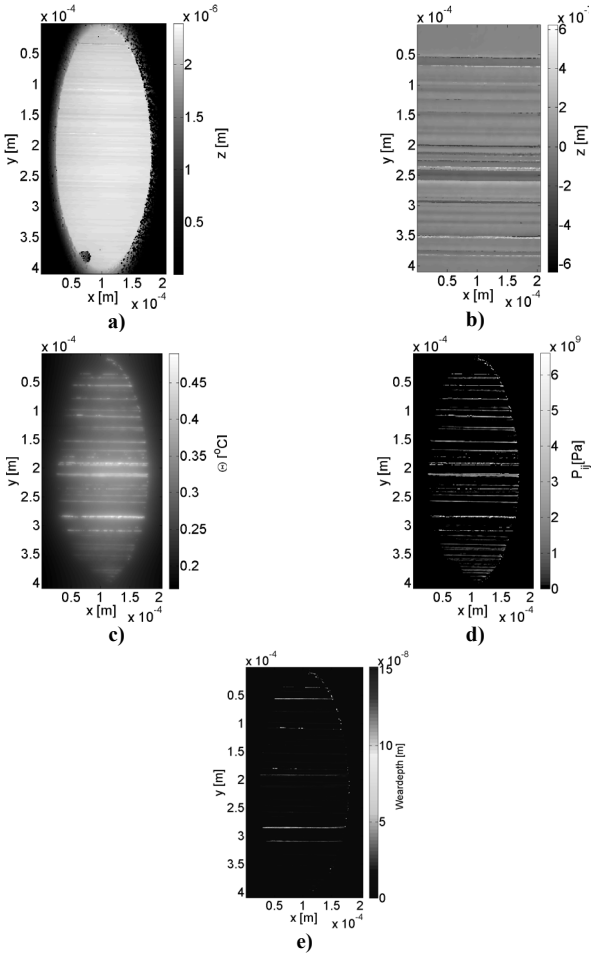


**Figure 9: a)** Surface profile of a roller run for 8 hours under the conditions given in `Table 1` **b)** Counter surface topography. **c)** Temperature field in the contact and **d)** Pressure field in the contact. **e)** Resulting wear depth.

| **Transition Points** | | | | |
|---|---|---|---|---|
| F | [*N*] | 700 | 550 | 400 |
| $V_{meas}$ | [*m/s*] | 3.25 | 5.75 | 9.75 |
| $V_{calc}$ | [*m/s*] | 3.25 | 6.5 | - |
| μ | [–] | 0.100 | 0.091 | 0.053 |
| $2b_{meas}$ | [μm] | 332 | 390 | 270 |
| $2b_{calc}$ | [μm] | 280 | 320 | - |

**Table 3:** Transition point for a commercial ZDDP oil at room temperature (25 °C).

A complete wear map including the transition from mild to severe wear for both a lubricated line contact (cylinder on disk) as for a lubricated run-in elliptical contact are calculated. For these calculations it is assumed that the coefficient of friction within in the mild wear regime is constant. For the run in elliptical contact it is set to 0.15 and for the cylinder on disk setup to 0.1 as these values are good representations of the values obtained

during the measurements, see Tables 2 and 3. This yields small difference for the obtained transition points compared with the results given in Table 3. The resulting wear map for the run in elliptical contact is presented in Figure 11. The wear map consists of a contour plot with lines of constant specific wear rate as a function of normal load and sliding velocity, the so called "iso-wear" lines. Here it seems not logical that the specific wear rate after decreasing with load it increases again, especially in the low velocity regime. However, this effect can be explained by the hardening effect ("anvil effect") vs. the softening effect caused by the temperature. The combined average effect of the pressure and temperature are presented in Figure 12-b. Here it is also shown in Figure 12-b that the wear volume indeed does increase with increasing load/velocity combination as one expects, however trough the definition of the specific wear rate:

$$k = \frac{W}{Fs} \tag{10}$$

the wear rate shows a more unexpected relationship with the normal force and sliding velocity. This can be explained by the average "compensation" through temperature and pressure, as the lines are directed almost perpendicular to the transition line. This is due to the fact that first the pressure hardens the layer at high pressures and low speeds and the higher the speed the more pronounced the softening becomes, nullifying the hardening.

For the lubricated line contact (cylinder on disk setup) two different simulations are done. One with the load put instantaneously on the new surfaces of which the results are presented in Figure 14. The second simulation is done with the load profile shown in Figure 1 and the resulting wear map is presented in Figure 13.

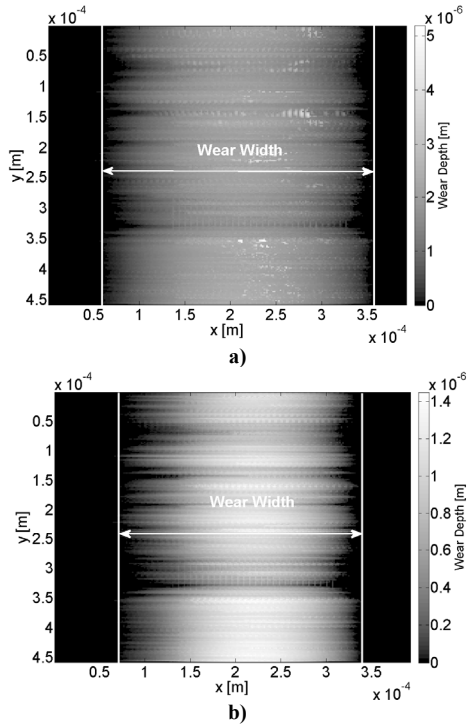


**Figure 10:** Wear volume expressed as a height profile for **a)** a combination of 550 N and 6 *m/s* and **b)** 700 N 3.5 *m/s*

Here the influence of running in becomes quite clear as the transition from mild to severe wear shifts towards higher load/velocity combination. Another interesting phenomenon seen is that the "strange" iso-wear lines are now gone and the lines are laying more along the transition line, this suggest a higher influence of the thermal softening than the mechanical hardening. This probably caused by the fact that the in a line contact the heat and pressure is distributed more evenly and the average mechanical properties are thus lowered more compared to concentrated contact is the case as for an elliptical contact.

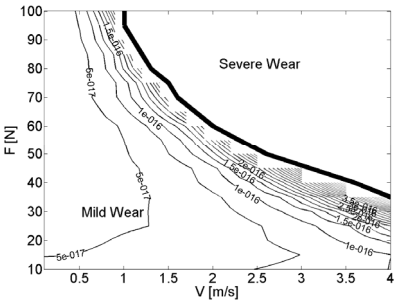


**Figure 11:** Transition diagram for the run-in elliptical contact including the specific wear rate.

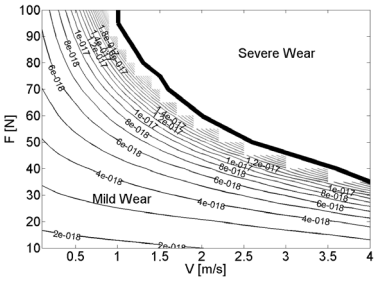


**a)**

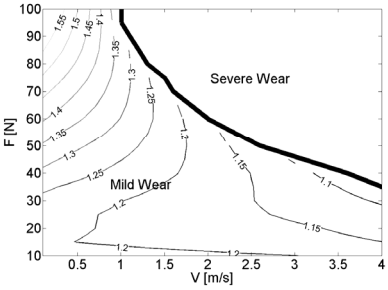


**b)**

**Figure 12: a)** Wear volume vs. sliding velocity and normal force. **b)** The combined effect of the temperature and pressure on the elastic properties of the chemical film normalized with the reference value at zero pressure and room temperature ($E_0$)

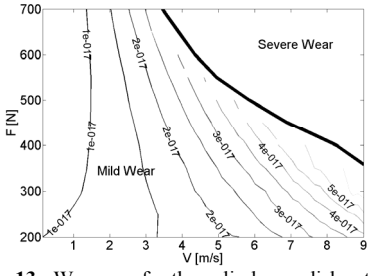


**Figure 13**: Wearmap for the cylinder on disk setup using a linear increase of the normal force as depicted in Figure 1.

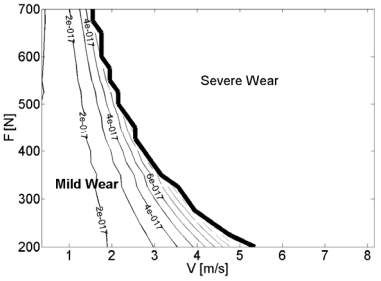


**Figure 14:** Wear map for the cylinder on disk setup if new surfaces are used with instantaneous load applied.

## CONCLUSIONS

In this study a novel model is presented to deal with mild wear in the boundary lubrication regime. The model uses the basic assumption that the improved wear resistance of a contact lubricated with additive rich oil originates from the sacrificial layer formed by the additive package on top of the native oxide layer. Since the thickness of the layer is very limited the model assumes that the "environment" which the layer needs to withstand is determined by the properties of the bulk material, while the mechanical properties of the layer itself determines the amount of material removed. The model is validated for different contact conditions and the results show that the model is capable of predicting the amount of mild wear occurring in well protected systems. To expand the practical implementation of the model it is combined with the theory that the transition from mild to severe wear is a thermal phenomenon. This enables the model to not only estimate the amount of wear present in a system but also if the system will fail, creating a complete wear map.

## REFERENCES

[1] A. William Ruff, Friction and Wear Data Bank, Modern Tribology Handbook, Two Volume Set, CRC Press. 2000.

[2] H. Blok: Seizure Delay Method for Determining the Protection Against scuffing Afforded by Extreme

Pressure Lubricants SAE Journal. 44 193-204 (1939).
[3] M.van Drogen, The Transition to adhesive wear of Lubricated Concentrated Contacts, PhD Thesis, University of Twente www.tr.ctw.utwente.nl, 2005 p 105
[4] R. Bosman: Mild microscopic wear in the boundary lubrication regimeGeringer mikroskopischer Verschleiß geschmierter Kontakte in Grenzflächen. Materialwissenschaft und Werkstofftechnik. 41 29-32 (2010).
[5] R. Bosman, D.J. Schipper: On the transition from mild to severe wear of lubricated, concentrated contacts: The IRG (OECD) transition diagram. Wear. 269 581-589 (2010).
[6] M.A. Nicholls, T. Do, P.R. Norton, M. Kasrai, G.M. Bancroft: Review of the lubrication of metallic surfaces by zinc dialkyl-dithiophosphates. Tribology International. 38 15-39 (2005).
[7] M. Reichelt, U. Gunst, T. Wolf, J. Mayer, H.F. Arlinghaus, P.W. Gold: Nanoindentation, TEM and ToF-SIMS studies of the tribological layer system of cylindrical roller thrust bearings lubricated with different oil additive formulations. Wear. 268 1205-1213 (2010).
[8] D. Shakhvorostov, B. Gleising, R. Büscher, W. Dudzinski, A. Fischer, M. Scherge: Microstructure of tribologically induced nanolayers produced at ultra-low wear rates. Wear. 263 1259-1265 (2007).
[9] D. Shakhvorostov, K. Pohlmann, M. Scherge: Structure and mechanical properties of tribologically induced nanolayers. Wear. 260 433-437 (2006).
[10] W. Yan, L. Fang, Z. Zheng, K. Sun, Y. Xu: Effect of surface nanocrystallization on abrasive wear properties in Hadfield steel. Tribology International. 42 634-641 (2009).
[11] M.Z. Huq, P.B. Aswath, R.L. Elsenbaumer: TEM studies of anti-wear films/wear particles generated under boundary conditions lubrication. Tribology International. 40 111-116 (2007).
[12] M. Scherge, J.M. Martin, K. Pohlmann: Characterization of wear debris of systems operated under low wear-rate conditions. Wear. 260 458-461 (2006).
[13] R. Bosman, D.J. Schipper: Running in of systems protected by additive rich oils. Tribology Letters. In Production (2010).
[14] M.A. Nicholls, P.R. Norton, G.M. Bancroft, M. Kasrai, T. Do, B.H. Frazer, G.D. Stasio: Nanometer scale chemomechanical characterizaton of antiwear films. Tribology Letters. 17 205-336 (2003).
[15] Z. Zhang: Tribofilms generated from ZDDP and DDP on steel surfaces:Part I. Tribology Letters. 17 211-220 (2005).
[16] J.P. Ye, S. Araki, M. Kano, Y. Yasuda: Nanometer-scale mechanical/structural properties of molybdenum dithiocarbamate and zinc dialkylsithiophosphate tribofilms and friction reduction mechanism. Japanese Journal of Applied Physics Part 1-Regular Papers Brief Communications & Review Papers. 44 5358-5361 (2005).
[17] J.M. Martin, C. Grossiord, T. Le Mogne, S. Bec, A. Tonck: The two-layer structure of zndtp tribofilms Part 1: AES, XPS and XANES analyses. Tribology International. 34 523-530 (2001).
[18] M. Kasrai, S. Marina, B.G. Micheal, Y.E. S. Ray: X-ray adsorption study of the effect of calcium sulfonate on antiwear film formation generated from neutral and basic ZDDPs: Part 1 -Phosporus species. Tribology Transactions. 46 434-442 (2003).

[19] M. Aktary, M.T. McDermott, G.A. McAlpine: Morphology and nanomechanical properties of ZDDP antiwear films as a function of tribological contact time. Tribology Letters. 12 155-162 (2002).
[20] M.A. Nicholls, G.M. Bancroft, P.R. Norton, M. Kasrai, G. De Stasio, B.H. Frazer, L.M. Wiese: Chemomechanical properties of antiwear films using X-ray absorption microscopy and nanoindentation techniques. Tribology Letters. 17 245-259 (2004).
[21] J.P. Ye, M. Kano, Y. Yasuda: Evaluation of nanoscale friction depth distribution in ZDDP and MoDTC tribochemical reacted films using a nanoscratch method. Tribology Letters. 16 107-112 (2004).
[22] H.B. Ji, M.A. Nicholls, P.R. Norton, M. Kasrai, T.W. Capehart, T.A. Perry, Y.T. Cheng: Zinc-dialkyl-dithiophosphate antiwear films: dependence on contact pressure and sliding speed. Wear. 258 789-799 (2005).
[23] S. Bec, A. Tonck, J.M. Georges, R.C. Coy, J.C. Bell, G.W. Roper: Relationship between mechanical properties and structures of zinc dithiophosphate anti-wear films. Proceedings of the Royal Society of London Series a-Mathematical Physical and Engineering Sciences. 455 4181-4203 (1999).
[24] K. Komvopoulos, V. Do, E.S. Yamaguchi, P.R. Ryason: Nanomechanical and nanotribological properties of an antiwear tribofilm produced from phosphorus-containing additives on boundary-lubricated steel surfaces. Journal of Tribology-Transactions of the Asme. 126 775-780 (2004).
[25] O.L. Warren: Nanomechanical properties of films derived from zinc dialkyldithiophosphate. Tribology Letters. 4 189-198 (1998).
[26] C. Minfray, J.M. Martin, C. Esnouf, T. Le Mogne, R. Kersting, B. Hagenhoff: A multi-technique approach of tribofilm characterisation. Thin Solid Films. 447 272-277 (2004).
[27] G.M. Bancroft, M. Kasrai, M. Fuller, Z. Yin, K. Fyfe, K.H. Tan: Mechanisms of tribochemical film formation: stabilityof tribo- and thermally-generated ZDDP films. Tribology Letters. 3 47-51 (1997).
[28] K. Topolovec-Miklozic, T. Forbus, H. Spikes: Film thickness and roughness of ZDDP antiwear films. Tribology Letters. 26 161-171 (2007).
[29] R. Bosman, D.J. Schipper: Running-In of Systems Protected by Additive-Rich Oils. Tribology Letters. 1-20 (2010).
[30] C. Minfray, J.-M. Martin, T. Lubrecht, M. Belin, T.L. Mogne, M.P.G.D. D. Dowson, A novel experimental analysis of the rheology of ZDDP tribofilms, Tribology and Interface Engineering Series, Elsevier. 2003, pp. 807-817.
[31] R. Bosman, D.J. Schipper: Running-In of Systems Protected by Additive-Rich Oils. Tribology Letters. 1-20 (2010).
[32] G. Pereira, D. Munoz-Paniagua, A. Lachenwitzer, M. Kasrai, P.R. Norton, T.W. Capehart, T.A. Perry, Y.-T. Cheng: A variable temperature mechanical analysis of ZDDP-derived antiwear films formed on 52100 steel. Wear. 262 461-470 (2007).
[33] K. Demmou, S. Bec, J.L. Loubet, J.M. Martin: Temperature effects on mechanical properties of zinc dithiophosphate tribofilms. Tribology International. 39 1558-1563 (2006).
[34] K. Demmou, S. Bec, J.L. Loubet (2007) Effect of hydrostatic pressure on the elastic properties of ZDTP tribofilms. Cornell University Library.
[35] J. Rottler, M.O. Robbins: Yield conditions for deformation of amorphous polymer glasses. Physical Review E. 64 051801 (2001).

[36] I.A. Polonsky, L.M. Keer: A numerical method for solving rough contact problems based on the multi-level multi-summation and conjugate gradient techniques. Wear. 231 206-219 (1999).
[37] S. Liu, Q. Wang, G. Liu: A versatile method of discrete convolution and FFT (DC-FFT) for contact analyses. Wear. 243 101-111 (2000).
[38] R. Bosman, M.B.de Rooij: Transient Thermal Effects and Heat Partition in Sliding Contacts. Journal of Tribology. 132 021401 (2010).
[39] A. Voght, Tribological Reactions Layers in BL contacts. 2008, Bosh-CR: Schillerhohe.

Stellingen behorende bij het proefschrift:
"Mild Microscopic Wear Modeling in the Boundary Lubrication Regime".

1) Voor een groot aantal vrouwen geldt hetzelfde als voor een slecht convergerend algoritme; het blijft maar om het eindpunt heen draaien zonder er te komen.

2) De Multi-Grid methode is een verouderde en onnodig ingewikkelde methode om de rekentijden in contact simulaties die gebruik maken van een halfoneindig lichaam aanname te beperken.

3) Een goed antislijtage additief is corrosief. (zie dit proefschrift sectie 2.2)

4) Als het slagen van promoveren afhangt van de mate waarin iemand zelfstandig onderzoek heeft gedaan, neemt de kans van slagen af met iedere naam genoemd in het dankwoord voor een bijdrage aan het onderzoek.(zie dankwoord dit proefschrift)

5) Een goede manager moet inhoudelijk verstand hebben van het proces dat hij moet aansturen. De vraag wordt dan echter hoe kan iemand die een opleiding heeft gevolgd waar de nadruk ligt op management zelf ooit iets goed aansturen?

6) Als dit proefschrift op absorberend papier was gedrukt zou het meerdere doeleinden hebben gehad.

7) Zoogdieren hebben al bewezen dat 1+1 niet altijd 2 is.

8) Als een ezel zich nooit twee keer aan de zelfde steen stoot is hij slimmer dan menig mens.

9) Het succes van een opleiding waarbij het uiterlijk vertoon verkozen wordt boven functionaliteit is een goede weerspiegeling van de hedendaagse oppervlakkigheid van een samenleving waarin een gedegen inhoud niet meer van belang is, als het er maar leuk uitziet.

10) Als je het leven van mensen omdraait, eindig je meestal met het hoogtepunt van een ander.